Synthese neuer mono-, gemischt-valenter und bimetallischer Metall-organischer Gerüstverbindungen auf Basis von Kupfer und 4-(3,5-dimethyl-1*H*-pyrazol-4-yl)benzoesäure

Inaugural-Dissertation

zur Erlangung des Doktorgrades
der Mathematisch-Naturwissenschaftlichen Fakultät
der Heinrich-Heine-Universität Düsseldorf

vorgelegt von

Saskia Menzel
aus Düsseldorf

Düsseldorf, März 2022

aus dem Institut für Anorganische Chemie und Strukturchemie I
der Heinrich-Heine-Universität Düsseldorf

Gedruckt mit der Genehmigung der
Mathematisch-Naturwissenschaftlichen Fakultät der
Heinrich-Heine-Universität Düsseldorf

Berichterstatter:

1. Prof. Dr. Christoph Janiak

2. Prof. Dr. Christian Ganter

Tag der mündlichen Prüfung: 13.05.2022

Eidesstattliche Erklärung

Ich versichere an Eides statt, dass die Dissertation von mir selbstständig und ohne unzulässige fremde Hilfe unter der Beachtung der „Grundsätze zur Sicherung guter wissenschaftlicher Praxis” an der Heinrich-Heine-Universität Düsseldorf erstellt worden ist. Die aus fremden Quellen direkt oder indirekt übernommenen Gedanken sind als solche kenntlich gemacht. Die Arbeit wurde bisher weder im Inland noch im Ausland in gleicher oder ähnlicher Form einer anderen Prüfungsbehörde vorgelegt. Es wurden keine früheren erfolglosen Promotionsversuche unternommen.

....

Ort, Datum Unterschrift

Danksagung

An erster Stelle möchte ich meinem Doktorvater Herrn Prof. Dr. Christoph Janiak danken, welcher mir die Möglichkeit gegeben hat meine Dissertation in seinem Arbeitskreis anzufertigen. Ich bedanke mich für den wissenschaftlichen Freiraum in Bezug auf Forschungs- und Projektwahl, die konstruktiven Diskussionen sowie Hilfestellungen beim Anfertigen der Publikationen während meiner Zeit in seinem Arbeitskreis.

Herrn Prof. Dr. Christian Ganter danke ich recht herzlich für die Übernahme des Koreferates. Außerdem möchte ich mich bei Ihnen für die Übernahme des Mentorats bedanken. Ich habe Ihre stetige Ansprechbarkeit und fachlichen Rat über das ganze Studium hinweg sehr geschätzt.

Herrn Prof. Dr. Gerhard Hägele danke ich für die interessanten Projekte, die einen Teil meiner Dissertation ausgemacht haben. Anhand der tollen und engen Zusammenarbeit konnte ich über den Tellerrand hinausschauen und tiefere Einblicke in die NMR-Spektroskopie erhalten.

Herrn Dr. Ishtvan Boldog danke ich für seine große Hilfsbereitschaft und Ideenreichtum.

Des Weiteren möchte ich mich bei den angestellten Mitarbeitern Frau Jutta Bourgeois, Frau Birgit Tommes, Frau Annette Ricken und Herrn Marcell Demandt für die analytischen Untersuchungen und Ihre Ansprechbarkeit bei allen anderen größeren und kleineren Problemchen bedanken. Mein besonderer Dank geht an Frau Beate Rau für die tollen gemessenen NMR-Spektren.

Meiner Bachelorstudentin Aysenür Gönülalan und meinem Masterstudenten Dustin Jordan danke ich für Ihr Vertrauen in Bezug auf das Anfertigen Ihrer Arbeiten unter meiner Obhut. Dustin du bist absolut ein würdiger Nachfolger und ich wünsche dir alles Gute!

Ein weiterer Dank gilt meinen Bürokollegen Simon Millan, Anna Goldmann, Ülkü Gökcam-Demir, Serkan Gökpinar und Daniel Komisarek. Ihr seid mit mir durch viele wissenschaftliche und private Höhen und Tiefen gegangen und standet stets mit Rat und Tat zur Seite.

Aber auch den anderen Kollegen Alexander Nuhnen, Alexa Schmitz, Simon-Patrick Höfert, Carsten Schlüsener, Moritz Steinert, Secil Öztürk, Philipp Brandt, Stefanie Bügel, Bastian Moll, Christian Jansen, Alexander Spieß, Karsten Klauke, Yang-Yang Sun, Jun Liang und Dennis Woschko möchte ich meinen Dank für die Hilfsbereitschaft und das Ablenken vom Promotionsstress aussprechen.

Meinem Lebensgefährten und Fels in der Brandung Chris Hoffmann bin ich zu tiefem Dank verpflichtet. Du warst die ganze Zeit während des Studiums und der Promotion über an meiner Seite und hast mir Mut, Zuversicht und Ruhe gegeben, wenn ich sie gebraucht habe. Darüber hinaus konnte ich mich immer bei organischen Problemen an dich wenden. Ohne dich hätte mich die OC manches mal um den Verstand gebracht. Mein Kekschen ich liebe Dich!

Zu guter Letzt danke ich meinen Eltern Helga und Thomas Menzel für Ihre stetige Unterstützung, bedingungslosen Rückhalt und Rücksichtnahme während des ganzen Studiums. Ohne euch wäre diese Arbeit nicht möglich gewesen. Ich danke euch von ganzem Herzen.

„Der Wille gestaltet den Menschen, zum Erfolg braucht er jedoch Mut und Ausdauer.“

Bruce Lee

Kurzzusammenfassung

Bifunktionelle Liganden bestehend aus Carboxylat und Pyrazolat sind aufgrund ihres harten/weichen Charakters prädestiniert dafür vielfältige Koordinationsgeometrien im Festkörper einzugehen. Im Rahmen der vorliegenden Arbeit wurde der N,O-heteroditope, bifunktionelle Ligand 4-(3,5-dimethyl-1*H*-pyrazol-4-yl)benzoesäure (H_2mpba) zur Synthese neuer Kupfer basierter Metall-organischer Gerüstverbindungen verwendet.

Es wurden die beiden neuen 2D MOFs **sql**-$[Cu(Hmpba)_2]\cdot L$ (L= DMF oder ACN), welche supramolekulare Isomere zum bereits literaturbekannten 3D **lvt**-$[Cu(Hmpba)_2]\cdot 4MeOH\cdot 1H_2O$ sind, synthetisiert. Die Verbindungen **sql**-DMF und **sql**-ACN erwiesen sich bei der Charakterisierung mittels 195 K CO_2-Sorptionsmessung als poröse Materialien (**sql**-DMF-act., **sql**-ACN-act.) mit Sättigungsaufnahmen von 111 cm^3/g und 90 cm^3/g. Beide Materialien zeigten gute CO_2- und CH_4-Adsorptionseigenschaften bei 273 K und 293 K. Anhand der Wasser- und Ethanolsorption konnten die Verbindungen als hydrophob klassifiziert werden. Das **lvt**-$[Cu(Hmpba)_2]\cdot 4MeOH\cdot 1H_2O$ Netzwerk konnte ebenfalls aktiviert und als poröses Material klassifiziert werden. Über die CO_2-Sorptionsmessung bei 195 K konnte eine Sättigungsaufnahme von 113 cm^3/g bestimmt werden. Über die Ethanol- und Wassersorptionsmessung konnte das Material als hydrophil klassifiziert werden. Darüber hinaus konnte in der **lvt**-$[Cu(Hmpba)_2]\cdot 4MeOH\cdot 1H_2O$ Struktur das Kristalllösungsmittel vollständig durch Wasser ersetzt werden, so dass ein reines Wassernetzwerk **lvt**-H_2O erhalten werden konnte. Dieses enthielt 3D-Anordnungen von S_4-symmetrischen $(H_2O)_{20}$-Clustern.

Mit Hilfe desselben Liganden wurde ein gemischt-valentes, kupferhaltiges 1D-Koordinationspolymer $[Cu^{II}\{Cu^{I}_3(Hmpba)(mpba)_2\}DMF]\cdot{\sim}3DMF$ erhalten, welches als zentralen Baustein einen $\{Cu^{I}_3(Hmpba)(mpba)_2\}^{2-}$ Metallo-Linker enthält, bei welchem gemäß des HSAB-Prinzips das verhältnismäßig weichere Pyrazolat das weichere Cu^{I} linear koordiniert. Dieser Metallo-Linker verbindet dann die härteren Cu^{II}-Ionen über seine härteren Carboxylat-Gruppen zu einer Kettenstruktur. Zwei Cu^{II}-Ionen bilden eine Schaufelradeinheit ähnlich derer von HKUST-1. Die parallelen Ketten sind durch das gemeinsame $R_2^2(8)$-Wasserstoffbrückenmotiv der einfach deprotonierten Carboxylat-Gruppe des Linkers zu supramolekularen Schichten verbunden. Diese Schichten werden durch Cu^{I}-Cu^{I}-Wechselwirkungen zu einer supramolekularen 3D-Anordnung weiter verbunden.

Aufbauend auf dieser Arbeit, wurden dann drei neue bimetallische MOFs $[Me_2NH_2][Zn_4\{Cu^I_3(mpba)_3\}_3Me_2NH(DMF)_2]$ (**1**), $[Zn_6\{Cu^I_3(mpba)_3\}_4(DMF)_5$ (**2**) und $[\{Zn_3\{Cu^I_3(mpba)_3\}_2(DMF)_3(H_2O)][Zn_4(\mu_4\text{-}O)\{Cu^I_3(mpba)_3\}_2(H_2O)_4]$ (**3**) mit verschiedenen Zn^{II}-Koordinationsumgebungen hergestellt umso ein potenziell poröses Material zu erhalten. Die drei erhaltenen Verbindungen bestehen alle aus den dreieckigen und dreikernigen 3-c $\{Cu^I_3(mpba)_3\}^{3-}$ Metallzyklus, welcher als Tricarboxylat-Linker zwischen den verschiedenen 4-6-c $\{Zn_x(O)_y(COO)_z\}$ (x=2-4, y=0-1, z=4-6) Sekundärbausteinen fungiert. Die $\{Cu^I_3(pz)_3\}$-Anteile (pz=pyrazolat) in allen drei Strukturen sind durch kuprophile Wechselwirkungen in unendliche Säulen gestapelt. Die geometrisch variablen Zn-Cluster passen sich dabei der gestapelten Orientierung der Carboxylatgruppen der $\{Cu^I_3(mpba)_3\}^{3-}$ Metallzyklen an. Als Resultat können die gebildeten Strukturen als Ableitung gestapelter, wabenförmiger, hexagonaler Netze (**hcb**= honeycomb) durch ‘Fusion’ alternierender gestapelter Knoten betrachtet werden. Die Verbindung **3** (**3**-act.) stellte sich bei der Charakterisierung als permanent poröses Material mit einer BET Oberfläche von 762 m^2/g, gemessen über eine 87 K Ar-Sorptionsmessung, und guten CO_2- und CH_4-Adsorptionseigenschaften bei 273 K und 293 K heraus.

Abstract

Bifunctional ligands, consisting of carboxylate and pyrazolate, are predestined to form diverse coordination geometries in the solid state due to their hard/soft character. In this work, the N,O-heteroditopic, bifunctional ligand 4-(3,5-dimethyl-1*H*-pyrazol-4-yl)-benzoic acid) (H_2mpba) was used to synthesize new metal-organic frameworks.

The two novel 2D MOFs **sql**-[Cu(Hmpba)$_2$]-L (L= DMF or ACN) were synthesized, which are supramolecular isomers to 3D **lvt**-[Cu(Hmpba)$_2$]·4MeOH·1H_2O. The material **sql**-DMF and **sql**-ACN are porous materials (**sql**-DMF-act., **sql**-ACN-act.) with Lagmuire surface areas of 111 cm^3/g and 90 cm^3/g, respectively, using a 195 K CO_2 sorption measurement. Both materials showed good CO_2 and CH_4 adsorption properties and could be classified as hydrophobic materials based on water and ethanol sorption measurements. Additionally, **lvt**-[Cu(Hmpba)$_2$]·4MeOH·1H_2O could also be activated and classified as porous material by CO_2 sorption measurement at 195 K with a Lagmuire surface area of 113 cm^3/g. Based on ethanol and water sorption measurements, this material could be classified as hydrophilic. Furthermore, in the **lvt**-[Cu(Hmpba)$_2$]·4MeOH·1H_2O structure, the crystalline solvent was completely replaced by water, resulting into a pure water network **lvt**-H_2O, which contained 3D arrays of S_4-symmetric $(H_2O)_{20}$ clusters.

In addition, a mixed-valent copper-containing 1D coordination polymer [Cu^{II}{Cu$^{I}_3$(Hmpba)(mpba)$_2$}DMF]·~3DMF was obtained by using H_2mpba, which contains a {Cu$^{I}_3$(Hmpba)(mpba)$_2$}$^{2-}$ metallo-linker as the central building block. According to the HSAB concept, the relatively softer pyrazolate coordinates linear the softer Cu^{I}. This metallo-linker linked the harder Cu^{II} ions with its harder carboxylate groups to form a chain structure. Two Cu^{II} ions form a paddle-wheel unit similar to HKUST-1. The parallel chains form supramolecular layers by the common $R_2^2(8)$ hydrogen bond motif of the single deprotonated carboxylate group of the linker. These layers were further connected by Cu^{I}-Cu^{I} interactions to form a 3D supramolecular arrangement.

Based on this results, three novel bimetallic MOFs [Me_2NH_2][Zn$_4${Cu$^{I}_3$(mpba)$_3$}$_3$$Me_2$NH(DMF)$_2$] (**1**), [Zn$_6${Cu$^{I}_3$(mpba)$_3$}$_4(DMF)_5$] (**2**) and [{Zn$_3${Cu$^{I}_3$(mpba)$_3$}$_2(DMF)_3$($H_2O$)][Zn$_4$($\mu_4$-O){Cu$^{I}_3$(mpba)$_3$}$_2$($H_2O$)$_4$] (**3**)) with different Zn^{II} coordination environments were synthesized to get a potential porose compound. All the three compounds contain the triangular and trinuclear 3-c {Cu$^{I}_3$(mpba)$_3$}$^{3-}$ metal cycle, which act as a tricarboxylate linker between the 4-6-c {Zn$_x$(O)$_y$(COO)$_z$} (x=2-4, y=0-1, z=4-6) secondary building units. The {Cu$^{I}_3$(pz)$_3$} (pz=pyrazolate) moieties in all three structures are stacked into infinite columns by cuprophilic interactions. The

geometrically variable Zn clusters thereby match the stacked orientation of the carboxylate groups of the $\{Cu^{I}_{3}(mpba)_{3}\}^{3-}$ metal cycles. On this point of view, the formed structures could consider as derivatives of stacked hexagonal networks (**hcb** = **honecomb**) by 'fusion' of alternating stacked nodes. The compound **3** (**3**-act.) was characterized by 87 K Ar sorption measurement as a meso-microporous material with a BET surface area of 762 m^2/g. Furthermore, the material showed good CO_2 and CH_4 adsorption properties.

Publikationsliste

Saskia Menzel, Simon Millan, Simon-Patrick Höfert, Alexander Nuhnen, Serkan Gökpinar, Alexa Schmitz and Christoph Janiak: Increase of network hydrophilicity from **sql** to **lvt** supramolecular isomers of Cu-MOFs with the bifunctional 4-(3,5-dimethyl-1H-pyrazol-4-yl)benzoate linker
Dalton Trans. **2020**, *49*, 12854-12864. DOI: 10.1039/d0dt02642e

Saskia Menzel, Simon-Patrick Höfert, Secile Öztürk, Alexa Schmitz, Christoph Janiak: A mixed-valence copper(I/II) coordination polymer directed with a bifunctional soft-hard pyrazolate-carboxylate ligand
Z. Anorg. Allg. Chem. **2021**, *647*, 803-808. DOI: 10.1002/zaac.202000428

Saskia Menzel*, Tobias Heinen*, Istvan Boldog, Thi Hai Yen Beglau, Shanghua Xing, Alex Spieß, Dennis Woschko and Christoph Janiak: Stacked hexagonal metal-organic framework structures through cuprophilic interactions based on a triangular $Cu(I)_3$(pyrazolate-benzoate)$_3$ metallolinker
Manuskript akzeptiert bei CrystEngComm. DOI: 10.1039/d2ce00268j
* geteilte Erstautorenschaft

Saskia Menzel, Konstantinos D. Demadis, Christoph Janiak, Gerhard Hägele : The fully deprotonated anion of 1,3,5-benzenetriphosphonicacid: ^{1}H, ^{31}P, and ^{13}C{^{1}H} NMR and some comments on corresponding $[AX]_3$ and AXX'_2 spin systems and spectra
Phosphorus, Sulfur, and Silicon and the Related Elements **2020**, *195*, 830-835.
DOI: 10.1080/10426507.2020.1757675

Abkürzungsverzeichnis

1D	eindimensional
2D	zweidimensional
3D	dreidimensional
BTC	1,3,5-Benzoltricarboxylat
BIPY	4,4‘-Bipyridin
DMF	*N,N*-Dimethylformamid
DMSO	Dimethylsulfoxid
FDM	Fudan Material
H_2dmpz-ba	3,5-dimethyl-4-caboxypyrazole
H_2PyC	4-pyrazolcarbonsäure
HSAB-Konzept	Hard and Soft Acids and Bases (Konzept der Harten und Weichen Säuren und Basen)
IRMOF	IsoReticular Metal-Organic Framework (lat. reticulum = Netz)
IUPAC	International Union of Pure and Applied Chemistry
MOF	Metal-organic Framework (Metall-organische Gerüstverbindung)
NMP	*N*-Methyl-2-pyrrolidon
PCN	Porous Coordination Network
ppm	Parts per million
PSM	Post synthetic modification
SBU	Secondary building unit
VOC	Volatile organic compounds (flüchtige organische Verbindungen)

Inhalt

1 Einleitung

1.1 Metall-organische Gerüstverbindungen

Metall-organische Netzwerke, welche im Englischen als *metal-organic frameworks* (MOFs) bezeichnet werden, bestehen aus der Kombination von ein- oder mehrwertigen Metallionen und funktionalisierten, organischen Liganden. Sie werden nach einer Definitionsempfehlung der IUPAC als potenziell poröse zwei- und dreidimensionale Koordinationsnetzwerke bezeichnet.[1,2] Die Koordinationsnetzwerke selbst, sind als eine Unterkategorie der Koordinationspolymere zu verstehen, dessen Ursprung in der Synthese von Metall-Cyanid-Netzwerken wie dem Berliner Blau[3] und den Hofmann-Clathraten [4,5] liegt. Die klassischen Werner-Komplexe der Zusammensetzung [M(4-Methylpyridin)$_4$(SCN)$_2$] (M = Co^{2+}, Ni^{2+} oder Mn^{2+}) gelten als Vorreiter kristalliner Koordinationspolymeren mit permanenter Porosität und der Adsorptionsmöglichkeit von Gasen.[6] Dementsprechend ergibt sich eine hierarchische Begriffsabfolge beginnend mit dem Koordinationspolymer über das Koordinationsnetzwerk bis hin zum MOF (Abbildung 1).[2]

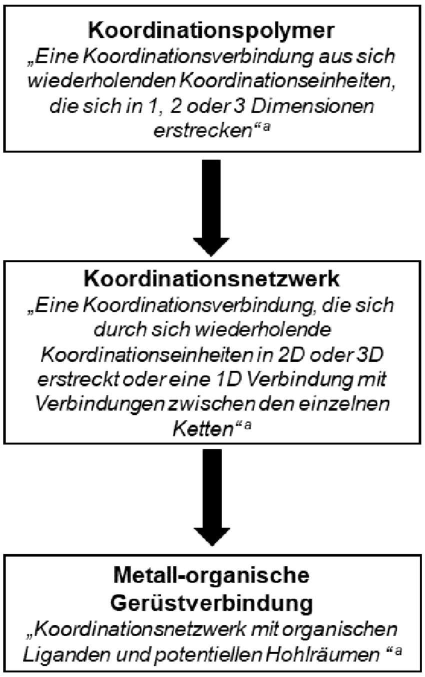

Abbildung 1: Schema zur hierarchischen Begriffsterminologie der Koordinationspolymere, Koordinationsnetzwerke und Metall-organischen Gerüstverbindung. Quelle: R.A. Fischer, *Angew. Chem.* **2014**, *126*, 7209-7214.

Der Begriff *metal-organic framework* selbst wurde erstmals von *Yaghi et al.* im Jahre 1995 in Publikationen verwendet, um die beiden porösen 3D-Netzwerke Cu^{II}-BIPY (BIPY= 4,4‘-Bipyridin) und Co^{II}-BTC (BTC = 1,3,5-Benzoltricarboxylat) zu beschreiben.[7,8] Das Vorhandensein von *potenziellen Hohlräumen*[1,2] in den Materialien weitet die ursprüngliche Definition der MOFs auch auf Materialien mit dynamischer Porosität aus.[9] Denn diese kann durch äußere Einflüsse wie Druck, Temperatur oder Gastmoleküle beeinflusst werden. Das Kriterium der Kristallinität wurde deshalb nicht mit in die Definition der MOFs mitaufgenommen.

Metall-organische Gerüstverbindungen bestehen wie zuvor erwähnt, aus Metallkationen oder aus Metallclustern, den sog. *secondary building units* (abgekürzt SBU) die über funktionalisierte organische Liganden (Linker) zu Netzwerken weiter verknüpft werden.[10] Je nach Beschaffenheit der gewählten Bausteine können so eindimensionale Ketten, zweidimensionale Schichtstrukturen oder dreidimensionale Netzwerke aufgebaut werden (Abbildung 2).

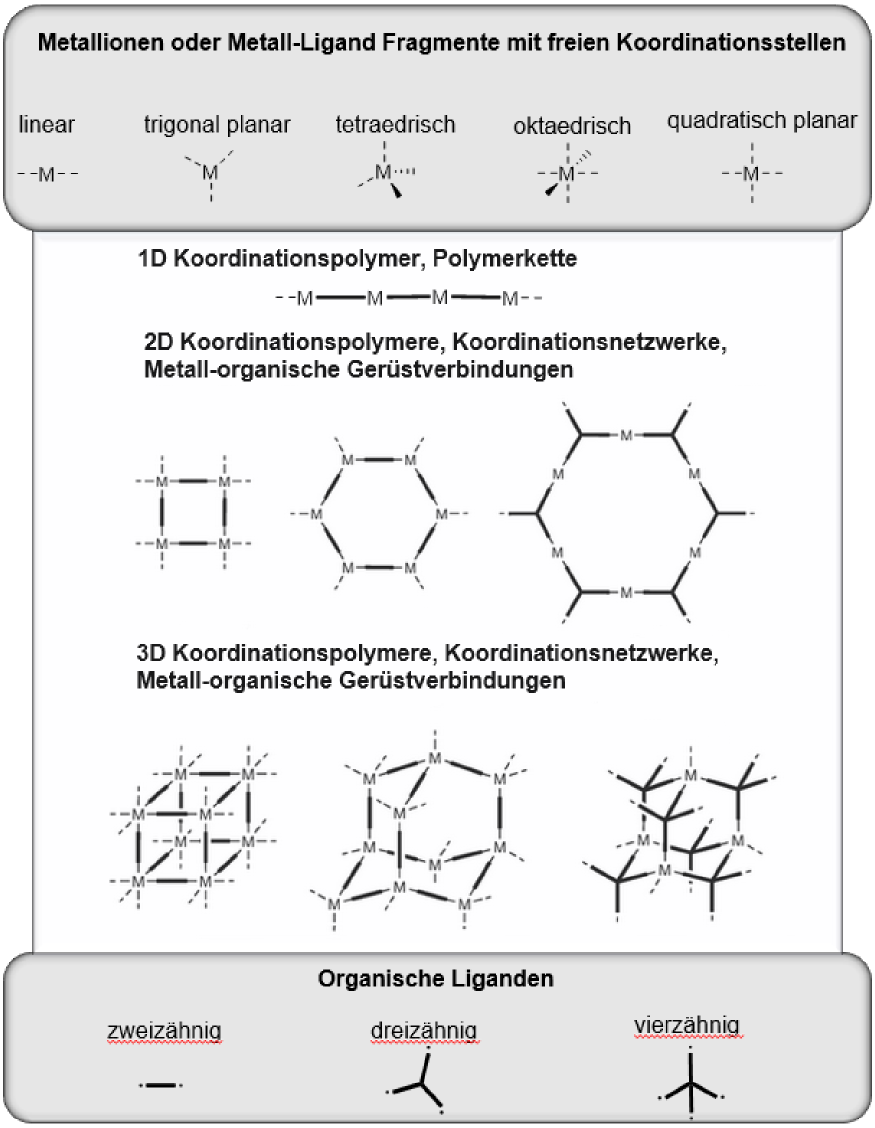

Abbildung 2: Schematische Übersichtsdarstellung einiger Kombinationsmöglichkeiten von Liganden und Metall-Ionen bzw. Metall-Ligand Fragmenten zum Aufbau von 1D-, 2D-, 3D-Strukturen. Abbildung reproduziert nach Janiak et al.[11], Nachdruck mit Genehmigung der Royal Society of Chemistry (RSC), ©2010.

Als Metallbaustein können neben den Übergangsmetallen auch Lanthanoide[12] und Hauptgruppenelemente wie z.B Magnesium,[13, 14] Calcium,[15, 16] Strontium[17, 18] oder Aluminium[19,20] gewählt werden. Bei den Übergangsmetallen wird häufig Chrom,[21,22] Eisen,[23] Kobalt,[14, 24] Kupfer,[25, 26] Zink[27, 28] oder Zirkonium[29, 30] verwendet. Die Koordination der Metallzentren kann je nach Koordinationsgeometrie der Metalle zwei-, drei-, vier oder sogar sechs-fach sein.[31, 32] Die Metallatome lagern sich zu Metallclustern (SBU) zusammen, welche aus den Metallatomen die über verbrückende Teile des Liganden bzw. über einzelne Atome (Sauerstoff, Stickstoff) miteinander verbunden werden. In nachfolgender Abbildung 3 sind einige häufig auftretenden SBUs der anorganischen Metallcluster und der organischen Liganden abgebildet.[33]

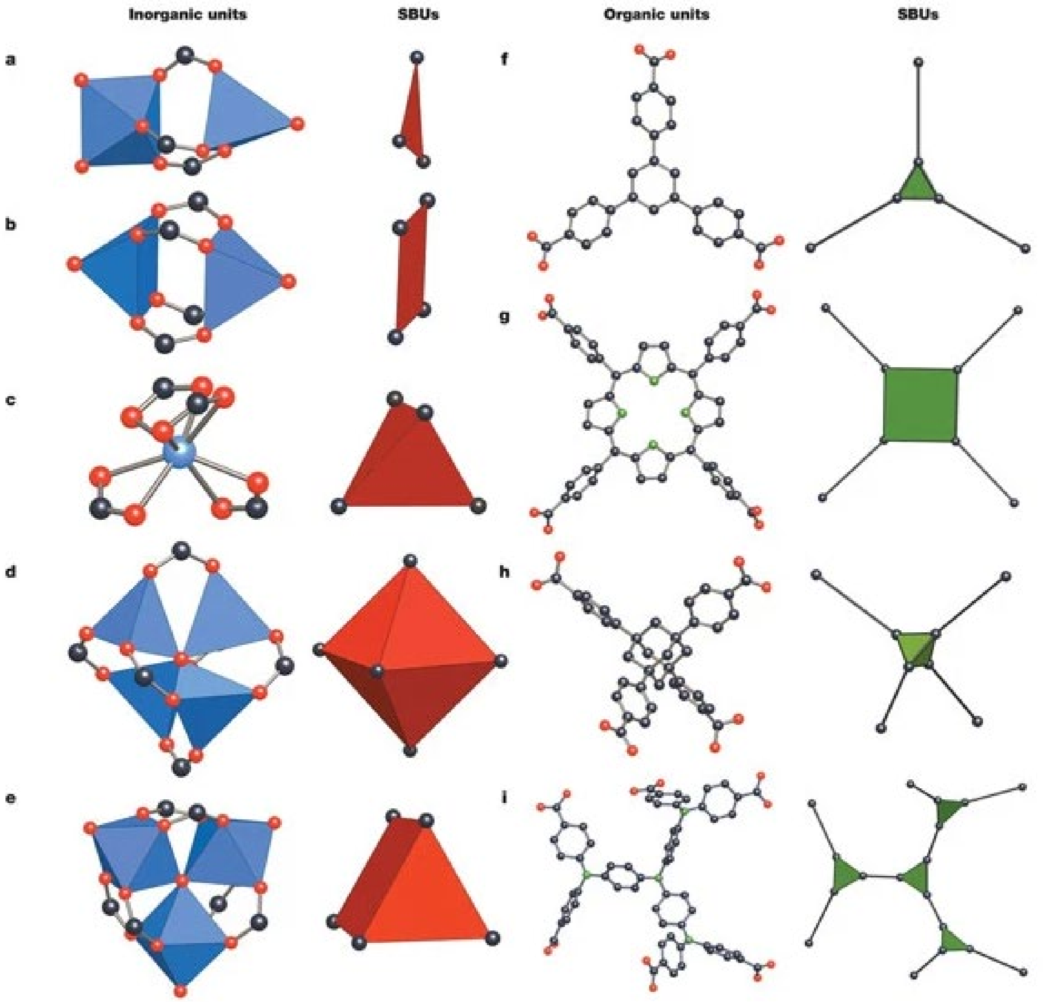

Abbildung 3: Beispielhafte Darstellung einiger SBUs von Carboxylat-MOFs. O-Atom: rot, N-Atom: grün, C-Atom: schwarz. In blau sind die anorganischen Metall-Sauerstoff Polyeder Einheiten abgebildet. Mit rot gekennzeichnte sind die durch Carboxylat-Kohlenstoff aufgespannten Polygon oder Polyeder (SBU). In grün sind die organischen SBUs dargestellt. Nachdruck mit Genehmigung von Ref. 33 Copyrigth 2013 Springer Nature.

Die Funktionalität der Liganden ermöglicht eine Koordination dieser an die Metallzentren. Diese Funktionalität kann z.B. durch Carboxylate, Phosphonate oder N-Heterozyklen mit freien Elektronenpaaren von Stickstoffatomen und/oder einer NH-Funktion gewährleistet sein (Abbildung 4).

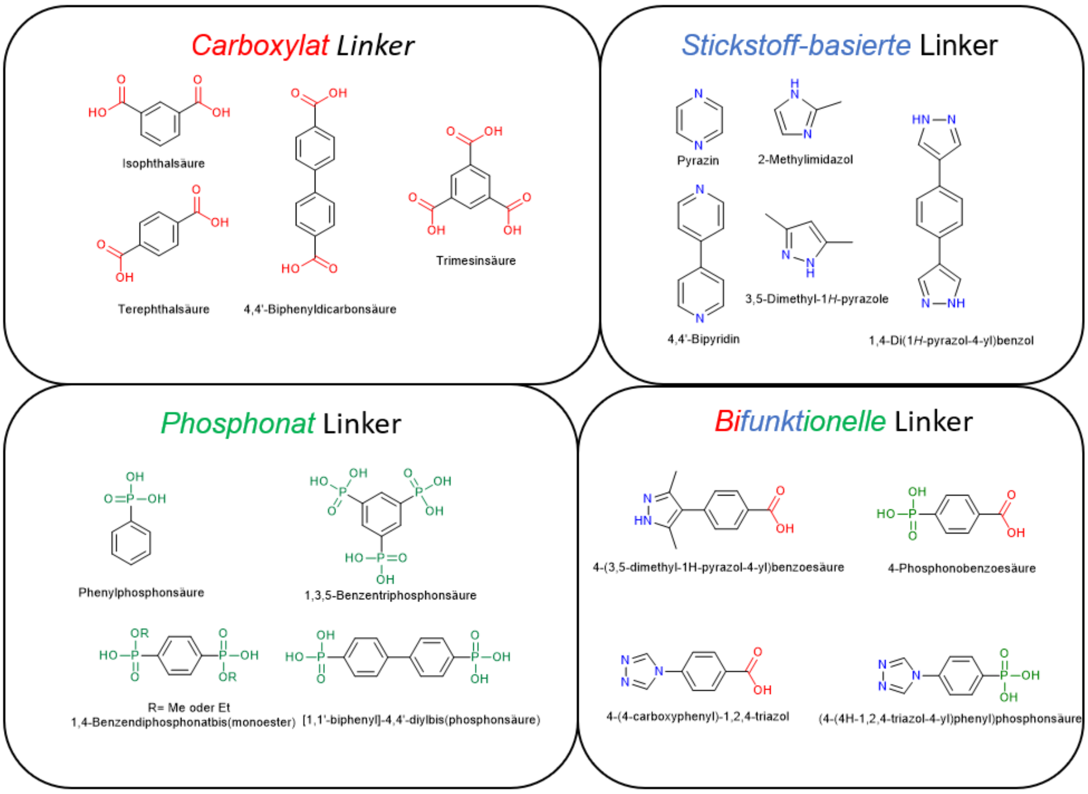

Abbildung 4: Darstellung ausgewählter Carbonsäure-, Stickstoff-basierter-, Phosphonat- und bifunktioneller-Linker. Die Funktionalitäten sind mit entsprechenden Farben hervorgehoben.

Besonders Azole werden in der MOF Chemie gerne eingesetzt, da diese den Vorteil gegenüber anderer N-Heterozyklen-basierten Liganden haben, gerichtete und äußerst inerte koordinative Bindungen zu Metallkationen einzugehen. Die N-Donoratome in den Azolen sind, wie die im Pyridin, sp^2-hybridisiert. Demzufolge ist ihre Koordinationschemie identisch. Azole wie Imidazol, Triazol, Tetrazol, insbesondere aber das Pyrazol können sowohl in neutraler als auch in ihrer anionischen Form als Azolate in MOFs eingebaut werden. Die Deprotonierung der Azole zum Azolat geht mit einer Erhöhung der Haptizität im Vergleich zu den Pyridinen einher. Neben der Lewis-sauren pyrrolischen N-H-Gruppe besitzen Pyrazole dazu benachbart einen Lewis-basischen, pyridinischen N-Donor. Demzufolge können Pyrazole sowohl als σ-Donor als auch als π-Akzeptor Ligand fungieren. Deshalb sind sie neben der hohen chemischen und thermischen Stabilität als Liganden besonders interessant. *Galli et al.* liefert in seiner Publikation einen umfassenden Überblick über die Pyrazolat-basierten teilweise porösen Koordinationspolymere.[34] Das Pyrazol kann im κ^{1-}Bindungsmodus sowohl deprotoniert als auch neutral vorliegen.[35] Im Koordinationsmodi exo-bidentat (κ^1- κ^1-verbrückend) und endo-bidentat (κ^2-chelatisierend) liegt das Pyrazol nur in der deprotonierten Form als Pyrazolat vor (Abbildung 5). Somit führt auch hier die

Deprotonierung zu einer Erhöhung der Haptizität. Nach der Lewis-Säure-Base-Theorie ist die Basizität ein Maß für die Fähigkeit Elektronen zu donieren. Durch die Deprotonierung der NH-Funktion des Pyrazols wird die Basizität erhöht, wodurch eine stärkere Metall-Ligand-Bindung erwartet werden kann. Wird darüber hinaus das HSAB-Konzept (auch Pearson-Konzept genannt) mitberücksichtigt, kann die hohe chemische und thermische Stabilität der Pyrazole sowie der Azole im Allgemeinen mit späten Übergangmetallen gut erklärt werden.[36,37] Denn im Verständnis des HSAB-Konzeptes ist das Pyrazol im Vergleich zu Carboxylaten als eher weiche Lewis-Base und die niedrig geladenen Übergangsmetalle als weiche Lewissäure zu verstehen.[38,39] Besonders stabile Komplexe sind mit einwertigen Metallkationen wie Cu(I), Ag(I) und Au(I) zu erwarten,[40] in denen der κ_1-κ_1-verbrückende Koordinationsmodus, welcher analog zu dem in Carboxylat-SBUs von Carboxylat-basierten MOFs, anzutreffen ist (Abbildung 5). Der Synergismus zwischen den Koordinationsmodi der Carboxylate und der Pyrazolate in MOFs wurde erstmals von *Chen et al.* gezogen.[41]

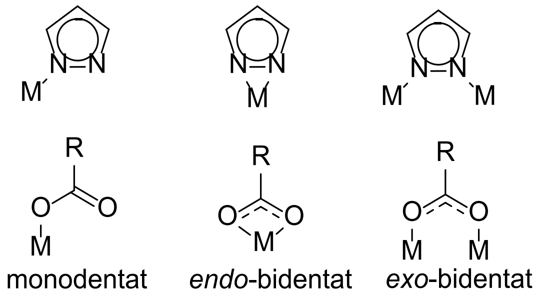

monodentat *endo*-bidentat *exo*-bidentat

Abbildung 5: Vergleichende Darstellung der gängigen Koordinationsmodi des Pyrazolats mit denen des Carboxylats.

Neben dem Einsatz von Linkern mit nur einer Art von funktionellen Gruppen, werden immer häufiger Ligandsysteme mit verschiedenen funktionellen-Gruppen kombiniert z.B Dicarboxylate mit Bipyridinen[42] oder Bipyrazolen[43,44]. Dies ermöglicht weitere Variation der MOF-Strukturen und damit einhergehend der Einfluss auf deren Eigenschaften. Dies führte zur Entwicklung bifunktioneller (heteroditoper) Liganden wie Pyridin-carboxylate,[45,46] Phosphonat-carboxylate,[47,48,49] Pyrazolat-phosphonate,[50] aber auch zu den für diese Arbeit sehr interessanten Pyrazolat-carboxylaten[51,52,53,54] (Abbildung 4).

Dabei wurden bifunktionelle doppelt deprotonierte Pyrazolat-carboxylat Liganden gezielt eingesetzt, um stabilere Versionen ihrer Dicarboxylat-Analoga zu synthetisieren, da die Metall-pyrazolat-Bindung im Vergleich zur Metall-carboxylat-Bindung einen höheren kovalenten Charakter aufweist. So synthetisierte *Janiak et al.*[55] mit Hilfe der dianionischen Form des bifunktionellen Liganden 3,5-dimethyl-4-

caboxypyrazol (H_2dmpz-ba) und Kobalt^{II}-Ionen bzw. Zink^{II}-Ionen das MOF-5-Analogon [M_4(μ_4-O)(dmpz-ba)$_3$]. In diesem {M_4(μ_4-O)-(pz/COO)$_6$}-Cluster besteht die SBU wie in MOF-5 aus einem Sauerstoffatom, welches tetraedrisch von den Zink-Ionen bzw. Kobalt-Ionen umgeben ist. Eine Verbrückung der einzelnen Cluster erfolgt jeweils durch den Hdmpz-ba-Liganden analog zum dicarboxylischen Terephthalat Liganden im MOF-5. Jedoch sind die bifunktionellen Liganden nicht gleichmäßig verteilt, sodass die {M_4(μ_4-O)}-Cluster eine unterschiedliche Pyrazolat- und eine Carboxylat-Umgebung besitzen. Dabei hervorzuheben ist allerdings, dass Pyrazolat und Carboxylat gemeinsame Cluster ausbilden können, in denen beide aufgrund der ähnlichen Koordinationsmodi (κ_1-κ_1-verbrückend) gegenseitig substituiert werden können. Darüber hinaus gibt es auch die Möglichkeit, dass Carboxylat und Pyrazolat ein gemeinsames Cluster formen, wobei aber die beiden Funktionalitäten unterschiedliche Koordinationsmodi aufweisen.[56, 57] Neben der Ausbildung eines gemeinsamen Clusters können sich auch getrennte Metall-Pyrazolat und Metall-Carboxylat SBUs ausbilden. Als Beispiel hierfür dient die Arbeit von *Wei et al.*[58] welcher den H_2dmpz-ba-Liganden zum Aufbau eines 3D porösen Koordinationspolymers (PCN-91) benutzte, welches aus einem getrennten Cu^{II}-Paddle-Wheel-Cluster und der trigonalen {Cu^I_3(mpba)$_3$}$^{3-}$-SBU besteht.

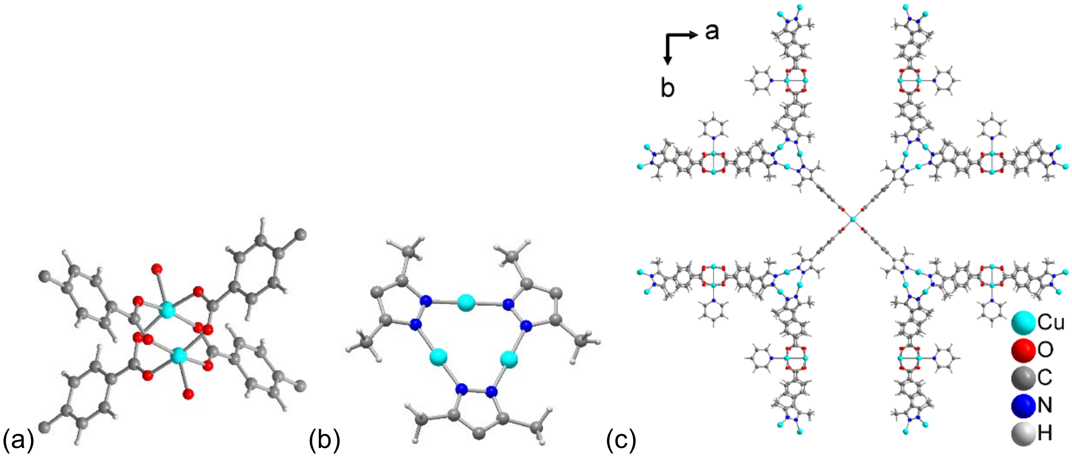

Abbildung 6: Darstellung des Cu^{II}-Paddle-Wheel-Cluster (a) und der trigonalen {Cu^I_3(mpba)$_3$}$^{3-}$-SBU (b) in PCN-91 (c) (Refcode MILROQ)[58] Das Bild wurde mit dem Darstellungsprogramm Diamond 4.0 erzeugt.[59]

Neben der Herstellung von mono-metallischen Verbindungen auf Basis von bifunktionellen Carboxylat-Pyrazolat-Liganden können auch gemischt metallische Verbindungen hergestellt werden,[60, 61] wodurch die Eigenschaften und damit die Anwendungsvielfalt der MOFs allgemein noch einmal erweitert werden kann.[62] Die Schwierigkeit hierbei besteht allerdings darin geeignete Syntheseparameter zu finden damit sich beide Cluster getrennt voneinander ausbilden. Denn die Wahl der Synthesebedingungen hat einen erheblichen Einfluss auf die spätere MOF-Struktur im Allgemeinen.[64] Neben der Wahl des verwendeten Metallsalzes/Metallanions (Acetat, Chlorid, Nitrat, Sulfat usw.), dem Linker (de- oder protonierte Form), den verschiedenen Lösungsmitteln sowie den Reaktionsparametern Druck, Temperatur und Zeit, kann auch zwischen den verschiedenen Synthesearten gewählt werden.

Grundsätzlich gibt es für die Synthese von Metall-organischen Gerüstverbindungen ein breites Spektrum an Synthesemethoden. Oft benutzt werden Niedertemperatursynthesen bei denen sich die Reaktionstemperatur zwischen Raumtemperatur und dem Siedepunkt des eingesetzten Lösungsmittels befindet. Werden Temperaturen oberhalb der Raumtemperatur und bei Normaldruck gewählt, spricht man von Hydro- (wenn das Lösungsmittel Wasser ist) bzw. Solvothermalsynthese. Dabei werden der Linker und das Metallsalz in einem Lösungsmittel oder Lösungsmittelgemisch gelöst und anschließend zur Kristallisation unter Selbstassemblierung der eingesetzten bzw. in situ gebildeten SBUs in ein abgeschlossenes Reaktionsgefäß (Autoklaven oder Pyrex-Röhrchen) gegeben und für eine bestimmte Zeit bei einer bestimmten Temperatur oder einem Temperaturprogram in einen Ofen gegeben. Auf diese Weise können sowohl einkristalline MOFs als auch kristalline Pulver-MOFs synthetisiert werden. Des Weiteren können MOFs z.B. über Mikrowellensynthesen, elektrochemische Synthesen oder mechanochemisch (Kugelmühle) hergestellt werden (Abbildung 7).[63]

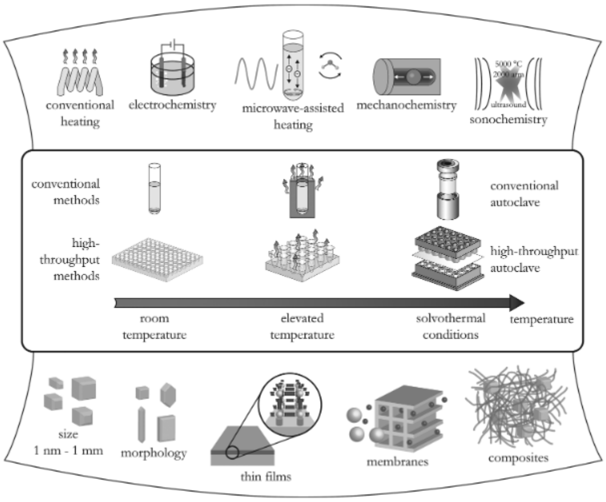

Abbildung 7: Übersichtsgrafik über die verschiedenen Synthesemethoden für MOFs (oben), mögliche Reaktionstemperaturen (mittig) und mögliche Reaktionsprodukte (unten). Abbildung entnommen aus Ref.63 mit Genehmigung, Copyright ©2012, American Chemical Society.

Um die Kristallqualität und Kristallgröße positiv zu beeinflussen, können auch Additive wie Modulatoren zur Synthese hinzugegeben werden. Modulatoren verlangsamen dabei die Nukleation und damit das Kristallwachstum, in dem die Modulatoren, welche dieselbe funktionelle Gruppe wie der in der Synthese eingesetzte Linker besitzen, um die freien Koordinationsstellen am Metall konkurrieren. Da die Modulatoren oft kleinere, monodentate Moleküle sind, binden diese oft zuerst an das Metall, da sie sterisch weniger gehindert sind. Erst nach einiger Zeit kommt es dann zum Austausch der Modulator-Moleküle gegen den Linker.[64,65] Durch die Zugabe von Basen (NaOH, KOH), [66] halogenierte Säuren (HF, HBF_4, HCl) [67] oder HNO_3 [68] kann das Kristallwachstum ebenfalls verlangsamt werden, wodurch eine Kontrolle über die Bildungsgeschwindigkeit der Metall-Carboxylat- bzw. Metall-Pyrazolat-Bindung erreicht werden kann. Dadurch kann die Größe der Kristalle kontrolliert und die Kristallinität der MOFs verbessert werden. Oft kann durch Säurezugabe auch die Löslichkeit der Metallkationen durch Einstellung eines geeigneten pH-Wertes verbessert werden, wodurch eine Nukleation erleichtert wird. Darüber hinaus kann so auch das Vorliegen eines protonierten bzw. deprotonierten Liganden gewährleistet werden, wodurch die Koordination an ein Metallkation erleichtert wird. Als Beispiel hierfür können z.B Phosphonat-Liganden angeführt werden. Diese sind bzgl. ihrer pKs-Werte gut untersucht. [69,70]

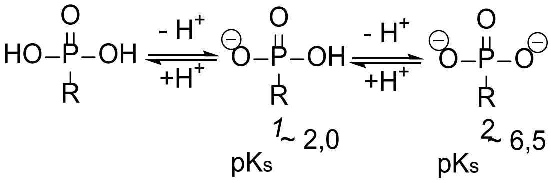

Scheme 1: Die einfach deprotonierte Form (*1*) und die vollständig deprotonierte Form (*2*) mit den dazu gehörigen pK_s-Werten eines Phosphonat-Liganden mit dem organischen Rest *R*.

Die Synthese bimetallischer MOFs kann ebenfalls über eine solvothermale Synthese, auch als *one-pot-synthesis* bezeichnet, erfolgen.[62, 71, 72] Dabei werden die beiden Metallsalze sowie der Linker direkt mit dem Lösungsmittel zusammengegeben und zur Reaktion gebracht. Als ein Beispiel kann das von *Li et al.* synthetisierte FDM-4 und dessen Analoga FDM-5 erwähnt werden.[60] FDM-4 (FDM = Fudan Material) ist ein zwei Komponenten MOF, welches durch die Kombination des organischen, bifunktionellen Liganden 4-Pyrazolcarbonsäure (H_2PyC), Kupfer- und Zinknitrat in einem Lösungsmittelgemisch aus DMF und NMP (N-methyl-2-pyrrolidon) hergestellt wurde. Die porösen Verbindungen bestehen aus verschiedenen oktaedrischen Zn-basierten

SBUs ($Zn_4O(COO)_6$) und den dreieckigen Kupfer-Pyrazolat-Komplexen (vgl. Abbildung 6b).

Aufgrund der unterschiedlichen MOF-bildenden Kinetik, der in der Synthese von bimetallischen MOFs verwendeten Metallkationen, gibt es allerdings keine Garantie dafür, dass sich wirklich (stabile) bimetallische-Strukturen ausbilden. Denn oft bilden sich fragile Gerüste mit unvorhersehbaren Topologien oder gemischte MOF-Phasen aus.[62, 73] Deshalb ist eine sensible Reaktionsparametersteuerung bei der direkten Synthese notwendig.

Wenn eine direkte Synthese der MOFs nicht möglich ist oder um eine bessere Reaktionskontrolle von gemischt-metallischen MOFs zu erhalten, können postsynthetische Metallionen-Austauschprozesse (PSM) als Alternative genutzt werden. Darunter wird die chemische Modifikation eines Gerüsts, nach der eigentlichen Synthese, verstanden.[74,75] Im Rahmen der Synthese von bimetallischen MOFs bedeutet dies, dass es im Sinne einer Transmetallierung (Metallmetathese) an den Knotenpunkten zu einem teilweisen oder vollständigen Ersatz der Metalle kommen kann.[76] Die Geschwindigkeit und die Reversibilität des Austauschprozesses wird dabei maßgeblich durch die Koordinationszahl, die Wertigkeit und den Ionenradius des Metallions sowie durch die Umgebung der SBU und das eingesetzte Lösungsmittel beeinflusst. Lösungsmittel mit einer kleinen Molekülgröße wie Methanol oder Wasser können die Austauschrate im Vergleich zu größeren Lösungsmittelmolekülen wie Dimethylformamid, Dimethylsulfoxid oder Diethylformamid beschleunigen.[77,78] Besitzt das MOF eine große Gitterflexibilität können die Verzerrungen der SBU für einen Metallkationenaustausch leichter ermöglicht werden.[79] Cu^{II}-Ionen sind besonders gut für eine Transmetallierung geeignet. Sie können die meisten anderen Übergangsmetalle der zweiten Reihe (Zn^{II}, Cd^{II} und Mn^{II}) aufgrund ihrer hohen Elektronegativität ersetzen, um so kovalente Bindungen mit besserer thermodynamischer Stabilität zu erreichen. [80,81,82] Bei oktaedrischen Metallzentren z.B. würde die Stabilität dieser getreu der Irving-Williams-Reihe, welche die zunehmend stärkere Metall-Ligand-Wechselwirkungen in oktaedrischen high-spin Komplexen von 3d M^{2+} Spezies voraus sagt, für Cu^{II} über Ni^{II}, Co^{II} hin zum Zn^{II} abnehmen. Grund hierfür ist, dass Zn^{II} keine zusätzliche Kristallfeldstabilisierungsenergie wegen des vollbesetzten d-Orbitals besitzt (Abbildung 8). Diese Reihe korreliert gut mit der Stabilität von MOFs, welche oktaedrische (schaufelradbasierte) Struktureinheiten aufweisen.[83,79] Deshalb gibt es in der Literatur eine Vielzahl von Beispielen in denen die Transmetallierung zu Cu^{II} möglich ist.[84,85,86,87]

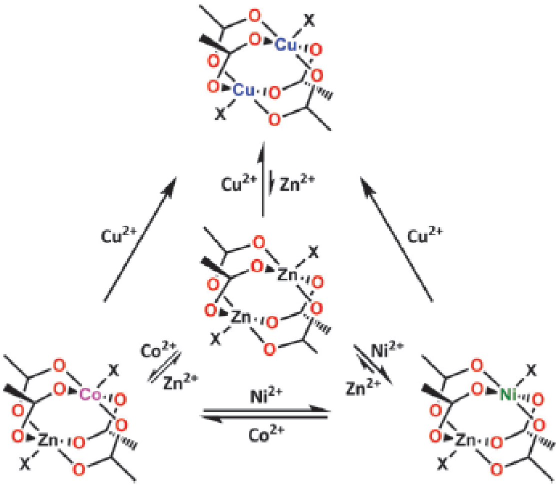

Abbildung 8: Partielle und vollständige Transmetallierung für die erste Reihe der Übergangsmetallionen. Abbildung entnommen aus Ref. 76 Copyright © 2014 Chemical Society Review.

Als Fazit aus den Synthesen von mono- und bimetallischen MOFs kann festgehalten werden, dass der synthetische Chemiker eine Vielzahl von Variationsmöglichkeiten besitzt, um seine angestrebte Verbindung zu erhalten und/oder zu optimieren. Dementsprechend langwierig kann eine Synthese/Syntheseoptimierung sein. Denn die perfekten Bedingungen zum perfekten reproduzierbaren Einkristall oder Pulver zu finden, kann trotz der guten theoretischen Grundlagen in der Praxis Schwierigkeiten bereiten.

Das Konzept des SBU-Ansatzes hilft jedoch erheblich bei der Syntheseplanung und Analyse der Netzwerke und wird auch als retikuläre (netzartige) Synthese bezeichnet.[33] Jedoch müssen für diesen *crystal engineering* Bauansatz gut definierte, starre Baueinheiten vorliegen. Das von Yaghi 2002 erhaltene Beispiel der IRMOF-Reihe zeigt, dass es möglich ist durch suggestive Ligandverlängerung die Netzwerkstruktur (Topologie) beizubehalten, aber die Poren zu vergrößern um damit die Porosität zu erhöhen. Dieser Zusammenhang wird auch als isoretikulare Synthesestrategie bezeichnet. Ausgehend von dem prototypischen MOF-5 (IRMOF-1) konnte *Yaghi et al.* eine ganze Reihe weiterer MOFs mit gleicher **pcu**-Topologie synthetisieren (Abbildung 9).[88]

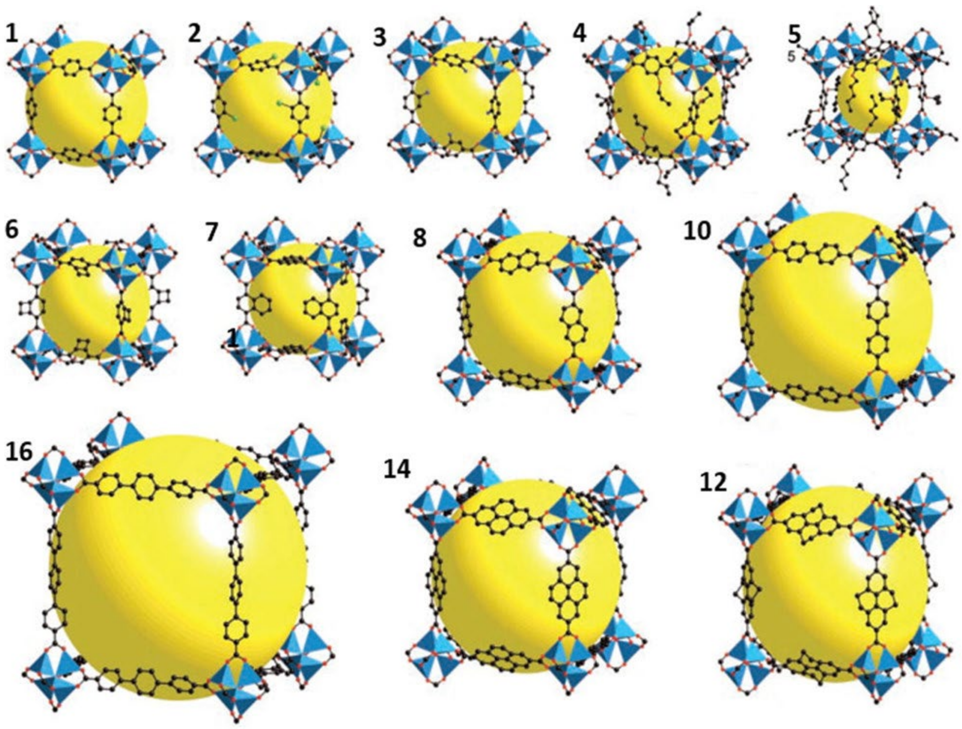

Abbildung 9: Einkristalline Röntgenstrukturen von IRMOF-n (n= 1-8, 10, 12, 14, 16) ohne Interpenetration. Zn-Koordinationsgeometrie: blaue Polyeder, O-Atom: rote Kugeln, C-Atom: schwarze Kugeln, Br-atome: grüne Kugeln, Aminogruppen: braune Kugeln, Die gelben Kugeln repräsentieren die größten van-der-Waals-Sphären, die in die Hohlräume passen würden, ohne die Gerüste zu berühren. Zur Übersicht fehlen die H-Atome. Nachdruck mit Genehmigung von Ref. 88. Copyright 2019 American Chemical Society.

Das von *Furukawa et al.* hergestellte MOF-399 stellt ein weiteres Beispiel der isoretikulären Synthese dar. Das dort als Ligand verwendete 4,4',4''-(Benzol-1,3,5-triyl-tris(benzol-4,1-diyl))tribenzoat (bbc^{3-}) = 1,3,5-tris(4'-carboxy[1,1'-biphenyl]-4-yl-)benzol (tcbpb^{3-}) stellt eine erweiterte Version des in HKUST-1 verwendeten Trimesinsäure (Benzol-1,3,5-tricarbonsäure, btc^{3-}) dar.[89] Ebenfalls als erweiterte Versionen des btc^{3-}-Liganden gilt das 4,4',4''-Benzol-1,3,5-triyl-tribenzoat (btb^{3-}),[90,91,92,93,94,95] 4,4',4''-(benzol-1,3,5-Triyl-tris(ethyne-2,1-diyl))tribenzoat (bte^{3-}),[93] 4,4',4''-*s*-triazin-2,4,6-triyl-tribenzoat (tatb^{3})[96,97,98] und 4, 4',4''-(Triazin-2,4,6-triyl-tris(benzol-4,1-diyl))tribenzoat (tapb^{3-}).[91]

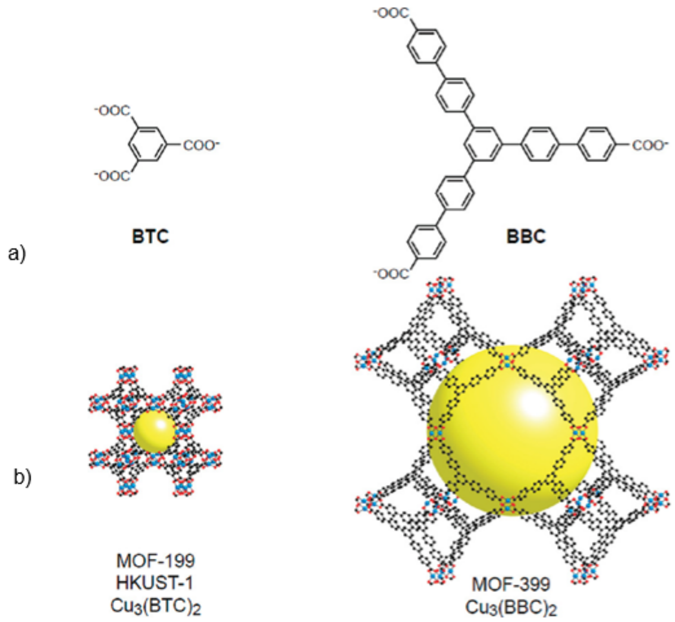

Abbildung 10: a) Molekülstrukturen der organischen Liganden Benzol-1,3,5-tricarbonsäure (btc^{3-}) und 4,4',4''-(Benzol-1,3,5-triyl-tris(benzol-4,1-diyl))tribenzoat (bbc^{3-}); b) Einkristallstrukturen von HKUST-1 (MOF-199) und MOF-399. Die gelbe Kugel stellt den Platz im Käfig dar. Nachdruck mit Genehmigung von Ref. 91. Copyright 2011 American Chemical Society.

Durch die Vielzahl an Variationsmöglichkeiten der Metallkationen sowie der Linker, besitzen die MOFs ein breites Anwendungsspektrum.[99] Einen Überblick der bisherigen Anwendungsgebiete nach derzeitigem Forschungsstand, liefert Abbildung 11.

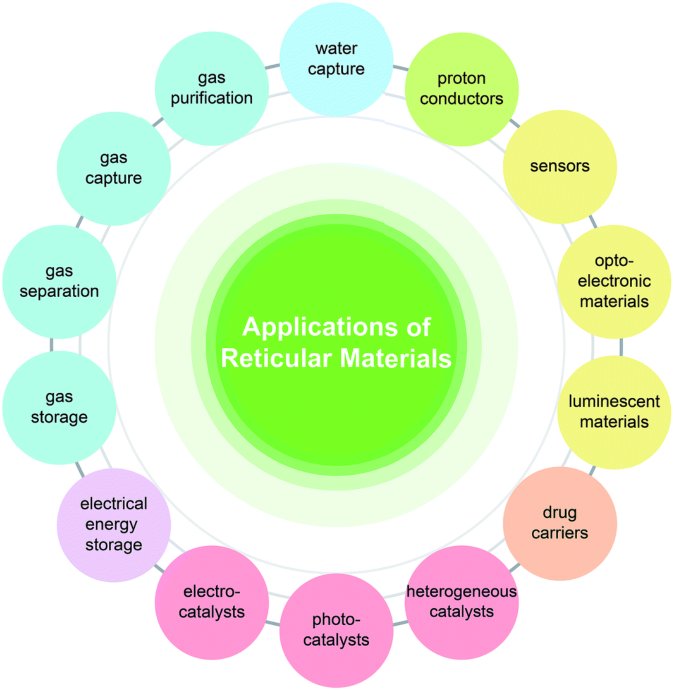

Abbildung 11: Übersicht über die Vielzahl von möglichen Anwendungsbereichen der Metall-organischen Gerüstverbindungen. Abbildung mit Copyright © 2017 mit Erlaubnis von The Royal Society of Chemistry in Anlehnung an Yaghi et al. [8,99]

Aufgrund der potenziell porösen Eigenschaft der MOFs, finden diese Anwendung in der Gasspeicherung, -aufbereinigung und -trennung sowie in der VOC Sorption.[100,101,102] Dabei handelt es sich um die Ad- und Desorption von flüchtigen, organischen Verbindungen (Methanol, Ethanol, Toluol etc.).[103,104] Bei der Gastrennung wird sich die individuelle Eigenschaft unterschiedliche Gase unterschiedlich schnell zu adsorbieren zu Nutze gemacht. Die Länge der Adsorption ist hierbei von der Stärke der zugrundeliegenden Wechselwirkungen innerhalb des MOFs und mit dem Gas selbst abhängig. Besonders interessant ist hierbei die Trennung von CO_2/CH_4 und CO_2/N_2 Gasmischungen, denn CO_2 gehört zu einem der vorherrschenden Treibhausgase, die die globale Erwärmung begünstigen.[105,106,107] Deshalb ist die Senkung der CO_2-Emission zu einem der dringendsten Umweltthemen geworden. CO_2 ist mit seinem kinetischen Durchmesser von 3,3 Å im Vergleich zu den meisten anderen Gasen relativ klein. CH_4 und N_2 besitzen zum Vergleich einen kinetischen Durchmesser von 3,8 Å bzw. 3,2-3,6 Å. Schon in der Vergangenheit haben sich MOFs als ideale Kandidaten für eine selektive CO_2-Trennung erwiesen.[108,109] Die Schwierigkeit bei neu synthetisierten Materialien liegt allerdings darin, MOFs mit Porengrößen zu entwickeln, die zwischen dem kinetischen Durchmesser von CO_2 und den anderen zu selektierenden Gasen liegen. Allerdings ist dies in der Praxis eine größere Herausforderung, denn es gibt auch Materialien, die trotz größerer Poren kein N_2 oder Ar aufnehmen können (kinetischer Molekularsiebeffekt), wodurch diese dann eine hohe CO_2 Selektivität aufweisen.[110,111,53] Besitzt das MOF funktionelle Gruppen wie Amine[112,113,114] oder ist strukturell flexibel,[53,115,116,117] kann dies auch die CO_2 Selektivität erhöhen. Strukturell flexibel meint dabei, dass sich das Volumen der Elementarzelle während des Adsorptionsprozesses ändert. Dabei sollten zwischen dem breathing Effekt der Struktur und dem sogenannten „gate-opening“, unterschieden werden.[102] Das „gate-opening“ äußert sich in einer Diskontinuität in der Adsorptionsisotherme. Dabei wird oft ein „Sprung“ der Adsorptionsisotherme beobachtet (vgl. Abbildung 12). An diesem Punkt findet der Übergang einer nicht-porösen in eine poröse Phase statt, ausgelöst durch die Wirt-Gast-Wechselwirkungen. Der dazugehörige Druck wird auch als „gate-opening“-Druck beschrieben.[118] Beim breathing (= Atmung) handelt es sich um eine Ausdehnung einer bereits porösen Struktur.[119] Dieses Phänomen wurde erstmals von *Kitagawa et al.* beobachtet.[120] Der breathing Effekt macht sich auch hier in einem Sprung in der Adsorptionsisotherme bemerkbar (vgl. Abbildung 12). Die Drücke für das breathing der Struktur ist auch hier von den adsorbierten Gastmolekülen abhängig. *Zawarotko et al.* veröffentlichte zur

Beschreibung der Adsorptionsisothermen von flexiblen Materialien ein ergänzendes Schema zur normalen Isothermenform von starren, mikroporösen Materialien.[121,122]

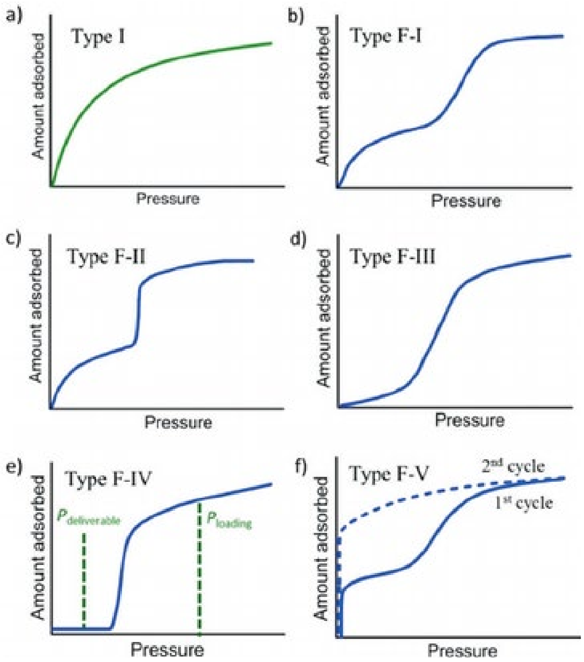

Abbildung 12: Klassifizierungsvorschlag der Adsorptionsisothermenprofile für flexible mikroporöse Materialien: (a) Typ I: Starres mikroporöses Material, (b) Typ F-I: Flexibles mikroporöses Material mit allmählicher Porenöffnung von kleinen Poren zu größeren Poren, (c) Typ F-II: Flexibles mikroporöses Material mit einer plötzlichen Porenöffnung der kleinen Poren in eine größere Porenform, (d) Typ F-III: Flexibles mikroporöses Material mit einem allmählichen Übergang einer nicht-porösen in eine poröse Form, (e) Typ F-IV: Flexibles mikroporöses Material mit einem plötzlichen Übergang von einem nicht-porösen in ein poröses Material. Abbildung mit Copyright © 2018 mit Erlaubnis von Wiley-VCH Verlag GmbH & Co. KGaA, Weinheim in Anlehnung an Ref.122.

2 Motivation

Das Hauptziel dieser Arbeit ist die Synthese und Charakterisierung neuer mono-, gemischt-valenter und bimetallischer Metall-organischer Gerüstverbindungen auf Basis von Kupfer und des literaturbekannten N,O-heteroditopen, bifunktionellen Liganden 4-(3,5-Dimethyl-1*H*-pyrazol-4-yl)benzoesäure (H_2mpba). Dieser Ligand besitzt zwei verschiedene Funktionalitäten. Zum einen die Carboxylatgruppe, welche im Sinne des HSAB-Prinzips als eher hart eingestuft wird, und die als eher weich eingestufte Pyrazolgruppe. Aus voran gegangenen Arbeiten ist bekannt, dass dieser Ligand an Kupfer koordiniert, weshalb dieses als Basismetall gewählt worden ist. Durch systematische Variation der Synthesebedingungen (Lösungsmittel, Temperatur, Additiv und Gegenion) soll so der Einfluss auf die Konnektivität des Liganden zum Kupfer genommen werden, welches zu einem positiven Effekt sowohl für die Stabilität als auch für die Verwendungsmöglichkeit als Gasabsorbens führen soll. Durch den Einsatz von Zink als zweites Metallkation soll ein noch breiteres Spektrum an Strukturen erhalten werden, welche potenziell poröse Eigenschaften besitzen sollen. Es wird dabei erwartet, dass sowohl das Kupfer als auch das Zink geometrisch unterschiedliche Netzwerkknoten bilden, welche sich anschließend zu einem gemeinsamen Netzwerk vereinen. Alle im Rahmen dieser Arbeit erhaltenen Koordinationsnetzwerke sollen umfangreich mit den gängigen Charakterisierungsmethoden analysiert, diskutiert und in Publikationen zusammengefasst werden.

3 Kumulativer Teil

Die nachfolgenden Unterkapitel 3.1 –3.3 beinhalten die Ergebnisse der Doktorarbeit, welche in Form von Erstautorenschaften in internationalen Journalen veröffentlicht wurden. Jede aufgeführte Publikation wird so dargestellt, wie sie auch in dem jeweiligen Journal erschienen ist. Demzufolge steht jede Publikation mit einer eigenen Aufzählung für sich. Abbildungs-, Tabellen- und Schemata-Nummerierungen folgen hierbei nicht dem Haupttext. Zudem beinhaltet jede Veröffentlichung ein separates Quellenverzeichnis. Die Publikationen werden in chronologischer Reihenfolge aufgeführt. Die reine NMR-Publikation befindet sich in einem separaten Anhang mit weiteren unveröffentlichten Ergebnissen.

Die jeweiligen Veröffentlichungen werden durch den Titel, die Namen der Autoren, den Namen des Journals, einer kurzen Einordnung in den Kontext dieser Dissertation und durch Darlegung der Anteile an der Publikation eingeleitet.

3.1 Increase of network hydrophilicity from sql to lvt supramolecular isomers of Cu-MOFs with the bifunctional 4-(3,5-dimethyl-1*H*-pyrazol-4-yl)benzoate linker

Die in diesem Kapitel vorgestellte Arbeit wurde veröffentlich in:

Saskia Menzel, Simon Millan, Simon-Patrick Höfert, Alexander Nuhnen, Serkan Gökpinar, Alexa Schmitz and Christoph Janiak *Dalton Trans.* **2020**, *49*, 12854-12864. DOI: 10.1039/d0dt02642e

The article is reprinted with permission of the Royal Society of Chemistry.

Die nachfolgend aufgeführte Publikation beschreibt die Synthese und Charakterisierung zweier neuartiger 2D Metall-organische Gerüstverbindungen, die mit dem bifunktionellen Liganden 4-(3,5-Dimethyl-1*H*-pyrazol-4-yl)benzoesäure und $Cu(NO_3)_2 \cdot 2.5H_2O$ aus einem Dimethylformamid/Wasser und einem Acetonitril/Wasser Gemisch erhalten worden sind. Die beiden neuen **sql** 2D MOFs $[Cu(H_2mpba)_2] \cdot L$ (L = DMF oder ACN) sind supramolekulare Isomere des bereits bekannten 3D **lvt**-Netzwerkes $[Cu(H_2mpba)_2] \cdot 4MeOH \cdot 1H_2O$ von Richardson *et al.* und Mitarbeitern.[123] Sowohl die beiden neuen **sql**-Netzwerke als auch das Literatur bekannte **lvt**-Netzwerk sind potenziell poröse Strukturen mit Lösungsmittelmolekülen in den Kanälen. Nach erfolgreicher Aktivierung zeigten alle drei Materialien gute CO_2-Adsorptionskapazitäten Sättigungsaufnahmen von 90 cm^3/g für **sql**-ACN-act., 111 cm^3/g für **sql**-DMF-act. und 113 cm^3/g für **lvt**-MeOH-act. gemessen bei 195 K. Anhand einer Wasser- und Ethanolsorptionsmessung konnten die neuen **sql**-Verbindungen, im Gegensatz zum hydrophilen **lvt**-Gerüst, als hydrophobe Materialien kategorisiert werden. Das besondere an der Struktur von $[Cu(H_2mpba)_2] \cdot 4MeOH \cdot 1H_2O$ war die vollständige Ersetzbarkeit des Kristalllösungsmittels durch Wasser, wodurch ein reines Wasser Netzwerk (**lvt**-H_2O) mit einer 3D-Anordnung von S_4-symmetrischen $(H_2O)_{20}$-Cluster erhalten werden konnte.

Anteile an der Publikation:

- Idee und Konzeption in Zusammenarbeit mit Herrn Dr. Simon Millan.
- Synthese der Koordinationspolymere in experimenteller Arbeit inklusive Durchführung der Charakterisierung und Sorptionsmessungen.
- Eigenständige Auswertung, Interpretation und Darlegung aller Ergebnisse in Form einer wissenschaftlichen Veröffentlichung.
- Die anderen Mitautoren waren an der Durchführung genutzter Analysen beteiligt. Die Einkristallstrukturmessung und Verfeinerung erfolgte durch Herrn Simon-Patrick Höfert.
- Überarbeitung, finale Abstimmung und Revision des Manuskripts wurde in Zusammenarbeit mit Herrn Prof. Dr. Christoph Janiak durchgeführt.

Dalton
Transactions

ROYAL SOCIETY
OF CHEMISTRY

PAPER

View Article Online
View Journal

Check for updates

Cite this: DOI: 10.1039/d0dt02642e

Increase of network hydrophilicity from sql to lvt supramolecular isomers of Cu-MOFs with the bifunctional 4-(3,5-dimethyl-1*H*-pyrazol-4-yl) benzoate linker†

Saskia Menzel, Simon Millan, Simon-Patrick Höfert, Alexander Nuhnen, Serkan Gökpinar, Alexa Schmitz and Christoph Janiak*

Received 27th July 2020,
Accepted 2nd September 2020

DOI: 10.1039/d0dt02642e

rsc.li/dalton

The bifunctional linker 4-(3,5-dimethyl-1*H*-pyrazol-4-yl)benzoic acid (H_2mpba) was used for the synthesis of new (square lattice) **sql** 2D metal–organic frameworks (MOFs) [Cu(Hmpba)$_2$]·L (L = DMF or ACN) in a solvent-mixture of dimethylformamide/water and acetonitrile/water. These **sql** 2D MOFs are supramolecular isomers of the **lvt** 3D network [Cu(Hmpba)$_2$]·4MeOH·1H_2O (**lvt**-MeOH) that was synthesized previously by Richardson and co-workers. All these frameworks are potentially porous structures with solvent molecules included in the channels of the as synthesized materials. After activation all three materials showed good CO_2 adsorption capacity, demonstrated here for **lvt**-MeOH for the first time, with a saturation uptake of 113 cm^3 g^{-1} (**lvt**-MeOH-act.), 111 cm^3 g^{-1} (**sql**-DMF-act.) and 90 cm^3 g^{-1} (**sql**-ACN-act.) at 195 K. The flexibility of the **lvt**-MeOH-act. network is evidenced by a gate-opening effect seen in the CO_2 measurement at 195 K and under gravimetric high-pressure CO_2 adsorption. According to the water and ethanol sorption measurements the new **sql** frameworks can be categorized as hydrophobic materials in contrast to the hydrophilic **lvt** framework. In the **lvt**-MeOH structure the crystal solvent can be replaced with water to yield the structurally authenticated water-only network **lvt**-H_2O containing 3D arrays of S_4-symmetric $(H_2O)_{20}$ clusters.

Introduction

New ligand classes are still important for the progress of metal–organic frameworks (MOFs).[1] For example, the ligand donor group is crucial to increasing MOF stability and/or to tune the MOF structure for potential applications in gas storage/separation,[2] catalysis,[3] optics,[4] magnetism,[5] sensing,[6] biomedicine[7] or as porous fillers in mixed-matrix membranes.[8,9]

In MOFs, the usage of mixed-ligand systems of different functionality is common, for example dicarboxylates are combined with bipyridines[10] or bipyrazoles.[11,12] This led to the evolution of bifunctional (also termed heteroditopic) ligands like pyridine-carboxylates,[13,14] phosphonate-carboxylates,[15,16] pyrazolate-carboxylates,[17,18] or pyrazolate-phosphonates.[19] Bifunctional doubly-deprotonated pyrazolate-carboxylate ligands have specifically been employed to synthesize more stable versions of their dicarboxylate analogs due to the greater covalency of the metal-pyrazolate bond compared to metal carboxylate bond.

The introduction of linkers with donor groups of stronger basicity such as imidazolates or pyrazolates can thus contribute to markedly increase the stability of MOFs toward water. In metal-azolate frameworks (MAFs), including zeolitic-imidazolate frameworks (ZIFs), the metal centers are coordinated by linkers from imidazolate, pyrazolate, triazolate or tetrazolate derivatives. MAFs can show high thermal and chemical stability. In addition, the substituents of the azolate linkers could efficiently tune the hydrophobicity of the framework, contributing to higher kinetic stability against water.[8,9]

MOFs with bifunctional pyrazole-carboxylic acid linkers (Scheme 1) have been utilized to capture nerve gas agents,[17] as hydrophobic materials for solid-phase extraction,[20] to synthesize MOFs with ordered vacancies[21] and incorporated into mixed-matrix-membranes.[8,9] If the pyrazole group is not deprotonated during the MOF formation then the pyrazole-carboxylate linker mimics a pyridine-carboxylate linker with the adjacent NH-function as an additional interaction site.[17,18,20–24]

The combination of a carboxylate and a pyrazole group in one ligand can give different topological networks based on

---

Institut für Anorganische Chemie und Strukturchemie, Heinrich-Heine Universität Düsseldorf, 40204 Düsseldorf, Germany. E-mail: janiak@hhu.de

† Electronic supplementary information (ESI) available: IR, PXRD, crystal data, TGA, NMR, gas sorption, porosity, heat of adsorption. CCDC 1999766–1999768. For ESI and crystallographic data in CIF or other electronic format see DOI: 10.1039/d0dt02642e

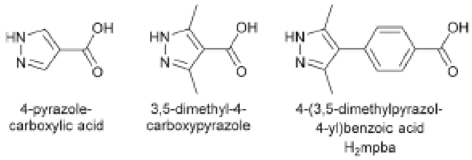

Scheme 1 Bifunctional pyrazole-carboxylic acid linkers reported in the literature and the 4-(3,5-dimethyl-1*H*-pyrazol-4-yl)benzoic acid linker, H_2mpba used in this work.

the same building blocks upon variation of the synthesis conditions.[25] Generally, the product in a MOF-synthesis can vary with solvent,[26,29,31] temperature,[27,28] the metal salt to ligand ratio, the metal counterions and additives.[28] This phenomenon can be exemplified through the three isolated solvent-dependent supramolecular isomers with dia-topology (dia = diamond net) of [Zn(Hmpba)$_2$]·L$_{solv}$ with L$_{solv}$ = dioxane,[29] ethanol/water,[29] DMF/water,[22] methanol/water[22] and guest-free (non-porous) by using pure water as solvent.[29] In addition, a supramolecular isomer with afw-topology[30] based on the identical tetrahedrally coordinated zinc-knots, but with larger porosity has been synthesized by using toluene as a templating solvent.[31]

Besides the arrangement of the same building blocks in the supramolecular isomers with different net topologies, changes in the reaction conditions can also yield a different packing of nets with overall same topologies guided by weak supramolecular interactions.[32]

The occurrence of such supramolecular isomers can be an opportunity for better understanding the factors which influence nucleation and crystal growth, because at the moment little is known on the controlling factors of such supramolecular isomers, except that the probability for the formation of supramolecular isomers increases in structures with flexible parts and ligands with functional groups that can form hydrogen bonds.[28]

Herein, we report the 2D nets sql-[Cu(Hmpba)$_2$]·*x*DMF and sql-[Cu(Hmpba)$_2$]·2ACN, which are two crystallographically distinct supramolecular isomers to the known 3D net lvt-[Cu(Hmpba)$_2$]·4MeOH·1H$_2$O (lvt-MeOH), synthesized by Richardson and co-workers (lvt is a $4^2.8^4$ net[30]).[22] We examined both supramolecular isomers regarding their vapor and gas sorption properties, thereby highlighting the seemingly important role of the N–H donor function of the pyrazole-moiety. In addition, we were able to obtain a 3D lvt-H$_2$O net by replacing the solvent in lvt-MeOH with water.

Experimental

Materials and methods

Reagents were obtained from commercial sources and used as received without further purification: Cu(NO$_3$)$_2$·2.5H$_2$O (99%+, Alfa Aesar), CuSO$_4$·5H$_2$O (99%+, Alfa Aesar), acetonitrile, methanol, *N*,*N*-dimethylformamide (ACS grade, VWR), deionized water (DI). The synthesis of 4-(3,5-dimethyl-1*H*-pyrazol-4-yl)benzoic acid (H$_2$mpba), was carried out according to the literature procedure.[22]

Elemental analyses (CHN) were performed using a PerkinElmer 2400 series II elemental analyzer. IR-spectra were recorded on a Bruker FT-IR Tensor 37 spectrometer in the 4000–500 cm^{-1} region with 2 cm^{-1} resolution as KBr disks. Thermogravimetric analysis (TGA) was performed using a Netzsch TG 209 F3 Tarsus from 20 to 600 °C with a heating range of 5 K min^{-1} under nitrogen atmosphere. ^{1}H NMR spectra were measured with a Bruker Avance III-300. The powder X-ray diffraction (PXRD) measurements were carried out on samples at ambient temperature with a Bruker D2 Phaser powder diffractometer using a flat silicon, low-background sample holder at 30 kV, 10 mA (100 W) for Cu-Kα radiation (λ = 1.54184 Å). In all diffractograms, the most intense reflection was normalized to 1. Simulated powder X-ray diffractograms were obtained from single-crystal data using the MERCURY 3.5.1 software programme.[33] Gas sorption measurements up to one bar were performed on an ASAP 2020 automatic sorption analyzer (Micromeritics). High-pressure gravimetric adsorption of CO$_2$ was conducted on a RUBOTHERM (IsoSORB) STATIC and the mass change was measured with a magnetic suspension balance (resolution 0.01 mg; reproducibility, *i.e.* standard deviation 0.03 mg) between 0–20 bar. Water and ethanol sorption measurements were carried out on a VSTAR™ sorption analyzer (Model number Vstar4-0000-1000-XS) from Quantachrome. The gas sorption experiments and the liquid sorption measurements were performed on sample amounts of at least 30 mg, which were degassed on the ASAP 2020 at 160 °C for 8 h (sql-DMF and lvt-MeOH) and at 110 °C for 3 h (sql-ACN). N$_2$ sorption measurements were carried out at 77 K, CO$_2$ at 293 K, 273 K (ice/deionized water) and 195 K (acetone/dry ice bath) and CH$_4$ at 293 K and 273 K.

X-ray crystallography

Suitable single crystals were carefully selected under a polarized-light microscope and mounted in a perfluorinated oil drop. The single-crystal diffraction data was collected using a Bruker Kappa APEX2 Duo CCD diffractometer with a microfocus source for Mo–Kα radiation (λ = 0.71073 Å) and multi-layer mirror monochromator. The data were collected under a cold nitrogen gas-stream at 140 ± 2 K using the APEX2 software[34] for unit-cell determination and data collection. Data reduction was performed by SAINT 8.34A (integration) and SADABS (empirical absorption correction).[35] The structures were solved by direct methods using SHELXT-2015.[36] Full-matrix least squares refinements on F^2 were carried out with SHELXL-2017/1. All non-hydrogen atoms were refined with anisotropic temperature factors. Hydrogen atoms for aromatic and aliphatic CH and CH$_3$ groups were positioned geometrically (C–H = 0.95 Å for CH and 0.98 Å for CH$_3$) and refined using a riding model (AFIX 43 for CH and AFIX 137 for CH$_3$), with U_{iso}(H) = 1.2U_{eq}(CH) and U_{iso}(H) = 1.5U_{eq}(CH$_3$). The hydrogen atoms of the NH group were positioned and refined freely with $U_{iso}(H) = 1.5U_{eq}(N)$.

The hydrogen atoms of the solvent water molecules were found and refined freely with $U_{iso}(H) = 1.5U_{eq}(O)$ and restrained using DFIX with $d = 0.82$ and DANG with $d = 1.3$.

For sql-[Cu(Hmpba)$_2$]·*x*DMF (sql-DMF) one DMF molecule was found and refined with full occupancy. Disordered solvent molecules resulting in non-refinable electron density were removed *via* the SQUEEZE command in PLATON.[37] The resulting solvent accessible volume of 404 Å^3 per unit cell contained 88 electrons, which would correspond to 2DMF molecules (40 e each) or 0.5DMF for the given asymmetric formula unit (Z = 4). For sql-[Cu(Hmpba)$_2$]·2ACN (sql-ACN) two ACN molecules were refined with full occupancy. For lvt-[Cu(Hmpba)$_2$]·9H$_2$O (lvt-H$_2$O) H$_2$O molecules were found with refined site occupancy factors ranging from 0.858 to 0.963 resulting in a total of 8.97 H$_2$O molecules.

Crystallographic and refinement details are collected in Table S1, ESI.† The structural data have been deposited with the Cambridge Crystallographic Data Center under deposition numbers CCDC 1999766–1999768.† The supramolecular packing interactions have been analyzed with PLATON.[37]

Synthetic procedures

[Cu(Hmpba)$_2$]·*x*DMF (sql-DMF, x = 1–1.5). A solution of H$_2$mpba (20 mg, 0.092 mmol) and of Cu(NO$_3$)$_2$·2.5H$_2$O (11 mg, 0.047 mmol) in *N*,*N*-dimethylformamide (DMF, 1.65 mL) and deionized water (0.15 mL) was sealed in a glass vial with screw cap and heated at 60 °C for three days after which deep blue star-shaped crystal clusters with single thin needles had formed and were collected after cooling to room temperature (yield 21 mg, 79%, based on the metal salt and one DMF molecule in the product). Calc. for $C_{27}H_{29}CuN_5O_5$ (x = 1, 567.10 g mol^{-1}) C 57.18, H 5.15, N 12.35, for $C_{28.5}H_{32.5}CuN_{5.5}O_{5.5}$ (x = 1.5, 603.64 g mol^{-1}) C 56.71, H 5.43, N 12.76; found C 55.94, H 5.58, N 12.42%.

[Cu(Hmpba)$_2$]·2ACN (sql-ACN). A solution of H$_2$mpba (20 mg 0.092 mmol) and of Cu(NO$_3$)$_2$·2.5H$_2$O (11 mg 0.047 mmol) in acetonitrile (ACN, 1.65 mL) and deionized water (1.15 mL) were sealed in a glass vial with screw cap and heated at 80 °C for three days after which deep violet needle-shape crystals had formed (yield 20 mg, 72%, based on the metal salt). Calc. for $C_{28}H_{28}CuN_6O_4$ (2ACN, 576.10 g mol^{-1}) C 58.37, H 4.90, N 14.59; found C 58.35, H 4.81, N 13.87%.

[Cu(Hmpba)$_2$]·4MeOH·1H$_2$O (lvt-MeOH) was synthesized as described by Richardson and co-workers.[22]

[Cu(Hmpba)$_2$]·9H$_2$O (lvt-H$_2$O) was synthesized by exchanging the methanol in lvt-MeOH against water. The methanol was removed with a pipette and the crystals placed on filter paper for brief (5 min) air drying. After this the crystals of lvt-MeOH (44 mg) were put in DI water (13 mL) at room temperature. During the first fourteen days, the DI water was replaced twice a day (removal with a pipette) to allow the softest exchange as possible to maintain the crystal quality. During the next seven days, the solvent exchange was continued at 40 °C and the DI water was replaced once a day. After 21 days bright violet crystals were collected (yield 38 mg, 86%). Calc. for $C_{24}H_{40}CuN_4O_{13}$ (9H$_2$O, 656.15 g mol^{-1}) C 43.93, H 6.14, N 8.54; found C 43.85, H 6.81, N 8.11%.

Results and discussion

Crystal structures of sql-DMF and sql-ACN

Deep blue star-shaped crystal clusters with single thin needles of [Cu(Hmpba)$_2$]·*x*DMF, denoted as sql-DMF and violet needle-shaped crystals of [Cu(Hmpba)$_2$]·2ACN (sql-ACN) were obtained from Cu(NO$_3$)$_2$·2.5H$_2$O and H$_2$mpba in the solvent mixtures of DMF/H$_2$O or ACN/H$_2$O, respectively (see the images of the crystalline phases in Fig. S3, ESI†). The phase purity was ascertained by PXRD (Fig. S1a, ESI†). The compound sql-DMF crystallizes in the monoclinic space group $P2_1/n$. The asymmetric unit contains one Cu(II) atom, two monodeprotonated ligands Hmpba$^-$ and one DMF solvent molecule of crystallization (Fig. 1). Each copper ion is surrounded square-planar by two *trans* carboxylate-oxygen atoms and two *trans* pyrazole-nitrogen atoms from four different ligands representing the 4-c square {CuN$_2$O$_2$}-nodes of a two-dimensional sql-framework. The Cu–O and Cu–N bond lengths lie between 1.950(5)–1.970(4) Å and 1.980(5)–1.985(5) Å, respectively.

The compound sql-ACN crystallizes in the monoclinic space group $P2_1/c$. The asymmetric unit contains two Cu(II) ions with a symmetry induced site-occupancy-factor of 0.5, two monodeprotonated Hmpba$^-$ ligands and two disordered ACN molecules, representing two independent building units or a Z' = 2 structure (Fig. S4b, ESI†). The coordination environment of the two copper ions is also square planar, with *trans*-O and *trans*-N coordination and with Cu–O and Cu–N bond lengths between 1.937(8)–1.953(8) Å and 1.961(0)–1.998(5) Å, respectively. The two crystallographically distinct

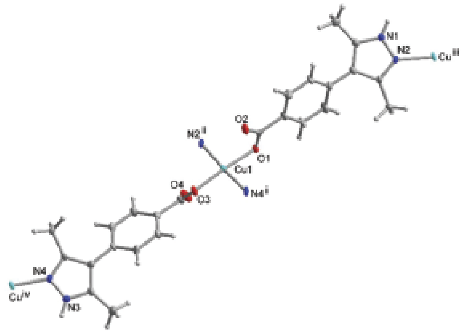

Fig. 1 Metal–ligand coordination in [Cu(Hmpba)$_2$]·*x*DMF (sql-DMF) (70% thermal ellipsoids). Symmetry transformations: i = $x + 1/2, -y + 3/2, z + 1/2$; ii = $x - 1/2, -y + 1/2, z - 1/2$; iii = $x + 1/2, -y + 1/2, z + 1/2$; iv = $x - 1/2, -y + 3/2, z - 1/2$. The DMF solvent molecule is omitted for clarity (see Fig. S4a†). The essentially identical metal–ligand coordination for sql-ACN is shown in Fig. S4b, ESI.†

copper ions are the 4-c square $\{CuN_2O_2\}$-nodes of two independent **sql**-networks.

Because of the structural similarity and for the better highlight of their structural differences, the supramolecular features of **sql**-DMF and **sql**-ACN are discussed together. The most important supramolecular interactions in both compounds are interlayer NH⋯O hydrogen bonds from the NH function to an oxygen atom of a carboxylate group and CH⋯π interactions[38] between the phenyl-rings of adjacent layers (Fig. 7).

By these interlayer NH⋯O hydrogen bonds and C–H⋯π interactions, the layers in both **sql**-DMF and **sql**-ACN are arranged in an eclipsed fashion with formation of a potentially porous supramolecular network with channels along the *a* direction (Fig. 2). The channels have a lozenge shape with diagonals of 6.3 Å and 6.8 Å in **sql**-DMF and of 5.0 Å and 6.2 Å in **sql**-ACN with the van der Waals surface taken into account (Fig. 2). The stacking sequence for **sql**-DMF is AA′ because adjacent layers are related by an inversion symmetry operation. In the **sql**-ACN structure the two crystallographically independent networks yield an eclipsed AB sequence. The networks **sql**-DMF and **sql**-ACN can be interpreted as packing polymorphs.[39,40] The role of the DMF and ACN solvent of crystallization is attributed to a templating effect together with an

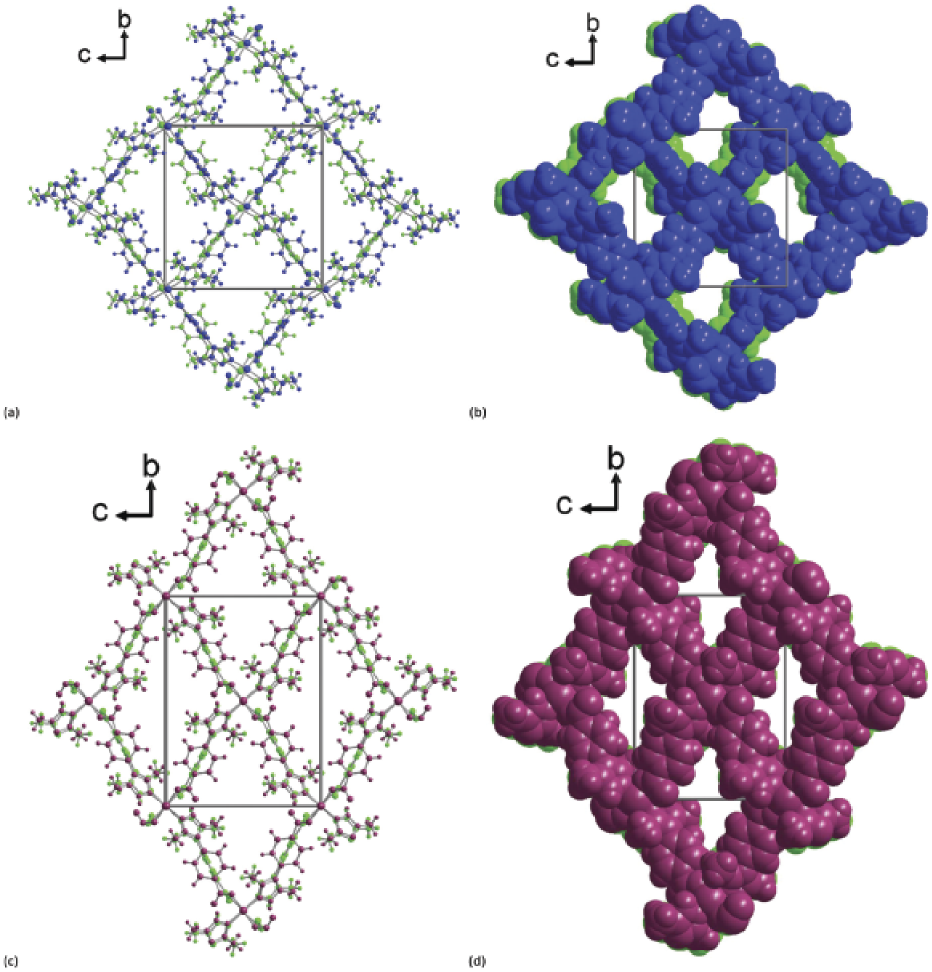

Fig. 2 Top row: Inversion-symmetric AA′ stacking of the nets along the *a* direction in **sql**-DMF in (a) ball-and-stick and (b) space-filling presentation. Bottom row: AB stacking of two symmetry-independent A and B nets along *a* in **sql**-ACN in (c) ball-and-stick and (d) space-filling presentation. The two nets are represented in different color for clarity.

influence on the linker conformation in form of weak interactions.[32] The solvent is obviously the controlling parameter for the crystallization.

Crystal structure of lvt-H_2O

In order to obtain a structure of [Cu(Hmpba)$_2$] with water as the only guest molecule, we replaced the methanol in (lvt-MeOH)[22] by water. A direct synthesis was not possible when water was attempted to be used as the only solvent during the synthesis. The solvent exchange from lvt-MeOH to [Cu(Hmpba)$_2$]·9H_2O (lvt-H_2O) was verified by a single-crystal X-ray structure and NMR spectroscopy (absence of MeOH, see Fig. S11, ESI†). In the structure of lvt-H_2O all five symmetry independent water molecules with their hydrogen atoms were found and refined. The diffractogram collected after 14 days matches the simulation based on the single crystal analysis of lvt-H_2O (Fig. 3) and is distinctively different from lvt-MeOH, although a small contribution lvt-MeOH cannot be fully ruled out. When the solvent exchange was prolonged to 21 days the crystallinity seemed to deteriorate as evidenced by a lower reflection intensity (Fig. S1b, ESI†)

The all-water structure, lvt-H_2O, is of interest in the context of cycling water sorption of MOF for heat transformation.[41–44] The compounds lvt-MeOH and lvt-H_2O are isostructural and crystallize in the $I4_1/a$ tetragonal space group with very similar cell parameters. The 3D framework lvt-H_2O, just as lvt-MeOH yields a triply interpenetrated structure (Fig. S5 ESI†). The copper atom has a centrosymmetric *trans*-{CuN_2O_4} environment. Two carboxylate groups form a short (1.942 Å) and a Jahn–Teller-distorted long (2.727 Å) Cu–O bond giving a tetragonally elongated or square-bipyramidal coordination environment for the copper atom (Fig. 4a). The NH donor function of the pyrazole unit does not participate in a hydrogen bond to the adjacent carboxylate group of the copper atom but donates to the oxygen atom of a water solvent molecule (Fig. 4, Table S3, ESI†). This represents the most significant difference to the sql-structures where the NH function interacts with the carboxylate function of the next layer. The waters of crystallization could be found and refined to be close to 4.5 water molecules, which are distributed over five positions (Fig. 4), corresponding to about nine water molecules per formula unit.

The water substructure in lvt-H_2O is an infinite 3D array of $(H_2O)_{20}$ clusters of S_4 symmetry (Fig. 5). The cluster can be

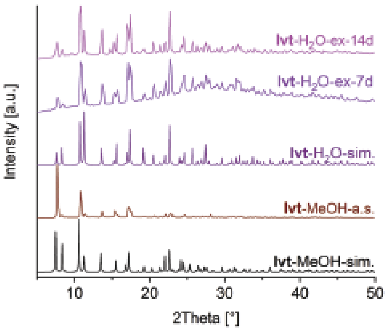

Fig. 3 PXRD patterns of the lvt-MeOH-sim., lvt-MeOH-a.s., lvt-H_2O-sim. and the different time steps of the exchange after 7 d and 14 d exchange.

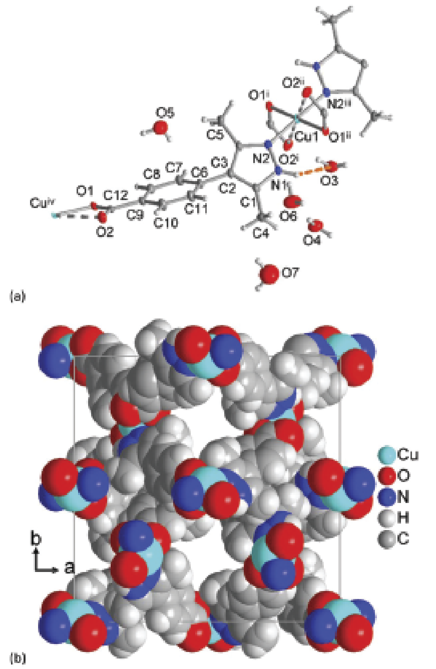

Fig. 4 (a) Metal–ligand coordination in [Cu(Hmpba)$_2$]·9H_2O, lvt-H_2O (H-bond in orange dashed line. 50% thermal ellipsoids). Symmetry transformations: i = $y - 3/4, -x + 3/4, -z + 3/4$; ii = $-y + 3/4, x + 1/4, z - 3/4$; iii = $-x, -y + 1, -z$; iv = $y - 1/4, -x + 3/4, z + 3/4$. (b) Section of the packing diagram in space-filling presentation with water omitted to indicate the potential porosity of the triply-interpenetrated lvt network.

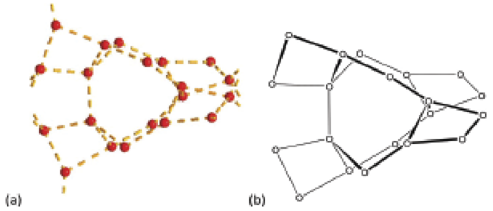

Fig. 5 (a) Structure of the S_4-symmetric $(H_2O)_{20}$ cluster in lvt-H_2O which is extended into a 3D array along the broken-off bonds. Only the O atoms are shown for clarity with the H-bridged O···O contacts (between 2.7–3.1 Å) as yellow dashed lines. (b) Schematic drawing of the $(H_2O)_{20}$ cluster.

described with a central $(H_2O)_{12}$ unit composed of four 7-membered rings, onto which four 4-membered rings are annelated (Fig. 5). The H-bridged O···O contacts vary between 2.7 and 3.1 Å. Such higher dimensionality water clusters are rare. A 1D water chain containing $(H_2O)_{20}$ was reported in the 2D framework $[Cd(phen)_2(male)(H_2O)]\cdot 9.5H_2O$ ($male^{2-}$ = maleate)[45] and a regular pentagonal $(H_2O)_{20}$ dodecahedra in the 2D network $[Ag_6(Pra_2biim)_3]\cdot 5.33H_2O$ (Pra_2biim^{2-} = 1,1′-di(propionate)-2,2′-biimidazole)[46] Theoretical calculations for $(H_2O)_{20}$ clusters looked at structures of annelated 4- to 6-membered rings (Fig. S6, ESI†).[47–50] Other large water clusters include, for example, a $(H_2O)_{14}$ cluster of S_6 symmetry,[51] a $(H_2O)_{12}$-containing infinite chain,[52] one-dimensional water helices,[53] 2D-water/ice layers with $(H_2O)_8$ subunits[54] and a three dimensional open framework.[55]

Comparison between sql-[Cu(Hmpba)$_2$] and lvt-[Cu(Hmpba)$_2$] networks

The 2D networks in sql-DMF and sql-ACN are supramolecular isomers to the 3D frameworks of lvt-MeOH[22] and lvt-H_2O. In the sql structure the $\{CuO_2N_2\}$ SBUs and the bonding directions of the linkers of a single network all lie in one plane (Fig. 6a). The angle between the $\{CuO_2N_2\}$ planes is 19°. In the lvt structures a 3D connectivity is brought about by the tilting of the adjacent $\{CuO_2N_2\}$ planes by 74° (Fig. 6b). The interplanar phenyl–pyrazole angle is similar in the sql and the lvt networks with 51.7(3)° and 47.6(4)°, respectively.

The difference between the 2D sql-networks and the 3D lvt-networks can be traced to the templating effect by the solvent of crystallization. The sql isomers have DMF and ACN incorporated into the structure. Subsequently, the N–H group seeks an acceptor in the network building blocks and becomes engaged into interlayer N–H···O hydrogen bonds to a carboxylate group from the adjacent layer (Fig. 7a and b). The strong hydrogen-bond acceptors methanol and water in lvt-MeOH

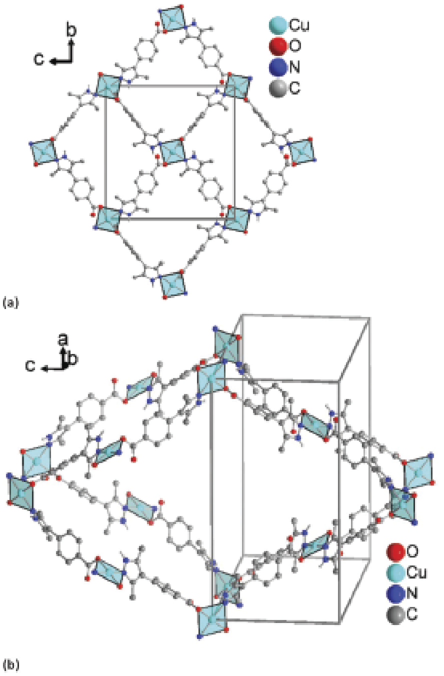

Fig. 6 Single network in (a) sql-DMF and in (b) lvt-H_2O to illustrate the different tilting of the adjacent $\{CuO_2N_2\}$ planes. See Fig. S5a and b (ESI†) for the triply-interpenetrating lvt-H_2O network (identical to lvt-MeOH[22]).

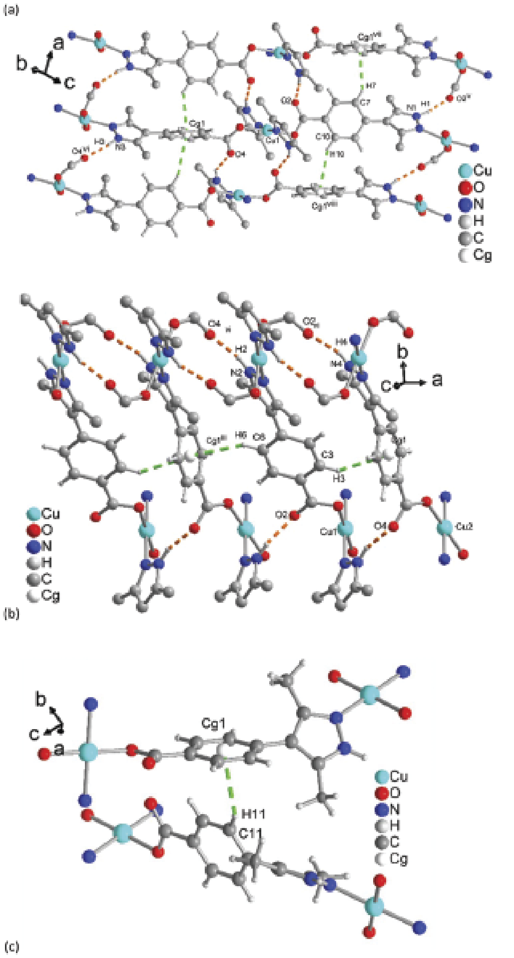

Fig. 7 Representation of the interlayer CH–π interactions (green-dashed lines) and the N–H···O hydrogen bonds (orange-dashed lines) in (a) sql-DMF and in (b) sql-ACN and (c) lvt-H_2O. See Table S3† for details and symmetry transformations.

and **lvt**-H_2O, respectively, engage the N–H function in a hydrogen bond (Fig. 4a). Thus, the tilting of the {CuO_2N_2} SBUs depends on the templating solvent. We note that DMF and ACN are not H-bond donors but are H-bond acceptors, albeit being weaker than water and methanol. Still their H-bond acceptor character is apparently not sufficient to engage the N–H function in a hydrogen bond in the absence of an H-bond donor capability which may be needed to "anchor" the templating solvent in this position.

Porosity and gas sorption studies

In the work of Richardson and co-workers there was no indication that the compound **lvt**-MeOH and the other reported 3D-**dia** and 2D-**sql** [M(Hmpba)$_2$] frameworks could be activated for gas sorption studies.[22] The eclipsed layer stacking in the **sql**-DMF and **sql**-ACN with continuous channel formation (Fig. 2) seemed, however, promising to achieve a permanently porous structure. The activation of the materials was carried by heating **sql**-DMF and **lvt**-MeOH to 160 °C and **sql**-ACN to 110 °C and verified by TGA (Fig. S7–S10, ESI†). While the non-activated **sql** compounds still showed a mass loss due to solvent in the expected temperature range, the activated materials did not exhibit any mass loss up to 300 °C, hence DMF and ACN were completely removed from **sql**-DMF and **sql**-ACN, respectively. After 300 °C decomposition occurred with an abrupt mass loss up to 350 °C of ~30 wt% for **sql**-DMF-act. and ~40 wt% for **sql**-DMF-act. The TGA of the as synthesized **lvt**-MeOH and **lvt**-H_2O compounds both showed a mass loss of 21% up to ~130 °C, which can be attributed to the loss of 4MeOH + 0.5H_2O or 7.5H_2O molecules, respectively, with retention of 1.5H_2O in the activated structure. The TGA of the activated compound **lvt**-MeOH (**lvt**-MeOH-act.) also shows a mass loss of 4–7%, which indicates the strong hygroscopic nature of the compound during the sample preparation (Fig. S10, ESI†). It follows that compound **lvt**-MeOH-act. still contained 1.5 water molecules above 150 °C and up to 250 °C as was authenticated by Richardson and co-workers with single-crystal X-ray diffraction (compound 8-*dry* in ref. 22). Consequently, **lvt**-MeOH-act. had a formula of [Cu(Hmpba)$_2$]·1.5H_2O and was used for the gas sorption measurements. Above 250 °C **lvt**-MeOH and **lvt**-MeOH-act. decomposed.

The experimental PXRD patterns from the activated **sql**-structures (**sql**-DMF-act.; **sql**-ACN-act.) show preservation of crystallinity: the simulated diffractograms from the X-ray structures, where the solvent of crystallization had been removed, match well with the experimental ones (Fig. 8). For the activated **lvt**-MeOH structure the experimental PXRD pattern matches well with the experimental PXRD pattern of the air-dried sample of **lvt**-MeOH reported by Richardson and co-workers (compound 8-*dry* in ref. 22) that still contained 1.5 water molecules (Fig. S2c, ESI†).[22]

CO_2 and CH_4 gas sorption studies were performed for the activated **sql**- and **lvt**-networks (Fig. 9, Fig. S15, ESI†). The N_2 gas adsorption was negligible at 77 K (Fig. S12, ESI†). We justify this with the small pore openings of 5 to 6.8 Å (see above) of these networks with possible pore blocking and

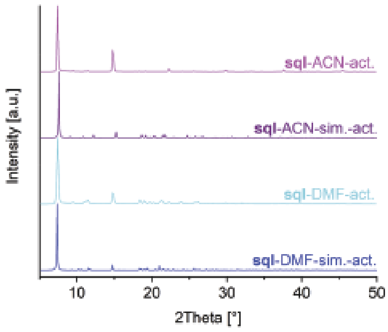

Fig. 8 PXRD patterns of the activated (act.) sql-DMF and sql-ACN and their simulated PXRD patterns based on the crystal structures with solvent of crystallization removed (sim.-act.). See Fig. S2a and b, ESI,† for the comparison between the PXRD patterns of the activated structures and the simulations based on the solvent-containing crystal structures.

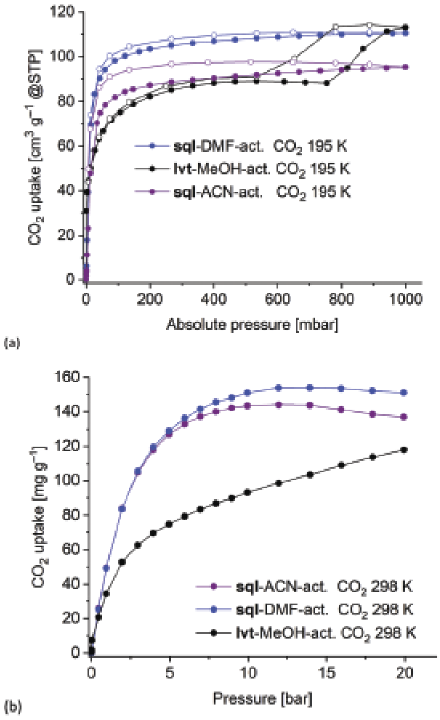

Fig. 9 (a) Low-pressure CO_2 sorption isotherms of lvt-MeOH-act., sql-DMF-act. and sql-ACN-act. at 195 K with the adsorption points as filled symbols and the desorption points as open symbols. (b) High-pressure CO_2 adsorption isotherms of lvt-MeOH-act., sql-DMF-act. and sql-ACN-act. at 298 K.

structure rearrangement at the pore mouths after removal of the solvent molecules. The diffusion of N_2 molecules with the kinetic diameter of N_2 3.6 Å at cryogenic temperature of 77 K into small pores is very slow, while kinetic inhibition is lower in the case of CO_2 and CH_4 sorption at 195 K to near room temperature (kinetic diameters 3.3 and 3.76 Å, respectively).

CO_2 adsorption was measured volumetrically at different temperatures at pressures up to 1 bar (Fig. 9a, Fig. S15, ESI†) and gravimetrically at 298 K and up to 20 bar (Fig. 9b). At low pressure all the three activated materials exhibit a steep CO_2 uptake at 195 K due to strong adsorbent-adsorbate interactions in narrow micropores. The low-pressure adsorption curvature for the **sql** nets at 195 K (Fig. 9a) is akin to a Type I isotherm, yet there is a noteworthy hysteresis.[56] The adsorption curvature for **lvt**-MeOH-act. at 195 K could be viewed as initially a Type Ib isotherm turning into a Type IV with its typical feature of a saturation plateau and a hysteresis (here of H2b). A Type H2b hysteresis is associated with pore blocking. Type Ib isotherms are found for materials with wider micropores and narrow mesopores and Type IV isotherms are typical for mesoporous adsorbents.[56] Alternatively, the stepped CO_2 isotherm for the **lvt**-network could be due to a pore opening effect at around 750 mbar (Fig. 9a, Fig S13, ESI†).

It is noteworthy that, **lvt**-MeOH-act. does not show the uptake step, which was observed at 195 K, when CO_2 adsorption was measured at 273 and 293 K (Fig. S15a, ESI†). This missing uptake step speaks for a pore opening effect at 195 K at 750 mbar (Fig. 9a). Based on the CO_2 saturation pressure of 1.00 bar at 195 K or a relative pressure of $P/P_0 = 0.75$, at 293 K or 298 K the gate opening at the same relative pressure would be expected around 43 bar or 48 bar, respectively. Consequently, a volumetric CO_2 measurement at 293 K up to 1 bar (with $P/P_0 = 0.017$) or a gravimetric high-pressure adsorption at 298 K up to 20 bar ($P/P_0 = 0.31$) does not yet induce the gate opening (Fig. 9b).

The CO_2 sorption data was used to derive the pore volume and pore-size distribution (Table 1, Fig. S14, ESI†) and Langmuir surface area for the activated materials. The lower CO_2 uptake of **sql**-ACN-act. (90 cm^3 g^{-1}) *versus* **sql**-DMF-act. (111 cm^3 g^{-1}, both at 1 bar) reflects the narrower pores and lower pore volume seen in the X-ray structures due to the different layer packing (Fig. 2). The **lvt**-network does not reach a plateau in high-pressure CO_2 sorption, but a pore volume of 0.17 cm^3 g^{-1} at 20 bar was derived under the assumption of the validity of the Gurvich-rule.[57]

The calculated pore volumes from the volumetric low-pressure and gravimetric high-pressure sorption data are in a good agreement. The pore volumes calculated from the 195 K saturation uptakes for the **sql**-networks are lower than the calculated pore volumes from the X-ray structures. This can be expected as very narrow pore regions (*cf.* Fig. 2) cannot be accessed by CO_2 with its kinetic diameter of 3.3 Å, while

Table 1 Gas sorption and porosity characteristics

	Uptake		Pore volume[a]	Langmuir surface area	ΔH°_{ads}	ΔH°_{ads}
	[cm^3 g^{-1}]	[mmol g^{-1}]	[cm^3 g^{-1}]	[m^2 g^{-1}]	[kJ mol^{-1}] CO_2	[kJ mol^{-1}] CH_4
sql-DMF-act.			0.26[b]; 0.28[c]			
CO_2, 195 K, 1.0 bar	111	4.90	0.20[d]	516		
CO_2, 273 K, 1.0 bar	60	1.37			−23	
CO_2, 293 K, 1.0 bar	33	0.76				
CO_2, 298 K, 20 bar	0.154 g g^{-1} [e]	3.50	0.22[d]			
CH_4, 273 K, 1.0 bar	27	1.20				−13
CH_4, 293 K, 1.0 bar	20	0.87				
sql-ACN-act.			0.23[b]; 0.26[c]			
CO_2, 195 K, 1.0 bar	90	4.00	0.16[d]	453		
CO_2, 273 K, 1.0 bar	60	1.36			−22	
CO_2, 293 K, 1.0 bar	34	0.78				
CO_2, 298 K, 20 bar	0.144 g g^{-1} [e]	3.30	0.20[d]			
CH_4, 273 K, 1.0 bar	22	1.00				−15
CH_4, 293 K, 1.0 bar	15	0.67				
lvt-MeOH-act.			0.25[b]; 0.33[c]			
CO_2, 195 K	0.75 bar: 88 1.0 bar: 113	0.75 bar: 3.90 1.0 bar: 5.00	0.16[c] 0.21[d]	407		
CO_2, 298 K, 20 bar	0.124 g g^{-1} [e]	2.80	0.17[d]			
CO_2, 273 K, 1.0 bar	48	1.09			−41	
CO_2, 293 K, 1.0 bar	31	0.73				
CH_4, 273 K, 1.0 bar	10	0.45				−26
CH_4, 293 K, 1.0 bar	6	0.25				

[a] Specific pore volume calculated according to (SAV × N_A)/($Z \times M_{asym\ unit}$) or (void volume × N_A)/($Z \times M_{asym\ unit}$); N_A = Avogadro's constant, 6.022 × 10^{23} mol^{-1}, Z = number of asymmetric formula units, $M_{asym\ unit}$ = molecular weight of asymmetric formula unit [in g mol^{-1}]. The potential solvent area volume (SAV) or void volume [in $Å^3$] was calculated from. [b] By the program Mercury[33] with a probe radius of 1.2 Å, grid spacing of 0.7 Å; values calculated using 'contact surface'. [c] From the crystal structures, where the solvent of crystallization had been removed, with PLATON for Windows ('calc. void' calculation)[37]. [d] Under the assumption of the validity of the Gurvich rule according to (specific amount adsorbed)/(density of liquid adsorbate) with the CO_2 saturation pressure at 298 K of 64.3 bar, at 293 K of 57.3 bar and at 195 K of 1.00 bar with ρ_{CO_2}(195 K) = 1.08 g cm^{-3} and ρ_{CO_2}(298 K) = 0.712 g cm^{-3}.[57] [e] The unit g g^{-1} is due to the gravimetric uptake in the high-pressure adsorption.

PLATON[37] uses a probe sphere of 1.2 Å radius rolling over the Connolly surface.

As expected, the uptake of the slightly larger non-polar gas CH_4 is significantly lower than for CO_2. Furthermore, **lvt**-MeOH-act. adsorbs notably less CH_4 than **sql**-DMF-act. and **sql**-ACN-act. (Fig. S15b†). The determined $CO_2 : CH_4$ selectivity by the Henry plots of the adsorption isotherms is slightly higher for the **lvt**-network than for the **sql**-networks (Fig. S19, Table S5, ESI†). This can be reasoned by the residual water content in the **lvt**-network, which disfavors the uptake of CH_4. The higher selectivity for CO_2 for the **sql**-ACN-act. network over **sql**-DMF-act. can be traced to the smaller limiting pore diameters in the former which better discriminates between the smaller CO_2 and larger CH_4 gas molecules.

The isosteric enthalpy of adsorption at zero coverage, ΔH°_{ads} for CO_2 and CH_4 from adsorption isotherms at 273–293 K (Fig. S15, ESI†) was calculated with the virial fit method (Table 1, Fig. S17 and S18, ESI†).[58] As expected, the values of the isosteric enthalpy of adsorption for CO_2 are significantly higher than for CH_4 for all three materials. At the same time, the magnitude of the isosteric enthalpy for CO_2 for the **lvt**-MeOH network is relatively high with −41 kJ mol^{-1} compared to other MOFs (typical range between 21–39 kJ mol^{-1}).[59,60] The still present water molecule in **lvt**-MeOH is seen as the basis for the high isosteric enthalpy. In contrast, ΔH°_{ads} for CO_2 in both **sql**-networks is at the lower end of the typical range.[59,60]

To classify the **sql** and **lvt** structures in terms of hydrophobicity and hydrophilicity, water (Fig. 10) and ethanol sorption measurements (Fig. S21, ESI†) were carried out and the Henry constants were determined (Table S6, Fig. S20a, ESI†). The activated **sql**-DMF network (**sql**-DMF-act.) was used exemplarily because of the better pore accessibility over the **sql**-ACN network (which was evident from CO_2 sorption).

For **sql**-DMF-act. the water uptake at high $P/P_0 > 0.4$ and a Henry constant value in the order of 10^{-7} g mol^{-1} Pa^{-1} corresponds to a hydrophobic character of the pores.[61] On the other hand, the early water uptake below $P/P_0 = 0.1$ and a Henry constant of 10^{-5} g mol^{-1} Pa^{-1} for **lvt**-MeOH-act. indicates a rather hydrophilic material.[62,63] At the adsorption maximum (P/P_0 = 0.9) the **lvt**-MeOH-act. structure has adsorbed 2.8 water molecules per formula unit (5.7 mmol g^{-1}). Together with the residual 1.5 water molecules, the structure then contains 4.3 water molecules per formula unit. This agrees well with the 4.5 water molecules found in the crystal structure of the water exchanged **lvt**-H_2O material.

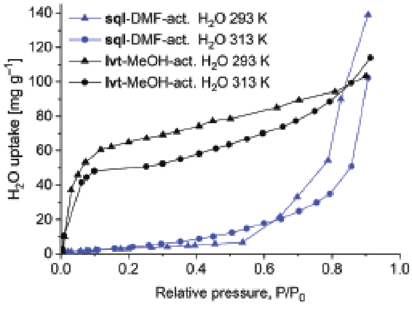

Fig. 10 Water adsorption isotherms of **sql**-DMF-act. and **lvt**-MeOH-act. at 293 K and at 313 K.

The isosteric enthalpy of water adsorption for the **sql**-DMF-act. material increases with the water uptake from −32 to −50 kJ mol^{-1} (Fig. S20b†), which is only slightly above the evaporation enthalpy of water (44 kJ mol^{-1}).[64] In contrast, ΔH_{ads} for the activated **lvt**-MeOH increases from −41 to −64 kJ mol^{-1}, which underlines the hydrophilicity of the material. For the initial increase in ΔH_{ads} for the hydrophobic **sql**-DMF a framework flexibility or phase change may be proposed, through which anchor points could be formed for the subsequent (increasing) adsorption of water. Such a flexibility or phase change induced by the first water molecules at high P/P_0 in **sql**-DMF could make the –NH groups of the Hmpba$^-$ ligand available as H-bond donor sites. For **lvt**-MeOH the initial increase in ΔH_{ads} is proposed to be due to a similar gate-opening effect as for the CO_2 adsorption. The isotherm of the ethanol sorption at 293 K (Fig. S21, ESI†) corroborates the flexibility of the **lvt**-network by showing a sudden opening at $P/P_0 \approx 0.1$ with a Type F-II isotherm.[65] For the **sql**-network the ethanol adsorption isotherm at 293 K shows a gradual increase.

Conclusion

In this contribution we present two new microporous 2D metal–organic frameworks **sql**-[Cu(Hmpba)$_2$]·*x*DMF and **sql**-[Cu(Hmpba)$_2$]·2ACN which are based on the linear, bifunctional 4-(3,5-dimethyl-1*H*-pyrazol-4-yl)benzoate linker in its monodeprotonated form Hmpba$^-$. The microporous character of the two activated MOFs was demonstrated by CO_2 and CH_4 sorption. The 2D MOFs are supramolecular isomers of already known 3D **lvt**-Cu frameworks [Cu(Hmpba)$_2$]·L$_{solv}$. Through a methanol-to-water solvent exchange we could derive from **lvt**-[Cu(Hmpba)$_2$]·4MeOH·1H_2O at the new all-water isomer 3D **lvt**-[Cu(Hmpba)$_2$]·9H_2O, with a water substructure of a 3D array of S_4-symmetric $(H_2O)_{20}$ clusters. The potential porosity of the **lvt**-[Cu(Hmpba)$_2$] isomers had not been described before and here we showed for the first time that the 3D network **lvt**-[Cu(Hmpba)$_2$]·4MeOH·1H_2O could be activated for CO_2 and CH_4 adsorption in with it displays a gate-opening effect. A crucial structural difference between the supramolecular **sql**- and **lvt**-[Cu(Hmpba)$_2$] isomers is the engagement of the –NH group of the pyrazolyl moiety in inter-network H-bonding in the former and in crystal-water H-bonding in the latter. This difference then leads to a hydrophobic character of the **sql**-materials and a hydrophilic **lvt**-network, which was demonstrated here by water and ethanol sorption through their isotherm shape, relative uptake pressure and isosteric enthalpy of adsorption.

The [M(Hmpba)$_2$]·solvent materials reported here are relatively rare examples of supramolecular framework isomers where subtle changes in H-bonding around metal centers result in substantial changes in structure and sorption properties. The combination of the heteroditopic approach in combination with different synthetic conditions (solvent templating) are the reason for these different isomers.

Conflicts of interest

There are no conflicts to declare.

Acknowledgements

The authors thank Dr Christian Heering for the preparation of the water structure, Mrs Birgit Tommes for carrying out the FT-IR experiments and Dr Ishtvan Boldog for the introduction to the topic of bifunctional pyrazolate-carboxylate MOFs, for supervision of students and for the numerous advices regarding the scientific work in general and in manuscript writing.

Notes and references

1 C. Janiak and J. K. Vieth, MOFs, *New J. Chem.*, 2010, 34, 2366–2388.

2 (*a*) R. B. Getman, Y.-S. Bae, C. E. Wilmer and R. Q. Snurr, *Chem. Rev.*, 2012, 112, 703–723; (*b*) K. Adil, Y. Belmabkhout, R. S. Pillai, A. Cadiau, P. M. Bhatt, A. H. Assen, G. Maurin and M. Eddaoudi, *Chem. Soc. Rev.*, 2017, 46, 3402–3430.

3 S. M. J. Rogge, A. Bavykina, J. Hajek, H. Garcia, A. I. Olivos-Suarez, A. Sepúlveda-Escribano, A. Vimont, G. Clet, P. Bazin, F. Kapteijn, M. Daturi, E. V. Ramos-Fernandez, F. X. Llabrés i Xamena, V. Van Speybroeck and J. Gascon, *Chem. Soc. Rev.*, 2017, 46, 3134–3184.

4 R. Medishetty, J. K. Zareba, D. Mayer, M. Samoc and R. A. Fischer, *Chem. Soc. Rev.*, 2017, 46, 4976–5004.

5 G. Mínguez Espallargas and E. Coronado, *Chem. Soc. Rev.*, 2018, 47, 533–557.

6 W. P. Lustig, S. Mukherjee, N. D. Rudd, A. V. Desai, J. Li and S. K. Ghosh, *Chem. Soc. Rev.*, 2017, 46, 3242–3285.

7 X. Lian, Y. Fang, E. Joseph, Q. Wang, J. Li, S. Banerjee, C. Lollar, X. Wang and H.-C. Zhou, *Chem. Soc. Rev.*, 2017, 46, 3386–3401.

8 J. Dechnik, C. J. Sumby and C. Janiak, *Cryst. Growth Des.*, 2017, 17, 4467–4488.

9 J. Dechnik, J. Gascon, C. J. Doonan, C. Janiak and C. J. Sumby, *Angew. Chem., Int. Ed.*, 2017, 56, 9292–9310.

10 F. ZareKarizi, M. Joharian and A. Morsali, *J. Mater. Chem. A*, 2018, 6, 19288–19329.

11 L. Hou, Y.-Y. Lin and X.-M. Chen, *Inorg. Chem.*, 2008, 47, 1346–1351.

12 L.-N. Jia, Y. Zhao, L. Hou, L. Cui, H.-H. Wang and Y.-Y. Wang, *J. Solid State Chem.*, 2014, 210, 251–255.

13 G. Mehlana, V. Chitsa and T. Mugadza, *RSC Adv.*, 2015, 5, 88218–88233.

14 P. Pachfule, B. Garai and R. Banerjee, *Inorg. Chem.*, 2016, 55, 7200–7205.

15 C. Heering, B. Francis, B. Nateghi, G. Makhloufi, S. Lüdeke and C. Janiak, *CrystEngComm*, 2016, 18, 5209–5223.

16 M. Deng, Y. Liang, B. Xing, Z. Chen, Y. Zhou, X. Liu, B. Yue and H. He, *Chem. – Eur. J.*, 2011, 17, 10323–10328.

17 C. Montoro, F. Linares, E. Quartapelle Procopio, I. Senkovska, S. Kaskel, S. Galli, N. Masciocchi, E. Barea and J. A. R. Navarro, *J. Am. Chem. Soc.*, 2011, 133, 11888–11891.

18 C. Heering, I. Boldog, V. Vasylyeva, J. Sanchiz and C. Janiak, *CrystEngComm*, 2013, 15, 9757–9768.

19 B. Nateghi and C. Janiak, *Z. Naturforsch. B*, 2019, 74, 891–899.

20 C.-T. He, J.-Y. Tian, S.-Y. Liu, G. Ouyang, J.-P. Zhang and X.-M. Chen, *Chem. Sci.*, 2013, 4, 351–356.

21 B. Tu, Q. Pang, D. Wu, Y. Song, L. Weng and Q. Li, *J. Am. Chem. Soc.*, 2014, 136, 14465–14471.

22 M. R. Bryant, A. D. Burrows, C. M. Fitchett, C. S. Hawes, S. O. Hunter, L. L. Keenan, D. J. Kelly, P. E. Kruger, M. F. Mahon and C. Richardson, *Dalton Trans.*, 2015, 44, 9269–9280.

23 X.-L. Qi, C. Zhang, B.-Y. Wang, W. Xue, C.-T. He, S.-Y. Liu, W.-X. Zhang and W.-M. Chen, *CrystEngComm*, 2013, 15, 9530–9536.

24 S. Millan, B. Gil-Hernandes, E. Milles, S. Gökpinar, G. Makloufi, A. Schmitz, C. Schlüssener and C. Janiak, *Dalton Trans.*, 2019, 48, 8057–8067.

25 T. A. Makal, A. A. Yakovenko and H.-C. Zhou, *J. Phys. Chem. Lett.*, 2011, 2, 1682–1689.

26 B. Moulton and M. J. Zaworotko, *Chem. Rev.*, 2001, 101, 1629–1658.

27 P. M. Forster, A. R. Burbank, C. Livage, G. Férey and A. K. Cheetham, *Chem. Commun.*, 2004, 368–369.

28 J.-P. Zhang, X. C. Huang and X.-M. Chen, *Chem. Soc. Rev.*, 2009, 38, 2385–2396.

29 C.-T. He, P.-Q. Liao, D.-D. Zhou, B.-Y. Wang, W.-X. Zhang, J.-P. Zhang and X.-M. Chen, *Chem. Sci.*, 2014, 5, 4755–4762.

30 (*a*) O. D. Friedrichs, M. O'Keeffe and O. M. Yaghi, *Acta Crystallogr., Sect. A: Found. Crystallogr.*, 2003, 59, 515–525; (*b*) M. O'Keeffe, M. A. Peskov, S. J. Ramsden and O. M. Yaghi, *Acc. Chem. Res.*, 2008, 41, 1782–1789; (*c*) V. Alexandrov, V. A. Blatov and D. M. Proserpio, *Acta Crystallogr., Sect. A: Found. Crystallogr.*, 2012, 68, 484–493.

31 Z.-M. Ye, C.-T. He, Y.-T. Xu, R. Krishna, Y. Xie, D.-D. Zhou, H.-L. Zhou, J.-P. Zhang and X.-M. Chen, *Cryst. Growth Des.*, 2017, 17, 2166–2171.

32 G. Mehlana, C. Wilkinson, C. N. Dzesse T., G. Ramon and S. A. Bourne, *Cryst. Growth Des.*, 2017, 17, 6445–6454.

33 C. F. Macrae, I. J. Bruno, J. A. Chisholm, P. R. Edgington, P. McCabe, E. Pidcock, L. Rodriguez-Monge, R. Taylor, J. van de Streek and P. A. Wood, *J. Appl. Crystallogr.*, 2008, 41, 466–470.

34 *Apex2 - Data Collection Program for the CCD Area-Detector System; SAINT - Data Reduction and Frame Integration*

Program for the CCD Area-Detector System. Bruker Analytical X-ray Systems, Madison, Wisconsin, USA, 1997–2014.

35 (*a*) G. Sheldrick, *Program SADABS: Area-detector absorption correction*, University of Göttingen, Germany, 1996–2014; (*b*) L. Krause, R. Herbst-Irmer, G. M. Sheldrick and D. Stalke, *J. Appl. Crystallogr.*, 2015, 48, 3–10.

36 G. M. Sheldrick, *Acta Crystallogr., Sect. A: Found. Adv.*, 2015, c71, 3–8.

37 A. L. Spek, Structure Validation in Chemical Crystallography, *Acta Crystallogr., Sect. D: Biol. Crystallogr.*, 2009, 65, 148–155; A. L. Spek, *PLATON – A Multipurpose Crystallographic Tool*, Utrecht University, Utrecht, The Netherlands, 2008; Windows implementation; L. J. Farrugia, Version 280317, University of Glasgow, Scotland, 2020.

38 (*a*) M. Nishio, *Phys. Chem. Chem. Phys.*, 2011, 13, 13873–13900; M. Nishio, Y. Umezawa, K. Honda, S. Tsuboyama and H. Suezawa, *CrystEngComm*, 2009, 11, 1757–1788; (*b*) M. Nishio, *CrystEngComm*, 2004, 6, 130–158; (*c*) C. Janiak, S. Temizdemir, S. Dechert, W. Deck, F. Girgsdies, J. Heinze, M. J. Kolm, T. G. Scharmann and O. M. Zipffel, *Eur. J. Inorg. Chem.*, 2000, 1229–1241; (*d*) Y. Umezawa, S. Tsuboyama, K. Honda, J. Uzawa and N. Motoshiro, *Bull. Chem. Soc. Jpn.*, 1998, 71, 1207–1213; (*e*) M. Nishio, M. Hirota and Y. Umezawa, *The CH/π interaction (evidence, nature and consequences)*, Wiley-VCH, New York, 1998.

39 C. Glidewell, J. N. Low, J. M. S. Skale and J. L. Wardell, *Acta Crystallogr., Sect. B: Struct. Sci.*, 2006, 62, 666–675.

40 D. Chen, Y.-J. Liu, Y.-Y. Lin, J.-P. Zhang and X.-M. Chen, *CrystEngComm*, 2011, 13, 3827–3831.

41 F. Jeremias, D. Fröhlich, C. Janiak and S. K. Henninger, *New J. Chem.*, 2014, 38, 1846–1852.

42 M. F. de Lange, K. J. Verouden, T. J. Vlugt, J. Gascon and F. Kapteijn, *Chem. Rev.*, 2015, 115, 12205–12250.

43 D. Fröhlich, E. Pantatosaki, P. D. Kolokathis, K. Markey, H. Reinsch, M. Baumgartner, M. A. van der Veen, D. E. De Vos, N. Stock, G. K. Papadopoulos, S. K. Henninger and C. Janiak, *J. Mater. Chem. A*, 2016, 4, 11859–11869.

44 S. Gökpinar, S.-J. Ernst, E. Hastürk, M. Möllers, I. El Aita, R. Wiedey, N. Tannert, S. Nießing, S. Abdpour, A. Schmitz, J. Quodbach, G. Füldner, S. K. Henninger and C. Janiak, *Ind. Eng. Chem. Res.*, 2019, 58, 21493–21503.

45 X. Liu, W. C. Lu, C. Z. Wang and K. M. Ho, *Chem. Phys. Lett.*, 2011, 508, 270–275.

46 Y.-G. Sun, F. Ding, X.-F. Gu, W.-Z. Zhang, D.-Z. Wie and E.-J. Gao, *Chin. J. Chem.*, 2008, 26, 1843–1847.

47 G. S. Fanourgakis, E. Aprá and S. S. Xantheas, *J. Chem. Phys.*, 2004, 121, 2655.

48 B. Bandow and B. Hartke, *J. Phys. Chem. A*, 2006, 110, 5809–5822.

49 B. Hartke, *Phys. Chem. Chem. Phys.*, 2003, 5, 275–284.

50 R. L. Sang and L. Xu, *CrystEngComm*, 2010, 12, 1377–1381.

51 F. Zhuge, B. Wu, L. Dong, J. Yang, C. Janiak, N. Tang and X.-J. Yang, *Aust. J. Chem.*, 2010, 63, 1358–1364.

52 Q. Y. Liu and L. Xu, *CrystEngComm*, 2005, 7, 87–89.

53 S.-C. Chen, F. Tian, K.-L. Huang, C.-P. Li, J. Zhong, M.-Y. He, Z.-H. Zhang, H.-N. Wang, M. Du and Q. Chen, *CrystEngComm*, 2014, 16, 7673–7680.

54 C. Janiak, T. G. Scharmann and S. A. Mason, *J. Am. Chem. Soc.*, 2002, 124, 14010–14011.

55 R. Carballo, B. Covelo, C. Lodeiro and E. M. Vázquez-López, *CrystEngComm*, 2005, 7, 294–296.

56 M. Thommes, K. Kaneko, A. V. Neimark, J. P. Olivier, F. Rodriguez-Reinoso, J. Rouquerol and K. S. W. Sing, *Pure Appl. Chem.*, 2015, 87, 1051–1069.

57 L. Gurvich, *J. Soc. Phys.–Chim. Russe*, 1915, 47, 805–827.

58 A. Nuhnen and C. Janiak, *Dalton Trans.*, 2020, 49, 10295–10307.

59 K. Sumida, D. L. Rogow, J. A. Mason, T. M. McDonald, E. D. Bloch, Z. R. Herm, T.-H. Bae and J. R. Long, *Chem. Rev.*, 2012, 112, 724–781.

60 A. Das and D. M. D'Alessandro, *CrystEngComm*, 2015, 17, 706–718.

61 G. Wang, K. Leus, H. S. Jena, C. Krishnaraj, S. Zhao, H. Depauw, N. Tahir, Y.-Y. Liu and P. van der Voort, *J. Mater. Chem. A*, 2018, 6, 6370–6375.

62 S. Dissegna, R. Hardian, K. Epp, G. Kieslich, M.-V. Coulet, P. Llewellyn and R. A. Fischer, *CrystEngComm*, 2017, 19, 4137–4141.

63 J. Canivet, J. Bonnefoy, C. Daniel, A. Legrand, B. Coasne and D. Farrusseng, *New J. Chem.*, 2014, 38, 3102–3111.

64 F. Jeremias, A. Khutia, S. K. Henninger and C. Janiak, *J. Mater. Chem.*, 2012, 22, 10148–10151.

65 Q.-Y. Yang, P. Lama, S. Sen, M. Lusi, K.-J. Chen, W.-Y. Gao, M. Shivanna, T. Pham, N. Hosono, S. Kusaka, J. J. Perry IV, S. Ma, B. Space, L. J. Barbour, S. Kitagawa and M. J. Zaworotko, *Angew. Chem., Int. Ed.*, 2018, 57, 5684–5689.

Electronic Supplementary Material (ESI) for Dalton Transactions.
This journal is © The Royal Society of Chemistry 2020

Electronic Supplementary Information (ESI)

Increase of network hydrophilicity from lvt to sql supramolecular isomers of Cu-MOFs with the bifunctional 4-(3,5-dimethyl-1*H*-pyrazol-4-yl)benzoate linker

Saskia Menzel, Simon Millan, Simon-Patrick Höfert, Alexander Nuhnen, Serkan Gökpinar, Alexa Schmitz and Christoph Janiak*

Institut für Anorganische Chemie und Strukturchemie, Heinrich-Heine-Universität Düsseldorf, Universitätsstraße 1, D-40225 Düsseldorf, Germany. *E-mail: janiak@hhu.de

Additional Emails:
Saskia.menzel@hhu.de; simon.millan@hhu.de; Hoefert@hhu.de; Alexander.Nuhnen@hhu.de; Serkan.Goekpinar@hhu.de; Alexa.Schmitz@hhu.de

IR spectra

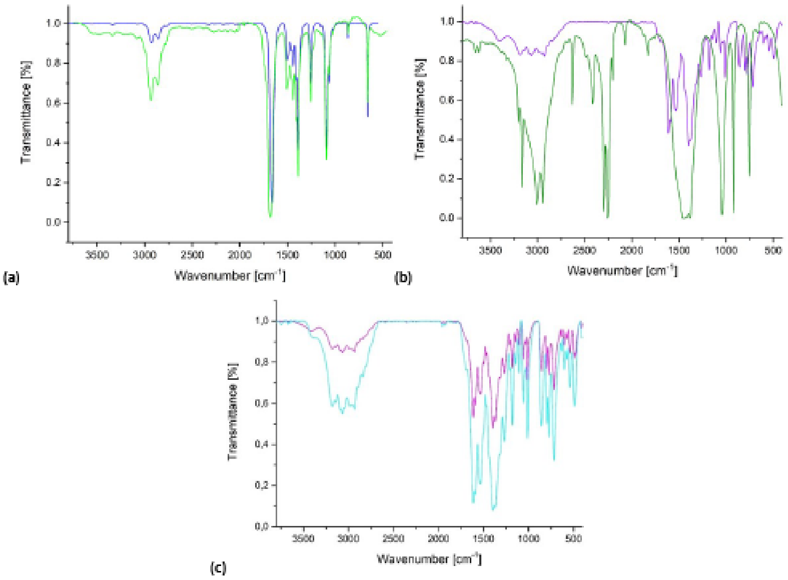

Fig. S0 (a) IR-Spectra (KBr) of as synthesized **sql**-[Cu(Hmpba)$_2$]·xDMF (**sql**-DMF-a.s., blue) and DMF (NIST, green);[1] (b) IR-Spectra (KBr) of as synthesized **sql**-[Cu(Hmpba$_2$]·2ACN (**sql**-ACN-a.s., violet) and ACN (NIST, dark green)[1] (c) IR-Spectra (KBr) of **sql**-DMF-act. (cyan) and of **sql**-ACN-act. (magenta). NIST: The data for the solvent IR-Spectra were download from the NIST database[1] and were plot in Origin.[2]

Powder X-ray diffractograms

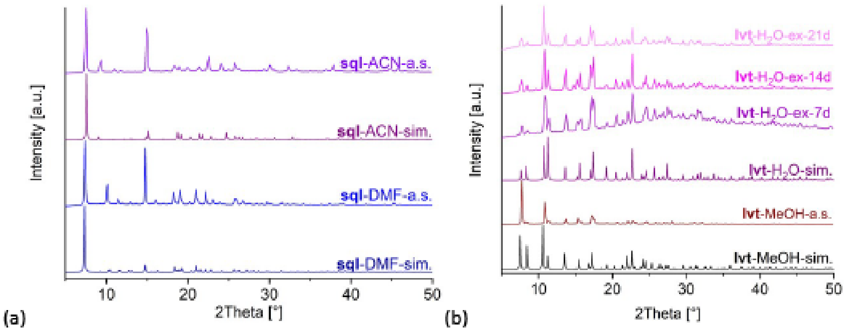

Fig. S1 (a) PXRD patterns of as synthesized **sql**-DMF, **sql**-ACN and their simulations from the single-crystal structure data. (b) PXRD patterns of **lvt**-MeOH-sim., **lvt**-MeOH-a.s., **lvt**-H_2O-sim. and the different control exchange steps after 7 d, 14 d and 21 d.

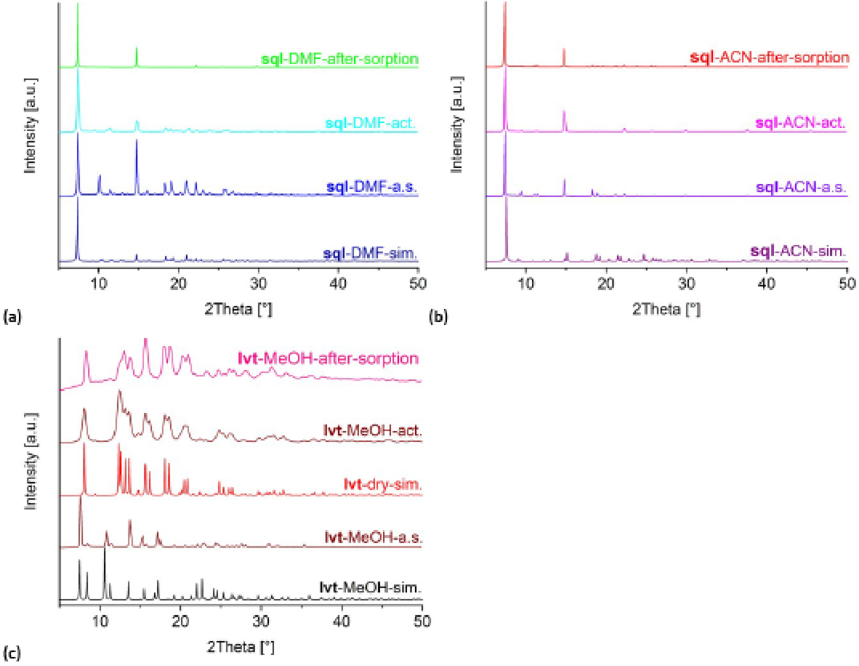

Fig. S2 (a) PXRD patterns for **sql**-DMF simulated (sim.), as synthesized (a.s.), activated (act.) and after gas sorption measurements; (b) PXRD patterns for **sql**-ACN simulated, as synthesized, activated and after gas sorption measurements. (c) PXRD patterns for **lvt**-MeOH simulated, as synthesized, activated and after gas sorption measurements. The PXRD pattern of **lvt**-MeOH-act. must be matched to the PXRD pattern of **lvt**-dry-sim., which represents the air-dried sample of **lvt**-MeOH by Richardson and co-workers *(*compound 8-*dry* in ref.3*)* that still contained 1.5 water molecules.[3] Small changes between the simulated and as-synthesized patterns are due to the unavoidable solvent loss during sample preparation and measurement.

Images of the crystals

Fig. S3 Picture of the crystals of **sql**-DMF (left), **sql**-ACN (middle), **lvt**-H_2O (right).

Crystal structure information

Table S1 Crystal data and structure refinement for **sql**-DMF, **sql**-ACN and **lvt**-H_2O.

Compound	$[Cu(Hmpba)_2]\cdot xDMF$* **sql**-DMF	$[Cu(Hmpba)_2]\cdot 2ACN$ **sql**-ACN	$[Cu(Hmpba)_2]\cdot 9H_2O$ **lvt**-H_2O [d]
CCDC no.	1999766	1999767	1999768
Empirical formula	$C_{24}H_{22}CuN_4O_4\cdot 1(C_3H_7O)$	$C_{24}H_{22}CuN_4O_4\cdot 2(C_2H_3N)$	$C_{24}H_{39.94}CuN_4O_{12.96}$
M_r /g mol^{-1}	567.09	576.10	655.47
Crystal system	monoclinic	monoclinic	tetragonal
Space group	$P2_1/n$	$P2_1/c$	$I4_1/a$
a /Å	10.0436(8)	9.7946(10)	23.2432(12)
b /Å	17.2646(14)	19.5794(17)	23.2432(12)
c /Å	17.3187(14)	14.8975(14)	11.9130(7)
β /°	105.201(4)	103.587(5)	90
V /Å^3	2898.0(4)	2777.0(5)	6436.0(8)
Z	4	4	8
μ / mm^{-1}	0.80	0.83	0.75
d_{calc} /g·cm^{-3}	1.300	1.378	1.353
$F(000)$	1180	1196	2757
Crystal size /mm	0.10 × 0.05 × 0.05	0.1 × 0.06 × 0.03	0.14 × 0.12 × 0.06
T_{min}, T_{max}	0.904/1.000	0.955/1.000	0.623/0.745
No. of meas./indep./obs. refl.	39626/6386/5474	80053/10577/8382	48071/3301/3060
R_{int}	0.065	0.029	0.123
$(\sin\theta/\lambda)_{max}$ /Å^{-1}	0.641	0.796	0.627
$R\ [F^2>2\sigma(F^2)]/wR(F^2)$ [a]	0.0909/0.2338	0.035/0.1022	0.0395/0.1088
R_1/wR_2 (all data) [a]	0.1003/0.2380	0.0485/0.1113	0.0420/0.1103
Goodness-of-fit on F^2 [b]	1.181	1.034	1.138
No. of reflections	6386	10577	3301
No. of parameters	355	367	236
No. of restrains	0	6	15
$\Delta\rho_{max}$, $\Delta\rho_{min}$ [c] /e Å^{-3}	2.10, −1.15	0.67, −0.40	0.71, −0.48

* x=1DMF found and refined, 0.5DMF squeezed; [a] $R_1 = [\sum(||F_o| - |F_c||)/\sum|F_o|]$; $wR_2 = [\sum[w(F_o^2 - F_c^2)^2]/\sum[w(F_o^2)^2]]^{1/2}$.
[b] Goodness-of-fit = $[\sum[w(F_o^2 - F_c^2)^2]/(n - p)]^{1/2}$. [c] Largest difference peak and hole.
[d] Cell constants for comparison for lvt-MeOH: a = 23.5927(4) Å, b = 23.5927(4) Å, c = 11.7356(3) Å.

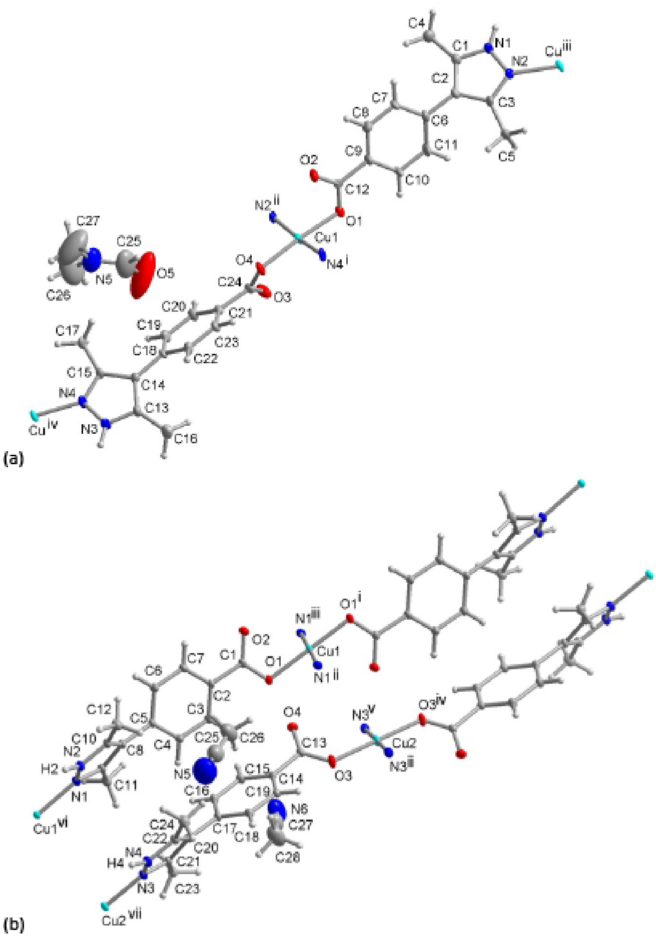

Fig. S4 (a) Metal-ligand coordination in [Cu(Hmpba)$_2$]·xDMF (**sql-DMF**) (70% thermal ellipsoids) with full atom numbering scheme and the located DMF solvent molecule. Disordered solvent molecules resulting in non-refinable electron density were removed via the SQUEEZE command in PLATON.[4] Symmetry transformations: i = x+1/2, -y+3/2, z+1/2; ii = x-1/2, -y+1/2, z-1/2; iii= x+1/2, -y+1/2, z+1/2; iv= x-1/2, -y+3/2, z-1/2. (b) Extended asymmetric unit of [Cu(Hmpba)$_2$]·2ACN (**sql-ACN**) with two symmetry-independent formula units (50% thermal ellipsoids). Symmetry transformations: i = -*x*+1, -*y*+1, -*z*+1; ii = *x*, -*y*+3/2, *z*-1/2; iii = -*x*+1, *y*-1/2, -*z*+3/2; iv = -*x*+2, -*y*+1, -*z*+1; v = -*x*+2, *y*-1/2, -*z*+3/2; vi = -*x*+1, *y*+1/2, -*z*+3/2; vii = -*x*+2, *y*+1/2, -*z*+3/2.

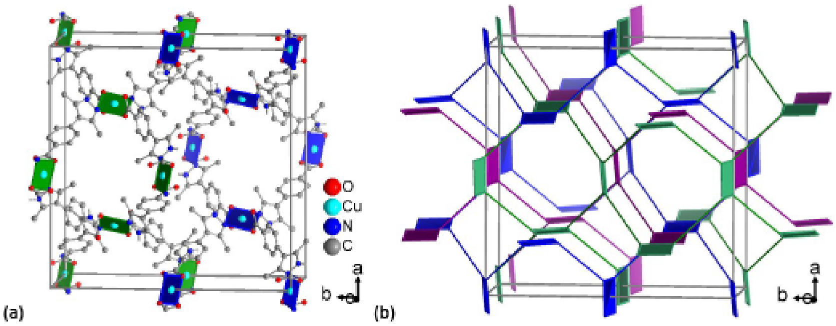

Fig. S5 (a) Section of two of the interpenetrating **lvt** nets of the structure [Cu(Hmpba)$_2$]·9H$_2$O, **lvt**-H$_2$O with indication of the square-planar Cu coordination sphere. (b) Schematic presentation of the three interpenetrating **lvt**-nets. In the **lvt**-network (Schäfli symbol $4^2.8^4$), the Cu atoms, which each connect to four ligands, can be described as 4-connecting nodes (square 4-c {CuN$_2$O$_2$}-Cluster). The Schäfli symbol indicates that the network contains 4- and 8-membered rings. The 8-membered rings span an oval pore along the ac plane (not shown). The interpenetration type is Ia, which means that the networks are connected via a single translation. The interpenetrating vectors are as follows: [3/2,3/2,3/2][0,1,0][1,0,0].

Table S2 Selected bond lengths (Å) and angles (°) for **sql-DMF**, **sql-ACN** and **lvt**-H$_2$O.

Bond lengths (Å)		**Angles (°)**	
sql-DMF			
Cu1- O3	1.949(4)	O3—Cu1—O1	175.74(19)
Cu1- O1	1.970(4)	O3—Cu1—N4^{i}	88.73(19)
Cu1- N4^{i}	1.980(5)	O1—Cu1—N4^{i}	88.82(18)
Cu1- N2^{ii}	1.986(5)	O3—Cu1—N2^{ii}	91.84(19)
		O1—Cu1—N2^{ii}	91.10(18)
		N4^{i}—Cu1—N2^{ii}	171.6(2)
Symmetry transformations: i = x+1/2, -y+3/2, z+1/2; ii = x-1/2, -y+1/2, z-1/2			
sql-ACN			
Cu1- O1	1.9532(8)	O1—Cu1—O1^{i}	180.0
Cu1- O1^{i}	1.9533(8)	O1—Cu1—N1^{ii}	90.44(4)
Cu1- N1^{ii}	1.9985(10)	O1^{i}—Cu1—N1^{ii}	89.57(4)
Cu1- N1^{iii}	1.9985(9)	O1—Cu1—N1^{iii}	89.56(4)
		O1^{i}—Cu1—N1^{iii}	90.43(4)
		N1^{ii}—Cu1—N1^{iii}	180.0
Cu2- O3^{iv}	1.9369(8)	O3^{iv}—Cu2—O3	180.0
Cu2- O3	1.9370(8)	O3^{iv}— Cu2—N3^{ii}	94.55(4)
Cu2- N3^{ii}	1.9610(10)	O3— Cu2—N3^{ii}	85.45(4)
Cu2- N3^{v}	1.9610(10)	O3^{iv} — Cu2—N3^{v}	85.45(4)
		O3 — Cu2—N3^{v}	94.55(4)
		N3^{ii}—Cu2—N3^{v}	180.0

Symmetry transformations: i= -*x*+1, -*y*+1, -*z*+1; ii= *x*, -*y*+3/2, *z*-1/2; iii= -*x*+1, *y*-1/2, -*z*+3/2; iv= -*x*+2, -*y*+1, -*z*+1.			
lvt-H_2O			
Cu1—O1^{i}	1.9446 (14)	O1^{i}—Cu1—O1^{ii}	180.00 (8)
Cu1—O1^{ii}	1.9446 (14)	O1^{i}—Cu1—N2^{iii}	88.45 (7)
Cu1—N2^{iii}	1.9849 (17)	O1^{ii}—Cu1—N2^{iii}	91.55 (7)
Cu1—N2	1.9850 (17)	O1^{i}—Cu1—N2	91.55 (7)
		O1^{ii}—Cu1—N2	88.45 (7)
		N2^{iii}—Cu1—N2	180.0
Symmetry transformations: i= y-3/4, -x+3/4, -z+3/4; ii= -y+3/4, x+1/4, z-3/4; iii= -x, -y+1, -z.			

Non-covalent interactions

PLATON was used for the investigation of the supramolecular interactions listed in Table S3.

Despite the presence of phenyl- and azole-π-systems, there are no π---π interactions. The structures feature rather long ring centroid-centroid distances (>4.0 Å) together with non-parallel ring planes (α >> 0°) and large slip angles (β, γ > 30°). In comparison, significant π-stacking shows rather short centroid-centroid contacts (<3.8 Å), near parallel ring planes (α < 10° to ~0° or even exactly 0° by symmetry), small slip angles (β, γ 25°) and vertical displacements (slippage <1.5 Å) which translate into a sizable overlap of the aryl-plane areas.[5] Significant intermolecular C-H···π contacts start below around 2.7 Å for the (C-)H···ring centroid distances with H-perp also starting at below 2.6-2.7 Å and C-H··Cg > 145° (Scheme S1).[6]

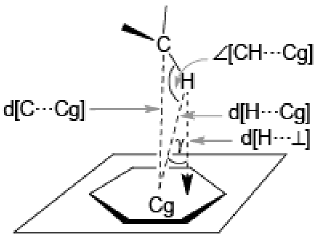

Scheme S1 Graphical presentation of the parameters used for the description of CH-π interactions.

Table S3 Interlayer CH-π and N-H···O hydrogen bonding interactions in **sql**-DMF, **sql**-ACN and **lvt**-H_2O.

	CH··π	**H···Cg1 / Å**	**H···⊥ / Å**	**γ/°**	**C-H···Cg1 /°**	**C···Cg1 / Å**	**C-H, Cg1 /°**
sql-DMF	C(7)-H(7) ··Cg1^{vii}	2.85	2.81	9.62	145	3.67	62
	C(10)-H(10) ··Cg1^{viii}	2.89	2.77	16.7	157	3.78	61
sql-ACN	C(3)-H(3) ··Cg1	2.81	2.76	11.1	139	3.58	59
	C(6)-H(6) ··Cg1^{iii}	2.85	2.84	5.61	146	3.68	59
lvt-H_2O	C(11)-H(11)·Cg1	3.00	2.91	13.6	147	3.83	53
	D-H··A	**D-H/Å**			**H··A /Å**	**D··A /Å**	**D-H··A /°**
sql-DMF	N(1)-H(1) ··O2^{v}	0.95(8)			1.77(8)	2.700(7)	165(7)
	N(3)-H(3) ··O4^{vi}	0.82(9)			1.94(8)	2.653(7)	145(8)
sql-ACN	N(2)-H(2) ··O4^{vi}	0.87(2)			1.85(2)	2.6791(14)	158(2)
	N(4)-H(4) ··O2^{vi}	0.83(2)			1.99(2)	2.7459(13)	150(2)
lvt-H_2O	N1—H1···O1^{ii}	0.85(3)			2.41(3)	2.831(2)	111(2)
	N1—H1···O3^{v}	0.85(3)			2.03(3)	2.811(3)	153(3)
	O3—H3B···O2^{i}	0.82(1)			1.94(1)	2.758(3)	178(4)
	O6—H6B···O2^{i}	0.82(1)			2.01(1)	2.814(3)	169(5)
	O7—H7A···O7^{vi}	0.82(1)			2.09(2)	2.897(8)	168(8)
	O4—H4B···O4^{vii}	0.81(1)			2.05(2)	2.784(4)	150(4)

Symmetry transformations: **sql**-DMF: v = $-x+3/2$, $y-1/2$, $-z+3/2$; vi = $-x-1/2$, $y+1/2$, $-z+1/2$; vii =1-x, 1-y, 1-z; viii = -x, 1-y, 1-z , **sql**-ACN: iii = $-x+1$, $y-1/2$, $-z+3/2$; vi = $-x+1$, $y+1/2$, $-z+3/2$; **lvt**-H_2O i= $y-3/4$, $-x+3/4$, $-z+3/4$; ii= $-y+3/4$, $x+1/4$, $z-3/4$; v= $y-1/4$, $-x+1/4$, $-z+1/4$; vi= $-x+1$, $-y+1$, $-z$; vii= $-x$, $-y+1/2$, z. **Cg1** refers to the ring centre of gravity in the ring C18-C19-C20-C21-C22-C23 for **sql**-DMF; C14-C15-C16-C17-C18-C19 for **sql**-ACN and C6-C7-C8-C9-C10-C11 for **lvt**-H_2O. **H···⊥:** Perpendicular distance of H to ring plane; **γ:** Angle between Cg-H vector and ring J normal; **C-H···Cg1:** C-H-Cg Angle; **C··Cg1:** Distance of C to Cg (see also Scheme S1); **C-H, Cg1:** Angle of the X-H bond with the π -plane (i.e.' Perpendicular = 90 degrees, Parallel = 0 degrees).

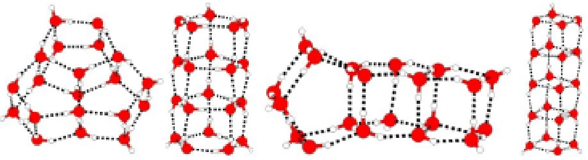

Fig. S6 Low-energy isomers for $(H_2O)_{20}$-clusters based on 4- to 6-membered ring structures (Figure taken from L. Xu et al.).[7]

Thermogravimetric analysis, TGA

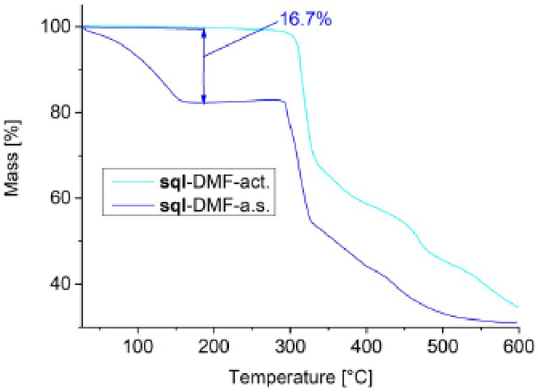

Fig. S7 TGA curves of the as-synthesized (a.s.) and activated (act.) materials for **sql**-$[Cu(Hmpba)_2]\cdot xDMF$, **sql**-DMF in the temperature range 25-600 °C with a heating rate of 5 K min^{-1} under nitrogen atmosphere. The loss of 16.7% corresponds to 1-1.5 DMF molecules calc. 12.84% for 1 DMF and 18.10% for 1.5 DMF. Deviations in the found and calculated mass percent for the solvent loss based on the single-crystal X-ray structure results are due to the already occurring solvent loss during sample preparation (drying and weighing) before the TGA measurement. The small mass increase by **sql**-DMF-a.s. is due to balance fluctuation.

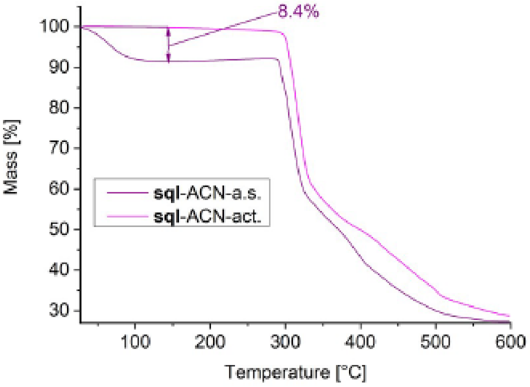

Fig. S8 TGA curves of the as-synthesized (a.s.) and activated (act.) materials for **sql**-$[Cu(Hmpba)_2]\cdot 2ACN$, **sql**-ACN in the temperature range 25-600 °C with a heating rate of 5 K min^{-1} under nitrogen atmosphere. The loss of 8.4% corresponds to 1.1 ACN molecules; calc. 7.64% for 1 ACN and 14.20% for 2 ACN molecules. Deviations in the found and calculated mass percent for the solvent loss based on the single-crystal X-ray structure results are due to the already occurring solvent loss during sample preparation (drying and weighing) before the TGA measurement. The small mass increase by **sql**-ACN-a.s. is solely due to balance fluctuation. $[Cu(Hmpba)_2]\cdot 1ACN$: $C_{26}H_{25}CuN_5O_5$, 535.06 g/mol; $[Cu(Hmpba)_2]\cdot 1.5ACN$: $C_{26.3}H_{25.45}CuN_{5.15}O_4$, 555.58 g/mol.

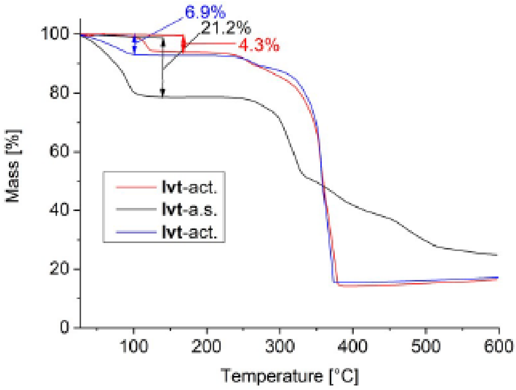

Fig. S9 TGA curves of the as-synthesized (a.s.) and activated (act.) materials for **lvt**-[Cu(Hmpba)$_2$]·4MeOH·1H$_2$O, **lvt**-MeOH (red curve: activated overnight at 160 °C; blue curve: activated at 160 °C for 8 h) in the temperature range 25-600 °C with a heating rate of 5 K min^{-1} under nitrogen atmosphere. The loss of 21.2% corresponds to 4 MeOH and 0.5/1H$_2$O; calc. 21.5/22.0%, 4.3% corresponds to 1.5 H$_2$O and 6.9% corresponds to 2 H$_2$O, which have been adsorbed by the activated compound upon handling. It has been authenticated by Richardson and co-workers with single-crystal X-ray diffraction (compound 8-dry in his publication) that compound **lvt**-MeOH-act. still contained 1.5 water molecules.[3]

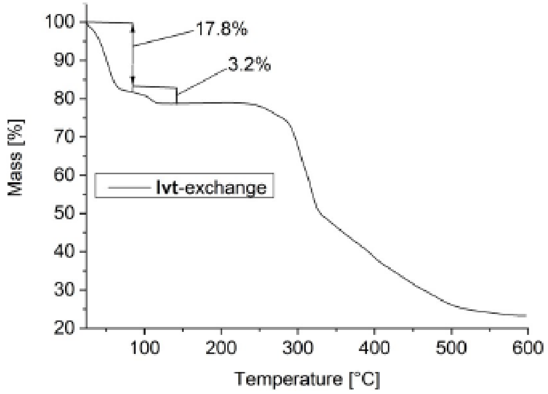

Fig. S10 TGA curves of the solvent-exchanged compound **lvt**-[Cu(Hmpba)$_2$] ·9H$_2$O, **lvt**-H$_2$O in the temperature range 25-600 °C with a heating rate of 5 K min^{-1} under nitrogen atmosphere. The loss of 17.8% corresponds to ~6.5 H$_2$O, the additional 3.2% corresponds to ~1 H$_2$O. Together, the loss of 21.0% matches the loss of 7.5 H$_2$O (calc. 20.6%). Deviations in the found and calculated mass percent for the solvent loss based on the single-crystal X-ray structure results are due to the already occurring solvent loss during sample preparation (drying and weighing) before the TGA measurement. As for **lvt**-MeOH, it can be assumed that 1.5 water molecules are still retained in the activated structure up to 250 °C. The digestion NMR of **lvt**-H$_2$O verifies the absence of MeOH.
[Cu(Hmpba)$_2$]·9H$_2$O: $C_{24}H_{40}CuN_4O_{13}$, 656.15 g/mol.

Characterization of the solvent exchange via ^{1}H-NMR studies

For the ^{1}H-NMR experiments 10 mg of the MOF sample were suspended in 0.7 mL DMSO-d_6 and digested by the addition of 20 µL of DCl (37% in D_2O). Complete exchange of MeOH against H_2O in **lvt-MeOH** can be assumed from the absence of the MeOH methyl group (at 3.10 ppm) (Figure S12). The signals around 6.73/6.78 ppm are from protonated water ($H_2O+H_3O^+$).

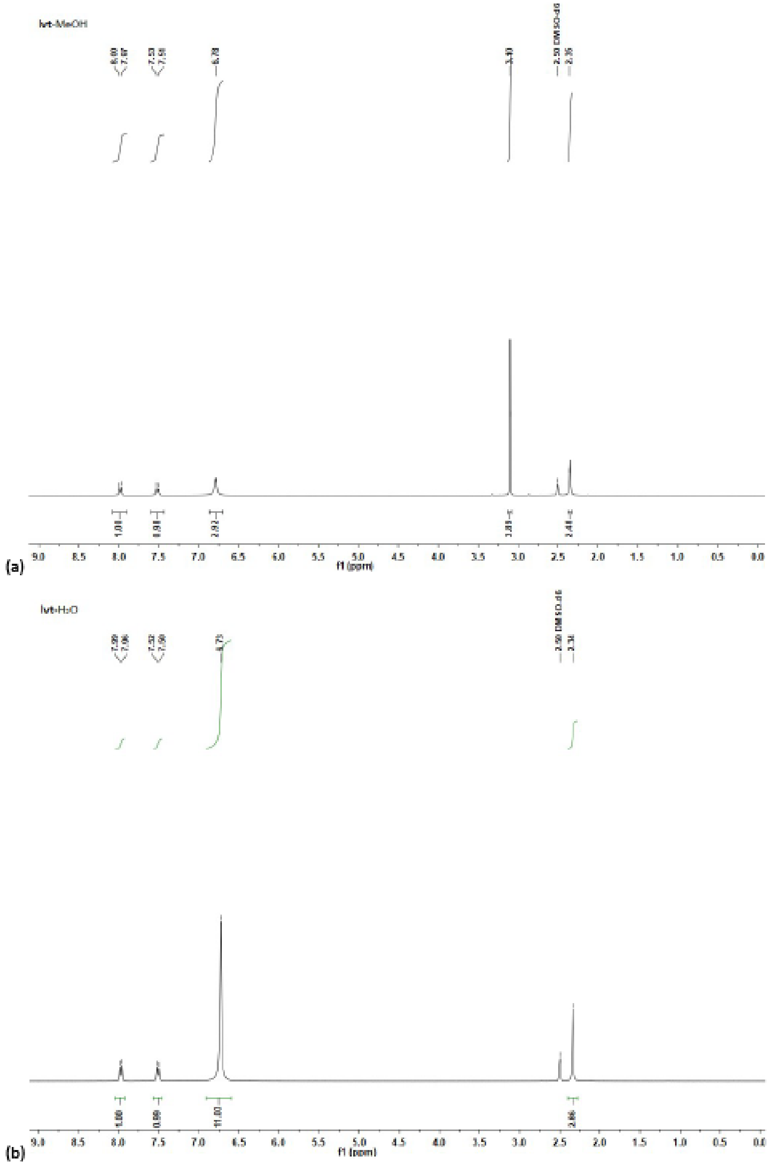

Fig. S11 ^{1}H-NMR digestion spectrum of (a) **lvt-MeOH** and (b) **lvt-H_2O** in DMSO-d_6 and DCl.

Gas sorption measurements

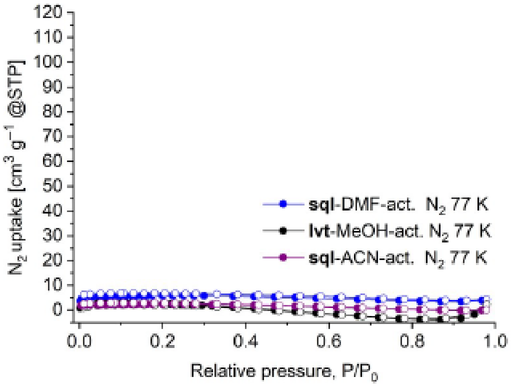

Fig. S12 N_2 Sorption isotherms for **sql**-DMF-act., **sql**-ACN-act. and **lvt**-MeOH-act. with the adsorption points as filled symbols and the desorption points as open symbols.

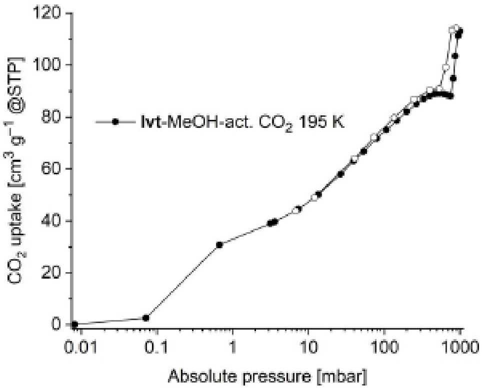

Fig. S13 CO_2 Sorption isotherm for **lvt**-MeOH-act. at 195 K with the adsorption points as filled symbols and the desorption points as open symbols.

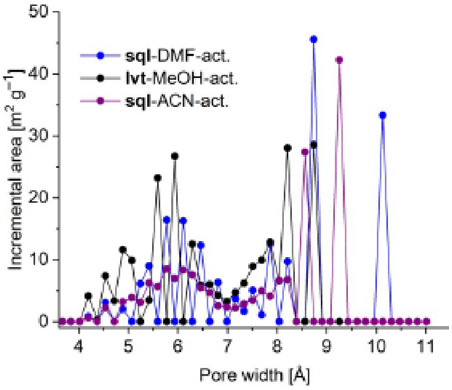

Fig. S14 NLDFT pore size distribution curves for **sql**-DMF-act., **sql**-ACN-act. and **lvt**-MeOH-act. from CO_2 adsorption isotherms (at 273 K, Fig. S16a). Note that the charts reflect a relatively crude DFT-based estimation and the jagged lines are caused by large quantization steps. The pore size distribution was estimated using nonlocal density functional theory (NLDFT) with a "slit-pore model".

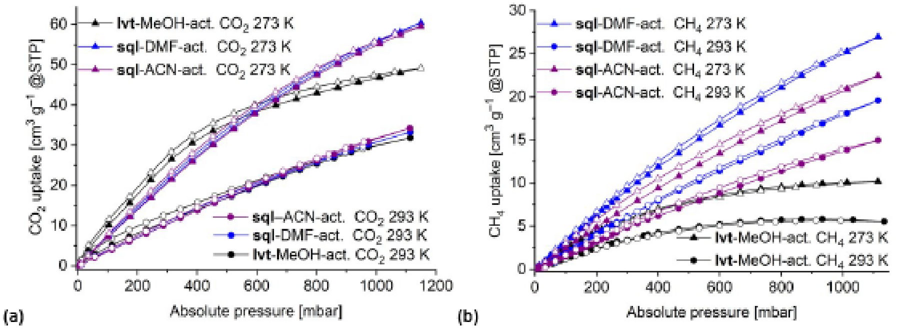

Fig. S15 (a) CO_2 Sorption isotherms of **lvt**-MeOH-act., **sql**-DMF-act. and **sql**-ACN-act. at 293 K and 273 K with the adsorption points as filled symbols and the desorption points as open symbols (b) CH_4 Sorption isotherms of **lvt**-MeOH-act., **sql**-DMF-act. and **sql**-ACN-act. at 293 K and 273 K with the adsorption points as filled symbols and the desorption points as open symbols.

Calculated pore volumes and experimental gas uptake

The theoretical surface area and pore volume of the 2D frameworks $[Cu(Hmpba)_2]\cdot xDMF$ (**sql**-DMF), $[Cu(Hmpba)_2]\cdot 2ACN$ (**sql**-ACN) and $[Cu(Hmpba)_2]\cdot 4MeOH\cdot 1H_2O$ (**lvt**-MeOH) were calculated with the program by a 'Void' calculation with Mercury[8] and by a 'Calc Void/Solv' calculation with PLATON.[4] The calculated values are listed in Table S4.

Table S4 Calculated surface areas and pore volumes.

	sql-DMF	sql-ACN	lvt-MeOH	lvt-H_2O (water completely deleted)	lvt-H_2O (O_3 left only)
Z; $M_{\text{asym unit}}$ [g mol^{-1}]; V from X-ray structures; cf. Table S1, ESI	4; 494; 2898	4; 494; 2777	8; 494 6532	8; 494 6436	8; 534 6436
Mercury 'Void' calculation [a]					
(probe radius 1.2 Å, grid spacing 0.7 Å)	calc. using solvent accessible surface				
void volume, $V_{\text{unit cell}}$ [Å^3] (% of unit cell volume) - specific [cm^3 g^{-1}] [a]	333 (11.5) 0.10	232 (8.30) 0.07	418 (6.40) 0.06	784 (12.2) 0.12	505 (7.80) 0.07
	calc. using contact surface				
void volume, $V_{\text{unit cell}}$ [Å^3] (% of unit cell volume) - specific [cm^3 g^{-1}] [a]	870 (30.0) 0.26	742 (26.7) 0.23	1693 (25.9) 0.25	2293 (35.6) 0.34	1809 (28.1) 0.26
Platon 'Calc Void/Solv' calculation [b]					
tot. pot. solv. area volume (SAV) [Å^3] (% of unit cell vol.) - specific pore volume [cm^3 g^{-1}] from SAV[a]	928 (32.0) 0.28	859 (30.9) 0.26	2164 (33.1) 0.33	2515 (39.1) 0.38	2029 (31.5) 0.29
results from experimental CO_2 sorption data [c]					
$V_{\text{micro}}(CO_2)$ [c] [cm^3 g^{-1}] at 195 K at 1.0 bar	0.20	0.23	at 0.75 bar 0.16 at 1.0 bar 0.21		
experimental gas uptake					
CO_2 [mmol·g^{-1}] (195 K, 1.0 bar)	4.90	4.00	at 0.75 bar 3.90 at 1.0 bar 5.00		
- x 44 g/mol = CO_2 [g g^{-1}]	0.22	0.18	at 0.75 bar 0.15 at 1.0 bar 0.22		
-- / ρ_{CO2} [d] = CO_2 [cm^3 liq. CO_2/g MOF]	0.20	0.16	at 0.75 bar 0.14 at 1.0 bar 0.20		
pore filling CO_2 [cm^3 liq. CO_2/g MOF] / specific pore volume [cm^3 g^{-1}] from SAV x 100%	71	76	at 0.75 bar 42 at 1.0 bar 61		
CO_2 [mmol·g^{-1}] (298 K, 20 bar)	3.5	3.3	2.8		
- x 44 g/mol = CO_2 [g g^{-1}]	0.15	0.14	0.12		
-- / ρ_{CO2} [d] = CO_2 [cm^3 liq. CO_2/g MOF]	0.22	0.20	0.17		
pore filling CO_2 [cm^3 liq. CO_2/g MOF] / specific pore volume [cm^3 g^{-1}] from SAV x 100%	79	95	52		

[a] Probe radius 1.2 Å, grid spacing 0.7 Å; values calculated using 'contact surface'. Mercury CSD 3.9, Program for Crystal Structure Visualisation, Exploration and Analysis from the Cambridge Crystallographic Data Center, Copyright CCDC 2001-2016, http://www.ccdc.cam.ac.uk/mercury/

[b] Specific surface area calculated according to $(S_{\text{unit cell}} \times N_A)/(Z \times M_{\text{asym unit}})$; specific pore volume calculated according to $(V_{\text{unit cell}} \times N_A)/(Z \times M_{\text{asym unit}})$ or $(SAV \times N_A)/(Z \times M_{\text{asym unit}})$; N_A = Avogadro's constant: $6.022\cdot 10^{23}$ mol^{-1}, Z = number of

asymmetric formula units, $M_{asym\ unit}$ = molecular weight of asymmetric formula unit [in g mol^{-1}]. As a help to reproduce the specific number the values for *Z* and $M_{asym\ unit}$ from the X-ray structures are included.

[c] Measurements on an ASAP 2020 automatic sorption analyzer (Micromeritics).

[d] density of 1.08 g cm^{-3} of liquid CO_2 at 195 K to approximate the volume of CO_2 adsorbed in the MOFs at 1.0 bar and density of 0.712 g cm^{-3} of liquid CO_2 at 298 K to approximate the volume of CO_2 adsorbed in the MOFs at 20.0 bar.

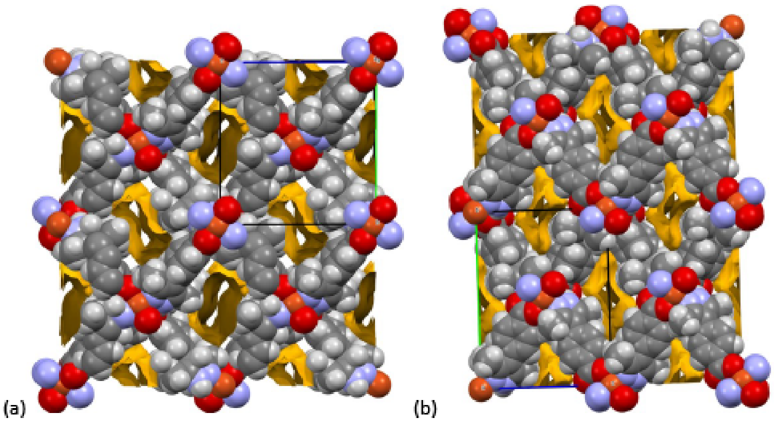

Fig S16 Solvent accessible surface (dark brown) using a probe radius of 1.2 Å for the cavities in (a) **sql**-DMF along the *a* direction, (b) **sql**-ACN along the *a* direction (the two images are not drawn to scale) from a 'void calculation' with the program Mercury (Mercury CSD 3.9, Program for Crystal Structure Visualisation, Exploration and Analysis from the Cambridge Crystallographic Data Center, Copyright CCDC 2001-2016, http://www.ccdc.cam.ac.uk/mercury/).

Heat of adsorption calculation

For the virial fit the three isotherms measured at two different temperatures are brought into an ln*p* vs. *n* form (Fig. S17). The following equation is then used to fit all three isotherms simultaneously, that is with the same fitting parameters *a*ᵢ and *b*ᵢ.

$$\ln p = \ln n + \frac{1}{T}\sum_{i=0}^{m} a_i n^i + \sum_{i=0}^{m} b_i n^i$$

In the equation, *p* is the pressure in kPa, *n* is the of total amount adsorbed in mmol/g, *T* is the temperature in K (e.g 273 K, 293 K), a_i and b_i are the virial coefficients and m represents the number of coefficients required to adequately fit the isotherms.

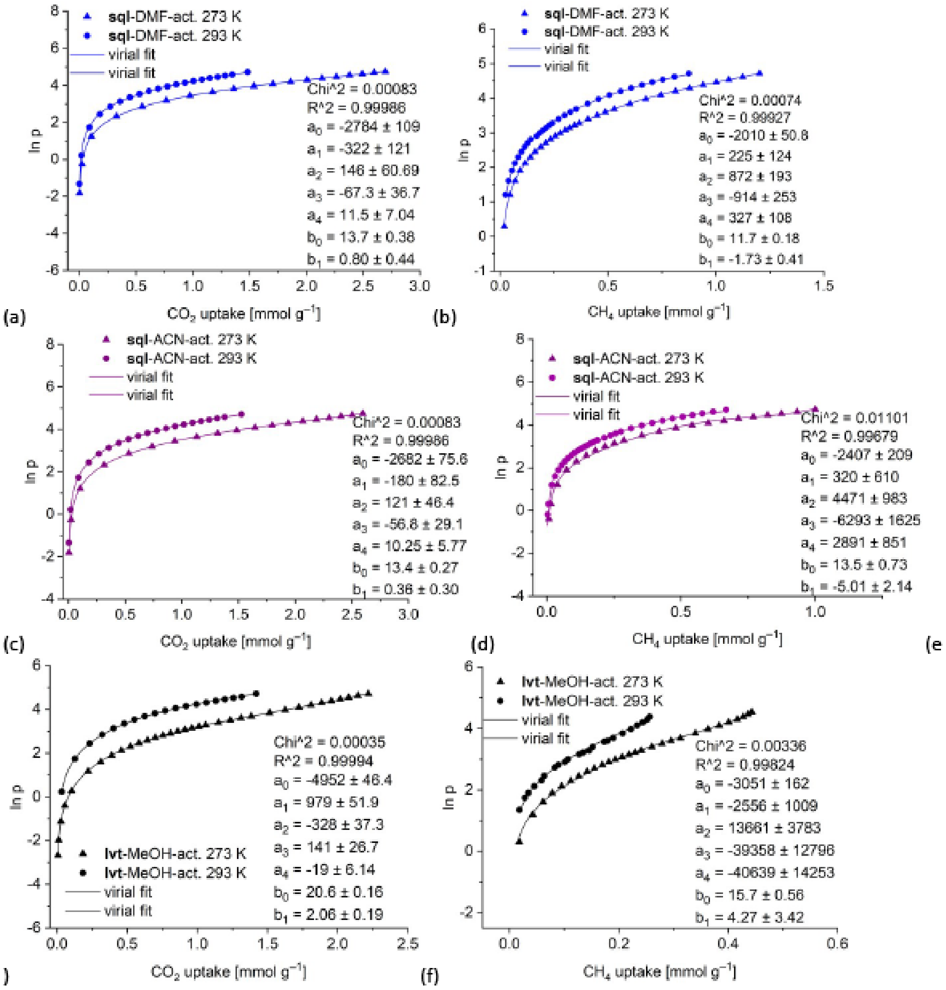

Fig S17 Virial analysis for CO_2 (a, c, e) and CH_4 (b, d, f) adsorption isotherms of **sql**-DMC-act. (a, b), **sql**-ACN-act. (c, d) and **lvt**-MeOH-act. (e, f) at 273 K and 293 K with the fitting parameters (virial coefficients) a_i and b_i.

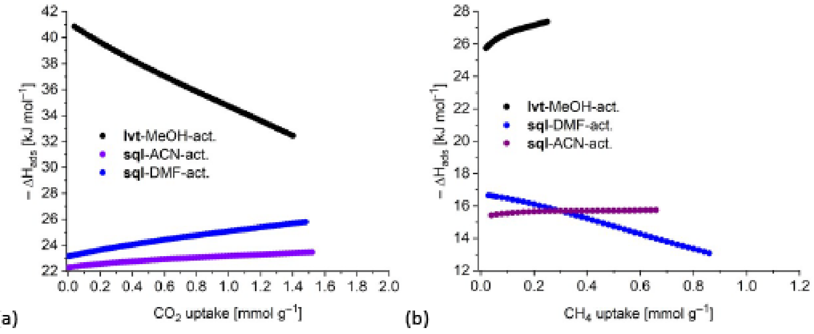

Fig S18 Isosteric enthalpy of adsorption of CO_2 (a) and CH_4 (b) for **sql**-DMF-act., **sql**-ACN-act. and **lvt**-MeOH-act. from the respective isotherms at 273 K and 293 K (cf. Fig. S16). The increase of ΔH_{ads} for CH_4 in **lvt**-MeOH can be attributed to the less steep CH_4 uptake of the 293 K versus the 273 K isotherm (Fig. S16b).

Table S5 Overview of the results from the Henry-Plots.

Compound	Temp. [K]	Gradient CO_2 [cm³/g]	Gradient CH_4 [cm³/g]	Selectivity CO_2: CH_4
lvt-MeOH-act.	273	0.118	0.025	4.4:1
lvt-MeOH-act.	293	0.035	0.012	2.9:1
sql-DMF-act.	273	0.068	0.032	2.1:1
sql-DMF-act.	293	0.034	0.020	1.7:1
sql-ACN-act.	273	0.069	0.024	2.8:1
sql-ACN-act.	293	0.034	0.016	2.1:1

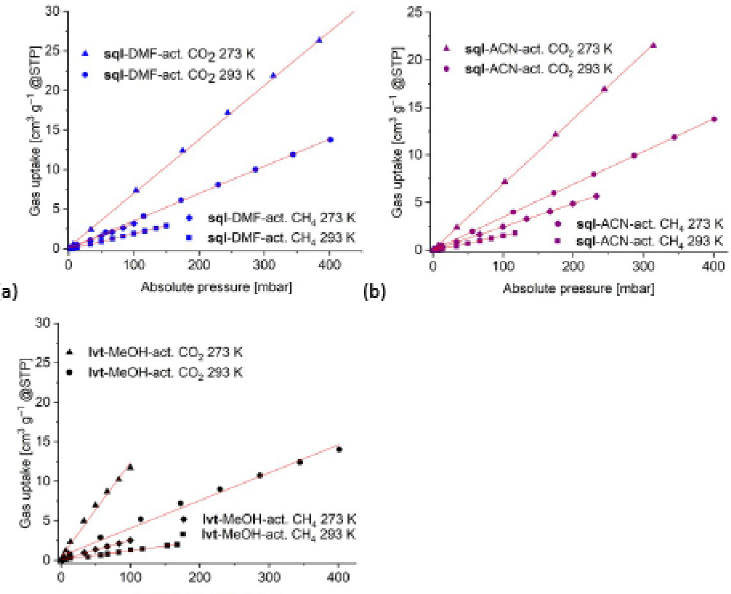

Fig. S19 Henry-Plots for CO_2 and CH_4 from the adsorption isotherms at 273 K and 293 K for (a) **sql**-DMF-act., (b) **sql**-ACN-act. and (c) **lvt**-MeOH-act.; the regression lines are in red color.

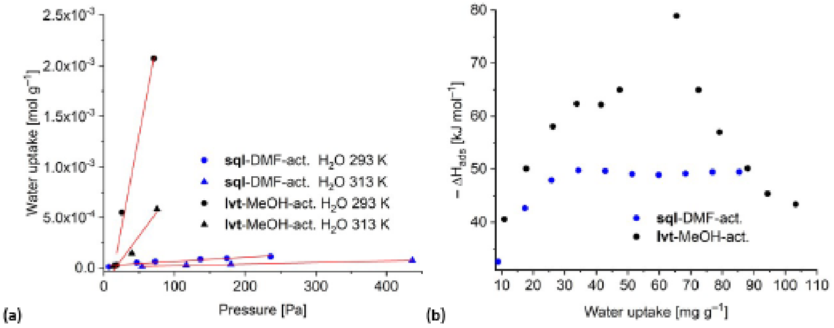

Fig. S20 (a) Henry-Plot from water adsorption isotherm at 293 K and at 313 K for **sql**-DMF-act. and **lvt**-MeOH-act.; the regression lines are in red color. (b) Isosteric enthalpy of adsorption for water adsorption at **sql**-DMF-act. and **lvt**-MeOH-act. Error margins for ΔH_{ads} can be ±10 kJ/mol.[9,10] Consequently too small deviations for ΔH_{ads} values should not overemphasized. The calculated increase for ΔH_{ads} in the range of 54-70 mg/g H_2O uptake was confirmed by repeated isotherm measurements and can be due to an exothermic process such as the rearrangement of already adsorbed H_2O molecules towards a closer, energetically more favorable configuration.

Table S6 Overview of the Henry constants from water sorption isotherms.

Compound	Temp. [K]	Henry-constant [g/mol·Pa]
lvt-MeOH-act.	293	$3.7 \cdot 10^{-5}$
lvt-MeOH-act.	313	$9.4 \cdot 10^{-6}$
sql-DMF-act.	313	$1.5 \cdot 10^{-7}$
sql-DMF-act.	293	$4.1 \cdot 10^{-7}$

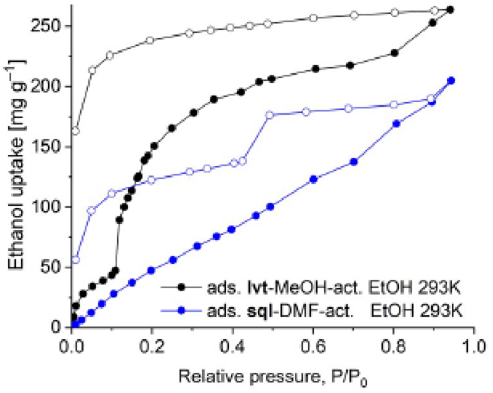

Fig. S21 Ethanol sorption of **lvt**-MeOH-act. and **sql**-DMF-act. at 293 K with the adsorption points as filled symbols and the desorption points as open symbols. Note that for **sql**-DMF the hysteresis loop contains a step at $P/P_0 \approx 0.45$ which hints at a framework flexibility.

References

1 Database NIST Chemistry WebBook; 25.06.2019; link https://webbook.nist.gov/chemistry/ accessed 13.24 h.

2 OriginPro, Version 2019, OriginLab Corporation, Northampton, MA, USA.

3 M. R. Bryant, A. D. Burrows, C. M. Fitchett, C. S. Hawes, S. O. Hunter, L. L. Keenan, D. J. Kelly, P. E. Kruger, M. F. Mahon and C. Richardson, *Dalton Trans.*, 2015, **44**, 9269–9280.

4 A. L. Spek, Structure Validation in Chemical Crystallography. *Acta Crystallogr. D*, 2009, **65**, 148–155; PLATON – A Multipurpose Crystallographic Tool, Utrecht University, Utrecht, The Netherlands, A. L. Spek, 2008; Windows implementation: L. J. Farrugia, University of Glasgow, Scotland, Version 280317, 2020.

5 X.-J. Yang, F. Drepper, B. Wu, W.-H. Sun, W. Haehnel and C. Janiak, *Dalton Trans.*, 2005, 256-267 and Supplementary

Material therein; C. Janiak, *J. Chem. Soc.*, *Dalton Trans.*, 2000, 3885-3896.

6 M. Nishio, *Phys. Chem. Chem. Phys.*, 2011, **13**, 13873-13900; M. Nishio, Y. Umezawa, K. Honda, S. Tsuboyama and H. Suezawa, *CrystEngComm*, 2009, **11**, 1757-1788; (d) M. Nishio, *CrystEngComm*, 2004, **6**, 130-158; C. Janiak, S. Temizdemir, S. Dechert, W. Deck, F. Girgsdies, J. Heinze, M. J. Kolm, T. G. Scharmann and O. M. Zipffel, *Eur. J. Inorg. Chem.*, 2000, 1229-1241; Y. Umezawa, S. Tsuboyama, K. Honda, J. Uzawa and M. Nishio, *Bull. Chem. Soc. Jpn.*, 1998, **71**, 1207-1213; M. Nishio, M. Hirota and Y. Umezawa, *The CH/π interaction (evidence, nature and consequences)*, Wiley-VCH, New York, 1998.

7 R. L. Sang and L. Xu, *CrystEngComm*, 2010, **12**, 1377-1381.

8 Mercury CSD 3.9, Program for Crystal Structure Visualisation, Exploration and Analysis from the CambridgeCrystallographic Data Center, Copyright CCDC 2001-2016, http://www.ccdc.cam.ac.uk/mercury/

9 F. Jeremias, A. Khutia, S. K. Henninger and C Janiak, *J. Mater. Chem.*, 2012, **22**, 10148–10151.

10 F. Jeremias, V. Lozan, S. K. Henninger and C. Janiak, *Dalton Trans.*, 2013, **42**, 15967–15973.

3.2 A mixed-valence copper(I/II) coordination polymer directed with a bifunctional soft-hard pyrazolate-carboxylate ligand

Die in diesem Kapitel vorgestellte Arbeit wurde veröffentlich in:

Saskia Menzel, Simon-Patrick Höfert, Secil Öztürk, Alexa Schmitz and Christoph Janiak *Z. Anorg. Allg. Chem.* **2021**, *647*, 803-808.
DOI: 10.1002/zaac.202000428

Die nachfolgend aufgeführte Publikation beschreibt die Synthese und Charakterisierung einer gemischt-valenten, eindimensionalen $Cu^{I/II}$ Koordinationsverbindung, welche solvothermal aus der Reaktion von $Cu(NO_3)_2 \cdot 2.5H_2O$ mit dem bifunktionellen Liganden 4-(3,5-Dimethyl-1*H*-pyrazol-4-yl)benzoesäure in *N,N*-Dimethylformamid mit Tetrafluoroborsäure erhalten wurde. Die synthetisierte Verbindung $[Cu^{II}\{Cu^{I})_3(H_2mpba)(mpba)_2\}DMF]\cdot{\sim}3DMF$ zeigte einen dreikernigen $\{Cu^{I}_3(H_2mpba)(mpba)_2\}^{2-}$ Metallo-Linker, wobei das weiche Pyrazolat zum weicheren Cu^{I} linear koordiniert ist. Dieser Metallo-Linker Kern verbindet die härteren Cu^{II}-Ionen über die härtere Carboxylatgruppe zu einer Kettenstruktur. Zwei Cu^{II}-Ionen bilden dabei zusammen mit den Linkern eine Schaufelradeinheit und sind somit von vier Carboxylatgruppen umgeben (vgl. HKUST-1). Das Cu^{II}-Ion ist jeweils fünfach koordiniert mit einem terminalen DMF Molekül als Ligand. Parallele Ketten sind über Wasserstoffbrückenbindungen der einfach deprotonierten Carboxylatgruppe des Hmpba-Liganden zu supramolekularen Schichten verbunden. Diese Schichten sind durch Cu^{I}-Cu^{I}-Wechselwirkungen weiter zu einer supramolekluaren 3D-Anordnung verbunden. Eine vollständige Charakterisierung war mittels Einkristallröntgenanalyse, Pulverdiffraktometrie, thermogravimetrischer Analyse, Elementaranalyse sowie Röntgenphotoelektronen-spektroskopie möglich. Eine Aktivierung des Materials hinsichtlich der Gassorption war nicht erfolgreich, da innerhalb des Materials die supramolekularen Strukturen durch Entfernen der Lösungsmittelmoleküle in sich zusammenfielen.

Die vollständig charakterisierte Verbindung $[Cu^{II}\{Cu^{I})_3(Hmpba)(mpba)_2\}DMF]\cdot{\sim}3DMF$ scheint zudem eine Vorstufe zum literaturbekannten porösen Material PCN-91 von *Wei* *et al.*[58] zu sein, da es aus denselben Baueinheiten (Schaufelrad und dreikerniges Cu^I-Cluster) besteht.

Anteile an der Publikation:

- Idee und Konzeptionsplanung des Projektes auf Basis einer ausgiebigen Literaturrecherche.
- Synthese des Koordinationspolymers in experimenteller Arbeit.
- Eigenständige Auswertung, Interpretation und Darlegung aller Ergebnisse in Form einer wissenschaftlichen Veröffentlichung.
- Die anderen Mitautoren waren an der Durchführung genutzter Analysen beteiligt. Frau Secil Öztürk führte die XPS Messung durch, Frau Dr. Alexa Schmitz die TGA. Die Einkristallstrukturmessung und Verfeinerung erfolgte durch Herrn Simon-Patrick Höfert.
- Überarbeitung, finale Abstimmung und Revision des Manuskripts wurde in Zusammenarbeit mit Herrn Prof. Dr. Christoph Janiak durchgeführt.

Journal of Inorganic and General Chemistry
ZAAC
Zeitschrift für anorganische und allgemeine Chemie
DOI: 10.1002/zaac.202000428 **SHORT COMMUNICATION**

A mixed-valence copper(I/II) coordination polymer directed with a bifunctional soft-hard pyrazolate–carboxylate ligand

Saskia Menzel,[a] Simon-Patrick Höfert,[a] Secil Öztürk,[a] Alexa Schmitz,[a] and Christoph Janiak*[a]

Dedicated to Professor Dr. Peter Klüfers on the Occasion of his 70th Birthday

A mixed-valent, one-dimensional Cu(I/II) coordination polymer with the formula $[\mathrm{Cu^{II}}\{\mathrm{Cu^{I}_3(Hmpba)(mpba)_2}\}\mathrm{DMF}]\cdot{\sim}3\mathrm{DMF}$ was obtained with the bifunctional ligand 4-(3,5-dimethyl-1*H*-pyrazol-4-yl)benzoic acid ($\mathrm{H_2mpba}$) in *N,N*-dimethylformamide (DMF) via solvothermal reaction. The compound exhibits a trinuclear $\{\mathrm{Cu^{I}_3(Hmpba)(mpba)_2}\}^{2-}$ metallo-linker with the softer Cu(I) linearly-coordinated by the softer pyrazolate nitrogen donor atom. This metallo-linker connects the harder Cu(II) ions through its harder carboxylate groups into a chain structure. Two Cu(II) ions form a paddlewheel unit and are, thus, surrounded by four carboxylate groups. Cu(II) is five-coordinated with a terminal DMF ligand. Parallel chains are connected into supramolecular layers through the common $R_2^2(8)$ hydrogen-bond motif of the singly-deprotonated carboxyl groups of the Hmpba ligand. These layers are further organized by Cu(I)–Cu(I) interactions into a 3D supramolecular array.

Introduction

Coordination polymers are of interest due to their difficult topologies and their wide-spread properties.[1,2] The structure of coordination polymers is not only directed by coordinative metal-ligand bonds but also by supramolecular interactions (e.g. hydrogen bonds, π-π stacking, halogen bonds, metal–metal stacking).[3] In this context, the structure design by bifunctional (also termed heteroditopic) ligands with two different types of donor atoms attracts interest.[4,5] Examples for the two different donor groups in bifunctional ligands are pyridine–carboxylates[6] phosphonate–carboxylates,[7] pyrazolate–carboxylates,[8] or pyrazolate–phosphonates.[9] In the deprotonated state, bifunctional pyrazolate–carboxylate ligands have specifically been employed to synthesize more stable versions of their dicarboxylate analogs due to the greater covalency of the metal–N bond compared to metal–OOC bond.[10] The HSAB concept of hard and soft acids and bases provides a reasoning that in relative comparison softer nitrogen donor atoms can preferentially bind softer metal ions, e.g. Cu(I), Ag(I), Au(I), while harder oxygen donor atoms bind harder metal ions, e.g. Cu(II), Co(III), Fe(III).[11] We note that N donors are not soft bases (ligands) in the HSAB concept but on a relative scale are softer than O donors. Also Cu(II) is not a hard acid (metal) but harder than the soft Cu(I) ion. With M(I) ions pyrazolate (pz) yields trinuclear, star-shaped $\{\mathrm{M_3(pz)_3}\}$ clusters (Figure 1). $\{\mathrm{Cu^{I}_3(pz)_3}\}$ clusters are often formed by the in-situ reduction of $\mathrm{Cu^{II}}$ starting materials upon reaction with reducing nitrogen ligands or reducing solvents like *N,N*-dimethylformamide (DMF) or *N,N*-dimethylacetamide (DMA).[12,13]

In continuation of our work[4,8b] we have reacted the bifunctional ligand precursor 4-(3,5-dimethyl-1*H*-pyrazol-4-yl)-

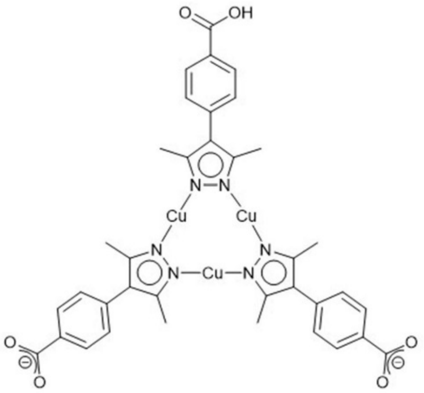

Figure 1. The tri-copper metallo-linker, $\{\mathrm{Cu^{I}_3(Hmpba)(mpba)_2}\}^{2-}$ as found in $[\mathrm{Cu^{II}}\{\mathrm{Cu^{I}_3(Hmpba)(mpba)_2}\}\mathrm{DMF}]\cdot{\sim}3\mathrm{DMF}$ (**1**). In PCN-91 also the third (top) carboxyl group is deprotonated to give $\{\mathrm{Cu^{I}_3(mpba)_3}\}^{3-}$ as the metallo-linker.[13]

---

[a] *S. Menzel, S.-P. Höfert, S. Öztürk, Dr. A. Schmitz, Prof. Dr. C. Janiak*
Institut für Anorganische Chemie und Strukturchemie
Heinrich-Heine-Universität Düsseldorf
40204 Düsseldorf, Germany
E-mail: janiak@uni-duesseldorf.de
janiak@hhu.de

Supporting Information for this article is available on the WWW under https://doi.org/10.1002/zaac.202000428

benzoic acid (H_2mpba) with copper(II) nitrate in DMF in the presence of tetrafluoroboric acid (HBF_4). Remarkably, the product reproducibly turned out to be a mixed-valent Cu(II)/Cu(I) coordination polymer, containing the $\{Cu^I_3(Hmpba)(mpba)_2\}^{2-}$ metallo-linker (Figure 1).

The partial reduction to Cu(I) was not necessarily expected as previous work with the H_2mpba ligand and Cu(II) salts in DMF yielded Cu(II) coordination polymers.[4,14] Here, we report the synthesis and characterization of the 1D, coordination polymer $[Cu^{II}\{Cu^I_3(Hmpba)(mpba)_2\}DMF]\cdot{\sim}3DMF$.

Result and Discussion

A solvothermal reaction between copper(II) nitrate and H_2mpba in dimethylformamide (DMF) at 60 °C for 5 d up to 80 °C for 15 d resulted in block shaped green crystals of formula $[Cu^{II}\{Cu^I_3(Hmpba)(mpba)_2\}DMF]\cdot{\sim}3DMF$ (**1**) (Figure S1a, Supporting Information). Different to the synthesis of valence-retained $[Cu^{II}(Hmpba)_2]\cdot L_{solv}$ networks, for **1** a longer synthesis time of 15 versus 3 d was chosen. Also, for **1** tetrafluoroboric acid, HBF_4, as a modulator was added to insure a slow crystallization by keeping the protolysis equilibrium on the side of the non-deprotonated H_2mpba ligand precursor.[15,16] At the same time the lower pH will change redox potentials in the reaction mixture. A mixed-valent copper(II/I) metal-organic framework (PCN-91) with $\{Cu^I_3(mpba)_3\}^{3-}$ as metallo-linker (cf. Figure 1) has been synthesized under basic conditions at 120 °C.[13]

The representative nature of the selected, as synthesized crystal of **1** with respect to the bulk and the phase-purity of the latter was verified by positive matching of the simulated and experimental powder X-ray diffractograms (Figure S1b, Supporting Information). The single-crystal X-ray analysis showed **1** to be a mixed-valent coordination polymer which is constructed from a trinuclear copper(I) metallo-linker, $\{Cu^I_3(Hmpba)(mpba)_2\}^{2-}$ (Figure 1), connecting Cu_2-paddlewheel units. Interestingly, there are two doubly deprotonated $mpba^{2-}$ and one singly deprotonated $Hmpba^-$ in this metallo-linker (see below), giving an overall charge of 2–.

As shown in Figure 1 and Figure 2a, three Cu(I) ions are joined with three pyrazolate ligands into a planar, trigonal metalla-cycle. The softer Cu(I) ions are selectively coordinated by the softer nitrogen donor atoms from the (H)mpba ligands with Cu^I–N bond lengths of 1.8526(14)–1.8670(14) Å (Table S3, Supporting Information).

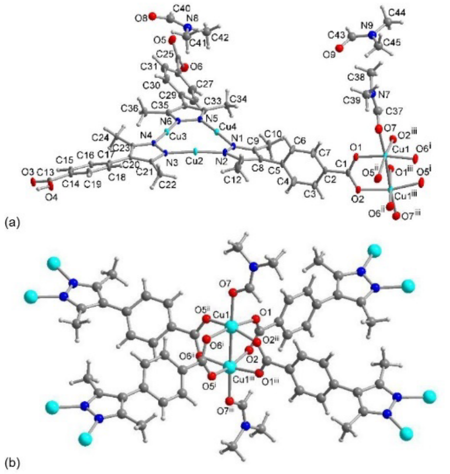

Figure 2. (a) Extended asymmetric unit of **1** (50 % thermal ellipsoids) with the three located DMF solvent molecules. (b) Dinuclear $\{Cu_2(O_2C{-})_4(DMF)_2\}$ paddlewheel unit in **1** surrounded by four mpba ligands. Symmetry transformations: (i) = −x, y + 1, −z + 1/2; (ii) = x, y + 1, z; (iii) = −x, y, −z + 1/2.

The two deprotonated carboxylate groups of $\{Cu^I_3(Hmpba)(mpba)_2\}^{2-}$ each coordinate to two Cu(II) ions which form Cu_2-paddlewheel units with four such carboxylate groups (Figure 2b and Figure S3, Supporting Information). In the HSAB concept the harder carboxylate group is coordinated to the harder Cu(II) ion. The Cu_2 paddle-wheel group is well-known from copper(II) acetate, $[Cu_2(O_2CCH_3)_4]$ and in MOF chemistry from $[Cu_3(BTC)_2]$ (BTC = benzene 1,3,5-tricarboxylate), also known as HKUST-1.[17] The Cu(II) ions in the paddle-wheel unit are five-coordinated with an axial, terminal DMF molecule as the fifth ligand. The Cu–Cu interaction in the paddle-wheel is not a formal bond but rather an interaction or contact.

Two DMF solvent molecules of crystallization, one with full atom occupancy and the other one slightly above half (~0.6) occupancy, complete the crystallographic formula unit. There are, however, an approximately additional 1.3 DMF disordered DMF molecules whose non-refinable electron density was removed via the SQUEEZE option in PLATON.[26] The total DMF solvent content of ~4 molecules (one coordinated, three as solvent of crystallization) per $[Cu^{II}\{Cu^I_3(Hmpba)(mpba)_2\}]$ formula unit was also quantified by thermogravimetric analysis (TGA). The TGA measurement of the as-synthesized material shows a one-step weight loss of 25 % up to 200 °C (24.7 % theoretically for 4 DMF molecules, Figure S6b, Supporting Information). After 300 °C decomposition occurred with an abrupt mass loss of ~40 wt%. The DMF is also seen in the elemental analysis data and by IR and ^{1}H-NMR spectroscopy (Experimental section and Figure S2, Figure S7, Supporting Information).

The $\{Cu^I_3(Hmpba)(mpba)_2\}^{2-}$ metallo-linker acts as a bent dicarboxylate linker. Two of these bent dicarboxylate linkers connect the same two Cu_2 groups and give rise to a coordination chain along the *b* direction (Figure 3a).

Parallel 1D strands are joined through the non-deprotonated carboxyl groups through hydrogen bonding in the expected $R_2^2(8)$ motif to a supramolecular 2D layer (Figure 3b). This 2D layer has the trinuclear Cu(I) nodes as three-connected 4.6^2 vertices and the dinuclear Cu(II) nodes as four-connected

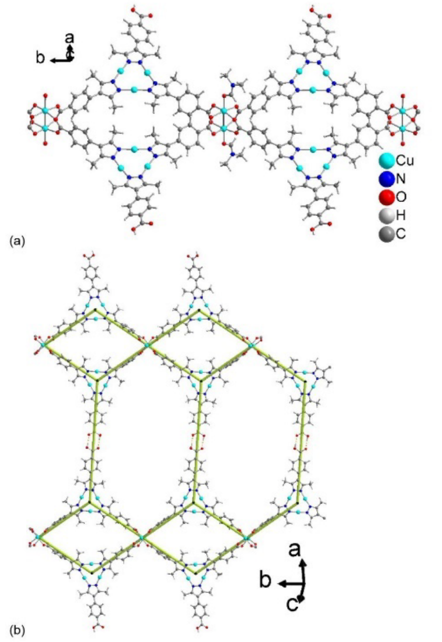

Figure 3. (a) Section of the 1D strand of dinuclear paddlewheel units and bridging metallo-linkers in **1**. (b) Hydrogen bond interactions O4–H···O3^{vii} with 0.82(4) Å (O–H), 1.81(4) Å (H···O), 2.626(3) Å (O···O), 171(3)° (vii = −x+2, −y+1, −z). The centers of the trinuclear Cu(I) nodes and the dinuclear Cu(II) nodes are joined by green lines to highlight the bex[18] or 3,4 L13 network topology.[19]

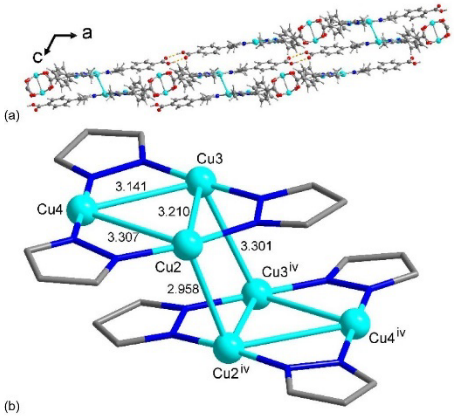

Figure 4. (a) Stacking of three of the 2D supramolecular layers with (interlayer) Cu(I)···Cu(I) contacts shown as blue lines. (b) Cu(I)···Cu(I) contact distances (in Å) within and between the {Cu$^{I}_{3}$(pz)} metallacycles of two layers. Symmetry transformation (iv) = −*x*+1, *y*, −*z* +1/2.

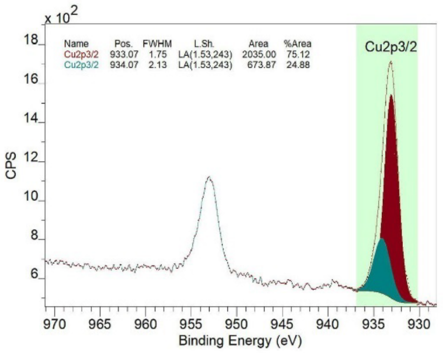

Figure 5. High resolution Cu 2p XPS spectrum for **1**.

$4^2.6^2$ vertices, giving rise to a common net of bex[18] or 3,4 L13 topology.[19]

The layers are then stacked roughly along the diagonal in the *ac* plane and oriented most notably by Cu(I)···Cu(I) d^{10}-d^{10} interactions (Figure 4a). The interlayer Cu(I)··· Cu(I) distances are 2.9576(6) Å and 3.3014(5) Å (Figure 4b). The Cu^{I}···Cu^{I} contacts within the {Cu$^{I}_{3}$(pz)} metalla-cycle are between 3.141 Å and 3.307 Å (Table S1, Supporting Information) with are all relatively short for Cu(I)···Cu(I) d^{10}-d^{10} contacts compared to the literature.[20,21]

X-ray photoelectron spectroscopy (XPS) was used to probe and quantify the two different oxidation states of copper. The survey spectrum (Figure S3 Supporting Information) confirms the expected presence of Cu, O, N and C in the material. The Cu 2p XPS spectrum in Figure 5 displays the core peaks at 952.9 eV and 933.1 eV for Cu 2p1/2 and Cu 2p3/2 respectively. The width of the 2p3/2 peak support the simultaneous presence of Cu(I) and Cu(II) as it can be deconvoluted into peaks at 933.1 eV and 934.1 eV, which correspond to the typical positions of Cu(I) and Cu(II), respectively.[22] The area ratio of the two peaks of 3:1 matches the determined Cu(I):Cu(II) formula ratio in [Cu^{II}{Cu$^{I}_{3}$(Hmpba)(mpba)$_2$}DMF]·~3DMF. The fitting of the C 1s spectrum (Figure S4a, Supporting Information) shows three peaks centered at 284.7, 285.7 and 288.6 eV which can be assigned to C–C/C=C/C–H, C–N, and –COO– respectively.[23] The O 1s peak observed at 531.5 eV confirms the presence of copper bound carboxyl oxygen, whereas the peak at 532.8 eV represents non-coordinated carboxyl oxygen. The area ratio of Cu–O(C)– to –COO(H) is ~2:1 (Figure S4b, Supporting Information), matching the ratio of the two coordinated –COO^- groups to the one non-coordinated –COOH groups in $\{Cu^I_3(Hmpba)(mpba)_2\}^{2-}$.[24]

An activation of **1** towards a porous material was not possible. An attempted activation by heating, solvent exchange or supercritical drying yielded a material without N_2 uptake in a volumetric gas sorption experiment at 77 K and also showing a powder X-ray diffractogram of an amorphous phase (Figure S1b, Supporting Information). Obviously, the supramolecular structure breaks down during solvent removal. In case conditions for solvent removal with structure retention could be found, the potential porosity is due to (solvent-filled) channel formation along the *c* direction (Figure 6a). Along the *a* and *b* direction a dense packing exists (Figure 6b).

The structure of the 3D porous framework PCN-91[13] is a mixed-valent copper(II/I) MOF (PCN-91) with fully-deprotonated $\{Cu^I_3(mpba)_3\}^{3-}$ as metallo-linker and was synthesized under solvothermal basic conditions at 120 °C with DMA as a potential reducing solvent. Unlike in **1** each carboxylate group of the $\{Cu^I_3(mpba)_3\}^{3-}$metallo-linker in PCN-91 coordinates to a different Cu_2-paddlewheel unit, thereby forming the 3D network structure (Figure S8, Supporting Information).

Conclusion

A mixed-valent Cu(I)/Cu(II), 1D coordination polymer $[Cu^{II}\{Cu^I_3(Hmpba)(mpba)_2\}DMF]\cdot{\sim}3DMF$ with $\{Cu^I_3(Hmpba)(mpba)_2\}^{2-}$ as metallo-linker was formed from copper(II) nitrate in DMF at elevated temperature. The orientation of the nitrogen and oxygen donor atoms of the bifunctional pyrazolate–carboxylate linker towards Cu(I) and Cu(II) atoms follows the softer/harder classification of the HSAB principle. Hydrogen-bonding of the 1D strands leads to a net of bex, i.e. 3,4 L13 topology. The 2D supramolecular layer are then organized into a 3D supramolecular framework by inter alia short Cu(I)···Cu(I) d^{10}-d^{10} contacts between 2.96 and 3.30 Å. XPS confirmed the 3:1 Cu(I):Cu(II) and the 2:1 (Cu–)O_2C–:–COOH ratio in the structure of $[Cu^{II}\{Cu^I_3(Hmpba)(mpba)_2\}DMF]$.

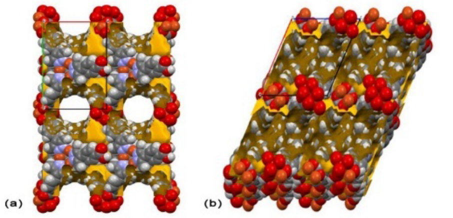

Figure 6. Illustration of the solvent accessible surface (dark brown) using a probe radius of 1.2 Å for the cavities in **1**. (a) View along the *c* direction. (b) View along the *b* direction with *c* running horizontal (the two images are not drawn to scale). Images from a 'void calculation' with the program Mercury (Mercury CSD 3.9, Program for Crystal Structure Visualization, Exploration and Analysis from the Cambridge Crystallographic Data Center, Copyright CCDC 2001–2016, http://www.ccdc.cam.ac.uk/mercury/).

Experimental Section

General: Reagents were obtained from commercial sources and used as received without further purification: The synthesis of 4-(3,5-dimethyl-1*H*-pyrazol-4-yl)benzoic acid (H_2mpba), was carried out according to the literature procedure. [14] Elemental analyses (CHN) were performed using a PerkinElmer 2400 series II elemental analyzer. IR-spectra were recorded on a Bruker FT-IR Tensor 37 spectrometer in the 4000–500 cm^{-1} region with 2 cm^{-1} resolution as KBr disks. Thermogravimetric analysis (TGA) was performed using a Netzsch TG 209 F3 Tarsus from 20 to 600 °C with a heating range from 0.1 K min^{-1} to 300 °C and 5 K min^{-1} from to 300 °C to 600 °C under nitrogen atmosphere. ^1H spectra were measured with a Bruker Avance III-300. Powder X-ray diffraction (PXRD) measurements were carried out on samples at ambient temperature with a Bruker D2 Phaser powder diffractometer using a flat silicon, low-background sample holder at 30 kV, 10 mA (100 W) for Cu-Kα radiation ($\lambda = 1.54184$ Å). In the diffractogram, the most intense reflection was normalized to 1. Simulated powder X-ray diffractograms were obtained from single-crystal data using the MERCURY 4.3.1 software programme.[25] X-ray photoelectron spectroscopy (XPS) was performed with an ULVAC-PHI VersaProbe II microfocus X-ray photoelectron spectrometer. The spectra were recorded with the usage of polychromatic aluminum Kα X-ray source (1486.8 eV) and referenced to the carbon 1 s orbital with a binding energy of 284.8 eV. CasaXPS, version 2.3.19PR1.0, copyright 1999–2018 Casa Software Ltd. program was utilized for the fit of the experimental XP spectra.

Single Crystal X-ray Structure: Suitable single crystals were carefully selected under a polarized-light microscope and mounted in a perfluorinated oil drop. When the crystals were viewed under the microscope, a rapid loss of solvent could be observed and the crystals gradually developed small cracks and "dark" spots, so that the crystallographer had to select a suitable single crystal for the measurement quickly. The single-crystal diffraction data was collected using a Bruker Kappa APEX2 Duo CCD diffractometer with a microfocus source for Mo-Kα radiation ($\lambda = 0.71073$ Å) and multi-layer mirror monochromator. The data were collected under a cold nitrogen gas-stream at 100±2 K using the APEX2 software[26] for unit-cell determination and data collection. Data reduction was performed by SAINT 8.34 A (integration) and SADABS (empirical absorption correction).[27] The structures were solved by direct methods using SHELXT-2015.[28] Full-matrix least squares refinements on F^2 were carried out with SHELXL-2017/1. All hydrogen atoms were positioned geometrically (with C–H = 0.95 Å for aromatic and aliphatic CH and 0.98 Å for CH_3) and refined using riding models (AFIX 43 and 137) with Uiso(H) = 1.2 Ueq(CH) and 1.5 Ueq(CH_3). The protic hydrogen atoms for OH were found and refined free with Uiso(H) = 1.5 Ueq. For $[Cu^{II}\{Cu^I_3(Hmpba)(mpba)_2\}DMF]\cdot{\sim}3DMF$ three DMF molecules are found and two of these refined with full and one with 0.588 occupancy. Highly disordered solvent molecules were removed via the SQUEEZE option in PLATON.[29] The resulting solvent accessible volume of 1015 $Å^3$ per unit cell contained 201 electrons, which corresponds to 5 DMF molecules (40 e each) per unit cell or 1.25 DMF per given asymmetric formula unit (Z = 4). This then leads to an estimate of 4.3 DMF molecules per formula units. Crystal data and details on the structure refinement are given in Table 1. Details about selected bond distances and angles are given in Table S1 in the Supporting Information. Graphics were drawn with program Diamond.[30]

Table 1. Crystal structure and refinement details of $[Cu^{II}\{Cu^{I}_3(Hmpba)(mpba)_2\}DMF]\cdot{\sim}3DMF$.

	$[Cu^{II}\{Cu^{I}_3(Hmpba)(mpba)_2\}DMF]\cdot 1.6DMF$[a]
Empirical formula	$C_{39}H_{38}Cu_4N_7O_7$,1.588(C_3H_7NO) [+solvent]
M/g mol^{-1}	1087.12
Crystal dimensions/mm	0.20×0.10×0.10
T/K	100
Crystal system	Monoclinic
Space group	*P*2/*c*
a/Å	17.2390(15)
b/Å	21.4071(18)
c/Å	16.3979(15)
b/°	117.045(4)
V/Å^3	5389.7(8)
Z	4
μ/mm^{-1}	1.61
F(000)	2226
Max./min. transmission	0.850/1.000
Measured, indep., observed reflections	133994, 17939, 15402 [$I > 2\sigma(I)$]
R_{int}	0.031
Data/restraints/parameters	17939/0/619
Max./min. $\Delta\rho$[b]/e Å^{-3}	1.66/−0.81
R, wR(F^2), S [$I > 2\sigma$ (I)][c]	0.0393, 0.1084, 1.040
R, wR(F^2), S [all data][c]	0.0473, 0.1140, 1.040

[a] For $[Cu^{II}\{Cu^{I}_3(Hmpba)(mpba)_2\}DMF]\cdot{\sim}3DMF$ three DMF molecules (one coordinated, two solvent of crystallization) are found and two of these refined with full and one with 0.588 occupancy. In addition, ~1.3 DMF molecules were estimated as squeezed solvent, bringing the ~1.6 found solvent of crystallization to ~3. [b] Largest difference peak and hole. [c] $R_1 = [\Sigma(||F_o|-|F_c||)/\Sigma|F_o|]$; $wR_2 = [\Sigma[w(F_o^2-F_c^2)^2]/\Sigma[w(F_o^2)^2]]^{1/2}$. Goodness-of-fit $= [\Sigma[w(F_o^2-F_c^2)^2]/(n-p)]^{1/2}$.

Crystallographic data (excluding structure factors) for the structure in this paper have been deposited with the Cambridge Crystallographic Data Centre, CCDC, 12 Union Road, Cambridge CB21EZ, UK. Copies of the data can be obtained free of charge on quoting the depository number CCDC-2044893 for $[Cu^{II}\{Cu^{I}_3(Hmpba)(mpba)_2\}DMF]\cdot{\sim}3DMF$ (Fax: +44-1223-336-033; E-Mail: deposit@ccdc.cam.ac.uk, http://www.ccdc.cam.ac.uk).

$[Cu^{II}\{Cu^{I}_3(Hmpba)(mpba)_2\}DMF]\cdot{\sim}3DMF$ (**1**): H_2mpba (20 mg, 0.092 mmol) and $Cu(NO_3)_2\cdot 2.5H_2O$ (11 mg, 0.047 mmol) were dissolved separately in 1 mL DMF. Both solutions were mixed and transferred in a Pyrex tube. As modulator tetrafluoroboric acid HBF_4 (10 μL) was added. The Pyrex tube was transferred in a preheated oven at 60 °C for 5 d and then in a preheated oven at 80 °C for 15 d. After this time green block crystals had formed and were collected after cooling to room temperature and washed three times with 2 mL DMF each. Yield: 9.8 mg (19 %, based on the metal salt and 3 DMF crystal solvent molecules in the product). Before analytical characterization was performed, the supernatant DMF was removed with a pipette and the crystals were placed on filter paper for brief air drying (5 min). $[Cu^{II}\{Cu^{I}_3(Hmpba)(mpba)_2\}DMF]\cdot{\sim}3DMF$, $C_{48}H_{59}Cu_4N_{10}O_{10}$: calcd. C 48.44, H 5.00, N 11.77 % (4 DMF total, 1190 g mol^{-1}) and C 48.38, H 4.69, N 11.28 (3 DMF total, 1117 g mol^{-1}) found C 48.38, H 4.50, N 10.98 %. **IR** (KBr, Figure S2, SI): $\tilde{v}$ = 3437 (br), 2918 (br), 2361 (br), 2342 (br), 1656 (m), 1611 (w), 1539 (w), 1490 (w), 1400 (m), 1255 (w), 1177 (w), 1099 (w), 1035 (w), 1010 (w), 864 (w), 770 (w), 717 (w), 660 (w), 609 (w), 529 (w) cm^{-1}.

Acknowledgements

We thank Mrs Birgit Tommes for the FT-IR experiments. Open access funding enabled and organized by Projekt DEAL.

Keywords: Mixed-valence · copper · bifunctional ligand · metallo-ligand · coordination polymer

[1] a) S. Kitagawa, R. Kitaura, S.-I. Noro, *Angew. Chem. Int. Ed.* **2004**, *43*, 2334–2375; *Angew. Chem.* **2004**, *116*, 2388–2430; b) O. M. Yaghi, M. O'Keeffe, N. W. Ockwig, H. K. Chae, M. Eddaoudi, J. Kim, *Nature* **2003**,*423*, 705–714; c) C. Janiak, *Dalton Trans.* **2003**, 2781–2804.

[2] L. Carlucci, G. Ciani, D. M. Proserpio, *Coord. Chem. Rev.* **2003**, *246*, 247–289.

[3] C. B. Aakeröy, N. R. Champness, C. Janiak, *CrystEngComm* **2010**, *12*, 22–43.

[4] S. Menzel, S. Millan, S.-P. Höfert, A. Nuhnen, S. Gökpinar, A. Schmitz, C. Janiak, *Dalton Trans.* **2020**, *49*, 12854–12864.

[5] a) F. ZareKarizi, M. Joharian, A. Morsali, *J. Mater. Chem. A* **2018**, *6*, 19288–19329; b) L. Hou, Y.-Y. Lin, X.-M. Chen, *Inorg. Chem.* **2008**, *47*, 1346–1351; c) L.-N. Jia, Y. Zhao, L. Hou, L. Cui, H.-H. Wang, Y.-Y. Wang, *J. Solid State Chem.* **2014**, *210*, 251–255.

[6] a) G. Mehlana, V. Chitsa, T. Mugadza, *RSC Adv.* **2015**, *5*, 88218–88233; b) P. Pachfule, B. Garai, R. Banerjee, *Inorg. Chem.* **2016**, *55*, 7200–7205.

[7] a) C. Heering, B. Francis, B. Nateghi, G. Makhloufi, S. Lüdeke, C. Janiak, *CrystEngComm* **2016**, *18*, 5209–5223; b) M. Deng, Y. Liang, B. Xing, Z. Chen, Y. Zhou, X. Liu, B. Yue, H. He, *Chem. Eur. J.* **2011**, *17*, 10323–10328.

[8] a) C. Montoro, F. Linares, E. Quartapelle Procopio, I. Senkovska, S. Kaskel, S. Galli, N. Masciocchi, E. Barea, J. A. R. Navarro, *J. Am. Chem. Soc.* **2011**, *133*, 11888–11891; b) C. Heering, I. Boldog, V. Vasylyeva, J. Sanchiz, C. Janiak, *CrystEngComm* **2013**, *15*, 9757–9768.

[9] B. Nateghi, C. Janiak, *Z. Naturforsch. B.* **2019**, *74*, 891–899.

[10] a) A. P. Sadimenko, S. S. Basson, *Coord. Chem. Rev.* **1996**, *147*, 247–297; b) M. A. Halcrow, *Dalton Trans.* **2009**, 2059–2073; c) M. Viciano-Chumillas, S. Tanase, L. J. de Jongh, J. Reedijk, *Eur. J. Inorg. Chem.* **2010**, 3403–3418; d) C. W. Lu, Y. Wang, Y. Chi, *Chem. Eur. J.* **2016**, *22*, 17892–17908; e) S. Millan, B. Gil-Hernández, E. Hastürk, A. Schmitz, C. Janiak, *Z. Anorg. Allg. Chem.* **2018**, *644*, 1311–1316.

[11] a) A. E. Martell, R. D. Hancock, in: *Metal Complexes in Aqueous Solutions*, (Ed.: J. P. Fackler) SpringerLink, **1996**; b) R. B. Martin, in: *Encyclopedia of Inorganic Chemistry*, (Ed.: R. B. King), Wiley, **1994**, p. 2185 ff, p. 2189; c) R. H. Crabtree, in: *Encyclopedia of Inorganic Chemistry*, (Ed.: R. B. King), Wiley, **1994**, S. 809.

[12] a) S. M.-F. Lo, S. S.-Y. Chui, L.-Y. Shek, Z. Y. Lin, X. X. Zhang, G.-H. Wen, I. D. Williams, *J. Am. Chem. Soc.* **2000**, *122*, 26, 6293–6294; b) X.-C Huang, J.-P. Zhang, Y.-Y. Lin, X.-L. Yua, X. M. Chen, *Chem. Commun.* **2004**, 1100–1101; c) K. Tomar, A. Verma, P. K. Bharadwaj, *Cryst. Growth Des.* **2018**, *18*, 2397–2404; d) N. Grosjean, C. Descorme, M. Besson, *Appl. Catal. B* **2010**, *97*, 276–283.

[13] Z. W. Wei, D. Q. Yuan, X. L. Zhao, D. F. Sun, H.-C. Zhou, *Sci. China Chem.* **2013**, *56*, 418–422.

[14] M. R. Bryant, A. D. Burrows, C. M. Fitchett, C. S. Hawes, S. O. Hunter, L. L. Keenan, D. J. Kelly, P. E. Kruger, M. F. Mahon, C. Richardson, *Dalton Trans.* **2015**, *44*, 9269–9280.

[15] F. Vermoortele, B. Bueken, G. Le Bars, B. Van de Voorde, M. Vandichel, K. Houthoofd, A. Vimont, M. Daturi, M. Waroquier, V. Van Speybroeck, C. Kirschhock, D. E. De Vos, *J. Am. Chem. Soc.* **2013**, *135*, 11465–11468.

[16] M. Taddei, *Coord. Chem. Rev.* **2017**, *343*, 1–24.
[17] S. S. Y. Chui, S. M. F. Lo, J. P. H. Charmant, A. G. Orpen, I. D. Williams, *Science* **1999**, *283*, 1148–1150.
[18] Reticular Chemistry Structure Resource, http://rcsr.net/.
[19] T. G. Mitina, V. A. Blatov, *Cryst. Growth Des.* **2013**, *13*, 1655–1664.
[20] B. Liu, Y.-C. Qiu, G. Peng, H. Deng, *CrystEngComm* **2010**, *12*, 270–276.
[21] R. Clerac, F. A. Cotton, L. M. Daniels, J. Gu, C. A. Murillo, H. C. Zhou, *Inorg. Chem.* **2000**, *39*, 4488–4493.
[22] a) S. Zhang, L. Zhao, *Nat. Commun.* **2019**, *10*, 4848; b) A. Ahmed, C. M. Robertson, A. Steiner, T. Whittles, A. Ho, V. Dhanak, H. Zhang, *RSC Adv.* **2016**, *6*, 8902–8905; c) H. Rupp, U. Weser, *Bioinorg. Chem.* **1976**, *6*, 45–59.
[23] D. Qu, M. Zheng, J. Li, Z. Xie, Z. Sun, *Light Sci. Appl.* **2015**, *4*, e364, 1–8.
[24] J. Wang, L. Zhu, L. Ji, Z. Chen, *J. Mater. Res.* **2018**, *33*, 581–589.
[25] C. F. Macrae, I. Sovago, S. J. Cottrell, P. T. A. Galek, P. McCabe, E. Pidcock, M. Platings, G. P. Shields, J. S. Stevens, M. Towler, P. A. Wood, *J. Appl. Crystallogr.* **2020**, *53*, 226–235.
[26] Apex2 – Data Collection Program for the CCD Area-Detector System; SAINT – Data Reduction and Frame Integration Program for the CCD Area-Detector System. Bruker Analytical X-ray Systems, Madison, Wisconsin, USA, 1997–2014.
[27] a) G. Sheldrick, Program SADABS: Area-detector absorption correction, University of Göttingen, Germany, 1996–2014; b) L. Krause, R. Herbst-Irmer, G. M. Sheldrick, D. Stalke, *J. Appl. Crystallogr.* **2015**, *48*, 3–10.
[28] G. M. Sheldrick, *Acta Crystallogr. Sect. A: Found. Adv.* **2015**, *c71*, 3–8.
[29] A. L. Spek, Structure Validation in Chemical Crystallography. *Acta Crystallogr. Sect. D: Biol. Crystallogr.* **2009**, *65*, 148–155; PLATON – A Multipurpose Crystallographic Tool, Utrecht University, Utrecht, The Netherlands, A. L. Spek, 2008; Windows implementation: L. J. Farrugia, University of Glasgow, Scotland, Version 280317, 2020.
[30] K. Brandenburg, *DIAMOND*, Version 4.5; Crystal and Molecular Structure Visualization; Crystal Impact – K. Brandenburg & H. Putz Gbr., Bonn, Germany, 2009–2018.

Manuscript received: November 17, 2020
Revised manuscript received: December 17, 2020
Accepted manuscript online: December 21, 2020

Zeitschrift für anorganische und allgemeine Chemie

Supporting Information

A mixed-valence copper(I/II) coordination polymer directed with a bifunctional soft-hard pyrazolate–carboxylate ligand

Saskia Menzel, Simon-Patrick Höfert, Secil Öztürk, Alexa Schmitz, and Christoph Janiak*

Supporting Information

Title: A mixed-valence copper(I/II) coordination polymer directed with a bifunctional soft-hard pyrazolate-carboxylate ligand

Author(s): S. Menzel, S.-P. Höfert, S. Öztürk, A. Schmitz, Christoph Janiak*

Ref.No.:

Supporting Information

A mixed-valence soft/hard copper(I/II) coordination polymer directed with bifunctional soft-hard pyrazolate-carboxylate ligand

Saskia Menzel, Simon-Patrick Höfert, Secil Öztürk, Alexa Schmitz, Christoph Janiak*

Institut für Anorganische Chemie und Strukturchemie, Heinrich-Heine-Universität Düsseldorf, Universitätsstraße 1, 40225 Düsseldorf, Germany. E-mail: janiak@uni-duesseldorf.de

* *Corresponding author*: C. Janiak Tel.: +49 211 81 12286; fax: +49 211 81 12287.

Additional E-Mail addresses: Saskia.menzel@hhu.de, Hoefert@hhu.de; secil.oeztuer@hhu.de; Alexa.Schmitz@hhu.de

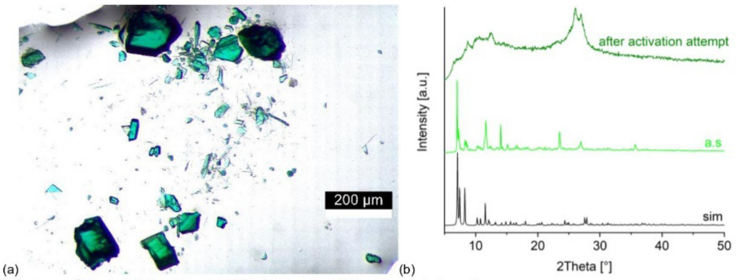

Figure S1. (a) Photographic image of the crystals of $[Cu^{II}\{Cu^{I}\}_3(Hmpba)(mpba)_2\}DMF]\cdot$~3DMF (**1**) obtained by the reaction of $Cu(NO_3)_2\cdot 2.5\ H_2O$ and H_2mpa in DMF as solvent and tetrafluoroboric acid, HBF_4 as a modulator. (b) Comparison of PXRD patterns of the simulated diffractogram (black), the experimental diffractogram of the as synthesized sample (green) and a selected example of a recorded PXRD diffractogram after an activation attempt (olive). Small changes between the simulated and as synthesized patterns are due to the unavoidable solvent loss during sample preparation and measurement and due to the different temperature between single-crystal measurement (100 K) and PXRD measurement (room temperature).

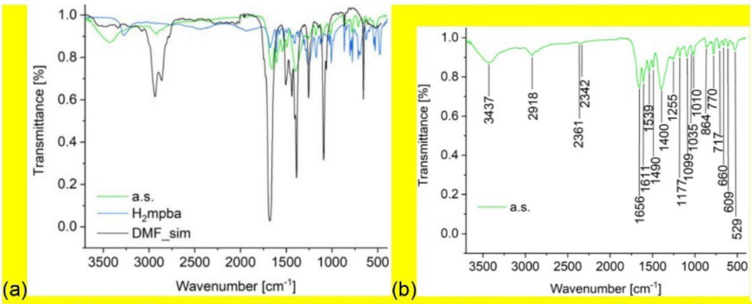

Figure S2. (a) IR-spectra (KBr) of as synthesized **1** (green), as synthesized ligand H_2mpba (blue) and DMF (NIST, black).[1] The data for the solvent IR-spectrum was download from the NIST database.[1] (b) Separate IR-spectrum (KBr) of as synthesized **1** (as in a) with marked bands.

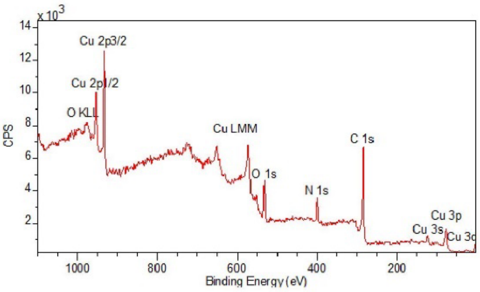

Figure S3. Survey XPS spectrum for **1**.

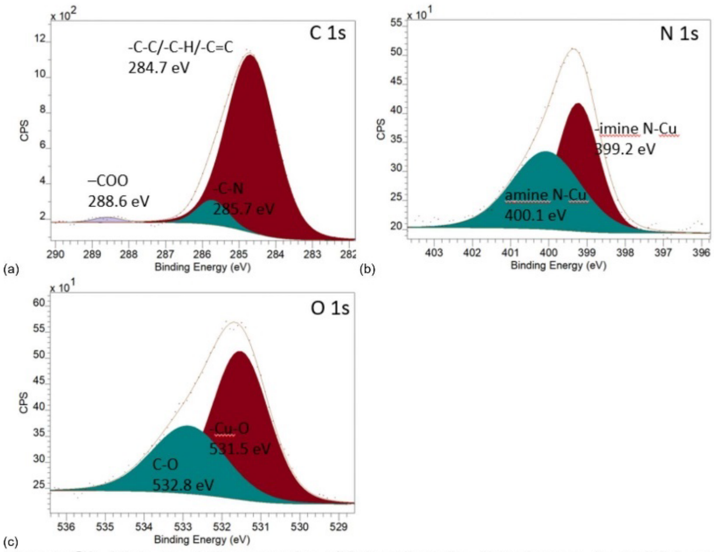

Figure S4. High resolution spectra of (a) carbon 1s, (b) nitrogen 1s and (c) oxygen 1s for **1.**

Table S1. Selected bond distances and angles (Å, º) for **1**.

Cu1—O1	1.9384 (13)	O1—Cu1—O6^{i}	170.53 (7)
Cu1—O6^{i}	1.9481 (14)	O1—Cu1—O5^{ii}	89.69 (6)
Cu1—O5^{ii}	1.9936 (15)	O5^{ii}—Cu1—O2^{iii}	165.42 (7)
Cu1—O2^{iii}	2.0102 (13)	O7—Cu1—Cu1^{i}	176.07 (5)
Cu1—O7	2.1238 (18)	N2—Cu2—N3	173.28 (7)
Cu1—Cu1^{iii}	2.6053 (6)	N6—Cu3—N4	176.16 (7)
Cu2—N2	1.8662 (15)	N1—Cu4—N5	176.54 (7)
Cu2—N3	1.8670 (14)		
Cu2—Cu2^{iv}	2.9579 (5)		
Cu3—N6	1.8526 (14)		
Cu3—N4	1.8539 (14)		
Cu4—N5	1.8603 (15)		
Cu4—N1	1.8581 (15)		
Cu4—Cu2	3.3068 (6)		
Cu4—Cu3	3.3068 (6)		
Cu2—Cu3	3.2103 (7)		
Cu3—Cu3^{iv}	3.3009 (5)		

Symmetry codes: (i) = -*x*, *y*+1, -*z*+1/2; (ii) = *x*, *y*+1, *z*; (iii) = -*x*, *y*, -*z*+1/2; (iv) = -*x*+1, *y*, -*z*+1/2.

Table S2. Hydrogen-bond geometry (Å, º) for **1**

D—H···*A*	*D*—H	H···*A*	*D*···*A*	*D*—H···*A*
O4—H4···O3^{vii}	0.82	1.81	2.6255 (19)	171
C37—H37···O2^{iii}	0.95	2.50	3.144 (3)	125

Symmetry codes: (iii) = -*x*, *y*, -*z*+1/2; (vii) = 2-*x*, -*y*+1, -*z*.

Non-covalent interactions

Despite the presence of phenyl- and azole-π-systems, there are no π---π interactions. The structures feature rather long ring centroid-centroid distances (>4.0 Å) together with non-parallel ring planes (α >> 0°) and large slip angles (β, γ > 30°). In comparison, significant π-stacking shows rather short centroid-centroid contacts (<3.8 Å), near parallel ring planes (α < 10° to ~0° or even exactly 0° by symmetry), small slip angles (β, γ 25°) and vertical displacements (slippage <1.5 Å) which translate into a sizable overlap of the aryl-plane areas.

Significant intermolecular C-H···π contacts start below around 2.7 Å for the (C-)H···ring centroid distances with H-perp also starting at below 2.6-2.7 Å and C-H··Cg > 145° (Scheme **S1** S1).

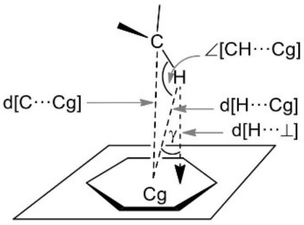

Scheme S1. Graphical presentation of the parameters used for the description of CH-π interactions.

PLATON was used for the investigation of the supramolecular interactions listed in the following Table S3.

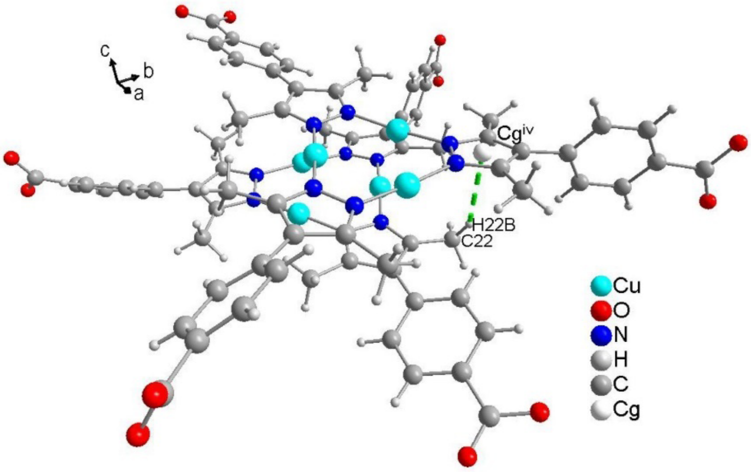

Figure S5. Representation of the interlayer CH-π interactions (green-dashed lines) for **1**. Symmetry codes: (iv) = -*x*+1, *y*, -*z*+1/2.

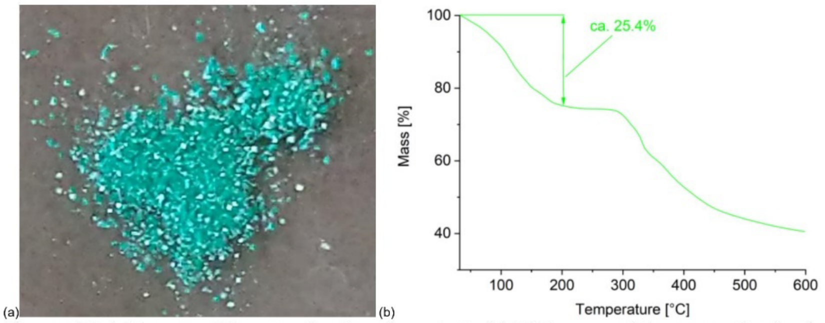

Figure S6. (a) Image of the sample after air contact. (b) TGA curve of the as-synthesized material for **1** in the temperature range 20-600 °C with a heating rate of 0.1 K min^{-1} to 300 °C and 5 K min^{-1} from to 300 °C to 600 °C under nitrogen atmosphere. The loss of 25% corresponds to ~4 DMF molecules (calc. 24.7 for 4 DMF).

For the ^{1}H-NMR experiments 10 mg of the MOF sample were suspended in 0.7 mL DMSO-d_6 and digested by the addition of 20 µL of D_2SO_4 (98 Gew. % in D_2O). The signals at 2.70 (CH_3), 2.86 (CH_3) and 7.94 (CH) ppm are from DMF.
Note that the sample or the H_2mpba ligand was only partly soluble even in DMSO. Hence, the ratio of the ligand to DMF signals is lower than expected.

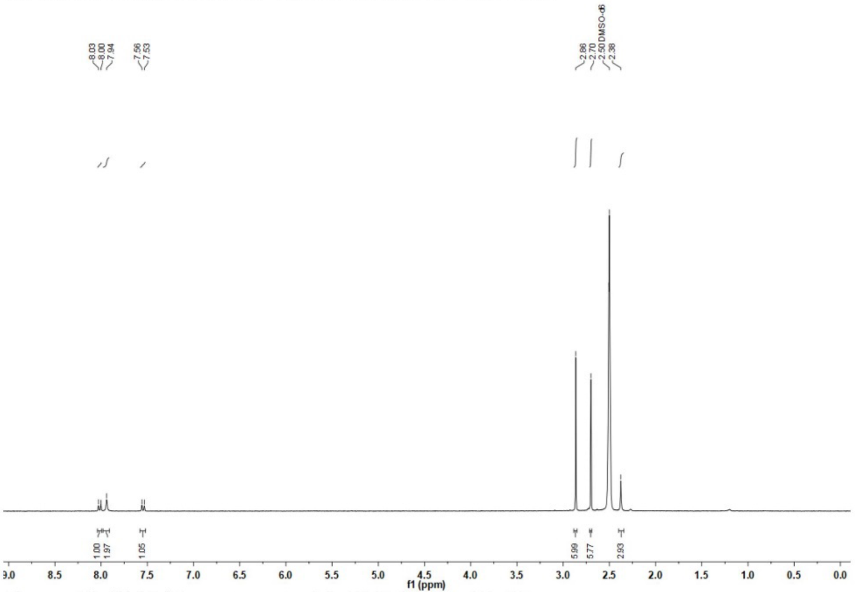

Figure S7. ^{1}H-NMR spectrum for **1** in DMSO-d_6 and D_2SO_4.

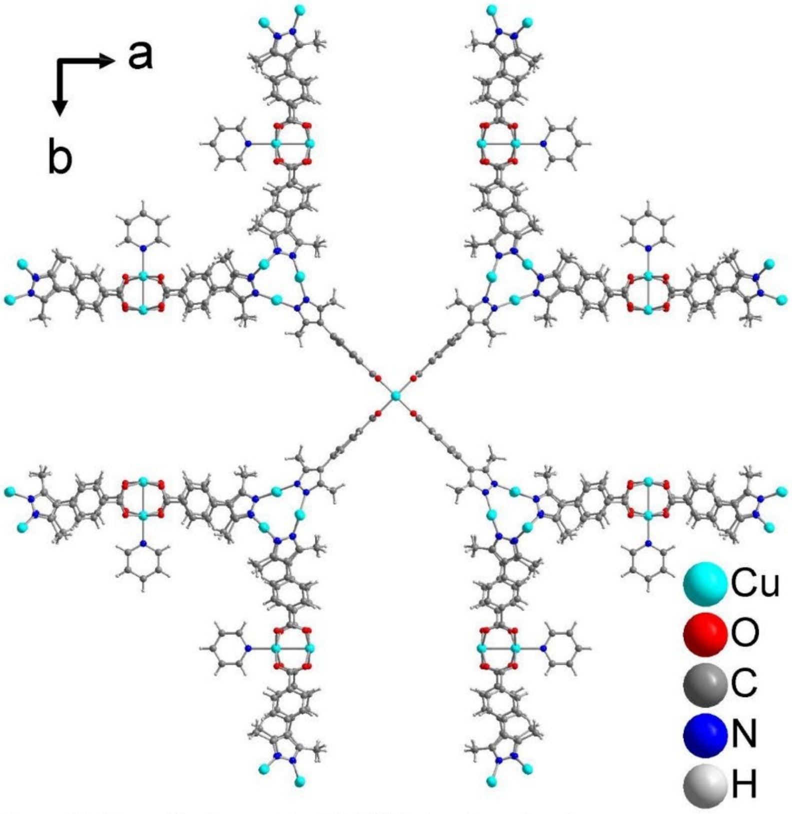

Figure S8. View of the framework of PCN-91 along the *c* direction.

Table S3. Calculated surface areas and pore volumes.

$[Cu^{II}\{Cu^{I}_3(Hmpba)(mpba)_2\}DMF]\cdot{\sim}3DMF\cdot$	
Z;	4
$M_{asym\ unit}$ [g mol^{-1}];	870
V from X-ray structures; cf. Table 2	5390
Mercury 'Void' calculation [a]	
(probe radius 1.2 Å, grid spacing 0.7 Å)	Calc. using solvent accessible surface
void volume, $V_{unit\ cell}$ [Å^3]	954
(% of unit cell volume)	(17.7)
- specific [cm^3 g^{-1}] [a]	0.16
	Calc. using contact surface
void volume, $V_{unit\ cell}$ [Å^3]	2049
(% of unit cell volume)	(38)
- specific [cm^3 g^{-1}] [a]	0.35
Platon 'Calc Void/Solv' calculation [b]	
tot. pot. solv. area volume (SAV) [Å^3]	1009
(% of unit cell vol.)	(18.7)
- specific pore volume [cm^3 g^{-1}] from SAV[a]	0.18

[a] Probe radius 1.2 Å, grid spacing 0.7 Å; values calculated using 'contact surface'. Mercury CSD 3.9, Program for Crystal Structure Visualisation, Exploration and Analysis from the Cambridge Crystallographic Data Center, Copyright CCDC 2001-2016 http://www.ccdc.cam.ac.uk/mercury/). [b] Specific surface area calculated according to ($S_{unit\ cell} \times N_A$)/($Z \times M_{asym\ unit}$); specific pore volume calculated according to ($V_{unit\ cell} \times N_A$)/($Z \times M_{asym\ unit}$) or ($SAV \times N_A$)/($Z \times M_{asym\ unit}$); N_A = Avogadro's constant: $6.022\cdot 10^{23}$ mol^{-1}, Z = number of asymmetric formula units, $M_{asym\ unit}$ = molecular weight of asymmetric formula unit [in g mol^{-1}]. As a help to reproduce the specific number the values for *Z* and $M_{asym\ unit}$ from the X-ray structures are included.

Reference

[1] Database NIST Chemistry WebBook; 25.06.2019; link https://webbook.nist.gov/chemistry/ accessed 13.24 h.

3.3 Metal-organic framework structures of fused hexagonal motifs with cuprophilic interactions of a triangular $Cu(I)_3$(pyrazolate-benzoate) metallo-linker

Saskia Menzel, Tobias Heinen, Istvan Boldog, Thi Hai Yen Beglau, Shanghua Xing, Alex Spieß, Dennis Woschko and Christoph Janiak

Publikation akzeptiert bei Royal Society of Chemistry in der Fachzeitschrift CrystEngComm.

The article is reprinted with permission of the Royal Society of Chemistry.

Die nachfolgende akzeptierte Publikation beschreibt die Synthese und Charakterisierung dreier neuartiger bimetallischer Metall-organischer Gerüstverbindungen, die mit dem N, O-heteroditopen, bifunktionellen Liganden 4-(3,5-Dimethyl-1*H*-pyrazol-4-yl)benzoesäure aus der Reaktion mit $Cu(NO_3)_2{\cdot}2.5H_2O$ und $Zn(NO_3)_2{\cdot}4H_2O$ oder $Zn(CH_3COO)_2{\cdot}2H_2O$ in *N,N*-Dimethylformamid erhalten worden sind. Die neuen Verbindungen $[Me_2NH_2][Zn_4\{Cu^I_3(mpba)_3\}_3Me_2NH(DMF)_2]$ (**1**), $[Zn_6\{Cu^I_3(mpba)_3\}_4(DMF)_5]$ (**2**) und $[Zn_3\{Cu^I_3(mpba)_3\}_2(DMF)_3(H_2O)][Zn_4(\mu_4\text{-}O)\{Cu^I_3(mpba)_3\}_2(H_2O)_4]$ (**3**) enthalten alle als zentralen Baustein den trigonal-planaren 3-c $\{Cu^I_3(pz)_3\}$ (pz = pyrazolat) Metallzyklus, welcher die verschiedenen 4-6-c $\{Zn_x(O)_y(COO)_z\}$ (x=2-4, y=0-1, z=4-6) Sekundärbausteine über die freien Carboxylatgruppen miteinander verknüpft. Es bilden sich somit getrennte Kupfer- und Zink-Cluster aus, die sich später zu einem gemeinsamen Netzwerk vereinen. In allen drei Strukturen ist der $\{Cu^I_3(pz)_3\}$-Anteil durch kuprophile Wechselwirkungen in unendliche Säulen gestapelt. Die in der Geometrie variable Zn-Cluster passen sich dabei der gestapelten Orientierung der Carboxylatgruppen der $\{Cu^I_3(mpba)_3\}^{3-}$ Metallzyklen an, wodurch die gebildeten Strukturen als Ableitung gestapelter, hexagonaler, wabenförmiger **hcb**-Netze, durch ‘Fusion’ alternierender gestapelter Knoten betrachtet werden können. Die Minderheitsphase **2** weißt dabei 2D-Schichten mit einem “doppelsträngigen” **hcb**-Netz auf, $\{4^3\}_2\{4^3.6^{12}\}$. Verbindung **1** besteht aus paarweise parallelen, interpenetrierten 2D+2D-Netzen $\{4.6^2\}_2\{4^2.6^6.8^2\}\{6^3\}\{6^5.8\}$, welche durch Kettenverkettung in einer 3D-Struktur verbunden sind. Die dritte Verbindung **3** besteht aus interpenetrierenden 3D+3D-Netze $\{4.6.8\}\{4^2.6^5.8^5.10^3\}$. Nach erfolgreicher Aktivierung von **3** (**3**-act.) zeigte diese permanente Porosität, wodurch die Verbindung als MOF mit einer Ar-basierten BET-Oberfläche von

762 m^2/g bei 87 K und einer CO_2-Aufnahmekapazität bei 1 bar von 78 cm^3/g (273 K) und 46 cm^3/g (293 K) klassifiziert werden konnte.

Anteile an der Publikation:

- Idee und Konzeptionsplanung des Projektes auf Basis einer ausgiebigen Literaturrecherche.
- Synthese der drei bimetallischen Verbindungen in experimenteller Arbeit.
- Eigenständige Auswertung, Interpretation und Darlegung aller Ergebnisse in Form einer wissenschaftlichen Veröffentlichung.
- Die anderen Mitautoren waren an der Durchführung genutzter Analysen beteiligt. Die Einkristallstrukturmessung und Verfeinerung erfolgte durch den ersten Mitautor Herrn Tobias Heinen und Herrn Dr. Istvan Boldog. Frau Thi Hay Yen Beglau führte die XPS Messung durch, Frau Dr. Shanghua Xing hat die Sorptionsmessungen am IQ durchgeführt, Herr Alex Spieß führte die EDX Analyse durch und Herr Dennis Woschko vermisste die Proben an der TGA.
- Überarbeitung und finale Abstimmung des Manuskripts wurde in Zusammenarbeit mit Herrn Prof. Dr. Christoph Janiak und Herrn Dr. Istvan Boldog durchgeführt.

CrystEngComm

ROYAL SOCIETY OF CHEMISTRY

PAPER

View Article Online
View Journal

Check for updates

Cite this: DOI: 10.1039/d2ce00268j

Metal–organic framework structures of fused hexagonal motifs with cuprophilic interactions of a triangular Cu(I)$_3$(pyrazolate-benzoate) metallo-linker†

Saskia Menzel, ‡[a] Tobias Heinen,‡[a] Ishtvan Boldog, *[a] Thi Hai Yen Beglau,[a]
Shanghua Xing,[ab] Alex Spieß,[a] Dennis Woschko [a] and Christoph Janiak *[a]

The reaction of the N,O-heteroditopic bifunctional ligand 4-(3,5-dimethyl-1*H*-pyrazol-4-yl)benzoic acid (H$_2$-mpba) with $Cu(NO_3)_2 \cdot 2.5H_2O$ and $Zn(NO_3)_2 \cdot 4H_2O$ or $Zn(CH_3COO)_2 \cdot 2H_2O$ in *N*,*N*-dimethylformamide (DMF) results in concomitant formation of three bimetallic metal–organic frameworks (MOFs) with open structures, $[Me_2NH_2][Zn_4(Cu^I_3(mpba)_3)_3(Me_2NH)\cdot(DMF)_2]$ (**1**), $[Zn_6(Cu^I_3(mpba)_3)_4(DMF)_6]$ (**2**) and $[Zn_3(Cu^I_3(mpba)_3)_2(DMF)_3\cdot(H_2O)][Zn_4(\mu_4\text{-}O)(Cu^I_3(mpba)_3)_2(H_2O)_4]$ (**3**). Compounds **1** and **3** are isolable in phase pure form under specified conditions. The HSAB hard/soft metal–ligand selectivity (Cu^I–N and Zn–O) allows the structure assembly based on the 3-c trigonal planar $\{Cu^I_3(pz)_3\}$ moiety (pz = pyrazolate) and various 4-6-c $\{Zn_x(O)_y(COO)_z\}$ (x = 2–4, y = 0–1, z = 4–6) secondary building units to be realized neatly. The *in situ* formed softer Cu^I atoms coordinate with the softer pyrazolate nitrogen donor atoms of the pyrazolate–carboxylate ligand, leaving the carboxylate groups for linking to the Zn atoms. The triangular and trinuclear $\{Cu^I_3(mpba)_3\}^{3-}$ metallacycle acts as a tricarboxylate linker between the Zn_x nodes and can be regarded as an expanded version of the benzene-1,3,5-tricaboxylate linker. In all structures the $\{Cu^I_3(pz)_3\}$ moiety is stacked in infinite columns by cuprophilic interactions suggesting the initial formation of the Cu_3(mpba) metallo-ligand. The variable geometry Zn clusters, which are paddle-wheel type, pyramidal and trigonal-prismatic, adapt to the stacked orientation of the carboxylate groups from the $\{Cu^I_3(mpba)_3\}^{3-}$ metallacycles. As a result, the formed structures could be viewed as derived from stacked hexagonal honeycomb **hcb** nets, *via* 'fusion' of alternating stacked nodes. The resulting nets retain the geometric similarity to the **hcb** net when viewed along the normal direction to the stack, and the individual topologies represent open structures. The minority phase **2** features 2D layers with a 'dual-strand' **hcb** net, $(4^3)_2(4^3 \cdot 6^{12})$. **1** consists of parallel polycatenation, 2D + 2D → 3D, of triple layers with a point symbol of $(4 \cdot 6^2)_2(4^2 \cdot 6^6 \cdot 8^2)(6^3)(6^5 \cdot 8)$, while **3** presents a pair of interpenetrated 3D + 3D $(4 \cdot 6 \cdot 8)(4^2 \cdot 6^5 \cdot 8^5 \cdot 10^3)$ nets as a rare case of hetero-interpenetration. The binodal net in **3** is a rare sqc-3,6-Fdd2-2 type sqc-subnet and the first example in a MOF. In spite of the interpenetration, **3** retains significant porosity and could be activated to demonstrate permanent porosity, thereby classifiable as a MOF with an Ar-based BET surface area of 762 $m^2\ g^{-1}$ (87 K) and a CO_2 adsorption capacity at 1 bar of 78 $cm^3\ g^{-1}$ (273 K) and 46 $cm^3\ g^{-1}$ (293 K). The structure organization similarities of **1**–**3**, stipulated by cuprophilic interactions, could have a general importance for linear heteroditopic ligands analogous to H$_2$mpba offering a 'fused-hcb' design approach towards open structures.

Received 25th February 2022,
Accepted 24th April 2022

DOI: 10.1039/d2ce00268j

rsc.li/crystengcomm

Introduction

The research area of metal–organic frameworks (MOFs) has reached a high degree of maturity with highly varied topologies[1,2] and wide-spread properties.[3–5] MOFs are built from metal clusters, also called secondary building units (SBUs), and bridging organic ligands, so-called linkers.[6,7] In the rational design of MOFs, the isoreticularity principle foresees the use of linkers with different sizes but the same geometry to obtain MOFs of the same topology. Benzene-

---

[a] *Institut für Anorganische Chemie und Strukturchemie, Heinrich-Heine-Universität Düsseldorf, Universitätsstraße 1, Düsseldorf 40225, Germany. E-mail: boldogi@hhu.de, janiak@uni-duesseldorf.de*

[b] *Hoffmann Institute of Advanced Materials, Shenzhen Polytechnic, 7098 Liuxian Blvd, Nanshan District, Shenzhen 518055, China*

† Electronic supplementary information (ESI) available: Synthesis, crystal photographs, X-ray data and refinement details, additional crystallographic figures, topological analysis, atomic absorption spectroscopy, SEM EDX, TGA, IR, XPS, gas sorption data, and linker flexibility. CCDC 2105164–2105166. For ESI and crystallographic data in CIF or other electronic format see DOI: https://doi.org/10.1039/d2ce00268j

‡ These authors contributed equally.

1,3,5-tricarboxylate (btc^{3-}, Scheme 1) is an important linker, used for example in the prototypical MOF Cu-btc (HKUST-1),[8] Zn-btc[9–12] or Cd-btc.[10] Extended versions of this linker are 4,4′,4″-benzene-1,3,5-triyl-tribenzoate, btb^{3-}, 4,4′,4″-(benzene-1,3,5-triyl-tris(benzene-4,1-diyl))tribenzoate, bbc^{3-} = 1,3,5-tris(4′-carboxy[1,1′-biphenyl]-4-yl-)benzene, $tcbpb^{3-}$, 4,4′,4″-(benzene-1,3,5-triyl-tris(ethyne-2,1-diyl))tribenzoate, bte^{3-},4,4′,4″-*s*-triazine-2,4,6-triyl-tribenzoate, $tatb^{3-}$ (Scheme 1) and 4,4′,4″-(triazine-2,4,6-triyl-tris(benzene-4,1-diyl))tribenzoate ($tapb^{3-}$) as used in the MOFs listed in Table 1.

The Zn-MOFs with the trigonal linkers Zn-btc,[9–12] MOF-177 (btb^{3-}),[13,14] MOF-180 (bte^{3-})[13] and MOF-200 (bbc^{3-})[13] are isoreticular to each other, and so is DUT-40 (bbc^{3-}) to DUT-41 (bbc^{3-}).[15]

The limits of isoreticular expansion as well as the influence of the ligand's nature in this regard is an interesting conceptual question. Our interest is focused on the triangular tri-copper metallo-linker, $\{Cu^I_3(mpba)_3\}^{3-}$ (in short Cu^I-mpba), which can be seen as belonging to the btc-type linker family (Scheme 1). Practically the only MOF-type open framework compound featuring the Cu^I-mpba unit is PCN-91, reported by Zhou and co-workers, which is a Cu^{II} coordination polymer with a Pt_3O_4 underlying net.[16] Cu^I-mpba is constructed from three Cu^I atoms, which linearly coordinate pyrazolate nitrogen donor atoms of three deprotonated bifunctional 4-(3,5-dimethyl-1*H*-pyrazol-4-yl)-benzoic acid (H_2mpba) ligands. In comparison to other trigonal linkers, the Cu^I-mpba metallo-linker is quite large with an edge length *d*(C—C) of 17.7–18.6 Å (Scheme 1). Its size is comparable to one of the largest typically used trigonal linkers bbc^{3-} (= $tcbpb^{3-}$) (*d*(C—C) = 19.8–20.0 Å, Scheme 1). Furthermore, Cu^I-mpba is not rigid and planar but somewhat flexible and distorted (*vide infra*), similar to bbc^{3-} and bte^{3-}.[13,30] The arms of the latter two ligands deflect from the plane of the central benzene ring by up to 10° (Fig. S44, ESI†). If the benzoate groups bend all out of the central ring plane to one side, a bowl-shaped linker is formed.[15,30] The linker bte^{3-} appears to be the most flexible example as the ethinyl-benzoate groups do not only bend out of the central ring plane but also deviate from a 120° angle between them (Fig. S44†).[30] The flexibility of the Cu^I-mpba ligand stems from the flexibility of the coordination-bonded core, with pyrazolate–phenyl non-planarity due to steric repulsion between the methyl groups of pyrazolate and the phenyl *ortho*-hydrogen atoms, which also endows the ligand branches with a limited rotational degree of freedom.

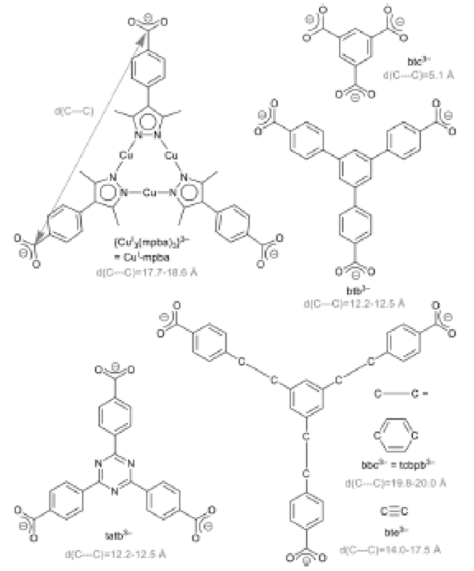

Scheme 1 Representation of extended versions of the benzene-1,3,5-tricarboxylate, (btc^{3-}) linker: $\{Cu^I_3(mpba)_3\}^{3-}$, 4,4′,4″-benzene-1,3,5-triyl-tribenzoate (btb^{3-}), 4,4′,4″-(benzene-1,3,5-triyl-tris(benzene-4,1-diyl))tribenzoate (bbc^{3-}) = 1,3,5-tris(4′-carboxy[1,1′-biphenyl]-4-yl-)benzene ($tcbpb^{3-}$), 4,4′,4″-(benzene-1,3,5-triyl-tris(ethyne-2,1-diyl))tribenzoate (bte^{3-}) and 4,4′,4″-*s*-triazine-2,4,6-triyl-tribenzoate ($tatb^{3-}$). The separation between the carbon atoms of the carboxyl groups is given as a size indicator in gray.

The trinuclear Cu^I-pyrazolate arrangement is well known in $\{Cu^I_3(pz)_3\}$ clusters (pz = 3,5-R-pyrazolate, where R is a group with intermediary steric volume, typically Me, sometimes CF_3 or Ph, and only rarely H. In the latter case the $\{Cu^I_2(pz)_2\}$ cyclic motif is rather realized). The more widespread, structurally close form of that cluster is $\{Cu_3(\mu_3\text{-}OH)(pz)_3\}^{n-}$, based on Cu(I/II) or Cu(II) only (importantly, the pz = 3,5-*H*-pyrazolate ligand is very typical for the μ_3-OH-centered clusters, unlike for the Cu(I)-only cluster).[37] As special feature of copper(I), the $\{Cu^I_3(pz)_3\}$ clusters are very prone to associate *via* intermolecular cuprophilic interactions, which could affect the course of self-assembly of potential MOFs.[38,39] There is a fortunate opportunity for the synthesis of potential mixed-metal M^{II-IV}/Cu^I pyrazolate–carboxylate coordination polymers staring from Cu^{II} as a precursor in *N*,*N*-dimethylformamide (DMF) and similar amide solvents. The latter are favorable for the crystallization of both carboxylate and pyrazolate coordination polymers, while elevated temperatures (80–120 °C) ensure partial or complete reduction of Cu^{II} to Cu^I.[40]

The doubly deprotonated bifunctional pyrazolate–carboxylate ligand $mpba^{2-}$, constituting $\{Cu^I_3(mpba)_3\}^{3-}$, has already been used in the synthesis of a few reported coordination-bonded frameworks with other coordination bonded clusters, namely Zn^{II},[41–43] Co^{II} [43] or Cu^{II}.[16,44] It is also worth mentioning the reported, mostly 2D, structures of the partially deprotonated pyrazole-carboxylate ligand $Hmbpa^-$ with Co(II), Ni(II), Zn(II), Cu(II), Cd(II)[45] and the mixed-metal 1D bimetallic coordination polymer $\{[(Ti_3O)(iPro)_8][Hmpba]_2[Cu_2I_2]_{0.5}\}$ (with iPro = isopropoxide).[46] In the case of the mixed-valent $Cu^{I/II}$ framework compound of PCN-91 (ref. 16) and the 1D Ti^{IV}–Cu^I coordination polymer, the harder carboxylate

Table 1 Extended versions of the benzene-1,3,5-tricarboxylate, (btc^{3-}) linker and their MOF-examples

Ligand[a]	Example[c]
btc^{3-}	Cu-btc (HKUST-1),[8] Zn-btc,[9–12] Cd-btc[10]
btb^{3-}	MOF-14(Cu),[17] MOF-143(Cu),[18] DUT-9(Ni),[19] MOF-177(Zn),[13,14,20] $[Cd_3(btb)_2(bib)(DMF)_3]$,[21] $\{[Ba_3(btb)_2(NMP)_2(H_2O)_2]\cdot 2NMP\cdot H_2O\}$,[22] $\{[Co(Hbtb)(pdp)]\cdot H_2O\}$,[23] $[Cd_2(tbib)(btb)(H_2O)_2]X$,[24] $\{[Eu(btb)(H_2O)_3]\cdot 1.5DMA\cdot 5H_2O\}_n$ (MHT-1),[25] MUV-12,[26] FJU-120 (ref. 27)
bbc^{3-} = tcbpb^{3-}	$\{[Zn_4(OH)_2(H_2O)_2(py)_2(tcbpb)_2]\cdot DMF\cdot py\cdot 3H_2O\}$,[28] $\{[Zn_8(OH)_4(tcbpb)_4]\cdot 2DMF\cdot 2EtOH\cdot 3H_2O\}$,[28] Al-tcbpb,[29] MOF-399(Cu),[18] DUT-40(Zn),[15] DUT-41(Zn),[15] MOF-200(Zn),[20] MOF-1005(Zr)[30]
bte^{3-}	MOF-180(Zn),[20] MOF-1004(Zr)[30]
tatb^{3-}	$[Ln_2(tatb)_2(DMSO)_6]$ (Ln = La, Ce, Pr, MOF-388Sm, Eu),[31] $\{[Ln_2(tatb)_2(DMSO)_2(CH_3OH)]\cdot DMF\cdot DMSO\cdot 2H_2O\}$ (Ln = Nd, Gd, Tb),[31] $[Cu_3(tatb)_2(H_2O)_3]$,[32] PCN-9(Co),[33] MIL-142(Sc)-tatb,[34] $[Co_4(SO_4)_2(F)_2(tpt)_2(tatb)]$,[35] $[Fe(tatb)(p/m\text{-}bib)]$[36]
tapb^{3-b}	MOF-388(Cu)[18]

[a] See Scheme 1. [b] Not shown in Scheme 1, but tapb is like bbc with a triazine instead of a benzene core. [c] Other abbreviations used: (bib = 1,4-bis(2-methylimidazol-1-yl)butane), NMP = *N*-methyl pyrrolidone, pdp = 2-(4,6-di(pyridine-2-yl)pyridine-2-yl)pyridine, tbib = 1,3,5-tri(1*H*-benzo[*d*]-imidazol-1-yl)benzene, tpt = 2,4,6-tris-(4-pyridyl)-1,3,5-triazine, *p*/*m*-bib = *para*/*meta*-bis((1*H*-imidazole-1-yl)methyl)benzene.

group combines with the HSAB-harder metal ions Cu^{II} and Ti^{IV} and the HSAB-softer pyrazolate or pyrazole donor is coordinated by Cu^{I} (according to the HSAB principle).[47] The hard/soft selectivity of the O,N heteroditopic mbpa^{2-} ligand offers a potentially productive approach towards mixed metal coordination polymers, based on the *in situ* synthesized $\{Cu^I_3(mpba)_3\}^{3-}$ cluster.

Carboxylate coordination polymers also featuring the $\{Cu^I_3(pz)_3\}$ cluster are rare. According to the CSD search, there are five compounds of this type, with three important MOF representatives, namely the mentioned PCN-91,[16] FDM-4 (ref. 48) and FMD-8.[49] The two other compounds are the CFA-13 MOF[50] with an extended $\{Cu^I_3(pz)_3\}$ cluster in the form of $Cu^I_3(3,5\text{-}CF_3\text{-pyrazolate})_4$, and the $[Cu^{II}\{Cu^I_3(Hmpba)(mpba)_2\}]$ 1D coordination polymer[51] reported by us. The FDM-4,5,6,7,8 series of Zn/Cu mixed-metal coordination polymers with surface areas up to 3728 m^2 g^{-1}, based on the fully deprotonated short 4-carboxypyrazole ligand as a sole organic ligand, or together with the 1,4-benzenedicarboxylate or 2,6-naphthalenedicarboxylate ligand, is particularly interesting. The series features reversible redox transformation between the $\{Cu^I_3(pz)_3\}$ and $\{Cu_3^{I,II}(OH)(pz)_3\}$ cluster without compromising the integrity of the structure (as some of the structures are reported only for the oxidized cluster, the CSD search does not cover the Cu^{I}-only variants in all cases). As mentioned above, 3,5-*H*-pyrazoles frequently constitute the $\{Cu_3(OH)(pz)_3\}$ clusters, but they are less frequent in geometrically well-formed $\{Cu^I_3(pz)_3\}$ clusters. The FDM-4-8 series demonstrate that in some cases both possibilities could be realized, resulting in highly porous robust structures, which substantiate the interest in mixed-metal and mixed-ligand complexes for longer ligands like mpba^{2-}, whose potential is proven by the known PCN-91 material.

The Cu^{I}-mpba metallo-linker has not been used in the construction of isoreticular Zn-MOF structures (as well as any other bimetallic MOFs) and in the current contribution we explore this possibility. The bifunctional ligand precursor 4-(3,5-dimethyl-1*H*-pyrazol-4-yl)benzoic acid (H_2mpba) was reacted with copper(II) nitrate in DMF in the presence of zinc(II) salts and, if necessary, a modulator (HBF_4) aiming for Zn frameworks with the metallo-linker, akin to those with the btc, btb, bte or bbc linker (*cf.* Table 1). The importance of the HSAB selectivity regarding the mixed valent Cu^{I}/Cu^{II} metals and the N,O-heteroditopic ligand is explicitly discussed for PCN-91.[16] The use of Cu^{I}/Zn^{II} in this work could be viewed as a continuation of that principle aiming for the utilization of zinc (oxo)carboxylate species as secondary building units.

Results and discussion

The solvothermal reaction between copper(II) nitrate, zinc(II) nitrate and H_2mba in *N*,*N*-dimethylformamide (DMF) at 80–90 °C for several days resulted in the formation of the bimetallic networks $[Me_2NH_2][Zn_4\{Cu^I_3(mpba)_3\}_3(Me_2NH)(DMF)_2]$ (**1**), $[Zn_6\{Cu^I_3(mpba)_3\}_4(DMF)_5]$ (**2**) and $[Zn_7\{Cu^I_3(mpba)_3\}_4(O)(H_2O)_3(DMF)_3]$ (**3**). The synthesis conditions had to be carefully adjusted with regard to time, temperature, Cu : Zn stoichiometry and the amount of HBF_4 modulator, as otherwise mixtures of **1**, **2** and **3** also form (Table S1, Scheme S1, ESI†).

MOF examples in the literature with Cu(I)$_3$(pyrazolate–carboxylate) motifs include PCN-91,[16] FDM-4-8,[48,49] CFA-13 (ref. 50) and $[Cu^{II}\{Cu^I_3(Hmpba)(mpba)_2\}]$.[51] The syntheses were all performed using Cu(II) as a precursor and in *N*,*N*-dimethylformamide (DMF) or similar amide solvents. DMF is favorable for the crystallization of both carboxylate and pyrazolate coordination polymers, while elevated temperatures (80–120 °C) in amide solvents ensure partial or complete reduction of Cu(II) to Cu(I).[52]

The $\{Cu^I_3(pz)_3\}$ SBU of PCN-91 forms as a result of the *in situ* reduction of Cu^{II} ($Cu(NO_3)_2\cdot 2.5H_2O$ precursor) in DMA and two drops of pyridine at elevated temperature (120 °C) and prolonged time (24 h). In the work of Tu and co-workers, the short 4-pyrazolecarboxylate linker was used to synthesize bimetallic, redox active materials. By varying the Cu : Zn ratio and the solvent mixture (ratio of DMF and NMP or DMF and DMA (only used for FDM-5)) the materials FDM-4 and FDM-5 were synthesized under solvothermal conditions. By adding the organic ligand 1,4-benzene dicarboxylic acid the material

FDM-6 was produced. FDM-8 and the substituted derivates NH$_2$-FDM-8 and C$_4$H$_4$-FDM-8 were synthesized under solvothermal conditions by adding 1,4-benzenedicarboxylate acid, 2,6-naphalenedicarboxylate acid (for FDM-8) and 2-aminoterephthalic acid or 1,4-naphthalenedicarboxylate acid for NH$_2$-FDM-8 and C$_4$H$_4$-FDM-8. In all FDM MOFs, the {Cu$^{I}_{3}$(pz)$_3$} moiety was obtained by *in situ* reduction from the Cu(II)-salt (Cu(NO$_3$)$_2$·3H$_2$O) in DMF/NMP or DMF/DMA at elevated temperature (85 °C for FDM-4 and FDM-5, 100 °C for FDM-6, FDM-8 and NH$_2$-FDM-8 and C$_4$H$_4$-FDM-8) and prolonged time (72 h for FDM-4 and FDM-5 and 16 h for FDM-6, FDM-8 and NH$_2$-FDM-8).

Regarding the question of pK_a, the carboxylic acid and pyrazole groups feature very different acidities (~5 *vs.* 14), but this does not preclude the concomitant formation of complexes even for Zn(II). The HSAB hard–hard soft–soft matching between Cu^{I} and pyrazolate as well as Zn^{II} and carboxylate makes the formation of the respective complexes highly predictable.

Compounds **1** and **3** could be obtained reproducibly as yellowish clear crystals (Fig. S1 and S2, ESI†) in phase pure form. Compound **2** was difficult to obtain in pure phase and in single crystal form, and it was only observed as an admixture of **1** and **3**. The identity of the three compounds could by elucidated by single-crystal diffraction (see below). The experimental and simulated powder X-ray diffractograms were matched and the correspondence was checked by Le Bail fitting (Fig. S3, ESI;† compound **2**, which could be obtained only in the form of a powder, is the least pure).

A common feature of the structures of **1–3** (Scheme 2) is the structural changeability of the Zn-SBU clusters, featuring nuclearities of 2–4 (distorted tetrahedral and pentagonal as well as trigonal-prismatic SBU-shapes) and frequent disorder. Such unconventional changeability contrasts the situation in PCN-91 with Cu(II), where the conventional {Cu$_2$(O$_2$C)$_4$}-paddle-wheel motif is formed.[16] Neither of **1–3** is isostructural to PCN-91, even if a paddle-wheel {Zn$_2$(O$_2$C)$_4$}-SBU is possible.[53] Instead, the structures of **1–3** have a common structure-guiding motif of columnar stacks, composed of Cu^{I}-mpba associated by cuprophilic interactions. The Zn-clusters appear to be flexible and adapt to the requirements imposed by the Cu^{I}-mpba stacks, which results in similarities in structure-organization dominated by the formation of hexagonal coordination-bonded rings within honeycomb **hcb** layers (Scheme 2; the summary of the work on the topological level is given below in Fig. 9, which follows the detailed description of the structures).

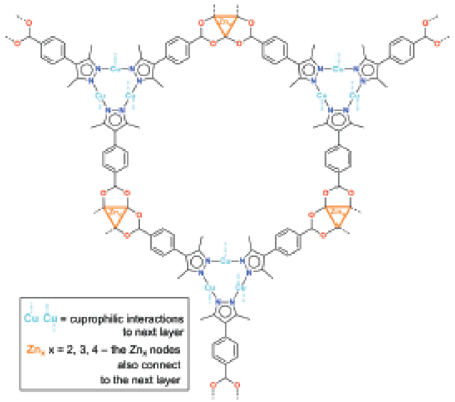

Scheme 2 Common features of the structures of **1–3** with Zn$_x$ nodes of different nuclearities (x = 2–4) and the trigonal {Cu$^{I}_{3}$(mpba)$_3$}$^{3-}$ nodes giving a hexagonal-ring layer. Both the Zn$_x$ nodes and the cuprophilic interactions from {Cu$^{I}_{3}$(mpba)$_3$}$^{3-}$ connect to the next layer.

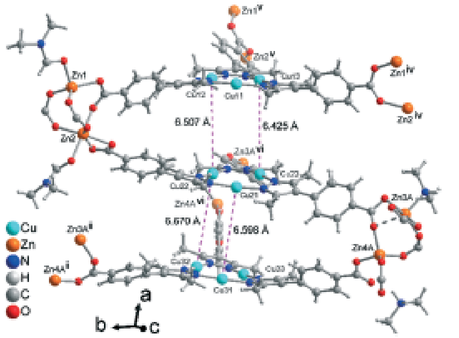

Fig. 1 Extended asymmetric unit of **1** with the two located coordinating DMF solvent molecules, one dimethylamine solvent molecule and one dimethylammonium counter-cation (for further details on these amine/ammonium groups see Fig. S4, ESI†). Each {Cu$^{I}_{3}$(mpba)$_3$}$^{3-}$ unit belongs to a different layer. In view of the structure complexity, a ball-and-stick presentation is used and only the major contribution to the disorder of Zn3 and Zn4 is shown. The Zn3/4 disorder is described in more detail in the ESI.† The distances between the Cu atoms (pink dashed lines) correspond to twice the distances of typical cuprophilic Cu⋯Cu contacts, as the interlayer space is filled by a symmetry equivalent Cu^{I}-mbpa unit (the stack is shown in Fig. 3 and 4). Symmetry codes: (ii) $x, y + 1, z$; (iv) $x, y - 1, z$; (v) $x, y - 1, z - 1$; (vi) $x, y, z - 1$.

Crystal structure of 1

The formula of compound **1** was established as [Me$_2$NH$_2$][Zn$_4${Cu$^{I}_{3}$(mpba)$_3$}$_3$(Me$_2$NH)(DMF)$_2$]. The formation of dimethylammonium [Me$_2$NH$_2$]$^+$ from DMF and its presence as a counter-cation has been seen in zinc-MOFs with benzene-1,4-dicarboxylate,[54] furan-2,5-dicarboxylate[55] or 1,1′-biphenyl-3,3′,4,4′-tetracarboxylate.[56] The asymmetric unit in **1** consists of three symmetry-independent {Cu$^{I}_{3}$(mpba)$_3$}$^{3-}$ units, each belonging to a different layer, which are associated *via* coordination with Zn-atoms (Fig. 1). The three

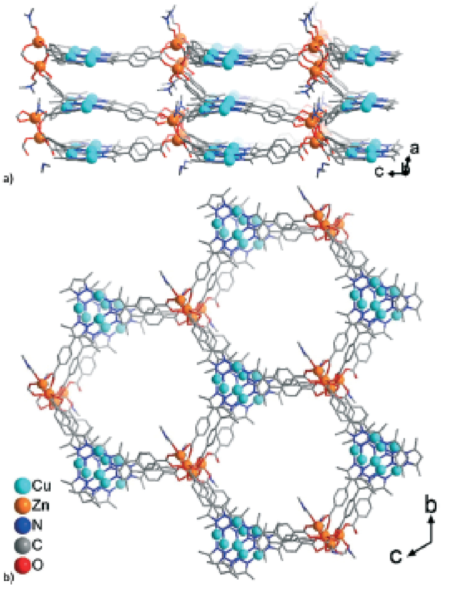

Fig. 2 Wire-frame model of (a) side-view and (b) on-top view (along the *b* and *a* axis, respectively) of a section of a single 3-layer stack in **1**. Only the major contribution to the disorder of Zn3 and Zn4 is depicted. See also the space-filling presentation in Fig. S5.†

layers give three-layer 2D sheets, referred to as 'stacks' (Fig. 2).

There are two dinuclear Zn-carboxylate clusters, which could be regarded as disrupted paddle-wheel arrangements. In the first cluster, the Zn1 atom has a tetrahedral $\{ZnO_{4+1}\}$ environment with an additional weaker Zn–O bond, while Zn2 has an octahedral environment, involving a chelating carboxylate, thereby not completing the usual paddle-wheel arrangement (both atoms coordinate one DMF molecule). In the second cluster, the Zn3 and Zn4 atoms are disordered over two different positions, A (81%) and B (19%), assuming alternating roles (Fig. S4, ESI† for the details of the disorder). In part A, the Zn3A atom coordinates a nitrogen atom from a dimethylamine solvent molecule in addition to five carboxylate oxygen atoms, two of which belong to a chelating carboxylate. This results in a strongly distorted octahedron as a coordination environment. The Zn4A atom is tetrahedrally coordinated by four oxygen atoms, two of which belong to monodentate carboxylates. In the absence of the second disordered component (Zn4B), the latter carboxylates are involved in hydrogen bonding with the charge compensating dimethylammonium cation, ensuring the coordination of five carboxylates per Zn_2-cluster, instead of four.

The connection of the $\{Cu^I_3(mpba)_3\}^{3-}$ metallo-linkers with the Zn_2-SBUs leads to hexagonal rings with the Cu_3-centroid

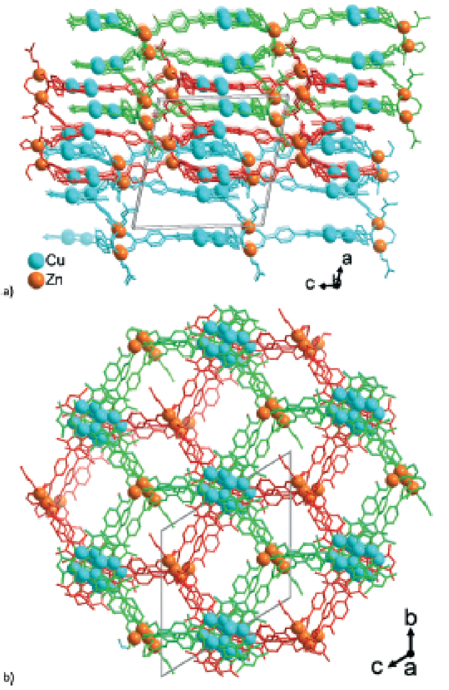

Fig. 3 Wire-frame model of (a) side-view and (b) on-top view (along the *b* and *a* axis, respectively) of a section of three polycatenated 3-layer stacks in **1**. The three stacks are differentiated by their green, red and cyan color. Hydrogen atoms are not shown for clarity. Only the major contribution to the disorder of Zn3 and Zn4 was used in the drawing. See also the space-filling presentation in Fig. S6, ESI.†

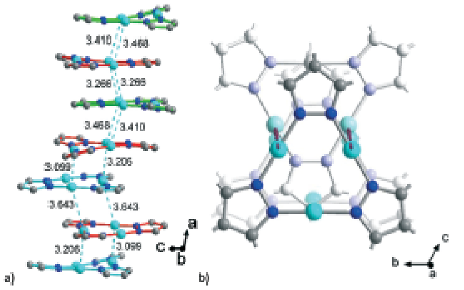

Fig. 4 a) Stacking of the $\{Cu^I_3(pz)_3\}$ moieties in **1** with $Cu^I \cdots Cu^I$ contacts (in cyan, in Å) between the polycatenated stacks which are differentiated by the same green, red and cyan color as in Fig. 3; the methyl groups are not shown for clarity. b) Alternation of the axial rotation of the $\{Cu^I_3(pz)_3\}$ moieties.

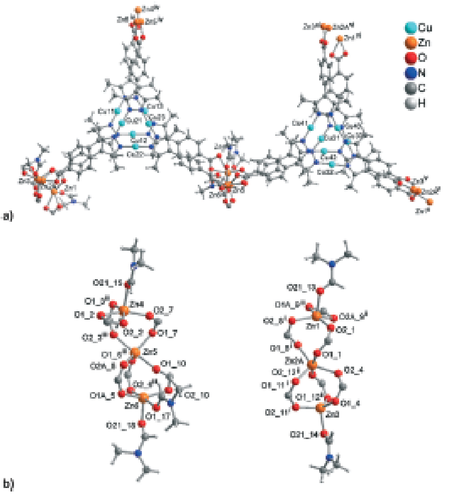

Fig. 5 (a) Extended asymmetric unit of 2. The emphasis in this image is placed on the slightly shifted eclipsed position of the metallo-linkers. The inter-linker Cu⋯Cu contacts range from 3.57–3.79 Å (Fig. 6c). (b) The two trinuclear hourglass-like SBUs. Symmetry codes: (i) $x - 1, y - 1, z + 1$; (ii) $x - 1, y, z + 1$; (iii) $x, y + 1, z$; (iv) $x, y - 1, z$; (v) $x + 1, y + 1, z - 1$; (vi) $x + 1, y, z - 1$. Only the major contribution to the disordered carboxylates and Zn2 atoms is shown, and the Zn2 disorder is described in more details in Fig. S9, ESI.†

and Zn_2-centroid as vertices and the mpba-ligands as edges (Fig. 2b). While $\{Cu^I_3(mpba)_3\}^{3-}$ is a three-connected node, the Zn1/Zn2 group acts as a four-connected node and the Zn3/Zn4 group as a five-connected node. Hence, each Zn1/Zn2 group belongs to the top and middle layer, and each Zn3/Zn4 group to the middle and bottom layer (according to the orientation in Fig. 1 and 2a).

The single 3-layer stack in **1** has a >6.4 Å separation between the metallo-linkers (Fig. 1, 2a, and S5a†) and possesses an open structure with hexagonal pores propagating along the *a*-direction (Fig. 2b and S5b†). A dense packing, however, minimizes the energy of a structure. Therefore, open frameworks often show phenomena of interpenetration, polycatenation or entanglement.[57–62] In **1** the lower/upper half of a 3-layer stack polycatenates into the upper/lower halves of its neighbors (Fig. 3a and S6a†). At the same time the stacks are packed along the *a*-direction in a staggered fashion in an ABAB sequence, such that the $\{Cu_3(pyrazolate)_3\}$, *i.e.*, $\{Cu_3(pz)_3\}$, parts of the metallo-linkers are stacked on top of each other (Fig. 3b and 4) and the Zn-SBUs fill most of the voids of the polycatenated stack (Fig. 3b and S6b, ESI†). Thereby, the available space in a single 3-layer stack is filled (compare Fig. 2b and 3b).

Two adjacent 3-layer stacks polycatenate in a parallel manner in a 2D + 2D motif. The infinite 2D + 2D polycatenation of upper/lower parts of neighboring 3-layer

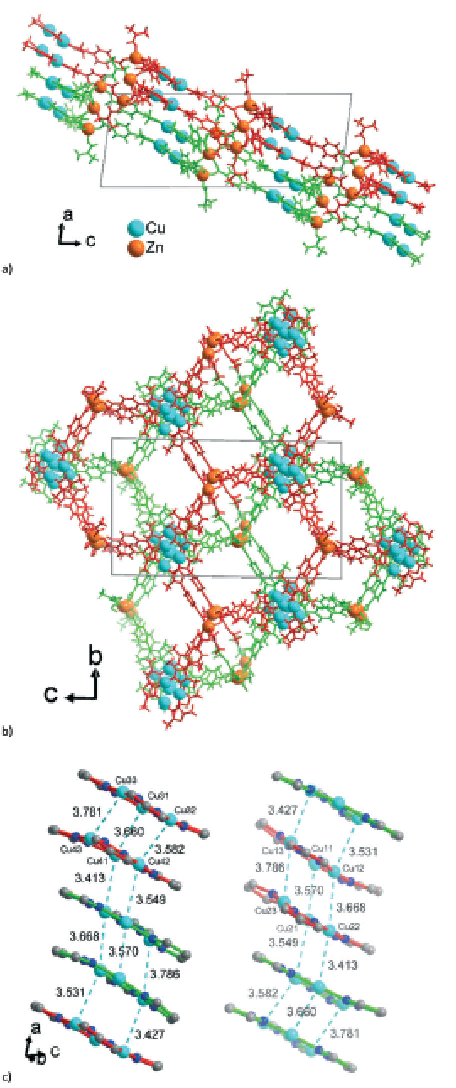

Fig. 6 Wire-frame model of (a) side-view and (b) on-top view (along the *b* and *a* axis, respectively) of two adjacent 2-layer stacks in 2. The two stacks are differentiated by their green and red color. See also the space-filling presentation in Fig. S10, ESI.† (c) Stacking of the $\{Cu^I_3(pz)_3\}$ moieties in 2 with $Cu^I \cdots Cu^I$ contacts (in cyan, distances in Å) between the layers. The inversion-symmetry relation of adjacent stacks renders the packing for the two symmetry-independent parts of the asymmetric unit of 2 (*cf.* Fig. 5a) equivalent. Thus, the red $\{Cu^I_3(pz)_3\}$ units in the left column correspond to the green $\{Cu^I_3(pz)_3\}$ units in the right column in Fig. 6c.

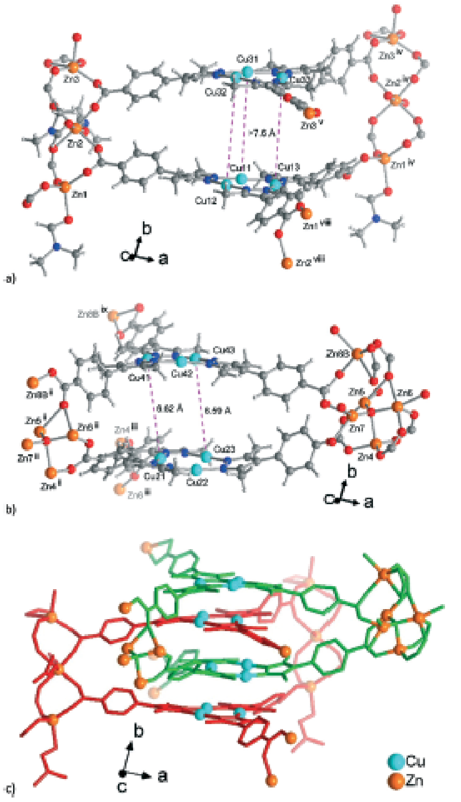

Fig. 7 Extended asymmetric units in 3. (a) Network A, constituted by the trinuclear Zn-SBUs with branches ending with Zn atoms showing the connections. (b) Similar image for network B constituted by the tetranuclear Zn-SBUs. The Zn atoms in the middle of the images which point to the front (in a) and to the rear (in b) propagate the structure along the *b*-axis. The distances between the Cu atoms (pink dashed lines) correspond to twice the distances of typical cuprophilic Cu⋯Cu contacts. (c) The mode of interpenetration of network A, shown with red bonds and network B, shown with green bonds. In (b) the major disorder contributions to the Zn-atoms in the structure are shown. From the disorder, the Zn-SBU in (b) looks like a pentanuclear interpretation, yet the 80% occupancy gives a Zn_4-SBU (see Fig. S11, ESI† for details). Symmetry codes: (ii) *x* − 1/2, *y* − 1/2, *z*; (iii) *x* − 1/2, −*y* − 3/2, *z* − 1/2; (iv) *x* + 1/2, *y* + 1/2, *z*; (v) *x* + 1/2, −*y* − 3/2, *z* + 1/2; (viii) *x* + 1/2, −*y* − 5/2, *z* + 1/2; (ix) *x* − 1/2, −*y* − 1/2, *z* − 1/2.

stacks along the perpendicular direction to the stack leads to a 3D network. Interpenetration which results in a higher dimensionality than the discrete network, that is, 2D → 3D, is termed polycatenation.[60] A similar upper/lower part 2D + 2D polycatenation, giving an overall 3D network, is also frequently seen for (4,4)la double-layer **sql** nets.[61]

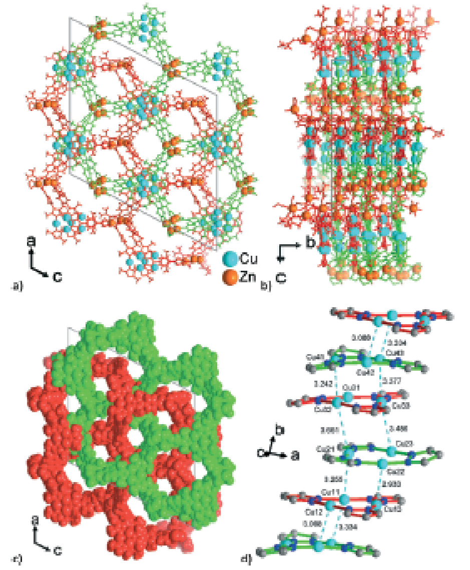

Fig. 8 View along the hexagonal channels of the two interpenetrating 3D-frameworks in 3 as (a and b) wire-frame, two projections and (c) space-filling modes. Network A in red with the Zn_3-SBU and network B in green with the Zn_4-SBU (*cf.* Fig. 7). (d) Stacking of the $\{Cu^I_3(pz)_3\}$ moieties in 3 with $Cu^I\cdots Cu^I$ contacts (in cyan, distances in Å) between the layers of the interpenetrating frameworks.

The polycatenation is invoked and stabilized through the inter-stack $Cu^I\cdots Cu^I$ contacts, with lengths between 3.099 Å and 3.643 Å (Fig. 4) which thus correspond to typical cuprophilic interactions.[43,63–65] We note that these inter-stack $Cu^I\cdots Cu^I$ separations are in the same range as the $Cu^I\cdots Cu^I$ distances within the $\{Cu_3(pz)_3\}$ clusters, which lie between 3.169 Å and 3.257 Å (Fig. S7, ESI†).

Crystal structure of 2

The asymmetric unit of 2 with the established formula of $[Zn_6\{Cu^I_3(mpba)_3\}_4(DMF)_5]$ (Fig. 5a) consists of four symmetry-independent $\{Cu^I_3(mpba)_3\}^{3-}$ metallo-linkers. They are pairwise stacked at short $Cu^I\cdots Cu^I$ distances of 3.413 Å and 3.786 Å and connected through two symmetry-independent $\{Zn_3(O_2C-)_6(DMF)_{2-3}\}$ SBUs (Fig. 5b) to a two-dimensional 2-layer stack. The three Zn atoms in $\{Zn_3(O_2C-)_6(DMF)_{2-3}\}$ form unsymmetrical hourglass-like trinuclear SBUs where the central Zn atoms (Zn2A, Zn5) rather have a square-pyramidal than bipyramidal environment (geometric index[66] τ = 0.42 and 0.32) coordinated by five carboxyl-O atoms from five different metallo-linkers (Fig. 5b).

The terminal Zn atoms possess either a tetrahedral (Zn3) or distorted square-pyramidal environment (Zn1, Zn4,

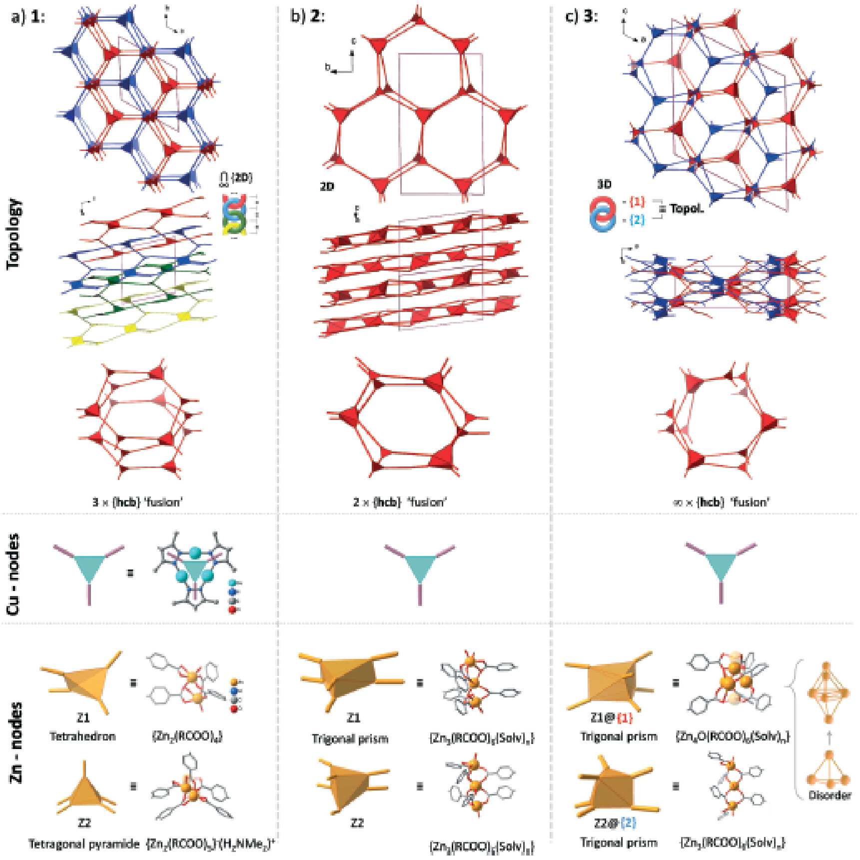

Fig. 9 Topological overview of the structures of **1–3** (the coloration of the separate networks is assigned for convenience: all structures contain only one type of network regarding their topology). The crystallographically distinct Cu-based nodes are structurally- and in most cases topologically equivalent (the exception is the structure of **1**, where there are two topologically distinct Cu-nodes among three crystallographically different ones with point symbols of $\{4{\cdot}6^2\}$ and $\{6^3\}$; see Table S4, ESI†). The Zn-based nodes are distinct in every case, except for the topological equivalence of the two different nodes in the structure of **3**. For an illustration of the interpenetration of hexagonal rings in the structures of **1** and **3** see Fig. S15, ESI.†

Zn6 τ = 0.23, 0.08, 0.54), although Zn4 and Zn6 have additional long (>2.5 Å) contacts completing a distorted octahedral environment.[66] The two Zn_3-SBUs possess three crystallographically different Zn^{II} ions. The coordination of the terminal Zn atoms Zn1, Zn3 and Zn4 is constructed from three carboxyl groups of metallo-linkers and one DMF molecule. For the five-coordinated atoms Zn1 and Zn4 one of the carboxyl groups is chelating and the DMF ligand is in the apical position. The five-coordinated Zn6 atom is bound to three monodentate carboxylates and two DMF ligands.

The 2D 2-layer stacks in **2** run parallel to the (1 0 1) plane (Fig. 6a). The combination of the $\{Cu^I_3(mpba)_3\}^{3-}$ metallo-linkers with the Zn_3-SBUs leads again to a structure based on hexagonal rings, when the Cu_3-centroids and the midpoints between two Zn atoms in the hourglass SBUs are considered as nodes of the underlying net and the mpba-ligands as edges (Fig. 6b). Two adjacent 2-layer stacks, related through a symmetry operation, become staggered along the *a*-direction, such that the Cu_3(pyrazolate)$_3$, *i.e.*, the $Cu_3(pz)_3$, parts of the metallo-linkers are again stacked on top of each other (Fig. 6c), as was also seen in **1** (*cf.* Fig. 3).

The terminal DMF ligands at the Zn_3 hourglass-SBUs stick out of the stack and protrude into the adjacent stack (Fig. 6a).

Crystal structure of 3

The established formula of **3**, $[Zn_3\{Cu^I_3(mpba)_3\}_2(DMF)_3(H_2O)][Zn_4(\mu_4\text{-}O)\{Cu^I_3(mpba)_3\}_2(H_2O)_4]$, reflects the presence of two symmetry-independent two-fold interpenetrating neutral networks, based on different Zn-SBUs. Network A = $[Zn_3\{Cu^I_3(mpba)_3\}_2(DMF)_3(H_2O)]$ has the trinuclear Zn-SBU $\{Zn_3(O_2C-)_6(DMF)_3\}$ (Fig. 7a). Network B = $[Zn_4(\mu_4\text{-}O)\{Cu^I_3(mpba)_3\}_2(H_2O)_4]$ has the tetranuclear $\{Zn_4(\mu_4\text{-}O)(O_2C-)_6(H_2O)_4\}$ Zn-SBU (Fig. 7b). While the trinuclear SBU could be well-refined, the interpretation of the second Zn-SBU is ambiguous. The conventional $\{Zn_4(\mu_4\text{-}O)(O_2C-)_6\}$ cluster is octahedral, while the demands imposed by the crystal structure of **3** prescribe a distorted trigonal-prismatic shape. The refined atoms, constituting the cluster, have large thermal displacement factors, allowing multiple interpretations. Based on the Zn : Cu ratio found by analytics and following general chemical logic, a complex, unresolved overlap of nearly regular $\{Zn_4(\mu_4\text{-}O)(O_2C-)_6\}$ clusters was assumed (Fig. S12, ESI†). An alternative, more straightforward interpretation is a pentanuclear $\{Zn_5(\mu_4\text{-}O)(OH)_2(O_2C-)_6\}$ cluster with a minor disorder. Also, an admixture of Cu(I) such that the disordered $\{Zn_4(\mu_4\text{-}O)\}$ cluster might be $\{Zn_4Cu^I(\mu_4\text{-}O)\}$ could not be completely ruled out. Despite the different possible Zn_4-SBU interpretations, the localization of the $\{Cu^I_3(mpba)_3\}$ moieties and hence the connectivity in the framework is unambiguous.

Aside from the two different Zn SBUs, the asymmetric unit of each network consists of two symmetry-independent $\{Cu^I_3(mpba)_3\}^{3-}$ metallo-linkers, which are stacked in an eclipsed fashion at twice the distance, ~6.5 Å, of optimal cuprophilic interaction between the $\{Cu_3(pz)_3\}$ moieties, leaving room for an interpenetrating network, as in **1**. The distance between the closest Cu^I atoms is over 6.5 Å (Fig. 7 and 8). Four of the six carboxylate groups of the two eclipsed $\{Cu^I_3(mpba)_3\}^{3-}$ metallo-ligands are pairwise 'clamped' by two of the Zn_3 or Zn_4 SBUs, similar to the arrangement in the structure of **2**. The difference is that the remaining two carboxylate branches extend the network to the third dimension, perpendicular to the layers (along the *b* axis, Fig. 7). The connection of the $\{Cu^I_3(mpba)_3\}^{3-}$ metallo-linkers with the Zn-SBUs in **3** leads again to a structure dominated by hexagonal rings in both of the interpenetrating frameworks (Fig. 8). The inter-linker cuprophilic contacts[43,63–65] condition the tight interpenetration with $Cu^I\cdots Cu^I$ distances between 2.933 Å and 3.661 Å (Fig. 8c) as in **1** (Fig. 4) and **2** (Fig. 6c).

Comparison of the structural organization and topology

Structures **1–3** demonstrate a distinct similarity regarding both the formation of hexagonal ring motifs (Fig. 3b, 6b, and Fig. 8a respectively; Fig. S14a, ESI†) and the columnar association of all present $\{Cu_3(pz)_3\}$ moieties by $Cu^I\cdots Cu^I$ cuprophilic interactions (the high similarity of the columnar arrangements with staggered neighbor units is shown in Fig. S13†). The hexagonal rings are situated in an eclipsed way within a separate network/topology constituting open channels. The channel openings are partially occupied or blocked by polycatenated (**1**), just neighboring (**2**) or interpenetrated (**3**) networks which are arranged with respect to each other in a slipped or staggered mode similar to the ABAB layer sequence in graphite (Fig. 9).

The Zn-SBU nuclearity increases from Zn_2 in **1** over hourglass-like Zn_3 in **2** to Zn_3 and Zn_4 in **3** (Fig. 9). The connectivity ensured by the Zn-SBU adapts to the demands imposed by the stacked Cu^I-mpba linker arrangement, conditioned by the cuprophilic interactions (Fig. S13, ESI†). The flexibility in the Zn coordination sphere with tetrahedral, trigonal-bipyramidal to square-planar or octahedral coordinated Zn atoms must be seen as instrumental to allow the formation of (energetically) similar structures.

From the topological analysis on the level of the 3-c $\{Cu_3(pz)_3\}$ node and of the Zn-SBU nodes of higher connectedness, the next point symbols were found: $\{4{\cdot}6^2\}_2\{4^2{\cdot}6^6{\cdot}8^2\}\{6^3\}\{6^5{\cdot}8\}$ for **1** (a new 2D net), $\{4^3{\cdot}6^{12}\}\{4^3\}_2$ for **2** (3,6L66 net), and $\{4{\cdot}6{\cdot}8\}_2\{4^2{\cdot}6^5{\cdot}8^5{\cdot}10^3\}$ for **3** (**sqc**-3,6-Fdd2-2 net) (the topological analysis was performed by ToposPro,[67,68] see Fig. 9 for the node representations and Table S4, ESI,† for node stoichiometry, vertex symbols and TD10).

The structures of **1–3** could be conceptualized through their relation with the hexagonal net, **hcb**. The latter is an expected outcome, when the trigonal $\{Cu_3(pz)_3\}$ SBUs are combined in a coplanar fashion. The cuprophilic interactions, perpendicular to the nets, would favor a stacked arrangement (the few reported structures of this kind are based on short non-planar bifunctional 3,5-R_2-pyrazolates of copper(I),[69,70] possessing 3D structures). The structures of **1–3** could be viewed as derivatives of the prototypal stacked **hcb** structure. Some of the alternating Cu-nodes are removed and the respective connectivity is added to the node in the layer above and/or below. The nodes with the increased connectivity are represented by a Zn-cluster and such redistribution of connectivity leads to 'fusing' of the separate **hcb**-nets. The Zn-clusters act as tetrahedral 4-c and tetragonal-pyramidal 5-c in **1** and trigonal-prismatic 6-c in **2** and **3** (Fig. 9). The Zn-clusters adopt different compositions and geometries, invariably ensuring the near coplanarity of the $\{Cu_3(pz)_3\}$ SBUs within the columnar stacks, associated by cuprophilic interactions, that run uninterrupted through the whole structure (Fig. 4, 6c, 8c and S13, ESI†).

The simplest structural organization of 'fused' **hcb** nets is observed in **2** (Fig. 5, 6 and 9). The trigonal-prismatic Zn clusters correspond to two triangular nodes joined together in parallel. The resultant planar 2D net could be viewed as a "double-strand" ("dual-layer") **hcb** net with two stacked nets fused together at alternating nodes. The Cu-nodes are associated by cuprophilic interactions both within the formed 2D network and between them forming a stack of networks, whose projection along the *a*-axis is nearly identical to a geometrically regular **hcb** net (Fig. 6 and 9). The structure features two crystallographically distinct, but chemically and topologically equivalent trinuclear Zn-clusters, $\{Zn_3(COO)_6\}$. Three chelating carboxylates adjoin the neighboring Zn atoms disposed in row of three; two sets of such triples are in an approximately staggered disposition, ensuring the trigonal-prismatic shape of the node (Fig. 5b and 9). Similar structural organization is observed for a number of other tritopic carboxylates featuring an $\{M_3(COO)_6\}$ SBU/cluster or functionally very similar unit (M = Zn, Co, Cd) (among 32 entries with the 3,6L66 net topology found in the Topcryst database,[71] nearly all are coordination polymers and 23 follow this organization; see also the footnote to Table S4†). We regard the 2-layer stack in **2** as the kinetic product from which the 3-layer stack in **1** and the infinite-layer stack in **3** develop.

The structure of **1** consists of 2D nets, which could be represented as a 'fusion' of three stacked hexagonal nets (Fig. 2 and 9). Half of the alternating nodes in the top and bottom layers are represented by 4-c and 5-c Zn-nodes (with an excess connectivity over 3-c of one and two, respectively), which distribute the connectivity of the imaginary triangular node in the middle layer. Each pair of the neighboring triple-layer stacks is polycatenated in a parallel fashion, with the Cu-nodes belonging to the neighboring topologies interdigitating to form a tight stack (Fig. 3 and 4). The triple-layered topologies are polycatenated *via* pairwise interpenetration and topologically constitute a 2D + 2D → 3D structure. The dinuclear Zn-nodes, $\{Zn_2(RCOO)_4\}$ and $\{Zn_2(RCOO)_5\}$ are close to a paddlewheel geometry with an added carboxylate in the second case, which is charge compensated by a nearby $[Me_2NH_2]^+$ cation.

The structure of **3** consists of two interpenetrated 3D nets, which are crystallographically and chemically distinct, but topologically equivalent (Fig. 7). Thereby, it represents formally a case of hetero-interpenetration, even if the topologies are very similar. The 'fusion' of the imaginary stacked **hcb** nets takes place not on the same level, but on alternating levels. Each of the two different six connected Zn-clusters acts as a trigonal node within its layer (Fig. 9) and the remaining excess connectivity (2 + 1) is redistributed above and below, respectively, the layer at the expense of the imaginary Cu-nodes of the prototypal stacked **hcb** net structure. It is interesting to note that each of the two distinct 6-c connected trigonal-prismatic Zn-nodes, $\{Zn_4O(RCOO)_6\}$ = Z1 and $\{Zn_3(RCOO)_6\}$ = Z2 (*cf.* Fig. 9), belongs only to one of the two interpenetrating 3D nets. The Z2 node is similar to the one in **2**, while Z1 is formally close to the expected zinc-oxidocarboxylate cluster (octahedral SBU at the highest symmetry) but with strong geometric distortions accompanied with a complex, not completely resolved crystallographic disorder (Fig. S11, ESI†). The binodal net observed in **3** is also known as the **sqc**-3,6-Fdd2-2 type **sqc**-subnet (for net relations, see ref. 72). It is relatively rare, with only five representatives known in the Topcryst database.[71] All of them are dense coordination polymers based on short bi-azole azole-carboxylate ligands and bear no direct similarity in structural organization with **3**. Hence the hetero-interpenetrated **3** is topologically unique as a MOF.

The general structure-formation logic for **1–3** explains the formation of a class of 'fused' **hcb**-nets rather than a singular compound. This class could be compared with the class of pillared **hcb** nets, which is also highly variable when the pillaring could occur both on one and both sides of the planes (connection isomerism). For the case of the 'fused' nets, which could be viewed as a zero-length pillaring, the variety stems from variable number of connections for a fused node (4–6 in this work).

The summary on topological characteristics of the nets in structures **1–3** is given in Table S4, ESI.† Except for the simple 'dual-strand' **hcb** net in **2**, the other cases are highly special. It is instructive to observe the dominance of 4- and 6-rings (and their exclusivity as smaller cycles). This is the reflection of the 'fused' **hcb** structure-organization. When two stacked **hcb** nets are fused *via* alternating vertices a 4-ring is formed (Fig. S16, ESI†). It is a sole outcome for the case of **2** with only one pair of fused-**hcb** nets, but larger rings appear when the fusing of the **hcb**-layers occurs on different levels as in **1** and **3**.

An aspect which should not be overlooked is the flexibility of the $\{Cu^{I}_3(mpba)_3\}^{3-}$ metallo-linker, which surpasses the bbc^{3-} and bte^{3-} flexibilities (*vide supra*, Fig. S44, ESI†). This flexibility can be characterized in terms of separate contributors, as a system of rigid elements, connected by hinges.[73] The flexibility factors regarding the $\{Cu^{I}_3(mpba)_3\}^{3-}$ metallo-linker are based on (i) the $\{Cu_3(pz)_3\}$ cluster level off-plane deformations, (ii) an equivalent flexibility of the phenyl connectors to the carboxylate group, and (iii) the flexibility due to a rotational degree of freedom between the pyrazolate and phenyl moieties. In the example structure of **2**, with its four crystallographically different $\{Cu^{I}_3(mpba)_3\}^{3-}$ metallo-linkers, the benzoate groups bend out of the plane through the three Cu atoms by 0.7° to 14.5°, most of them between 6° and 8° (Fig. S45, ESI†).

Cu/Zn analysis

In view of the disorder in the Zn-SBUs of all three compounds (*cf.* Fig. 1, 3b and 7b, see also Fig. S4, S9 and S11, ESI†) the elemental analysis of the Cu : Zn ratio and the confirmation of the sole presence of the Cu(I) oxidation state (exclusion of Cu(II)) became important. It seemed necessary to ensure that the Zn-SBUs were indeed Zn-only SBUs with no admixture of Cu(II).

The X-ray photoelectron survey spectra (Fig. S23, ESI†) confirm the expected presence of Cu, Zn, O, N and C in the materials. The Cu 2p XP spectra for all three compounds display the core band at around 933 eV for Cu $2p_{3/2}$ which corresponds to the typical position of Cu(I) (Fig. S24a–S26a, ESI†).[74] The near perfect single-peak fit indicates the presence of only one type of Cu(I) species. Cu(II) species are not present in any of the compounds, according to the absence of the characteristic band at ~934 eV in the Cu 2p XP spectra.[74] The band at ~1022 eV in the 2p XPS spectra corresponds to Zn(II) and is observed for all three materials (Fig. S24b–S26b, ESI†).[75]

The shape of the Cu LMM peak from the Auger electrons can also be useful in determining the chemical state of Cu. It is particularly indicative in the determination of Cu metal *versus* Cu(I) in the absence of Cu(II) species.[76] The Cu-LMM peak is observed at a kinetic energy of 916.5 eV in the Auger spectrum, which is a part of the XP spectrum (Fig. S27, ESI†). The modified Auger parameter α' was calculated by adding the binding energy of the Cu $2p_{3/2}$ photoelectron peak and the kinetic energy of the Cu L3M45M45 Auger peak.[76] The value of the modified Auger-α' parameter for Cu LMM and the Cu $2p_{3/2}$ electron was about (933 + 916.5 =) 1849 eV, which confirmed the +1 oxidation state of Cu.[77,78] For Cu(II) the Auger kinetic energy should lie at 918 eV and the modified Auger-α' parameter should be about 1851 eV.[77,78] The value of the modified Auger-α' parameter for Zn LMM (988 eV, Fig. S28, ESI†) and the Zn $2p_{3/2}$ electrons (1022 eV) was approximately 2010 eV, which also confirms the +2 oxidation state of Zn.[75,79]

The fitting of the C 1s spectra (Fig. S29, ESI†) yielded three bands centered at 285, 286 and 289 eV which can be assigned to C–H/C–C/C═C, C–N, and –COO, respectively.[80] The O 1s band observed at 531 eV (Fig. S29, ESI†) is due to Zn-bound oxygen, whereas the band at around 533 eV represents organic C–O.[81,82] The fitting of the N 1s curves shows two types of component peaks (Fig. S29, ESI†), with the major contribution corresponding to Cu–N (399 eV) and the minor one to amide N–(C═O) (400 eV) from coordinated and residual DMF solvent molecules.[83]

From atomic absorption spectroscopy (AAS) (Table S5, ESI†) and scanning electron microscopy energy-dispersive X-ray spectroscopy (SEM-EDX) (Section S17–S20, ESI,† Tables S6 and S7 ESI†), the molar Cu : Zn ratio for **1** was 1 : 0.44 (AAS) and 1 : 0.44 (EDX, Table S4, ESI†), which is in good agreement with the expectation from the X-ray refinement (Cu : Zn = 9 : 4 = 1 : 0.44). For **3** the analyses gave 1 : 0.53 (AAS) and 1 : 0.53 (EDX, Table S3, ESI†), slightly below the value from the X-ray refinement (Cu : Zn = 12 : 7 = 1 : 0.58).

Thermogravimetric and gas sorption studies

Thermogravimetric analysis (TGA) of the as-synthesized material **1** (Fig. S21a, ESI†) showed a mass loss of 18 wt% up to ~300 °C, which can be attributed to the loss of 9 DMF molecules (calc. 17.8% for 9 DMF). This is in good agreement with the refined coordinated (2 DMF) and SQUEEZE-removed DMF molecules (~7.5 DMF, Table S2, ESI†) per formula unit. For compound **2**, TGA gave a mass loss of 26 wt% up to ~270 °C, which can be ascribed to the loss of 18 DMF molecules (calc. 26.1% for 18 DMF) (Fig. S21b, ESI†). This agrees well with the found (5 DMF) and SQUEEZE-removed DMF molecules (~14 DMF, Table S2, ESI†) per formula unit. The TGA of the as-synthesized material **3** (Fig. S21b, ESI†) exhibited a mass loss of 20% up to ~300 °C, which can be attributed to the loss of 14 DMF molecules (calc. 20.0% for 13.6 DMF). This result is in acceptable agreement with the refined (3 DMF) and squeezed (~12 DMF, Table S2, ESI†) DMF molecules per formula unit. The TGA of the activated compound **3-act.** (Fig. S21b, ESI†) did not exhibit any mass loss up to ~300 °C. After 300 °C decomposition of all three materials occurred with a mass loss up to 300 °C of 25–30 wt% (Fig. S21, ESI†).

In view of the structural similarity of **1–3** regarding the formation of hexagonal nets in staggered stacking mode (Fig. 3b for **1**, Fig. 6b for **2** and Fig. 8a for **3**; Fig. S13 for comparison) it is no surprise that all three compounds yield a similar specific surface area from a crystal void calculation with CrystalExplorer[84] and a similar specific pore volume from CrystalExplorer, Mercury[85,86] and PLATON[87] (Table S11, ESI†).

Various attempts to activate **1** and to prove the presence of a porous material were not successful. Either direct activation in a vacuum under heating or milder approaches *via* preceding solvent exchange or supercritical drying yielded amorphous materials (**1-act.** Fig. S3, ESI†) which did not demonstrate appreciable Ar (87 K) or CO_2 (195 K) adsorption.

The activation attempts of **3** by heating under vacuum were more successful, and the resultant **3-act.** material demonstrated significant crystallinity, even if inferior to **3** as judged by the peak broadening in the PXRD pattern (Fig. S3, ESI†). The latter also witnesses a structural transformation caused by the loss of solvent molecules (Fig. S21b, ESI†). The two-fold interpenetrated 3D framework in **3** expectedly provides higher structural resilience and prevents a complete structural collapse compared to the polycatenated 2D framework in **1**. But even in **3** there is no prerequisite for a highly rigid structure because of the ligand flexibility (*vide supra*). Notwithstanding the crystallinity, **3-act.** demonstrated only a small N_2 uptake at 77 K with a hysteresis spanning the whole measurement range, indicating kinetic hindrances (Fig. S30, ESI†). At 87 K (liquid argon temperature) argon fills narrow micropores at significantly higher relative pressures in comparison with nitrogen at 77 K.[88,89] Accordingly, Ar with also a smaller kinetic diameter (3.4 *vs.* 3.64 Å for N_2) and weaker interaction with the adsorbent implying faster equilibration rates compared to N_2 was selected for further studies. The adsorption of Ar at 87 K by **3-act.** was indeed unhindered, followed a type I isotherm (Fig. 10) and allowed for BET surface analysis. The material possesses a total pore volume of 0.30 cm^3 g^{-1} at P/P_0 = 0.95, a micro pore volume of 0.25 cm^3 g^{-1} at P/P_0 = 0.1, and a BET surface area of 762 m^2 g^{-1} (Fig. S31b, ESI†). The desorption shows a small hysteresis loop (type H4) which is typical for micro-mesoporous materials.[89]

CO_2 (and also CH_4) gas sorption studies were performed for the **3-act.** material at 273 K and 293 K. Due to the higher

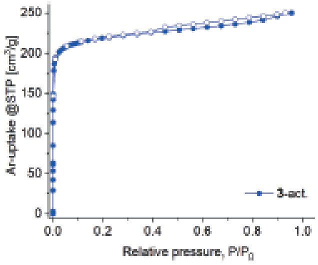

Fig. 10 Ar sorption isotherm at 87 K for **3**-act.

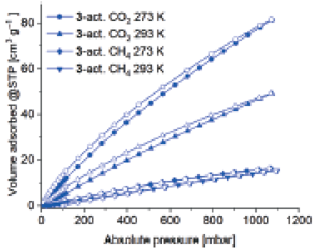

Fig. 11 CO_2 and CH_4 sorption isotherms of **3**-act. at 293 K and 273 K with adsorption as filled symbols and desorption as open symbols.

temperatures only minor kinetic hindrances were observed. The adsorption isotherms are of type Ia (Fig. 11), albeit not reaching saturation for CO_2 at 1 bar, which again underlines the microporous character of the material.

As expected, the uptake of the slightly larger non-polar gas CH_4 was significantly lower with 15 $cm^3\ g^{-1}$ (273 K) and 14 $cm^3\ g^{-1}$ (293 K) than for CO_2 78 $cm^3\ g^{-1}$ (273 K) and 46 $cm^3\ g^{-1}$ (293 K). Consequently, the determined $CO_2:CH_4$ selectivity by the Henry plots of the adsorption isotherms results in a higher selectivity for CO_2 (4.8 : 1 at 273 K, 3.5 : 1 at 293 K; Fig. S32, Table S10, ESI†).

The isosteric enthalpy of adsorption at zero coverage, ΔH^0_{ads} for CO_2 and CH_4 from adsorption isotherms at 273–293 K (Fig. 11) was calculated with the virial fit method (Fig. S33 and S34, ESI†).[90] As expected, the values of the isosteric enthalpy of adsorption ΔH_{ads} are significantly higher (*i.e.* more negative) for CO_2 than for CH_4 at the same gas uptake. At zero coverage ΔH^0_{ads} (CO_2) is −29 kJ mol^{-1} and ΔH^0_{ads}(CH_4) is −15 kJ mol^{-1}. Compared to other MOFs, these values are at the lower end for ΔH^0_{ads}.[91–93]

Conclusions

The N,O-heteroditopic semi-flexible $mbpa^{3-}$ ligand with carboxylate and dimethylpyrazolate tails was used for the exploration of mixed-metal Cu(I)/Zn(II) coordination networks, aiming to combine the probable $\{Cu_3(3,5\text{-dimethylpyrazolate})_3$ and $Zn_4O(O_2C)_6$ SBUs. An alternative viewpoint on the synthesis in polar media is the *in situ* formation of the $\{Cu^I_3(mpba)_3\}^{3-}$ metallo-ligand, as an intermediate product, which is engaged in minimal ligand-exchange concurrence in a hard-ligand environment. Accordingly, $\{Cu^I_3(mpba)_3\}^{3-}$ is viewed as a large triangular ligand, interesting in the context of reticular chemistry, where 1,3,5-benzenetricarboxylate and expanded analogues play an important role.

Three coordination networks, **1–3**, were obtained in a course of low-temperature solvothermal synthesis from *N*,*N*-dimethylformamide and, remarkably, there is a condition-range when all the three compounds formed simultaneously. In all compounds columnar stacks of Cu_3(3,5-dimethylpyrazolate)$_3$ clusters associated by cuprophilic interactions are the dominant structural feature. Parallel orientation of the stacks is the most general way to achieve an efficient packing; the various 2-4(5)-nuclear Zn-SBUs are rather adapting to this requirement. The resulting networks bear similarities to stacked **hcb** nets, which would be realized for trigonal SBU-only assembly. The additional connectivities of the Zn-SBU clusters 'fuse' the **hcb** nets together, yielding layered 2D, layered polycatenated 2D → 3D or 3D frameworks. Despite the interpenetration, the permanent porosity for **3** with a 3D porous structure was demonstrated by Ar, CO_2 and CH_4 sorption.

Thus, the structures **1–3** demonstrate similar underlying network-formation principles resulting in what could be named a 'fused' **hcb** structure class. The structure prediction could be only fuzzy or vague here, and yet such limited design accuracy could be productive. The $\{Cu^I_3(mpba)_3\}^{3-}$ metallo-linker has structural degrees of freedom which allow for certain self-adjustments regarding the relative angular positions of the carboxylate groups and this appears favorable for an explorative search approach not based on an exact prediction of a particular structural type. Further elongation of the ligand might yield similar structures due to the good stabilization granted by the cuprophilic stacking. Interesting possibilities of defective structures could be foreseen by using co-ligands with terminated connectivity, like $[Cu_3(3,5\text{-dimethylpyrazolate})_3]$, which could be incorporated in the stacks and decrease the general connectivity.

It is worth stressing the interest in mixed-metal MOFs based on heteroditopic ligands. In the case of mbpa, the Cu^I/Al^{III} combination seems to be particularly interesting due to the multitude of possible aluminum oxidocarboxylate MOFs. Another interesting aspect is the use of the limited-prediction approach when a dominant self-assembly factor is present and the semi-flexible ligands/clusters allow for some self-adjustment (ligands with a high level of flexibility are generally not compatible with permanent porosity). For example, for the octahedral $\{Zn_4O(COO)_6\}$ and the triangular planar $\{Cu^I_3(pz)_3\}$ SBUs a multitude of combination possibilities exist, provided that certain self-adjustment is possible. Among the suitable alternating two vertex 3,6-c nets, the rutile **rtl** net possesses the highest symmetry and suitable node geometries, however its demands an adjusting turn of the neighboring SBUs by ~45°, which could be supported by the mbpa moiety of the $\{Cu^I_3(mpba)_3\}^{3-}$ linker. Despite a multitude of possibilities, all three obtained compounds 1–3 follow the same structure-formation logic: the cuprophilic interactions between the $\{Cu^I_3(pz)_3\}$ SBUs, frequently occurring for such structures, evidently play an important pre-organizing role and dictate the course of the self-assembly, which is allowed by the geometric self-adjustment provided by the ligand and concomitant flexible cluster actualization.

Experimental section

Chemicals

Reagents and solvents were obtained from commercial sources and used as received without further purification. $Cu(NO_3)_2{\cdot}2.5H_2O$ (98%) was purchased from Alfa Aesar, $Zn(NO_3)_2{\cdot}4H_2O$ (98%) from ALFA Chemistry and $Zn(CH_3COO)_2{\cdot}2H_2O$ (98%) from VWR. *N*,*N*-Dimethylformamide (DMF) p.a. was obtained from Riedel-de Haën, tetrafluoroboric acid (HBF_4, 48 wt% in H_2O) from Sigma-Aldrich and conc. nitric acid from Chemsolute. The synthesis of 4-(3,5-dimethyl-1*H*-pyrazol-4-yl)benzoic acid (H_2-mpba) was carried out according to the literature procedure.[45]

Instrumentation

Elemental analysis measurements of carbon, hydrogen, nitrogen and sulfur (CHNS) were done with an Elementar Vario MICRO cube. IR-spectra were recorded on a Bruker FT-IR Tensor 37 spectrometer in the 4000–500 cm^{-1} region with 2 cm^{-1} resolution as KBr disks. Powder X-ray diffraction (PXRD) measurements were carried out with a Rigaku MiniFlex600 powder diffractometer using a flat silicon, low background sample holder at 40 kV, 60 mA (600 W) for Cu-Kα radiation (λ = 1.54184 Å). In all diffractograms, the most intense reflection was normalized to 1. Simulated powder X-ray diffractograms were obtained from single-crystal data using the MERCURY 3.5.1 software program.[94] Thermogravimetric analysis (TGA) was performed using a Netzsch TG 209 F3 Tarsus from 20 to 600 °C with a heating range of 5 K min^{-1} under nitrogen atmosphere. Atomic absorption spectroscopy (AAS) was carried out on a PinAAcle 900T from Perkin-Elmer with a copper or zinc hollow cathode in acetylene/air-flame at 2300 °C. Scanning electron microscopy (SEM) images were obtained using a Jeol JSM-6510LV QSEM advanced electron microscope equipped with a LaB_6 cathode at 5–20 kV. The microscope was equipped with a Bruker Xflash 410 silicon drift detector for energy-dispersive X-ray (EDX) spectroscopy. The samples were coated with gold (Au) using a Jeol JFC 1200 finecoater (20 mA for 25 s) before the measurements. X-ray photoelectron spectroscopy (XPS) measurements were made on an ULVAC-PHI VersaProbe II microfocus X-ray photoelectron spectrometer. Experimental XP spectra were fitted by the CasaXPS program, version 2.3.19PR1.0, copyright 1993–2018 Casa Software Ltd. Volumetric gas sorption measurements up to one bar were performed on a Quantachrome Autosorb iQ MP on sample amounts of at least 30 mg, which were degassed/activated under vacuum (10^{-3} mbar) at 200 °C, for 3 h.

Single crystal X-ray structure determination

Single crystal X-ray structures. Suitable single crystals of 1–3 were carefully selected under a polarized-light microscope and mounted in a perfluorinated oil drop. For 1, the single-crystal diffraction data was collected using a Bruker D8 VENTURE diffractometer with a CCD area detector (PHOTON III C14) and an INCOATEC microfocus sealed tube 3.0 for Mo-K_α radiation (λ = 0.71073 Å) with a multilayer mirror monochromator. The data were collected under a cold nitrogen gas-stream at 100(2) K using ω- and ϕ-scans. Data reduction was performed by APEX 3 (ref. 95) (integration) and TWINABS-2012/1 (ref. 96) was used for absorption correction.

For 2 and 3, the single-crystal diffraction data was collected using a Rigaku XtaLAB Synergy S four-circle diffractometer with a Hybrid Pixel Array Detector and a PhotonJet X-ray source for Cu-K_α radiation (λ = 1.54184 Å) with a multilayer mirror monochromator. The data were collected under a cold nitrogen gas-stream at 100.0(1) K using ω-scans. Data reduction and absorption correction were performed by CrysAlisPro 1.171.41.61a [Rigaku Oxford Diffraction, 2020 Yarnton, UK].

All three structures were solved by direct methods using SHELXT-2015.[97] Full-matrix least squares refinements on F^2 were carried out with SHELXL-2015. Crystal data and details on the structure refinement are given in Table S2, ESI.† Graphics were drawn with the program Diamond.[98] The structure of 3 was refined as a 2-component inversion twin.

In 1–3 in favour of clarity, the $mpba^{2-}$ units and DMF molecules were organized in residues (RESI). All hydrogen atoms were positioned geometrically and refined using riding models with $U_{iso}(H) = 1.2{\cdot}U_{eq}(CH_{arom.})/U_{eq}(NH)$ or $1.5{\cdot}U_{eq}(CH_3)$.

In 1–3 highly disordered solvent molecules were removed *via* the SQUEEZE (Platon) procedure (structures 1 and 3)[87] or by solvent masking as implemented in OLEX 2 (structure 2). In 1 the resulting solvent accessible volume of 2751 $Å^3$ per unit cell contained 604 electrons, which may correspond to 15 DMF molecules (40 e^- each) as the solvent of crystallization per unit cell or 7.5 DMF molecules per given asymmetric formula unit (Z = 2). In 2 the resulting solvent accessible volume of 4630 $Å^3$ per unit cell contained 1131 electrons, which may correspond to 28 DMF molecules as the solvent of crystallization per unit cell or 14 DMF molecules per given asymmetric formula unit (Z = 2). In 3 the resulting solvent accessible volume of 7369 Å3 per unit cell contained 1894 electrons, which may correspond to 47 DMF molecules as the solvent of crystallization per unit cell or ~12 DMF molecules per given asymmetric formula unit ($Z = 4$).

In **1** the Zn-cluster which contains the dimethylamine and dimethylammonium species which are disordered in an 81 : 19 ratio, affecting both Zn atoms and the proton of the counterion.

In **2** the phenyl rings of RESI 5, 9 and 12 are disordered over two positions due to rotation along the 1,4-axis which is a well-known phenomenon. Furthermore, one DMF molecule coordinating to Zn4 is disordered over two positions in an 86 : 14 ratio.

In **3** the zinc oxidocarboxylate coordination-bonded cluster ($\{Zn_4O\}$) involving the Zn4 to Zn8a,b atoms features a complex disorder, which could be described in the first approximation as three overlapping $\{Zn_4O\}$ arrangements. The disorder is driven by the demand imposed by the crystal structure/topology: six carboxylates, which are located within convenient reach, are not arranged suitably to sustain the regular octahedral $\{Zn_4O(RCOO)_6\}$ cluster. The 'three overlapping pyramids' model with a nearly common base (Zn5, Zn6, Zn7) assumes a much lower occupancy of the 'capping/axial' Zn-atoms (Zn4, Zn8a,b), however the refined equivalent U_{iso} values do not indicate dramatic differences. While the relatively large temperature factors could mask additional non-evident disorder possibilities, there is another possible reason for the higher occupancy of the 'capping' atoms: at least for Zn8 there is a weak residual electronic density in the vicinity. Instead of speculating the possibility of an increased number of Zn atoms in the cluster, the disorder was modelled as even *via* ascribing 0.8 occupancy for each of the five Zn atoms (the Zn8 atom is additionally split into two components, Zn8a and Zn8b, with refined contributions). This concise approach reflects both the experimental observations and the limited knowledge about disorder, whose occurrence is, however, not unusual in the given structural setting. Accordingly, the cluster composition, involving the Zn4 to Zn8a,b atoms, is assumed to be $\{Zn_4O(H_2O/DMF)_4(RCOO)_6\}$. The coordinated water molecules (O5S to O8S atoms) are a simplified description of site-sharing H_2O/DMF ligands; the too weak residual electron density made the refinement of the DMF constituents not practical.

The structural data have been deposited with the Cambridge Crystallographic Data Center under deposition numbers CCDC 2105164–2105166.†

Synthetic procedures

$[Me_2NH_2][Zn_4\{Cu^I_3(mpba)_3\}_3(Me_2NH)(DMF)_2]$ (1). 20.0 mg (0.092 mmol) of H_2mpba, 21.5 mg (0.092 mmol) of $Cu(NO_3)_2 \cdot 2.5H_2O$ and 16.9 mg (0.065 mmol) of $Zn(NO_3)_2 \cdot 4H_2O$ were each dissolved in 1 of mL *N*,*N*-dimethylformamide (DMF). The three solutions were combined in a glass vial equipped with a screw cap, sealed and transferred in a preheated oven at 90 °C for six days. After cooling to room temperature, the formed clear yellow parallelepiped-shaped crystals (Fig. S1†) were filtered and washed three times with 3 mL of DMF each (yield 25 mg, 56%, based on zinc salt). Calc. for $C_{108}H_{90}Cu_9N_{18}O_{18}Zn_4$ (2761.42 g mol^{-1}) C 46.97, H 3.28, N 9.13; found C 47.20, H 3.31, N 9.15%. IR: (KBr, Fig. S22, ESI†): $\tilde{\nu}$ = 3435 (br), 3067 (br), 2567 (br), 2501 (br), 2360 (br), 2341 (br), 2273 (br), 1661 (s), 1608 (s), 1542 (s), 1403 (br), 1284 (w), 1253 (w), 1179 (s), 1145 (w), 1093 (w), 1062 (w), 1034 (m), 1014 (w), 865 (w), 847 (w), 812 (w), 782 (s), 714 (s), 692 (m), 660 (w), 634 (m), 610 (w), 565 (w), 517 (s), 442 (w) cm^{-1}.

$[Zn_6\{Cu^I_3(mpba)_3\}_4(DMF)_5]$ (2). 20.0 mg (0.092 mmol) of H_2mpba, 21.5 mg (0.092 mmol) of $Cu(NO_3)_2 \cdot 2.5H_2O$ and 15.2 mg (0.070 mmol) of $Zn(CH_3COO)_2 \cdot 2H_2O$ were each dissolved in 1 mL of DMF. The three solutions were combined in a glass vial with a screw cap. After a few minutes, a greenish precipitate formed. This was dissolved again by adding 30 μL of aqueous tetrafluoroboric acid (HBF_4, 48% min w/w). The glass vial was then sealed and transferred in a preheated oven at 90 °C for nine days. After this time, an off-white precipitate was observed. After cooling to room temperature, the product was filtered and washed three times with 3 mL DMF (yield 15 mg, 35%, based on zinc salt). Calc. for $C_{144}H_{120}Cu_{12}N_{24}O_{24}Zn_6$ (3725.60 g mol^{-1}) C 46.42, H 3.25, N 9.02; found C 46.68, H 3.60, N 9.18%. IR: (KBr, Fig. S22, ESI†): $\tilde{\nu}$ = 3429 (br), 3184 (br), 3070 (br), 3042 (br), 2920 (m), 2854 (br), 1934 (br), 1811 (br), 1677 (s), 1610 (s), 1586 (w), 1537 (w), 1493 (w), 1405 (br), 1281 (br), 1257 (br), 1178 (w), 1145 (w), 1090 (w), 1013 (m), 860 (w), 805 (w), 777 (w), 712 (w), 660 (w), 609 (w), 559 (w), 516 (br), 442 (w) cm^{-1}.

$[Zn_3\{Cu^I_3(mpba)_3\}_2(DMF)_3(H_2O)][Zn_4(\mu_4\text{-}O)\{Cu^I_3(mpba)_3\}_2(H_2O)_4]$ (3). 20.0 mg (0.092 mmol) of H_2mpba, 21.5 mg (0.092 mmol) of $Cu(NO_3)_2 \cdot 2.5H_2O$ and 15.2 mg (0.070 mmol) of $Zn(CH_3COO)_2 \cdot 2H_2O$ were each dissolved in 1 mL of DMF. The three solutions were combined in a glass vial equipped with a screw cap. After a few minutes, a greenish precipitate formed. It was dissolved again by adding 10 μL of aqueous tetrafluoroboric acid (HBF_4, 48% min w/w). The glass vial was then sealed and transferred in a preheated oven at 90 °C for six days. The formed clear yellow trapezoidal prismatic crystals (Fig. S2a and b, ESI†) were filtered and washed three times with 3 mL DMF to obtain 28 mg (72%, based on the zinc salt). Calc. for $C_{144}H_{105}Cu_{12}N_{24}O_{23.67}Zn_7$ (3791.00 g mol^{-1}) C 45.62, H 3.19, N 8.87; found C 45.60, H 3.12, N 8.72%. IR: (KBr, Fig. S22, ESI†): $\tilde{\nu}$ = 3435 (br), 3067 (w), 3042 (w), 2953 (w), 2919 (w), 2854 (w), 2807 (w), 2568 (w), 2501 (w), 2361 (br), 2342 (br), 2273 (br), 1937 (w), 1813 (w), 1668 (s), 1608 (s), 1543 (s), 1492 (s), 1386 (br), 1284 (w), 1255 (w), 1179 (s), 1143 (w), 1094 (w), 1062 (w), 1034 (m), 1014 (w), 905 (w), 866 (w), 847 (w), 812 (w), 782 (s), 714 (s), 694 (w), 661 (w), 634 (m), 610 (w), 565 (w), 517 (s), 438 (w), 406 (w) cm^{-1}.

Author contributions

This manuscript was written through contributions of all the authors. All the authors have given approval to the final version of this manuscript.

Conflicts of interest

There are no conflicts to declare.

Acknowledgements

The authors thank Mrs Birgit Tommes for carrying out the FT-IR experiments and Annette Ricken for the AAS measurements. Dr. Christian Schürmann (Rigaku) and Dr. Tobias Stürzer (Bruker AXS) are thanked for their crucial crystal-screening and data-collection efforts. The Rigaku X-ray diffractometer was funded by the Deutsche Forschungsgemeinschaft (DFG, German Research Foundation) through project number 440366605. We thank the CeMSA@HHU (Center for Molecular and Structural Analytics@Heinrich Heine University) for recording the mass-spectrometric and the NMR-spectroscopic data.

Notes and references

1 O. K. Farha and J. T. Hupp, *Acc. Chem. Res.*, 2010, **43**, 1166–1175.
2 M. Taddei, *Coord. Chem. Rev.*, 2017, **343**, 1–24.
3 J. D. Evans, B. Garai, H. Reinsch, W. Li, S. Dissegna, V. Bon, I. Senkovska, R. A. Fischer, S. Kaskel, C. Janiak, N. Stock and D. Volkmer, *Coord. Chem. Rev.*, 2019, **380**, 378–418.
4 J. R. Long and O. M. Yaghi, *Chem. Soc. Rev.*, 2009, **38**, 1213–1214.
5 X. Han, S. Yang and M. Schröder, *Nat. Rev. Chem.*, 2019, **3**, 108–118.
6 S. R. Batten, N. R. Champness, X.-M. Chen, J. Garcia-Martinez, S. Kitagawa, L. Öhrström, M. O'Keeffe, M. Paik Suh and J. Reedijk, *Pure Appl. Chem.*, 2013, **85**, 1715–1724.
7 H.-C. J. Zhou and S. Kitagawa, *Chem. Soc. Rev.*, 2014, **43**, 5415–5418.
8 S. S. Y. Chui, S. M. F. Lo, J. P. H. Charmant, A. G. Orpen and I. D. Williams, *Science*, 1999, **283**, 1148–1150.
9 L. Xie, S. Liu, B. Gao, C. Zhang, C. Sun, D. Li and Z. Su, *Chem. Commun.*, 2005, 2402–2404.
10 L. H. Xie, J. B. Lin, X. M. Liu, W. Xue, W. X. Zhang, S. X. Liu, J. P. Zhang and X. M. Chen, *Sci. China: Chem.*, 2010, **53**, 2144–2151.
11 C. Ordonez, M. Fonari, J. Lindline, Q. Wei and T. Timofeeva, *Cryst. Growth Des.*, 2014, **14**(11), 5452–5465.
12 W. W. Lestari, M. Arvinawati, R. Martien and T. Kusumaningsih, *Mater. Chem. Phys.*, 2018, **204**, 141–146.
13 H. K. Chae, D. Y. Siberio-Pérez, J. Kim, Y. B. Go, M. Eddaoudi, A. J. Matzger, M. O'Keeffe and O. M. Yaghi, *Nature*, 2004, **427**, 523–527.
14 H. Furukawa, M. A. Miller and O. M. Yaghi, *J. Mater. Chem.*, 2007, **17**, 3197–3204.
15 I. M. Hauptvogel, V. Bon, R. Grünker, I. A. Baburin, I. Senkovska, U. Mueller and S. Kaskel, *Dalton Trans.*, 2021, **41**, 4172–4179.
16 Z. W. Wei, D. Q. Yuan, X. L. Zhao, D. F. Sun and H.-C. Zhou, *Sci. China: Chem.*, 2013, **56**, 418–422.
17 B. Chen, M. Eddaoudi, S. T. Hyde, M. O'Keeffe and O. M. Yaghi, *Science*, 2001, **291**, 1021–1023.
18 H. Furukawa, Y. B. Go, N. Ko, Y. K. Park, F. J. Uribe-Romo, J. Kim, M. O'Keeffe and O. M. Yaghi, *Inorg. Chem.*, 2011, **50**, 9147–9152.
19 K. Gedrich, I. Senkovska, N. Klein, U. Stoeck, A. Henschel, M. R. Lohe, I. A. Baburin, U. Mueller and S. Kaskel, *Angew. Chem., Int. Ed.*, 2010, **49**, 8489–8492.
20 H. Furukuwa, N. Ko, Y. B. Go, N. Aratani, S. B. Choi, E. Choi, A. O. Yazaydin, R. Q. Snurr, M. O'Keeffe, J. Kim and O. M. Yaghi, *Science*, 2010, **329**, 424–428.
21 J. Wang, C. Rao, L. Lu, S. Zhang, M. Muddassir and J. Liu, *CrystEngComm*, 2021, **23**, 741–747.
22 M. Wang, J. Liu, J. Jin, D. Wu, G. Yang, W.-Y. Zhang and Y.-Y. Wang, *CrystEngComm*, 2021, **23**, 663–670.
23 W. Li and J.-S. Tan, *J. Mol. Struct.*, 2021, **1237**, 130359.
24 R. A. Agarwal, *Cryst. Growth Des.*, 2021, **21**, 2046–2055.
25 M.-H. Tang, Y. Shi, X.-L. Jiang, H. Xu, Y. Ma and B. Zhao, *J. Mater. Chem. C*, 2021, **9**, 9643–9649.
26 E. Lopez-Maya, N. M. Padial, J. Castells-Gil, C. R. Ganivet, A. Rubio-Gaspar, F. G. Cirujano, N. Almora-Barrios, S. Tatay, S. Navalon and C. Marti-Gastaldo, *Angew. Chem., Int. Ed.*, 2021, **60**, 11868–11873.
27 J. Chen, T. Chen, S. Xiang, J. Zhang and Z. Zhang, *Z. Anorg. Allg. Chem.*, 2021, **647**, 1301–1304.
28 D. Sun, Y. Ke, T. M. Mattox, S. Parkin and H.-C. Zhou, *Inorg. Chem.*, 2006, **45**, 7566–7568.
29 D. Saha, R. Zacharia, L. Lafi, D. Cossement and R. Chahine, *Int. J. Hydrogen Energy*, 2012, **37**, 5100–5107.
30 S. Lee, H.-B. Bürgi, S. A. Alshmiri and O. M. Yaghi, *J. Am. Chem. Soc.*, 2018, **140**, 8958–8964.
31 J. Rong, W. Zhang and J. Bai, *CrystEngComm*, 2016, **18**, 7728–7736.
32 D. Sun, S. Ma, Y. Ke, D. J. Collins and H.-C. Zhou, *J. Am. Chem. Soc.*, 2006, **128**, 3896–3897.
33 S. Ma and H.-C. Zhou, *J. Am. Chem. Soc.*, 2006, **128**, 11734–11735.
34 R. R. R. Prasad, C. Pleass, A. L. Rigg, D. B. Cordes, M. M. Lozinska, V. M. Georgieva, F. Hoffmann, A. M. Z. Slawin and P. A. Wright, *CrystEngComm*, 2021, **23**, 804–812.
35 T. Liu, X. Shen, X. Shen, C. He, J. Liu and J.-J. Liu, *CrystEngComm*, 2021, **23**, 4667–4673.
36 K. Wang, S. Wang, J. Liu, Y. Guo, F. Mao, H. Wu and Q. Zhang, *ACS Appl. Mater. Interfaces*, 2021, **13**, 15315–15323.
37 A. M. Toader, M. C. Buta, F. Cimpoesu, A.-I. Toma, C. M. Zalaru, L. O. Cinteza and M. Ferbinteanu, *Chemistry*, 2021, **3**, 411–439.
38 N. V. S. Harisomayajula, S. Makovetskyi and Y.-C. Tsai, *Chem. – Eur. J.*, 2019, **25**, 8936–8954.
39 K. Singh, J. R. Long and P. Stavropoulos, *J. Am. Chem. Soc.*, 1997, **119**, 2942–2943.

40 (*a*) S. M.-F. Lo, S. S.-Y. Chui, L.-Y. Shek, Z. Y. Lin, X. X. Zhang, G.-H. Wen and I. D. Williams, *J. Am. Chem. Soc.*, 2000, **122**, 6293–6294; (*b*) X.-C. Huang, J.-P. Zhang, Y.-Y. Lin, X.-L. Yua and X. M. Chen, *Chem. Commun.*, 2004, 1100–1101; (*c*) K. Tomar, A. Verma and P. K. Bharadwaj, *Cryst. Growth Des.*, 2018, **18**, 2397–2404; (*d*) N. Grosjean, C. Descorme and M. Besson, *Appl. Catal., B*, 2010, **97**, 276–283.

41 C.-T. He, P.-Q. Liao, D.-D. Zhou, B.-Y. Wang, W.-X. Zhang, J.-P. Zhang and X.-M. Chen, *Chem. Sci.*, 2014, **5**, 4755–4762.

42 Z.-M. Ye, C.-T. He, Y.-T. Xu, R. Krishna, Y. Xie, D.-D. Zhou, H.-L. Zhou, J.-P. Zhang and X.-M. Chen, *Cryst. Growth Des.*, 2017, **17**, 2166–2171.

43 C. Heering, I. Boldog, V. Vasylyeva, J. Sanchiz and C. Janiak, *CrystEngComm*, 2013, **15**, 9757–9768.

44 S. Menzel, S. Millan, S.-P. Höfert, A. Nuhnen, S. Gökpinar, A. Schmitz and C. Janiak, *Dalton Trans.*, 2020, **49**, 12854–12864.

45 M. R. Bryant, A. D. Burrows, C. M. Fitchett, C. S. Hawes, S. O. Hunter, L. L. Keenan, D. J. Kelly, P. E. Kruger, M. F. Mahon and C. Richardson, *Dalton Trans.*, 2015, **44**, 9269–9280.

46 C. Wang, C. Liu, H.-R. Tian, L.-J. Li and Z.-M. Sun, *Chem. – Eur. J.*, 2018, **24**, 2952–2961.

47 (*a*) A. E. Martell and R. D. Hancock, in *Metal Complexes in Aqueous Solutions*, ed. J. P. Fackler, Plenum Press, 1996; (*b*) R. B. Martin, in *Encyclopedia of Inorganic Chemistry*, ed. R. B. King, Wiley, 1994, pp. 2185–2189; (*c*) R. H. Crabtree, in *Encyclopedia of Inorganic Chemistry*, ed. R. B. King, Wiley, 1994, p. 809.

48 B. Tu, Q. Pang, H. Xu, X. Li, Y. Wang, Z. Ma, L. Wenig and Q. Li, *J. Am. Chem. Soc.*, 2017, **139**, 7998–8007.

49 B. Tu, L. Diestel, Z.-L. Shi, W. R. L. N. Bandara, Y. Chen, W. Lin, Y.-B. Zhang, S. G. Telfer and Q. Li, *Angew. Chem., Int. Ed.*, 2019, **58**, 5348–5353.

50 J. Fritzsche, D. Denysenko, M. Grzywa and D. Volkmer, *Dalton Trans.*, 2017, **46**, 14907–14915.

51 S. Menzel, S.-P. Höfert, S. Öztürk, A. Schmitz and C. Janiak, *Z. Anorg. Allg. Chem.*, 2021, **647**, 803–808.

52 (*a*) S. M.-F. Lo, S. S.-Y. Chui, L.-Y. Shek, Z. Y. Lin, X. X. Zhang, G.-H. Wen and I. D. Williams, *J. Am. Chem. Soc.*, 2000, **122**, 6293–6294; (*b*) X.-C. Huang, J.-P. Zhang, Y.-Y. Lin, X.-L. Yua and X. M. Chen, *Chem. Commun.*, 2004, 1100–1101; (*c*) K. Tomar, A. Verma and P. K. Bharadwaj, *Cryst. Growth Des.*, 2018, **18**, 2397–2404; (*d*) N. Grosjean, C. Descorme and M. Besson, *Appl. Catal., B*, 2010, **97**, 276–283.

53 H. Li, M. Eddaoudi, T. L. Groy and O. M. Yaghi, *J. Am. Chem. Soc.*, 1998, **120**, 8571–8572.

54 J. Xiao, H. Zhou and A.-H. Yuan, *Acta Crystallogr., Sect. E: Struct. Rep. Online*, 2009, **65**, m1071.

55 Y. Mao and P. Y. Zavalij, *Acta Crystallogr., Sect. C: Struct. Chem.*, 2018, **74**, 1719–1724.

56 L. Zou, S. Yao, J. Zhao, D.-S. Li, G. Li, Q. Huo and Y. Liu, *Cryst. Growth Des.*, 2017, **17**, 3556–3561.

57 I. A. Baburin, V. A. Blatov, L. Carlucci, G. Ciani and D. M. Proserpio, *J. Solid State Chem.*, 2005, **178**, 2452–2474.

58 I. A. Baburin, V. A. Blatov, L. Carlucci, G. Ciani and D. M. Proserpio, *CrystEngComm*, 2008, **10**, 1822–1838.

59 V. A. Blatov, L. Carlucci, G. Ciani and D. M. Proserpio, *CrystEngComm*, 2004, **6**, 377–395.

60 L. Carlucci, G. Ciani and D. M. Proserpio, *Coord. Chem. Rev.*, 2003, **246**, 247–289.

61 L. Carlucci, G. Ciani, D. M. Proserpio, T. G. Mitina and V. A. Blatov, *Chem. Rev.*, 2014, **114**, 7557–7580.

62 E. Y. Alexandrov, V. A. Blatov and D. M. Proserpio, *CrystEngComm*, 2017, **19**, 1993–2006.

63 B. Liu, Y.-C. Qiu, G. Peng and H. Deng, *CrystEngComm*, 2010, **12**, 270–276.

64 R. Clerac, F. A. Cotton, L. M. Daniels, J. Gu, C. A. Murillo and H. C. Zhou, *Inorg. Chem.*, 2000, **39**, 4488–4493.

65 K. Singh, J. R. Long and P. Stavropoulos, *J. Am. Chem. Soc.*, 1997, **119**, 2942–2943.

66 A. W. Addison, T. N. Rao, J. Reedijk, J. van Rijn and G. C. Verschoor, *J. Chem. Soc., Dalton Trans.*, 1984, 1349–1356.

67 V. A. Blatov, A. P. Shevchenko and D. M. Proserpio, *Cryst. Growth Des.*, 2014, **14**, 3576–3586.

68 E. V. Alexandrov, V. A. Blatov, A. V. Kochetkov and D. M. Proserpio, *CrystEngComm*, 2011, **13**, 3947–3958.

69 J.-P. Zhang and S. Kitagawa, *J. Am. Chem. Soc.*, 2008, **130**, 907–917.

70 J. He, Y.-G. Yin, T. Wu, D. Li and X.-C. Huang, *Chem. Commun.*, 2006, 2845–2847.

71 E. V. Alexandrov, A. P. Shevchenko and V. A. Blatov, *Cryst. Growth Des.*, 2019, **19**, 2604–2614.

72 V. A. Blatov and D. M. Proserpio, *Acta Crystallogr., Sect. A: Found. Crystallogr.*, 2009, **65**, 202–212.

73 L. Sarkisov, R. L. Martin, M. Haranczyk and B. Smit, *J. Am. Chem. Soc.*, 2014, **136**, 2228–2231.

74 (*a*) S. Zhang and L. Zhao, *Nat. Commun.*, 2019, **10**, 4848; (*b*) A. Ahmed, C. M. Robertson, A. Steiner, T. Whittles, A. Ho, V. Dhanak and H. Zhang, *RSC Adv.*, 2016, **6**, 8902–8905; (*c*) H. Rupp and U. Weser, *Bioinorg. Chem.*, 1976, **6**, 45–59.

75 (*a*) S. Bera, S. Dhara, S. Velmurugan and A. K. Tyagi, *Int. J. Spectrosc.*, 2011, **2012**, 1–4; (*b*) X-ray photoelectron spectroscopy (XPS) reference page 27.08.2021, Link: http://www.xpsfitting.com/search/label/Zinc.

76 X-ray photoelectron spectroscopy (XPS) reference page 30.01.2022, Link: http://www.xpsfitting.com/2012/01/copper.html.

77 M. M. Sun and Y. Kim, *Bull. Korean Chem. Soc.*, 2001, **22**, 748–752.

78 M. C. Biesiner, *Surf. Interface Anal.*, 2017, **49**, 1325–1334.

79 L. Yin, T. Tsang, I. Adler and E. Yellin, *J. Appl. Phys.*, 1972, **43**, 3464–3467.

80 (*a*) D. Qu, M. Zheng, J. Li, Z. Xie and Z. Sun, *Light: Sci. Appl.*, 2015, **4**(e364), 1–8; (*b*) F. Arcudi, L. Dordevic and M. Prato, *Angew. Chem., Int. Ed.*, 2016, **55**, 2107–2112.

81 Thermo scientific XPS simplified, 18.08.2021, Link: https://xpssimplified.com/elements/oxygen.php.

82 S. U. Awan, S. K. Hasanain, J. Rashid, S. Hussain, S. A. Shah, M. Z. Hussain, M. Rafique, M. Aftab and R. Khan, *Mater. Chem. Phys.*, 2018, **211**, 510–521.

83 (*a*) W. He, R. Ifraemov, A. Raslin and I. Ho, *Adv. Funct. Mater.*, 2018, **28**, 1707244; (*b*) Z. Zude, Z. Xiong, Z. Tao, Y. Humaing and L. Qingliang, *J. Mol. Struct.*, 1999, **478**, 23–27.

84 (*a*) P. R. Spackman, M. J. Turner, J. J. McKinnon, S. K. Wolff, D. J. Grimwood, D. Jayatilaka and M. A. Spackman, *J. Appl. Crystallogr.*, 2021, **54**, 1006–1011; (*b*) CrystalExplorer21.5, © 2005–2021, University of Western Australia, 2021, **https://crystalexplorer.net/**.

85 Mercury 2021.2.0, Program for Crystal Structure Visualisation, Exploration and Analysis from the Cambridge Crystallographic Data Center, Copyright CCDC 2001–2021, **http://www.ccdc.cam.ac.uk/mercury/**.

86 Mercury 4.0: from visualization to analysis, design and prediction,C. F. Macrae, I. Sovago, S. J. Cottrell, P. T. A. Galek, P. McCabe, E. Pidcock, M. Platings, G. P. Shields, J. S. Stevens, M. Towler and P. A. Wood, *J. Appl. Crystallogr.*, 2020, **53**, 226–235.

87 A. L. Spek, Structure Validation in Chemical Crystallography, *Acta Crystallogr., Sect. D: Biol. Crystallogr.*, 2009, **65**, 148–155; A. L. Spek, PLATON– A Multipurpose Crystallographic Tool, Utrecht University, Utrecht, The Netherlands, 2008; L. J. Farrugia, PLATON for Windows implementation, Version 280317, University of Glasgow, Scotland, 2020.

88 J. Rouquerol, F. Rouquerol, K. S. W. Sing, P. Llewellyn and G. Maurin, *Adsorption by Powders and Porous Solids: Principles, Methodology and Applications*, Academic Press, 2014.

89 M. Thommes, K. Kaneko, A. V. Neimark, J. P. Olivier, F. Rodriguez-Reinoso, J. Rouquerol and K. S. W. Sing, *Pure Appl. Chem.*, 2015, **87**, 1051–1069.

90 A. Nuhnen and C. Janiak, *Dalton Trans.*, 2020, **49**, 10295–10307.

91 K. Sumida, D. L. Rogow, J. A. Mason, T. M. McDonald, E. D. Bloch, Z. R. Herm, T.-H. Bae and J. R. Long, *Chem. Rev.*, 2012, **112**, 724–781.

92 A. Das and D. M. D'Alessandro, *CrystEngComm*, 2015, **17**, 706–718.

93 D. M. D'Alessandro, B. Schmit and J. R. Long, *Angew. Chem., Int. Ed.*, 2010, **49**, 6058–6082.

94 C. F. Macrae, I. J. Bruno, J. A. Chisholm, P. R. Edgington, P. McCabe, E. Pidcock, L. Rodriguez-Monge, R. Taylor, J. van de Streek and P. A. Wood, *J. Appl. Crystallogr.*, 2008, **41**, 466–470.

95 APEX3, SAINT, SADABS and XP, Bruker AXS Inc., Madison, Wisconsin, USA, 2019.

96 Bruker, TWINABS-2012/1, Bruker AXS Inc., Madison, Wisconsin, USA, 2012.

97 G. M. Sheldrick, *Acta Crystallogr., Sect. A: Found. Adv.*, 2015, **71**, 3–8.

98 K. Brandenburg, *Diamond Crystal and Molecular Structure Visualization, Version 4.6.6*, Crystal Impact GbR, Bonn, Germany, 1997–2021.

Electronic Supplementary Material (ESI) for CrystEngComm.
This journal is © The Royal Society of Chemistry 2022

Electronic Supplementary Information (ESI)

Metal-organic framework structures of fused hexagonal motifs with cuprophilic interactions of a triangular Cu(I)$_3$(pyrazolate-benzoate) metallo-linker

Saskia Menzel,[a,#] Tobias Heinen,[a,#] Ishtvan Boldog,[a] Thi Hai Yen Beglau,[a] Shanghua Xing,[a,b] Alex Spieß,[a] Dennis Woschko[a] and Christoph Janiak[a]*

[a] Institut für Anorganische Chemie und Strukturchemie, Heinrich-Heine-Universität Düsseldorf, Universitätsstraße 1, 40225 Düsseldorf, Germany. E-mails: janiak@uni-duesseldorf.de

[b] Hoffmann Institute of Advanced Materials, Shenzhen Polytechnic, 7098 Liuxian Blvd, Nanshan District, Shenzhen 518055, China

[#] These authors contributed equally.

* *Corresponding authors*: C. Janiak Tel.: +49 211 81 12286; fax: +49 211 81 12287.

Additional E-Mail addresses: Saskia.menzel@hhu.de, T.Heinen@hhu.de, ishtvan.boldog@gmail.com, boldogi@hhu.de, beglau@hhu.de, shanghua.xing@hhu.de, xingshanghua@126.com, alex.spiess@hhu.de, dennis.woschko@hhu.de

Contents

1. Synthesis

Reagents and solvents were obtained from commercial sources and used as received without further purification. $Cu(NO_3)_2 \cdot 2.5H_2O$ (98%) was purchased from Alfa Aeser, $Zn(NO_3)_2 \cdot 4H_2O$ (98%) from ALFA Chemistry and $Zn(CH_3COO)_2 \cdot 2H_2O$ (98%) from VWR. *N,N*-dimethylformamide (DMF) p.a. were obtained from Riedel-de Haën, tetrafluoroboric acid (HBF_4) (48 wt% in H_2O) from Sigma-Aldrich and conc. nitric acid from Chemsolute. The synthesis of 4-(3,5-dimethyl-1*H*-pyrazol-4-yl)benzoic acid (H_2mpba), was carried out according to the literature procedure.[1]

The results of synthetic screening and synthesis of the final phase pure compounds are summarized in Table S1 and Scheme S1, S2.

Table S1 Summary of the synthetic conditions for the mixture, containing the phases **1**-**3** in single crystal form, and the phase pure compounds **1**, **2** (powder) and **3**.

	Metal salt 1	Metal salt 2	Molar ratio M1:M2:L	Solvent	HBF_4 [µL]	Temp. [°C]	Time [d]
1-3 mixed [a]	$Cu(NO_3)_2 \cdot 2.5H_2O$	$Zn(NO_3)_2 \cdot 4H_2O$	1:0.66:1	DMF	/	80,90	4,7
1	$Cu(NO_3)_2 \cdot 2.5H_2O$	$Zn(NO_3)_2 \cdot 4H_2O$	1:0.66:1	DMF	0	90	6
2 [b]	$Cu(NO_3)_2 \cdot 2.5H_2O$	$Zn(CH_3COO)_2 \cdot 2H_2O$	1:0.75:1	DMF	30	90	9
3	$Cu(NO_3)_2 \cdot 2.5H_2O$	$Zn(CH_3COO)_2 \cdot 2H_2O$	1:0.75:1	DMF	10	90	6

[a] The conditions correspond to concomitant formation of phases **1**-**3**, containing single-crystals, suitable for SCXRD determination. Phase **2** is a minor component and could be observed in single-crystal form only under the given conditions.

[b] The phase is represented by a powder.

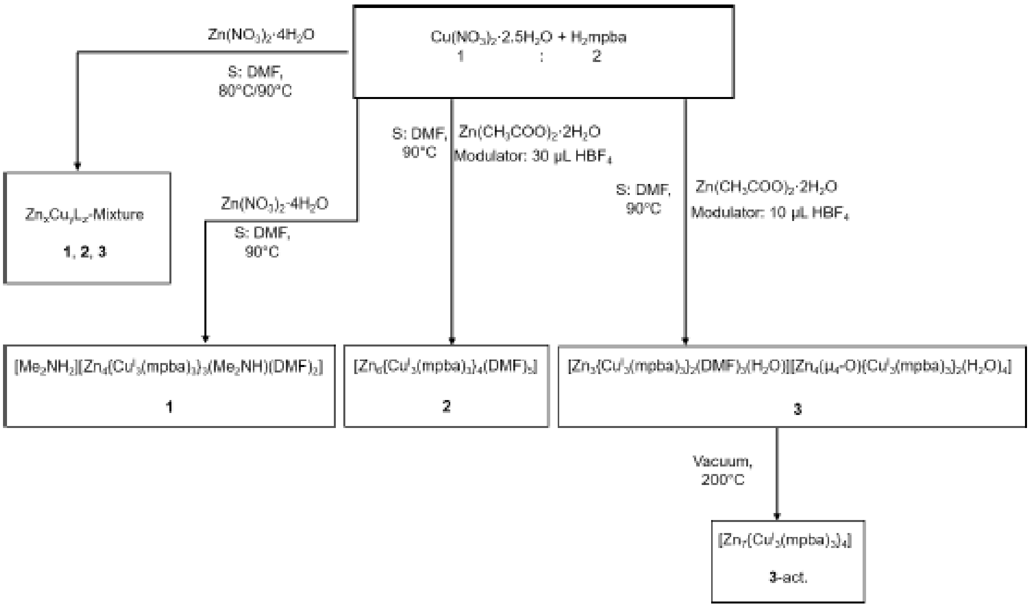

Scheme S1 Synthesis scheme of the compounds **1**-**3**.

*Preparation of the **1**-**3** mixture, containing **2** in single crystal form, suitable for SCXRD analysis::*

20.0 mg (0.092 mmol) of H_2mpba, 21.5 mg (0.092 mmol) of $Cu(NO_3)_2 \cdot 2.5H_2O$ and 16.9 mg (0.065 mmol) of $Zn(NO_3)_2 \cdot 4H_2O$ were separately dissolved in 1 mL of *N,N*-dimethylformamide (DMF). The solutions were then combined in a glass vial equipped with a screw cap, sealed and transferred in a preheated oven and heated 80 °C for four days and up to 90 °C for seven days. A mixture of clear yellow block-shaped crystals and a considerable amount of green amorphous admixture was obtained. The share of **2** varied strongly and in many cases, it was rather small compared to the content of phases **1** and **3**, so that it was not possible to separate a macroscopic amount for analysis.

*Synthesis optimization studies for compounds **1**-**3**:*

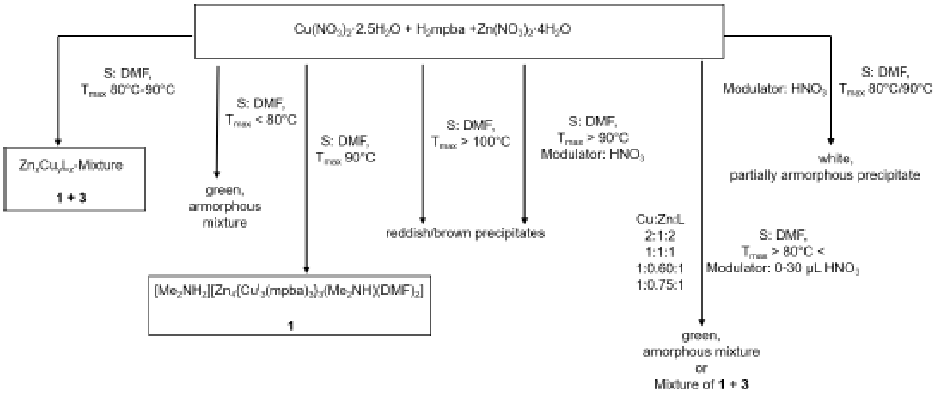

Scheme S2 Results of the optimization studies towards phase-pure compounds (L = H_2mpba).

The optimization studies included the variation of temperature (both maximum temperature and temperature-time profiles), concentration, type and ratio of the precursors, the use of HNO_3 or HBF_4 as an additive . First, the temperature was varied from 40 °C upwards to 110 °C. Temperatures below 80 °C led to amorphous products. Temperatures above 100 °C led to brown/reddish precipitates. At 90 °C, phase-pure **1** was formed. All other temperatures resulted in a mixture of **1** and 3 according to the powder diffractogram and optical examination under the microscope. Next, the molar ratios of Cu:Zn:L (L = H_2mpba) were systematically varied in small steps from 2:1:2 via 1:1:1 to 1:0.75:1 and the various solutions were placed in a preheated oven at 90°C for crystallization. As a result of varying the molar ratios, both amorphous products and mixed phases were obtained. Subsequently, the different molar ratios were also tested at different temperature profiles (T_{max}, time at T_{max} and cooling rates were varied), which led to no improvement regarding phase purity. The use of conc. HNO_3 as a modulator always resulted in a white precipitate at temperatures between 80/90 °C and a reddish/brown precipitation at temperatures above 100 °C. Last but not least, an attempt was made to obtain 2 by changing the starting material $Zn(NO_3)_2 \cdot 4H_2O$ to zinc acetate. Here, the same systematic experiments were carried out as described above. By the use of Cu:Zn:L in a molar ratio of 1:0.75:1 and by adding 10 µL of a 48% min w/w aqueous solution of tetrafluoroboric acid (HBF_4). Phase pure 3 could be obtained at a crystallization temperature of 90 °C for six days. By adding 30 µL HBF_4 and longer synthesis time, 2 could be obtained as an off-white powder (PXRD pattern given in Fig. S3).

2. Single crystal micrographs

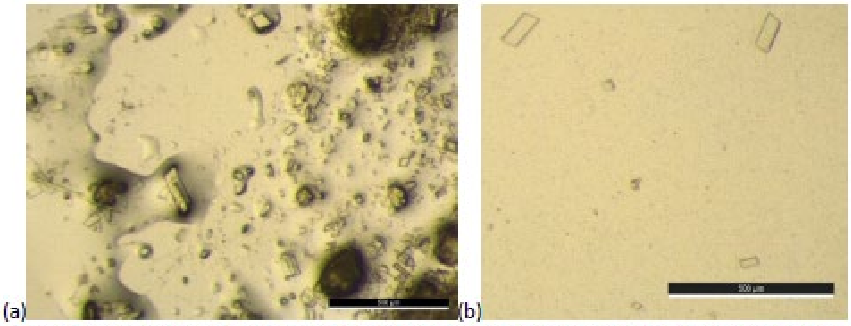

Fig. S1 Micrograph images of crystals of **1**: (a) overview; (b) selected crystals for single crystal X-ray structure determination.

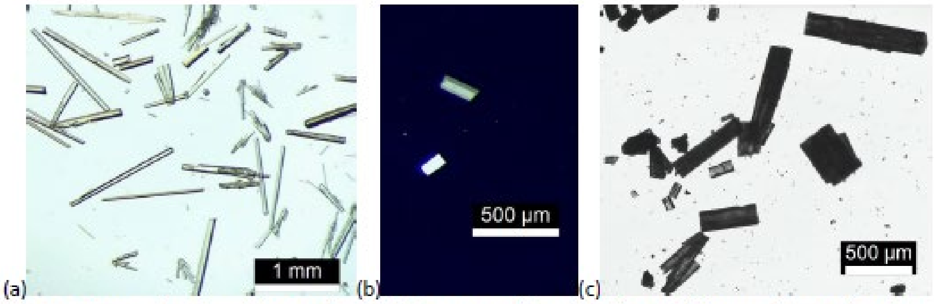

Fig. S2 Micrograph images of crystals of **3**: (a) overview; (b) selected crystals for single crystal X-ray structure determination; (c) crystals after drying.

3. Powder X-ray diffractograms

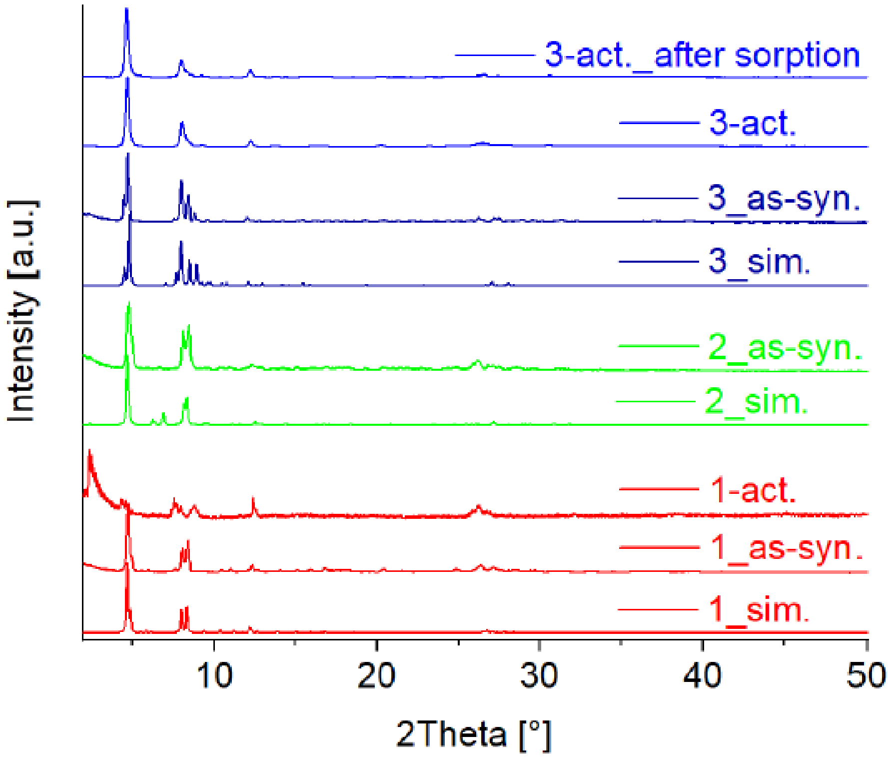

Fig. S3a PXRD patterns of the as-synthesized **1**, 2, 3 and their simulated PXRD patterns based on the crystal structure. The activated compound 3-act. and 3-act. after gas sorption measurements. Furthermore, the PXRD shows an example of the activation attempt of **1** (1-act.).

In order to access the purity of the samples a Le Bail fitting was performed (the Le Bail fitting tests the correctness of the cell dimensions and symmetry). As the primitive cell dimensions are principally different – see the next chapter – the Le Bail fitting was more practical compared to Rietveld refinement (the latter is quite cumbersome for such a large cells: the reflections are strongly overlapping after 2θ = 15°, and while selected regions could be fit with minimal adjustments, it is problematic to cover a significant angular range, assuming the only realistic possibility when most of the atom coordinates and thermal displacement parameters are fixed).

The Le Bail fittings (Fig. 3b,c,d) were performed using the Jana 2006 software. The short conclusion, also based on the change of the refined cell parameters, is that **1** is pure, **2** is quite non-pure, and **3** contains some amount of impurities.

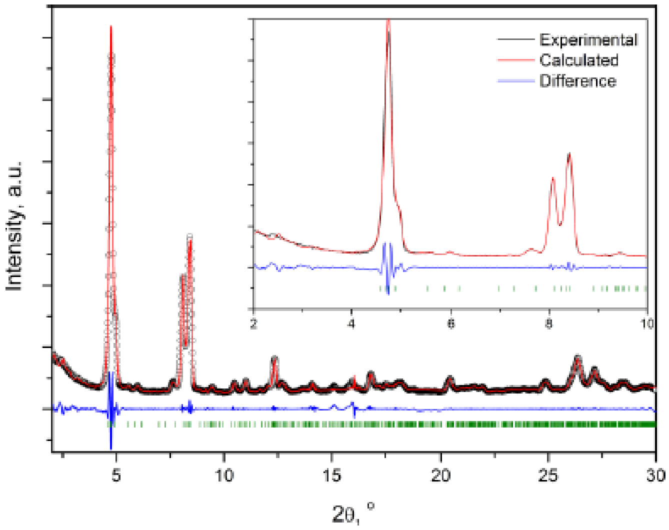

Fig. S3b Le Bail fit for**1**, Rp = 2.75% (2θ = 2-30°).

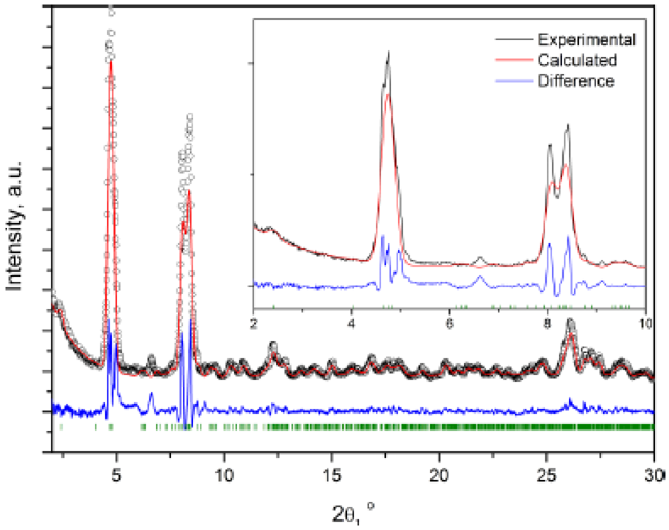

Fig. S3c Le Bail fit for 2, Rp = 11.11% (2θ =2-30°). The sample is of low purity.

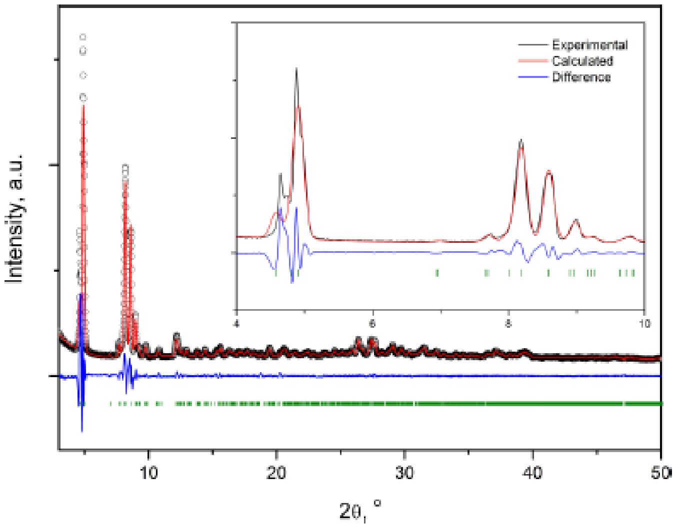

Fig. S3d Le Bail fit for 3, Rp = 4.24% (2θ = 2-50°). A significant amount of impurities is assumed to be present.

4. Crystallographic data and structure refinement details

The structures were solved by ShelXS and refined by ShelXL using Olex2 [2] (Table S2).

General refinement principles. Multiple fragments of the structures of **1**-**3** feature disorder, which was explicitly modelled in the case of the Zn atoms (**1**, **3**) or the $Me_2NH_2^+$ counter ion (**1**), as well as in the case of the particularly well resolved disorder of the mpba ligand (**1**-**3**). When the disorder contributions in the latter were small, the ligand molecules were refined using the averaged positions of the constituent atoms, with the interatomic distances restrained using DFIX/SAME/SADI/FLAT restraints (see cif files) and the thermal displacement factors using RIGU/SIMU restraints (see cif files). Several restraints were used to establish chemical and crystallographic satisfying structures. At some points minor disorders were ignored to simplify the overall structure and to emphasize the topological significance. The coordinated solvent molecules were interpreted as belonging to DMF or water molecules (the occupancies were not refined, but fixed at rounded approximate value, typically at 0.5). The non-coordinated solvent molecules, occupying the pores were modelled by the SQUEEZE (Platon) procedure (structures **1** and **3**) or by solvent masking as implemented in OLEX 2 (structure **2**). The hydrogen atoms in all structures were positioned geometrically and refined using riding models with $U_{iso}(H)$ values set equal to $1.2 \cdot U_{eq}(CH_{arom.})/U_{eq}(NH)$ or $1.5 \cdot U_{eq}(CH_3)$.

Table S2 Crystal data and structure refinement for **1**, **2** and **3**.

Compound	**1**	**2**	**3**
CCCD no.	2105164	2105165	2105166
Empirical formula	$C_{118}H_{119}Cu_9N_{22}O_{20}Zn_4$	$C_{159}H_{155}Cu_{12}N_{29}O_{29}Zn_6$	$C_{153}H_{136}Cu_{12}N_{27}O_{32.67}Zn_7$
	$C_{108}H_{90}Cu_9N_{18}O_{18}Zn_4$, C_2H_7N, C_2H_8N, 2(C_3H_7NO)	$C_{144}H_{120}Cu_{12}N_{24}O_{24}Zn_6$, 5($C_3H_7NO$)	$C_{144}H_{105}Cu_{12}N_{24}O_{23.67}Zn_7$, O, 5($H_2O$), 3($C_3H_7NO$)
$M/g \cdot mol^{-1}$	2998.68	4090.81	4095.71
Crystal dimensions/mm	0.09×0.08×0.04	0.25×0.11×0.04	0.20×0.11×0.07

T/K	100	100	100
Crystal system	Triclinic	Triclinic	Monoclinic
Space group	P-1	P-1	Cc
a /Å	20.2449(16)	14.5957(2)	41.6099(5)
b /Å	21.975(2)	21.9429(2)	13.3781(1)
c /Å	22.074(2)	37.0299(3)	44.2601(5)
α /°	119.388(3)	88.0398(3)	90.0522(6)
β /°	93.018(3)	82.7812(8)	117.8069(15)
γ /°	104.938(3)	82.6290(7)	89.9655(7)
V /Å^3	8078.2(12)	11666.43(18)	21792.8(5)
Z	2	2	4
μ/ mm^{-1}	1.80	2.25	2.54
F(000)	3044	4144	8250
Max./min. transmission	0.911/0.834	1.000/0.578	0.840/0.595
Meas., indep., obs. reflections	34651, 34651, 19641	169664/41507/36374	152524/35511/30944
R_{int}	0.0515	0.031	0.028
Data/restraints/parameters	34651/376/1556	41507/426/2418	35511/1210/2170
Max./min. $\Delta\rho$ [a] /e Å^{-3}	0.95, −0.82	1.45, -1.91	0.84, -0.81
R, wR(F^2), S [I> 2σ (I)] [b]	0.075, 0.208, 1.050	0.064/0.2105/1.156	0.079/0.234/1.07
R, wR(F^2), S [all data] [b]	0.144, 0.179, 1.054	0.069/0.2160/1.020	0.083/0.244/8.230
Squeeze void count electrons [c]	604	1131	1894

[a] Largest difference peak and hole. [b] $R_1 = [\sum(||F_o| - |F_c||)/\sum|F_o|]$; $wR_2 = [\sum[w(F_o^2 - F_c^2)^2]/\sum[w(F_o^2)^2]]^{1/2}$. Goodness-of-fit = $[\sum[w(F_o^2 - F_c^2)^2]/(n - p)]^{1/2}$. [c] Per unit cell.

5. Additional crystallographic images and figures

Compound **1**:

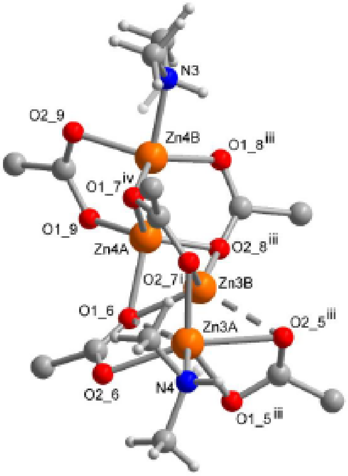

Fig. S4 Details of the Zn/Me_2NH, $Me_2NH_2^+$ disorder in **1** showing both major and minor components. For the Zn atoms these components are denoted with A (81%) and B (19%) suffixes. The ZnA,B atoms are alternating between two positions corresponding to pseudo-chelating carboxylate groups. The Me_2NH and $Me_2NH_2^+$ species are site sharing with the additional hydrogen of the latter shown half-transparent. When the Zn atom is located in the vicinity of the N atom, the latter represents the amine, while in the alternative case, it represents the charge-compensating dimethylammonium cation forming H-bonds with the non-coordinated O-atoms of the carboxylates, Symmetry codes: (i) x, y+1, z+1; (iii) x, y, z+1; (iv) x, y-1, z.

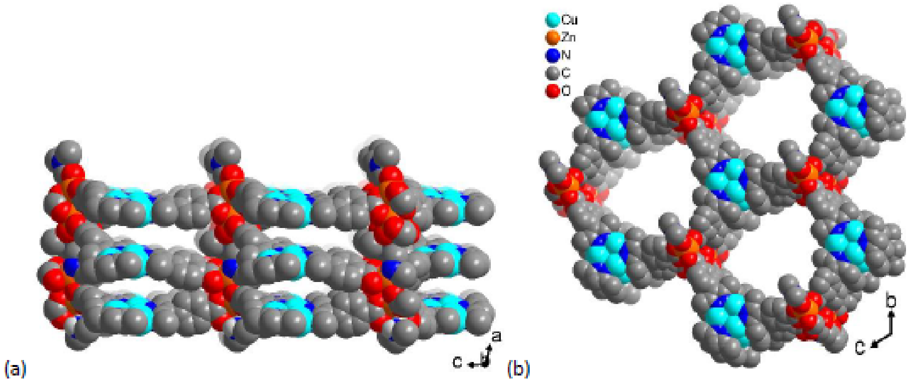

(a) (b)

Fig. S5 Space-filling representation of (a) side-view and (b) on-top view (along *b* and *a* axis, respectively) of a section of a single 3-layer slab in **1**. Only the major component of the disordered Zn atoms was used for the drawing. Hydrogen atoms are not shown for clarity, except for the $Me_2NH_2^+$ cation, which is site-sharing with the Me_2NH ligand.

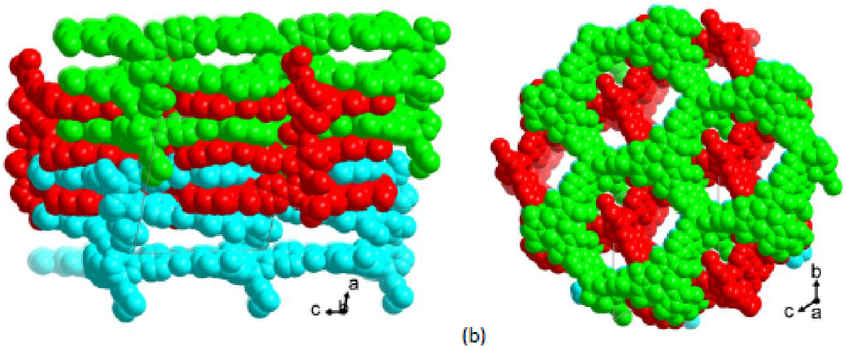

(a) (b)

Fig. S6 Space-filling representation of (a) side-view and (b) on-top view (along *b* and *a* axis, respectively) of a section of three polycatenated 3-layer slabs in **1**. The three slabs are differentiated by their green, red and cyan color. Hydrogen atoms are not shown for clarity. Only the major contribution to the disorder of Zn3 and Zn4 was used in the drawing.

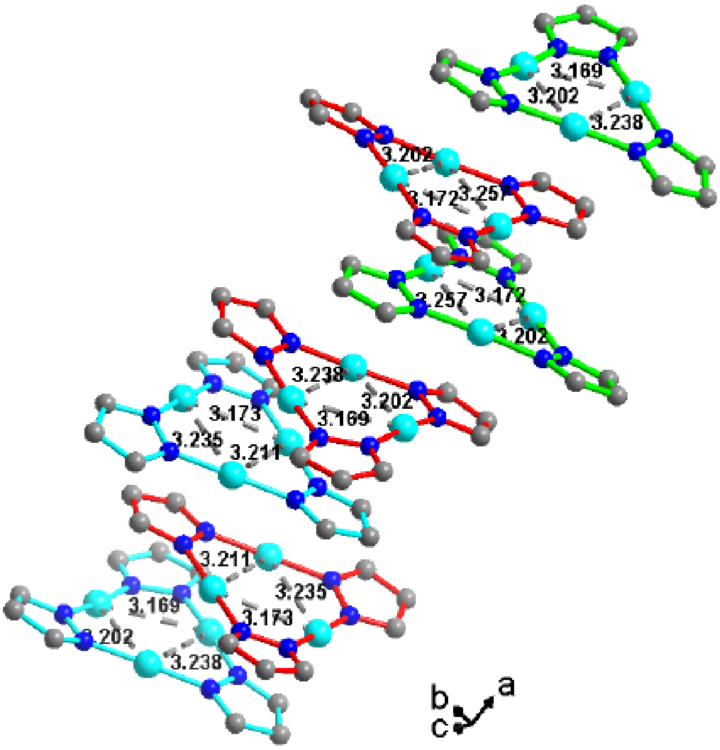

Fig. S7 $Cu^I\cdots Cu^I$ distances (grey dashed lines, in Å) within the $\{Cu^I_3(pz)_3\}$ moieties of the metallo-linkers in **1**.

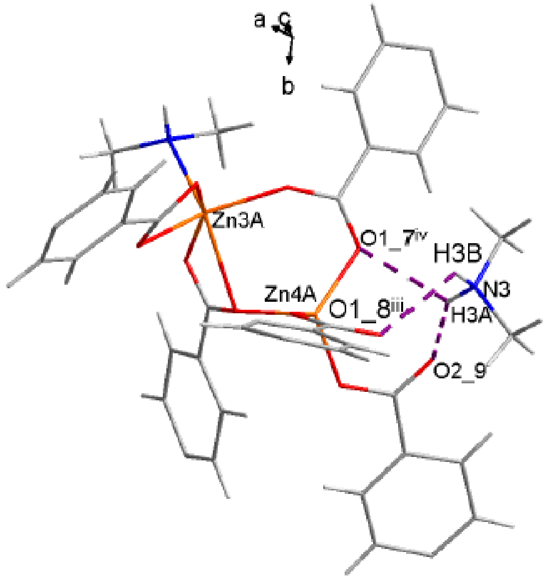

Fig. S8 Representation of the N-H···O hydrogen bonds in **1** (violet-dashed lines). Symmetry codes: (iii) =x, y, 1+z (iv) = x, -1+y, z. The dimethylammonium cation forms three N-H···O hydrogen bonds with the carboxylate groups in the major A component of the disorder; the B component features a similar set of H-bonds). Table S3 summarizes the N-H···O hydrogen bonding.[3]

Table S3 N-H···O hydrogen bonding interactions.

D-H··A	D-H/Å	H··A /Å	D··A /Å	D-H··A /°
N3-H3A ··O1_7^{iv}	0.91	2.56	3.19	127
N3-H3A ··O2_9	0.91	1.90	2.70	145
N3-H3B ··O1_8^{iii}	0.91	2.34	2.82	113

Symmetry codes: (iii) =x, y, 1+z; (iv) = x, -1+y, z.

Compound 2:

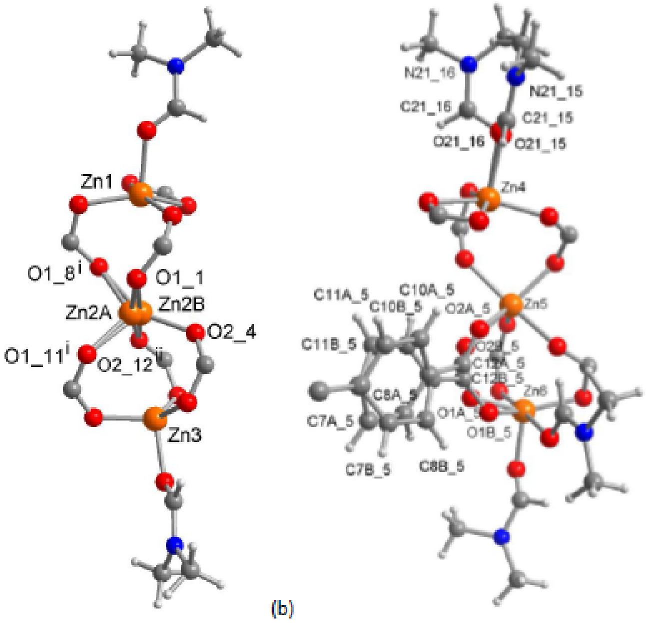

(a) (b)

Fig. S9 Details of the (a) Zn2 and (b) carboxylate and DMF disorder around Zn5/Zn6 and Zn4, respectively, in **2**. The contributions are Zn2A - 66(4)%, Zn2B - 34(4)%, carboxylate A_5 - 56.6(9)%, carboxylate B_5 - 34.4(9)%, DMF_15 - 85.9(8)%, DMF_16 - 14.1(8)%. Symmetry codes: (i) x-1, y-1, z+1; (ii) x-1, y, z+1.

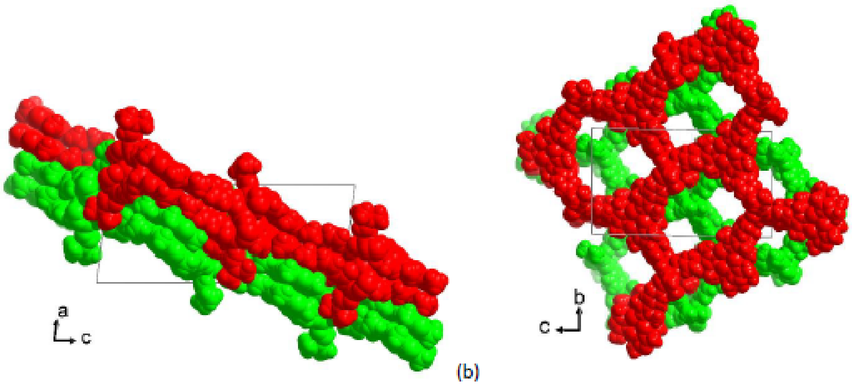

(a) (b)

Fig. S10 Space-filling representation of (a) side-view and (b) on-top view (along *b* and *a* axis, respectively) of two adjacent 2-layer slabs in **2**. The two stacks are differentiated by their green and red color. Only the major components of the disorder was used in the drawing.

Compound 3:

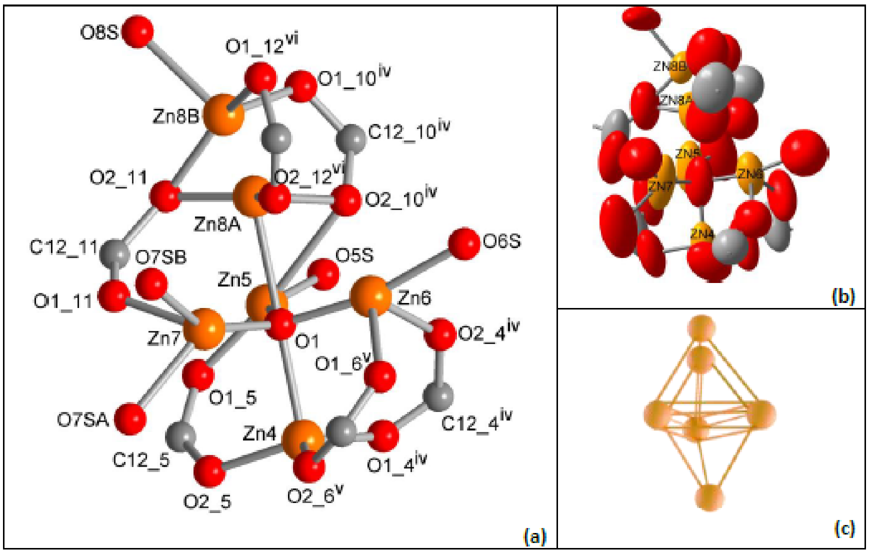

Fig. S11 The disorder model for the $\{Zn_4(\mu_4\text{-}O)(O_2C\text{-})_6\}$ cluster in 3. All Zn atoms in this SBU are refined with an occupation factor of 80%; the Zn8A and Zn8B components of the Zn8 atom have refined occupation factors of 32.8(7)%, and 47.2(7)%, respectively. (a) Ball and stick representation with atom numbering scheme; Symmetry codes: (iv) x+1/2, y+1/2, z; (v) x+1/2, -y-3/2, z+1/2; (vi) x+1/2, -y-1/2, z+1/2. (b) thermal ellipsoid plot. (c) Simplified interpretation of the disorder as consisting of three overlapping $\{Zn_4(\mu_4\text{-}O)(O_2C\text{-})_6\}$ clusters.

6. Topological analysis

Table S4 Topological overview of structures 1-3.

	Dimensionality [interpenetration]; node stoichiometry/ correspondence [a]		Point symbol [b]	Vertex symbol	Topolo-gical type	TD10
1	2D [2D+2D, parallel, 2-fold. ...{2D}∩{2D}∩... → 3D *via* infinite polycatenation]; (3-c)(3-c)(3-c)(4-c)(5-c) / (C1) (C2) (C3) (Z1) (Z2)	(C1),(C2): (Z2): (C3): (Z1):	{4.6^2}2 {4^2.6^6.8^2} {6^3} {6^5.8}	[4.6.6][4.6(2).6(2)] [4.4.6.6.6.6.6.6(2).8.8] [6.6.6(2)] [6.6.6.6.6.8(6)]	-	365
2 [c]	2D; (3-c)$_2$(6-c) (C1-4)(Z1,2)	(C1-4): (Z1,2):	{4^3}2 {4^3.6^12}	[4.4.4]; [4(2).4(2).4(2).6(2).6(2).6(2).6(2).6(2).6(2).6(2).6(2).6(2).6(2).6(2).6(2)]	3,6L66 [d]	251
3	3D [3D+3D, 2-fold] (3-c)2(6-c) (C1,2)(Z1) = (C3,4)(Z2)	(C1-4): (Z1,2):	{4.6.8} {4^2.6^5.8^5.10^3}	[4.6(2).8(6)] [4.4.6.6.6.6.6(2).8(2).8(2).8(3).8(3).8(8).10(4).10(10).10(10)]	sqc-3,6-Fdd2-2 (sqc subnet) [e]	1641

[a] C# - Cu based node, Z# - Zn-based node (Z# corresponds to the numeration in Fig. 9 in the main text).

[b] The nodes are listed in the order of appearance in the point symbol, given in ascending order of the ring sizes.

[c] Alternative interpretation: 'dual-strand' hexagonal network, which is formed from two stacked hexagonal networks with ½ of the alternating 3-c vertices merged in 6- c vertices.

[d] 32 representatives of the 3,6L66 net are listed by the topcryst.com resource (CSD codes are): APEBAZ*, BETXUW*, BOXVIV02*, BOXVOB*, BOXVUH*, CAXTOM*, CIKQEU*, COFCAD, COFCEH, DUMZAP*, EPEGUD*, GICNIR*, GICNOX, GOYCOP*, IRUYEB02 (erroneous assignment), ITOKAF, JUNLAI, JUNLAI, LAGKUA*, LEZMAG*, NALKIX*, PELVIO (erroneous assignment), POQSEW*, QELDIX*, SEQRUD*, TAFWOP*, TAFWUV*, UGONEL, VUCHIN*, ZESQIZ*, ZESQIZ01*, ZUMKUQ* (the entries marked by * are coordination polymers based on a tritopic near-triangular carboxylate ligand and approximately following the two stacked hcb network morphology, similar to the one found in 2).

[e] 4,8-c sqc derived net; sqc/I 41/a m d->F d d 2 (a-b,a+b,c; 0,3/4,1/4), bond sets: 2,3,4 (regarding net relations, see ref. [4]).
5 representatives of the sqc-3,6-Fdd2-2 net are listed by the topcryst.com resource: DOLDUE, BUVQIT, QUXZIV, OCOTUX, GOFNEV.

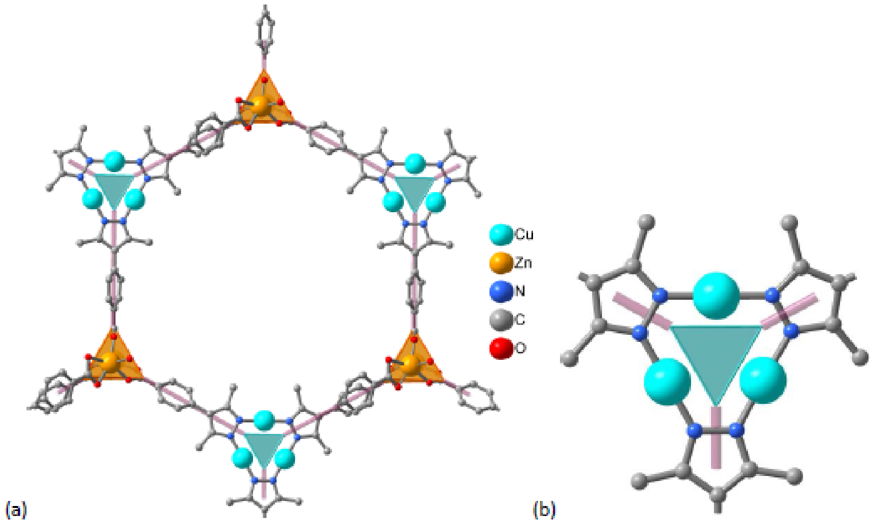

Fig. S12 (a) The dominant hexagonal motif in the structures of **1-3** shown on the example of a fragment in the structure of **1**. (b) The common SBU is the 3-c {$Cu_3(Me_2pz)_3$} motif, while the "extended" Zn-based SBUs are variable. The higher connectedness of the latter ensures additional connectivity between the hexagonal motifs.

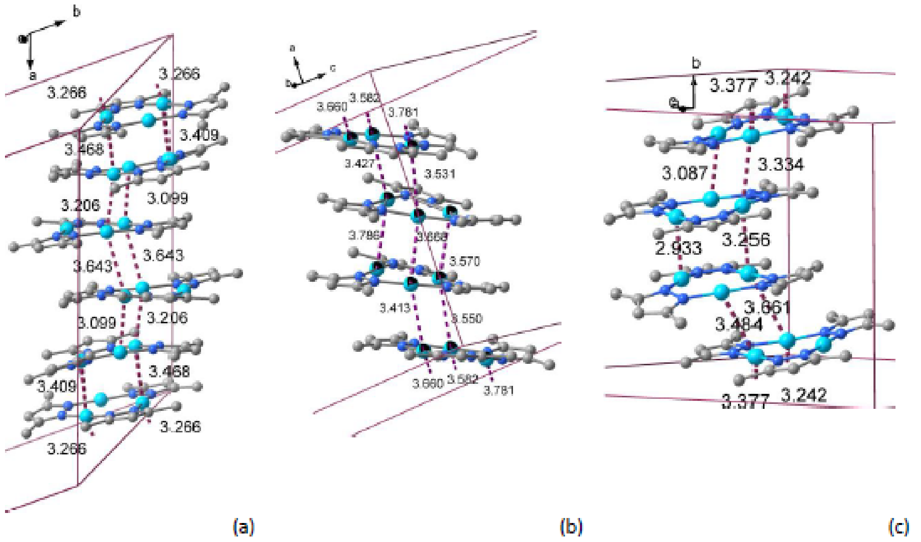

Fig. S13 Comparison of the stacking of the {$Cu_3(pz)_3$} units which is an immanent feature of the structures of **1** (a), **2** (b) and **3** (c). The stacked columns are infinite (*i.e.* there are no gaps) and similar regarding the 'staggered' orientation of the neighboring units. Hence, the columns could be regarded as approximately ABAB type for all the structures, even if the crystallographically independent part of the columns contains 6, 4, and 4 units for **1**, **2** and **3**, respectively.

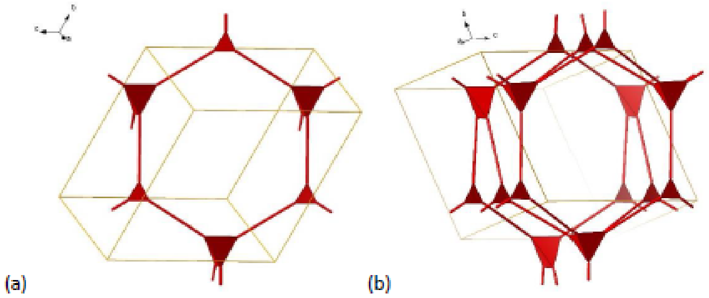

Fig. S14 The topological representation of a separated hexagonal ring (a), and the mode of their combination, or 'fusing', (b) in the structure of **1**.

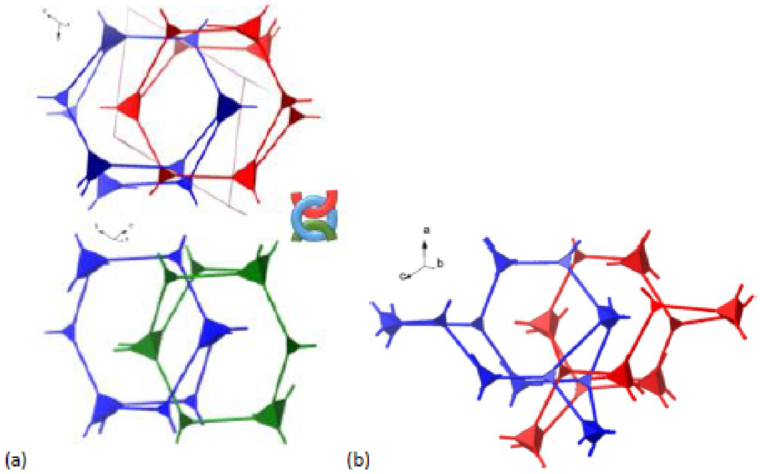

Fig. S15 Interlocked local fragments of the structures of **1** (a) and 3 (b) illustrating the interpenetration.

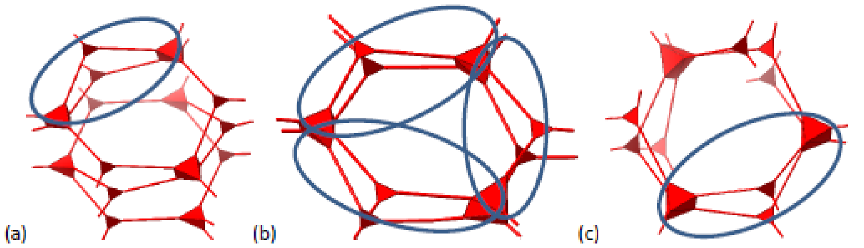

Fig. S16 Highlighting (encircling) of the 4-rings in the fused **hcb** nets of (a) **1**, (b) 2 and (c) 3. In **2** only 4- and 6-rings are observed as smallest cycles. In **1** and **3** also larger rings appear upon the 'fusing' of the **hcb** layers.

7. Atomic absorption spectroscopy

For atomic absorption spectroscopy measurements (AAS), the samples were dissolved by aqua regia or conc. HCl. For this purpose, a carefully weighted amount of 2.10 mg of sample **1** was mixed with 5 mL of aqua regia and heated to reflux. Heating was continued until only a white residue remained, which could be taken up in 1 mL of conc. HNO_3. The solution was transferred to a 20 mL graduated flask and filled up with Millipore water to the calibration mark. 1 mL of this stock solution was then taken and diluted again in a 20 mL volumetric flask. For the measurement of sample **3**, 2.10 mg of the sample was dissolved in 6 mL conc. HCl with constant heating and stirring. The solution was transferred to a 20 mL graduated flask and filled up with Millipore water to the calibration mark. 1 mL of this stock solution was then diluted again in a 20 mL volumetric flask.

Table S5 Atomic absorption spectroscopy measurement and calculations.

Compound	weighted mass	c(Cu) measured	c(Zn) measured	m(Cu)	m(Zn)	Cu	Zn	Molar ratio found [Cu:Zn]	Molar ratio calculated [a] [Cu:Zn]
	[mg]	[mg/L]	[mg/L]	[mg]	[mg]	found [wt%]	found [wt%]		
1	2.10	0.72	0.33	0.29	0.13	13.8	6.19	1:0.44	9:4 = 1:0.44
3	2.10	0.83	0.44	0.33	0.18	15.7	8.57	1:0.53	12:7 = 1:0.58

[a] based on SCXRD structure

8. Scanning electron microscopy (SEM) and energy-dispersive X-ray spectroscopic (EDX) elemental mapping

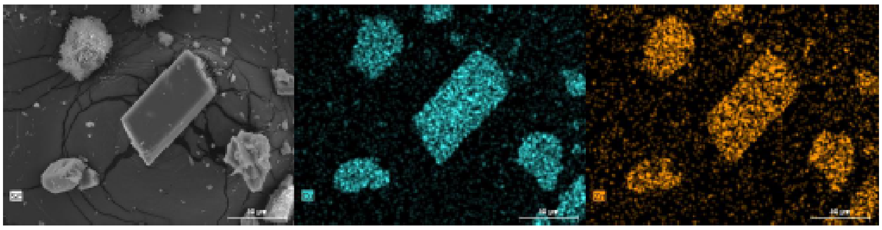

Fig. S17 SEM image and corresponding elemental mapping images of copper (cyan) and zinc (orange) in **1**.

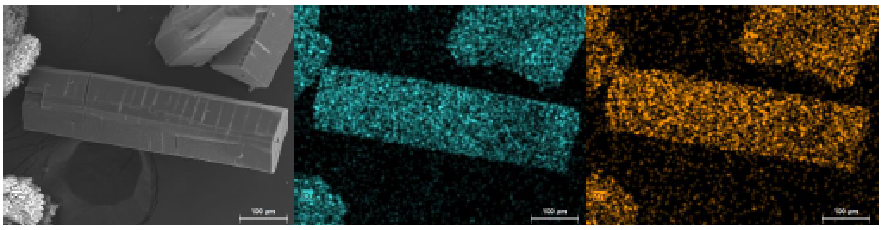

Fig. S18 SEM image and corresponding elemental mapping images of copper (cyan) and zinc (orange) in **3**.

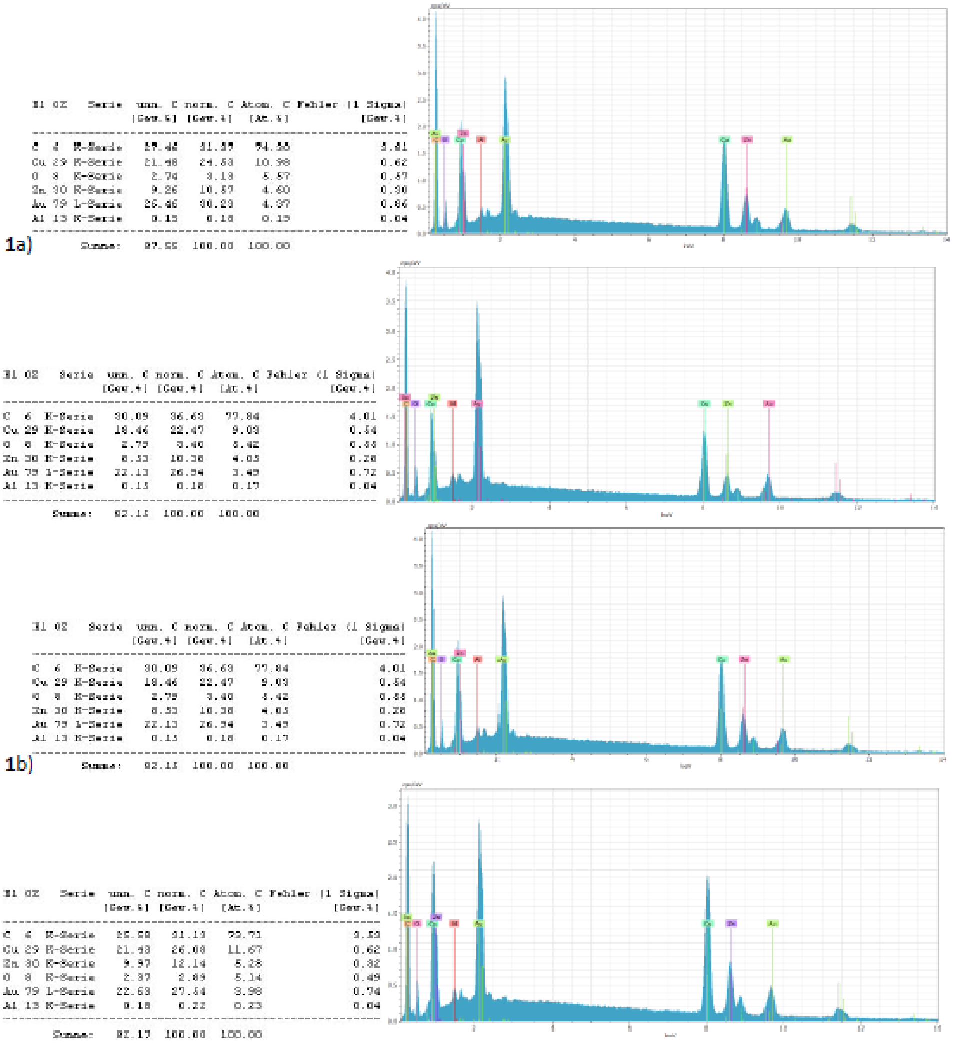

1a)

```
El OZ   Serie  unn. C norm. C Atom. C Fehler (1 Sigma)
               [Gew.%] [Gew.%]  [At.%]           [Gew.%]
------------------------------------------------------
C   6  K-Serie   27.46   31.37   74.33              3.81
Cu 29  K-Serie   21.48   24.53   10.98              0.62
O   8  K-Serie    2.74    3.13    5.57              0.57
Zn 30  K-Serie    9.26   10.57    4.60              0.30
Au 79  L-Serie   26.46   30.23    4.37              0.86
Al 13  K-Serie    0.15    0.18    0.15              0.04
------------------------------------------------------
        Summe:   87.55  100.00  100.00
```

```
El OZ   Serie  unn. C norm. C Atom. C Fehler (1 Sigma)
               [Gew.%] [Gew.%]  [At.%]           [Gew.%]
------------------------------------------------------
C   6  K-Serie   30.09   36.63   77.84              4.01
Cu 29  K-Serie   18.46   22.47    9.03              0.54
O   8  K-Serie    2.79    3.40    5.42              0.44
Zn 30  K-Serie    8.53   10.38    4.05              0.28
Au 79  L-Serie   22.13   26.94    3.49              0.72
Al 13  K-Serie    0.15    0.18    0.17              0.04
------------------------------------------------------
        Summe:   82.15  100.00  100.00
```

1b)

```
El OZ   Serie  unn. C norm. C Atom. C Fehler (1 Sigma)
               [Gew.%] [Gew.%]  [At.%]           [Gew.%]
------------------------------------------------------
C   6  K-Serie   30.09   36.63   77.84              4.01
Cu 29  K-Serie   18.46   22.47    9.03              0.54
O   8  K-Serie    2.79    3.40    5.42              0.44
Zn 30  K-Serie    8.53   10.38    4.05              0.28
Au 79  L-Serie   22.13   26.94    3.49              0.72
Al 13  K-Serie    0.15    0.18    0.17              0.04
------------------------------------------------------
        Summe:   82.15  100.00  100.00
```

```
El OZ   Serie  unn. C norm. C Atom. C Fehler (1 Sigma)
               [Gew.%] [Gew.%]  [At.%]           [Gew.%]
------------------------------------------------------
C   6  K-Serie   25.58   31.13   73.71              3.53
Cu 29  K-Serie   21.43   26.08   11.67              0.62
Zn 30  K-Serie    9.97   12.14    5.28              0.32
O   8  K-Serie    2.37    2.89    5.14              0.49
Au 79  L-Serie   22.63   27.54    3.98              0.74
Al 13  K-Serie    0.18    0.22    0.23              0.04
------------------------------------------------------
        Summe:   82.17  100.00  100.00
```

Fig. S19 EDX analysis of **1**.

Table S6 Overview of the EDX results of **1** and the calculated Cu/Zn ratio.

Sample	Cu	Zn	Molar ratio Cu/Zn
1a	10.98	4.60	1: 0.42
1a	6.89	2.87	1: 0.42
1b	9.03	4.05	1: 0.45
1b	11.67	5.28	1: 0.45
		average	1: 0.44

3a)

```
El OZ    Serie  unn. C norm. C Atom. C Fehler (1 Sigma)
               [Gew.%] [Gew.%]  [At.%]          [Gew.%]
--------------------------------------------------------
C  6  K-Serie   21.21   23.74   64.61             3.07
Cu 29 K-Serie   27.51   30.80   15.84             0.78
Zn 30 K-Serie   15.44   17.28    8.64             0.47
O  8  K-Serie    2.69    3.01    6.15             0.53
Au 79 L-Serie   21.99   24.61    4.09             0.72
Al 13 K-Serie    0.50    0.56    0.68             0.06
--------------------------------------------------------
        Summe:  89.33  100.00  100.00
```

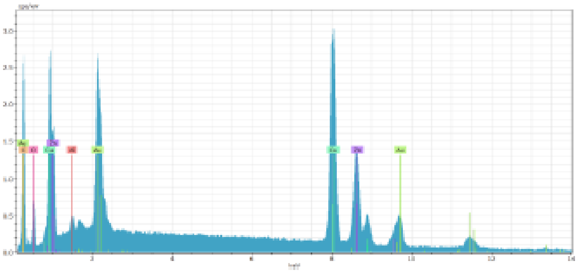

```
El OZ    Serie  unn. C norm. C Atom. C Fehler (1 Sigma)
               [Gew.%] [Gew.%]  [At.%]          [Gew.%]
--------------------------------------------------------
C  6  K-Serie   43.02   47.80   86.68             5.44
Cu 29 K-Serie   13.59   15.10    5.18             0.41
Au 79 L-Serie   24.44   27.15    3.00             0.79
Zn 30 K-Serie    7.36    8.17    2.72             0.25
O  8  K-Serie    1.60    1.78    2.42             0.39
--------------------------------------------------------
        Summe:  90.02  100.00  100.00
```

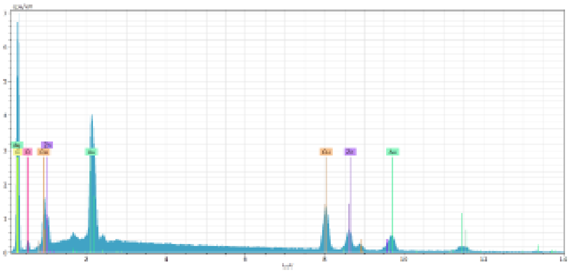

3b)

```
El OZ    Serie  unn. C norm. C Atom. C Fehler (1 Sigma)
               [Gew.%] [Gew.%]  [At.%]          [Gew.%]
--------------------------------------------------------
C  6  K-Serie   27.72   32.95   71.17             3.74
Cu 29 K-Serie   20.49   24.36    9.94             0.59
O  8  K-Serie    2.89    3.44    5.57             0.56
Zn 30 K-Serie   11.05   13.14    5.21             0.35
N  7  K-Serie    1.65    1.96    3.64             0.49
Au 79 L-Serie   19.01   22.60    2.98             0.63
Al 13 K-Serie    1.30    1.55    1.49             0.10
--------------------------------------------------------
        Summe:  84.11  100.00  100.00
```

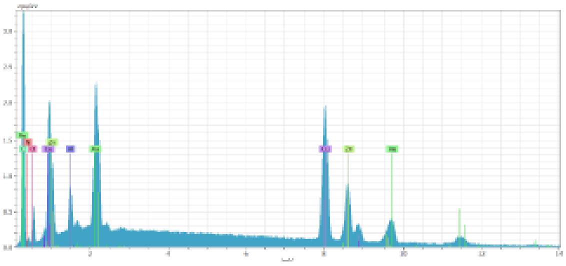

```
El OZ    Serie  unn. C norm. C Atom. C Fehler (1 Sigma)
               [Gew.%] [Gew.%]  [At.%]          [Gew.%]
--------------------------------------------------------
C  6  K-Serie   30.98   36.01   76.87             4.16
Cu 29 K-Serie   19.25   22.38    9.03             0.56
O  8  K-Serie    3.15    3.66    5.87             0.61
Zn 30 K-Serie   10.25   11.91    4.67             0.33
Au 79 L-Serie   22.22   25.83    3.36             0.73
Al 13 K-Serie    0.18    0.20    0.19             0.04
--------------------------------------------------------
        Summe:  86.01  100.00  100.00
```

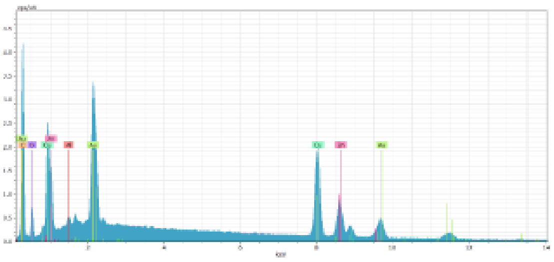

Fig. S20 EDX analysis of 3.

Table S7 Overview of the EDX results of 3 and the calculated Cu/Zn ratio.

Sample	Cu	Zn	Molar ratio Cu/Zn
3a	15.84	8.64	1: 0.55
3a	5.18	2.72	1: 0.53
3b	9.94	5.21	1: 0.52
3b	9.03	4.67	1: 0.52
		average:	1: 0.53

9. Thermogravimetric analysis (TGA) and IR-spectra

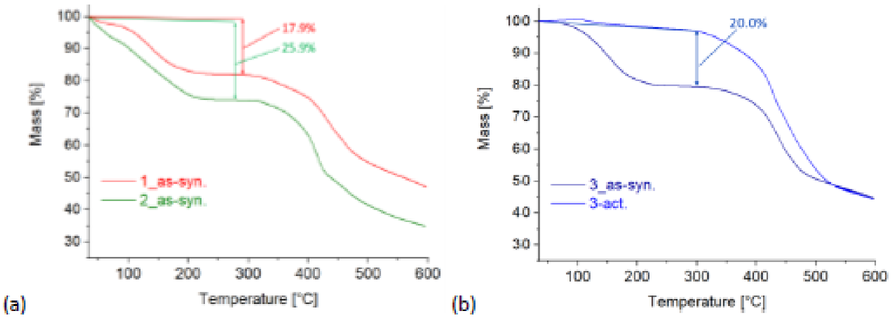

(a) (b)

Fig. S21 (a) TGA curve of **1** and **2** in the temperature range 20-600 °C with a heating rate of 5 K min^{-1} under nitrogen atmosphere. The loss of 17.9% corresponds to 9 DMF molecules calc. 17.8% for 9 DMF and the loss of 25.9% corresponds to 18 DMF molecules calc. 26.1% for 18 DMF. Deviations in the found and calculated mass percent for the solvent loss based on the single-crystal X-ray structure results are due to the already occurring solvent loss during sample preparation (drying and weighing) before the TGA measurement. (b) TGA curve of **3** and for **3**-act. in the temperature range 20-600 °C with a heating rate of 5 K min^{-1} under nitrogen atmosphere. The loss of 20.0% corresponds to 13.6 DMF molecules calc. 20.0% for 13.6 DMF. The small mass increase by **3**-act. is due to balance fluctuation.

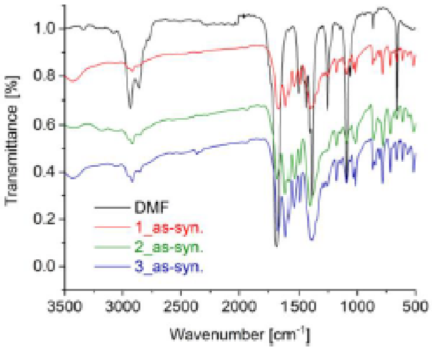

Fig. S22 IR-spectra (KBr) of **1**, **2**, **3** and DMF (NIST, black).[5]

10. X-ray photoelectron spectroscopy (XPS)

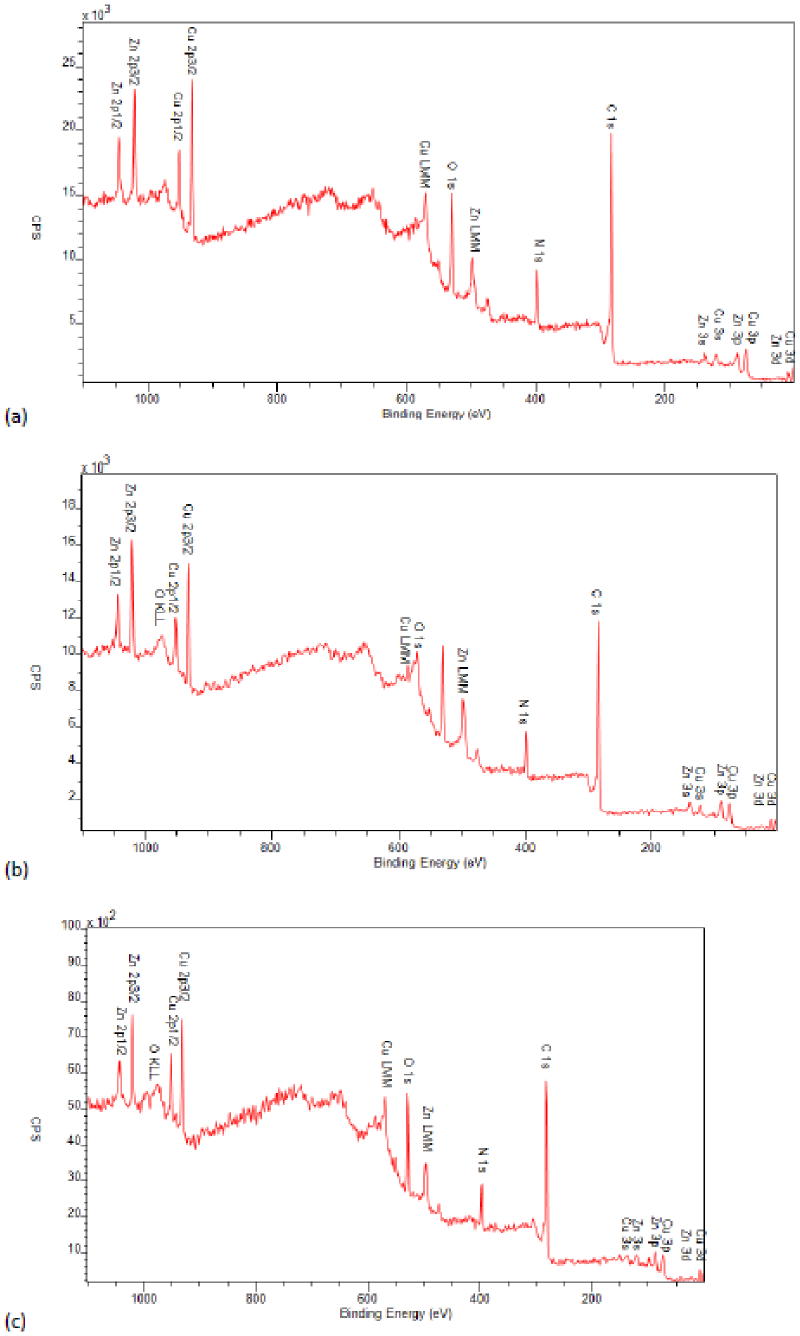

Fig. S23 Survey XP spectrum for **1** (a), **2** (b) and **3** (c).

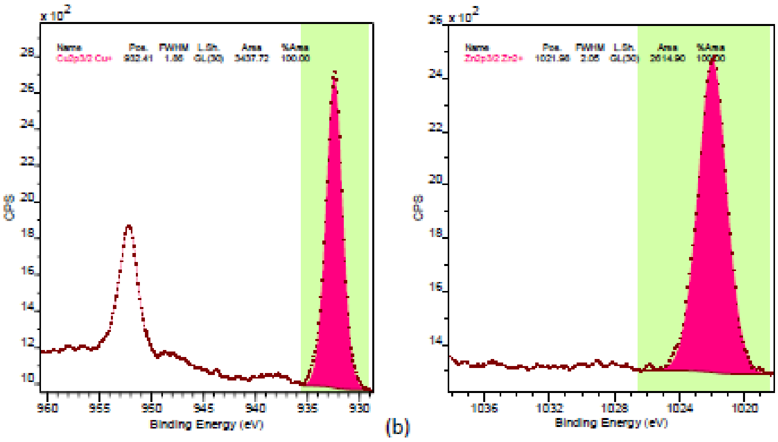

(a) (b)

Fig. S24 High resolution Cu 2p (a) and Zn 2p (b) XP spectrum for **1**.

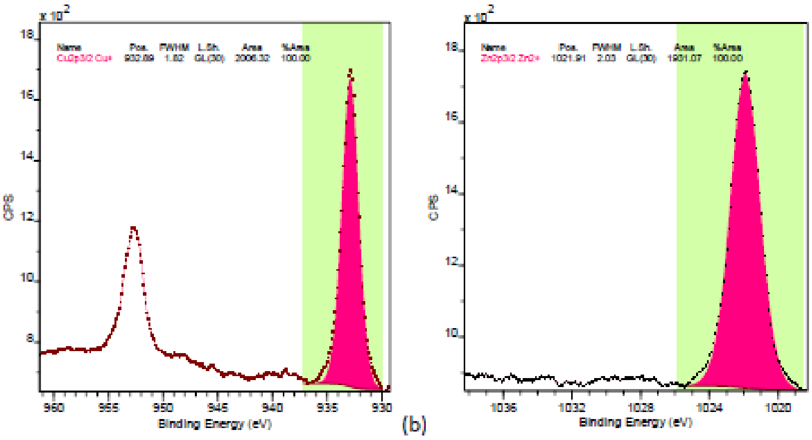

(a) (b)

Fig. S25 High resolution Cu 2p (a) and Zn 2p (b) XP spectrum for **2**.

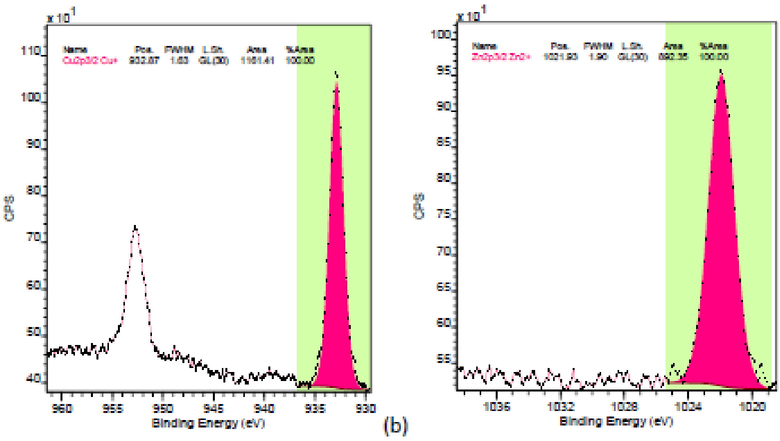

(a) (b)

Fig. S26 High resolution Cu 2p (a) and Zn 2p (b) XP spectrum for **3**.

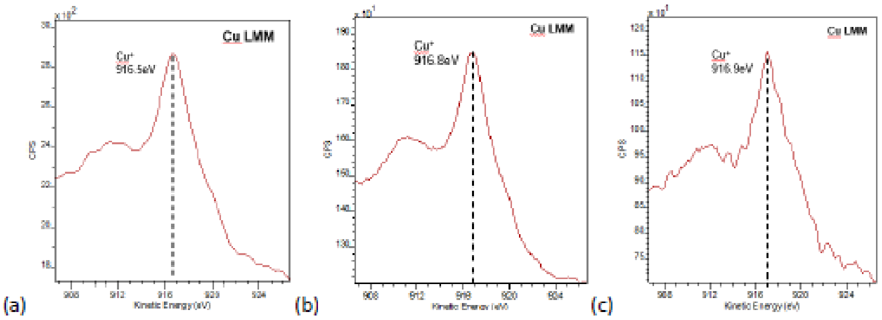

Fig. S27 Cu LMM Auger lines for **1** (a), **2** (b) and **3** (c).

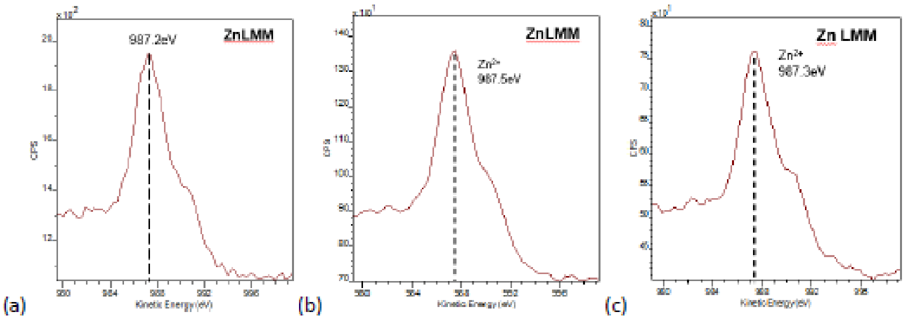

Fig. S28 Zn LMM Auger lines for **1** (a), **2** (b) and **3** (c).

Table S8 Atom composition from XPS.

Compound	C [at.%]	O [at.%]	N [at.%]	Cu [at.%]	Zn [at.%]	Cu/Zn exp.	Cu/Zn theor.
1	35.17	17.76	8.29	26.83	11.95	9:4 = 1: 0.44	9:4 = 1:0.44
2	29.29	17.06	7.85	22.93	22.86	1:1	12:6 = 1:0.5
3	34.19	19.75	8.264	22.94	14.86	1:54	12:7 = 1:0.58

Table S9 Quantification of copper and zinc by XPS analysis from the high resolution XP spectra.

Compound		Area	ASF [a]	Cu/Zn exp.	Cu/Zn theor.
1	Copper	3437.72	969.19[b,c]	1:0.72	9:4 = 1:0.44
	Zinc	2614.90	701.80[d,e]		
2	Copper	2006.32	565.64[b,c]	1:0.91	12:6 = 1:0.5
	Zinc	1931.07	518.27[d,e]		
3	Cooper	1161.41	327.43[b,c]	1:0.73	12:7 = 1:0.58
	Zinc	892.35	239.49[d,e]		

[a] The atomic sensitivity factor (F_{ASF}) is element specific.; ASF = Area/F_{ASF}. [b] The Cu 2p3/2 orbital was used for calculations. [c] F_{ASF} = 3.547. [d] The Zn 2p3/2 orbital were used for calculations. [e]F_{ASF} = 3.726.

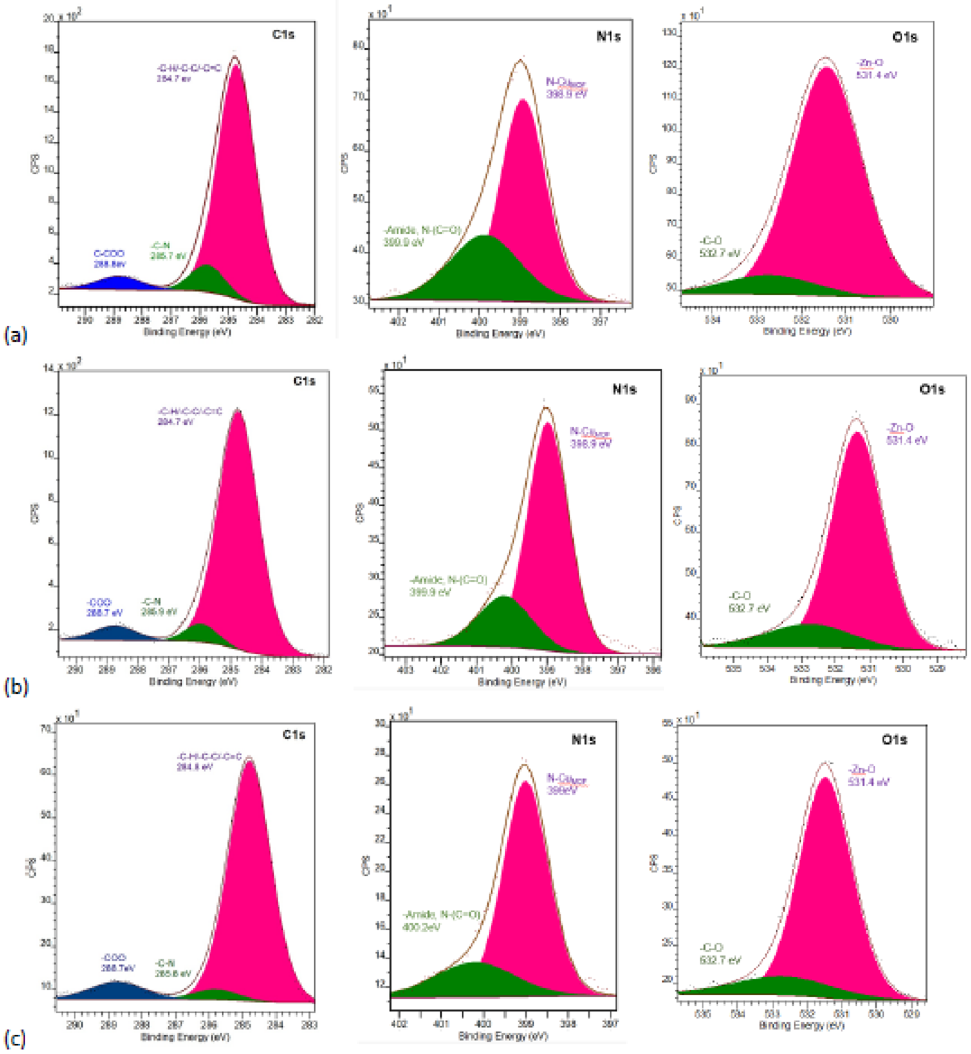

Fig. S29 High resolution spectra of carbon 1s, nitrogen 1s and oxygen 1s for **1** (a), **2** (b) and **3** (c).

11. Gas sorption measurements

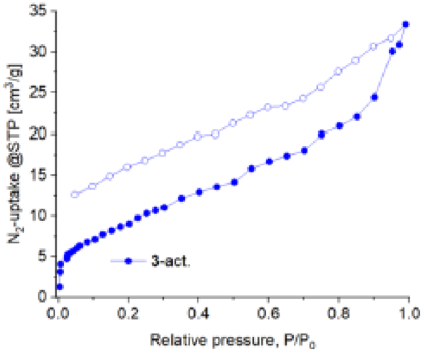

Fig. S30 N$_2$ sorption isotherm at 77 K for 3-act.

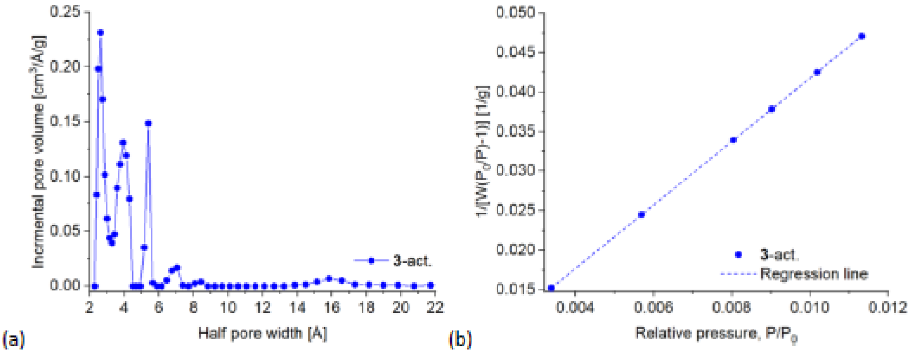

Fig. S31 (a) NLDFT pore size distribution curve for 3-act. from Ar adsorption isotherm (at 87 K, Fig. 6). The pore size distribution was estimated using non-localized density functional theory (NLDFT) with a "slit-pore model". (b) BET plot for 3-act. from Ar adsorption isotherm (at 87 K, Fig. 6).

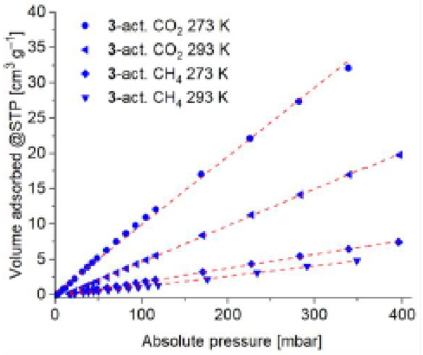

Fig. S32 Henry plots for CO$_2$ and CH$_4$ from the adsorption isotherms at 273 K and 293 K for 3-act. The regression lines are given as red dashed lines.

Table S10 Overview of the results from the Henry-Plots.

Compound	Temp. [K]	Gradient CO_2 [cm^3/g]	Gradient CH_4 [cm^3/g]	Selectivity CO_2: CH_4
3-act.	273	0.097	0.020	4.8:1
3-act.	293	0.052	0.015	3.5:1

Isosteric enthalpy of adsorption calculation

For the virial fit the isotherm measured at two different temperatures are brought into an ln*p* vs. *n* form (Fig. S33). The following equation is then used to fit all three isotherms simultaneously, that is with the same fitting parameters a_i and b_i.

$$\ln p = \ln n + \frac{1}{T}\sum_{i=0}^{m} a_i n^i + \sum_{i=0}^{m} b_i n^i$$

In the equation, *p* is the pressure in kPa, *n* is the of total amount adsorbed in mmol/g, *T* is the temperature in K (e.g 273 K, 293 K), a_i and b_i are the virial coefficients and *m* represents the number of coefficients required to adequately fit the isotherms.

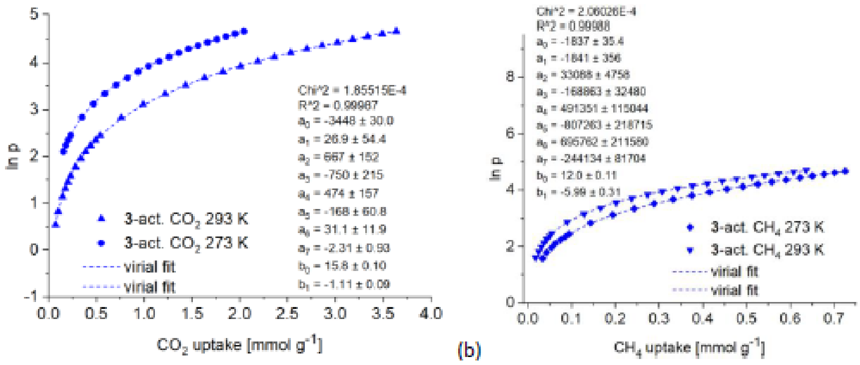

(a) (b)

Fig. S33 Virial analysis of the adsorption isotherms for CO_2 (a) and CH_4 (b) adsorption isotherms of 3-act. at 273 K and 293 K with the fitting parameters (virial coefficients) a_i and b_i.

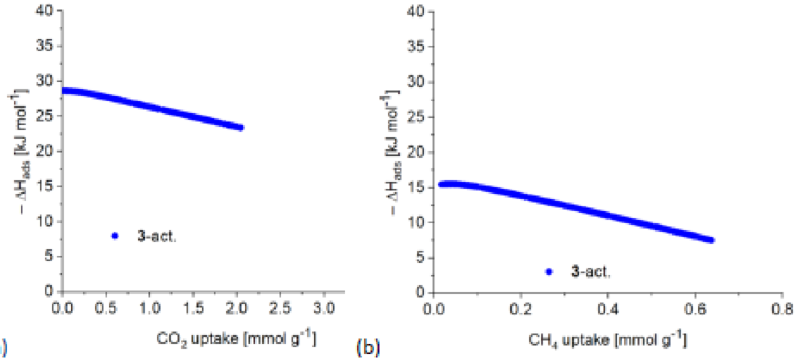

(a) (b)

Fig. S34 Isosteric enthalpy of adsorption, ΔH_{ads}, of CO_2 (a) and CH_4 (b) for 3-act. from the respective isotherms at 273 K and 293 K (cf. Figure 10).

Theoretical surface area, pore volume and experimental gas uptake

The theoretical surface area and pore volume of **1**-**3** was calculated using the program CrystalExplorer[6] following the methodology outlined in ref.[7], by a 'Void' calculation with Mercury[8,9] and by a 'Calc Void/Solv' calculation with Platon.[3]

The coordinated DMF solvent molecules were included in the calculations. Only the minor disordered parts in the asymmetric unit were removed. The calculated values are listed in Table S11.

Table S11. Surface areas and pore volumes for compounds **1**, **2** and **3**.

	1 (no disorder)		**2**		**3**	
Z, $M_{asym\,unit}$ (g mol^{-1}), V from X-ray structures; cf. Table S2 in Supp. Info.	2, 2998.68, 8078.2		2, 4090.81, 11666.43		4, 4095.71, 21792.8	
CrystalExplorer calculation (crystal voids)	isovalue					
surface area *(no disorder)*[b]	0.002	0.0003	0.002	0.0003	0.002	0.0003
- $S_{unit\,cell}$ (Å^2)	2575	1665	3378	2317	6911	4562
- specific (m^2 g^{-1}) [a]	2585	1672	2486	1705	2540	1677
					(low resolution) [d]	
pore volume *(no disorder)*[b]						
- $V_{unit\,cell}$ (Å^3)	2910	1687	4670	3078	8046	4735
- specific (cm^3 g^{-1}) [a]	0.292	0.169	0.344	0.227	0.296	0.174
					(low resolution) [d]	
Mercury 'Void' calculation						
(probe radius 1.2 Å, grid spacing 0.7 Å)	calc. using solvent accessible surface					
void volume, $V_{unit\,cell}$ (Å^3) *(no disorder)*[b] (% of unit cell volume V) - specific (cm^3 g^{-1}) [a]	931 (11.5) 0.093		2002 (17) 0.147		2629 (12) 0.097	
	calc. using contact surface					
void volume, $V_{unit\,cell}$ (Å^3) *(no disorder)*[b] (% of unit cell volume) - specific (cm^3 g^{-1}) [a]	2671 (33) 0.268		4436 (38) 0.326		7243 (33) 0.266	
Platon 'Calc Void/Solv' calculation						
tot. pot. solv. area volume (SAV) (Å^3) (% of unit cell vol. V) (*no disorder*) - specific pore volume (cm^3 g^{-1}) from SAV [a]	2749 (34) 0.276		4537 (39) 0.334		7602 (35) 0.279	
experimental gas uptake						
CO_2 (cm^3 g^{-1}) (273 K, 760 Torr)	--		--		78	
CO_2 (mmol·g^{-1}) (273 K, 760 Torr) [e]	--		--		3.43	
- x 44 g/mol = CO_2 (g/g)	-		-		0.15	
-- / ρ_{CO2} [c] = CO_2 (cm^3 liq. CO_2/gMOF)	-		-		0.15	
pore filling CO_2 (cm^3 liq. CO_2/gMOF) / specific pore volume (cm^3 g^{-1}) from SAV x 100%	-		-		54	

[a] Specific surface area calculated according to ($S_{unit\,cell} \times N_A$)/($Z \times M_{asym\,unit}$); specific pore volume calculated according to ($V_{unit\,cell} \times N_A$)/($Z \times M_{asym\,unit}$) or ($SAV \times N_A$)/($Z \times M_{asym\,unit}$); N_A = Avogadro's constant, $6.022 \cdot 10^{23}$ mol^{-1}, Z = number of asymmetric formula units, $M_{asym\,unit}$ = molecular weight of asymmetric formula unit (in g mol^{-1}). As a help to reproduce the specific number the values for *Z* and $M_{asym\,unit}$ from the X-ray structures are included.

[b] Disorder in **1**, **2** and **3** removed, leaving only the major contributions.

[c] Density of 1.032 g cm^{-3} of liquid CO_2 at 253 K to approximate the volume of CO_2 adsorbed in the MOFs at 760 Torr (1.0 bar) and 273 K

[d] Due to the large unit cell, the calculation had to be carried out with CrystalExplorer17.5 Version 3.1, Revision 1448, and using "Resolution: Low" upon surface generation. Attempted calculations with CrystalExplorer21.5, Version 21.5 failed.

[e] Value in cm^3 g^{-1} divided by 22.711 L/mol (= cm^3/mmol) (22.711 L is the molar volume of an ideal gas at 1 bar and 273 K).

Comment on the results from CrystalExplorer:

Fig. S35-S37 illustrate the iso-surface areas at 0.002 and 0.0003 au around the pore/channel windows.

The 0.0003 au calculated surface area is seen as a better choice for estimating the internal surface area in porous materials than the 0.002 isosurface.[7] The value of 0.002 au corresponds approximately to a smoothed van der Waals surface and 0.0003 au seems to be more appropriate for mapping "empty" space in molecular crystals.[7] From the above comparison in Table S11 it is, however, apparent that the isovalue of 0.002 gives a better match in the pore volumes which are also derived from Mercury and Platon.

The calculated surface area presents an upper bound which can be approached but it will be physically unrealistic to expect that the experimental measurements will surpass the calculated value.

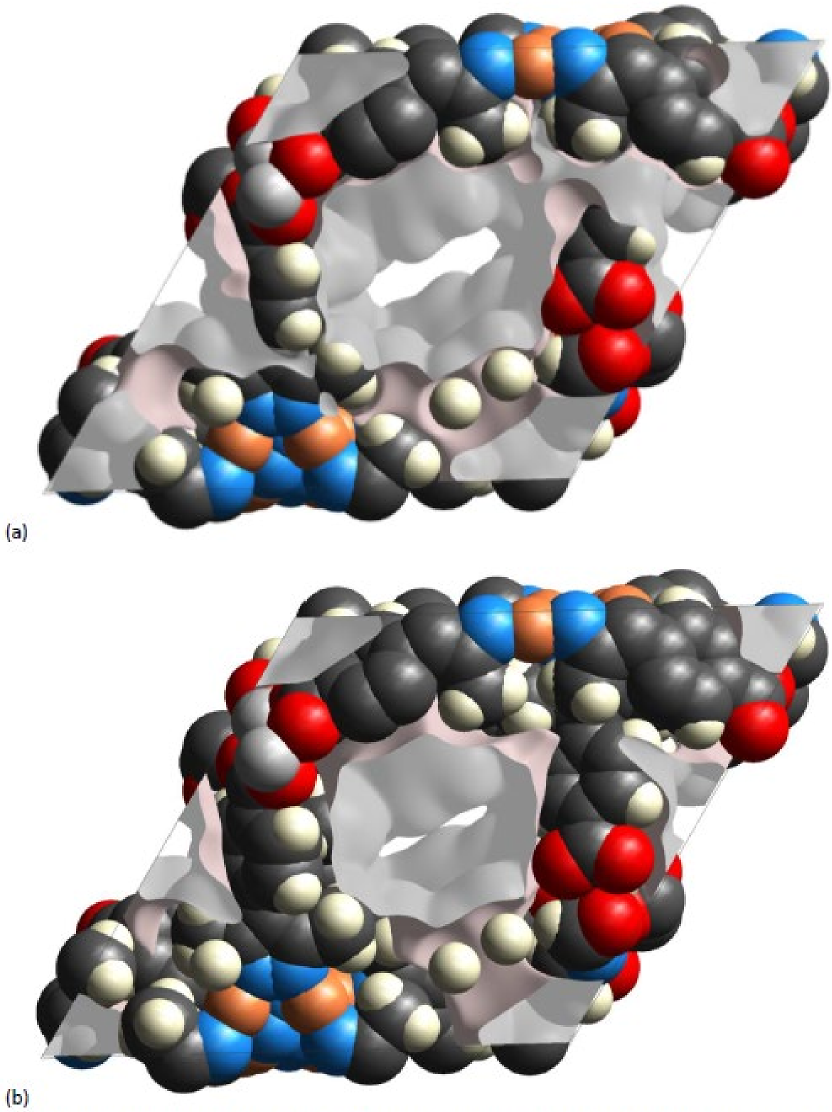

Fig. S35 Void surfaces (a) 0.002 au and (b) 0.0003 au around pore windows in **1** superimposed on space-filling representations of the unit cell content, view along *a*. From the vertical and horizontal axis lengths of of *c* = 22.07 and *b* = 21.98 Å, respectively, the open channel cross-sections are measured to about 3.3 x 6.6 Å (0.002 au) and 2.2 x 5.5 Å (0.0003 au).

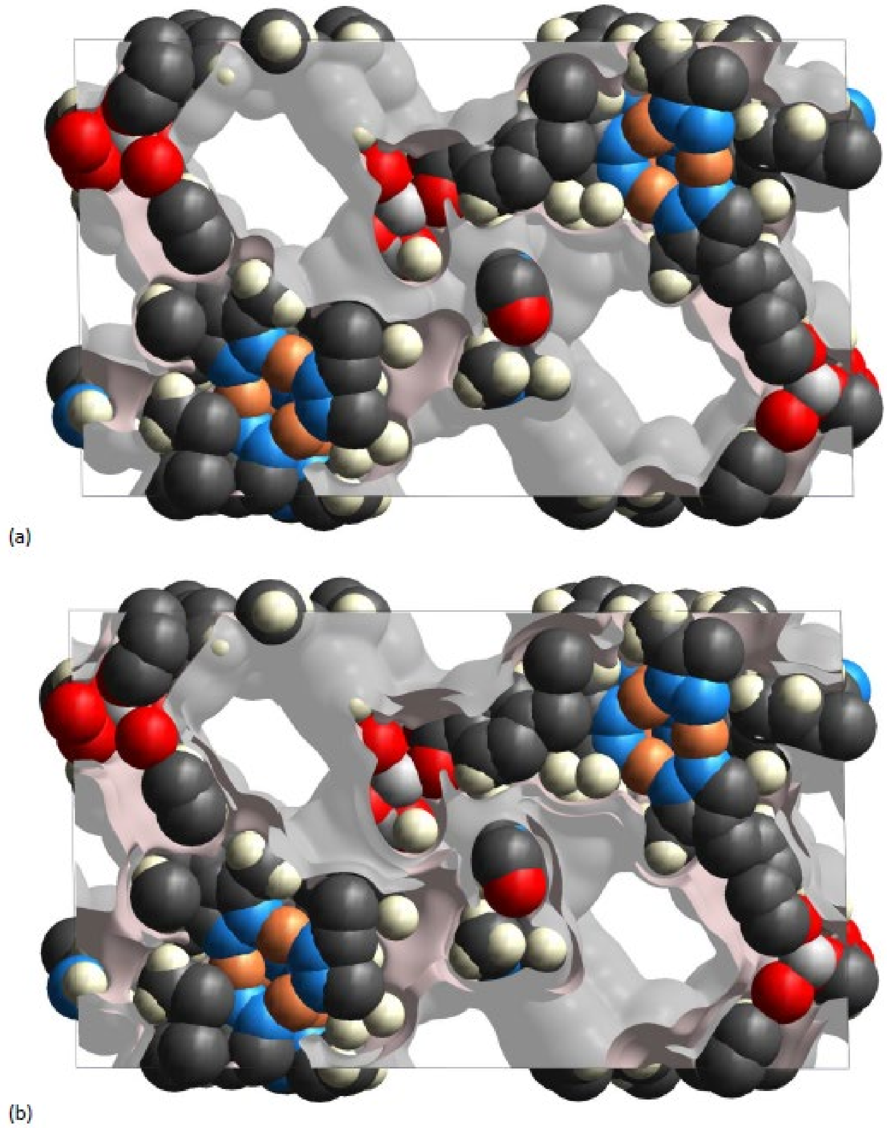

Fig. S36 Void surfaces (a) 0.002 au and (b) 0.0003 au around pore windows in 2 superimposed on space-filling representations of the unit cell content, view along *a*. From the vertical and horizontal axis lengths of *b* = 21.94 and *c* = 37.03 Å, respectively, the open channel cross-sections are measured to about 4.5 x 7.0 Å (0.002 au) and 3.2 x 5.7 Å (0.0003 au).

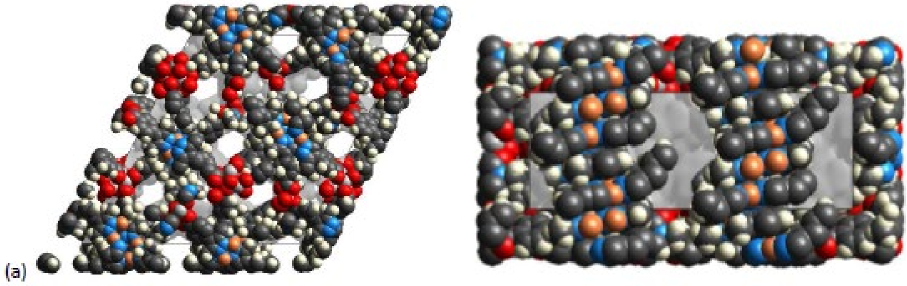

view along *b* (*a* to bottom, *c* to right) view along *c* (*a* to right, *b* to top)

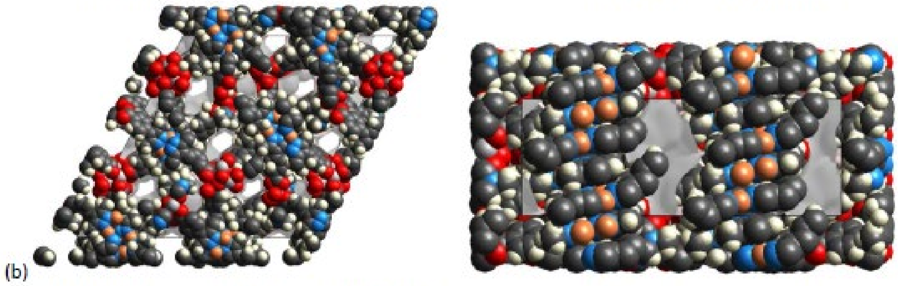

Fig. S37 Void surfaces (a) 0.002 au and (b) 0.0003 au around pore windows in 3 superimposed on space-filling representations of the unit cell content. From the axis lengths of *a* = 41.61, *b* = 13.38 and *c* = 44.26 Å the open channel cross-sections are measured to about 4.6 x 4.6 Å (0.002 au) and 3.3 x 3.3 Å (0.0003 au).

Images from Mercury void calculations

In Mercury[8] voids can be calculated using two different methods (probe radius 1.2 Å, grid spacing 0.7 Å):
- Calculate voids using Solvent Accessible Surface gives the volume which can be occupied by the center of a probe of a given radius.
- Calculate voids using Contact Surface maps the volume that can be occupied by the full probe (including its radius) and thus gives a better estimate of the volume that could be filled by solvent or guest molecules.
- A full description of these two different surfaces and the ways in which they can be used is given in: L. J. Barbour, *Chem. Commun.* 2006, 1163–1168.

The dimensions of the crystallograpic axes are given to facilitate the estimate of the cross-sections of the pore apertures:

	1	**2**	**3**
a/Å	20.2449(16)	14.5957(2)	41.6099(5)
b/Å	21.975(2)	21.9429(2)	13.3781(1)
c/Å	22.074(2)	37.0299(3)	44.2601(5)

Mercury-calculated void with *solvent accessible surface*:

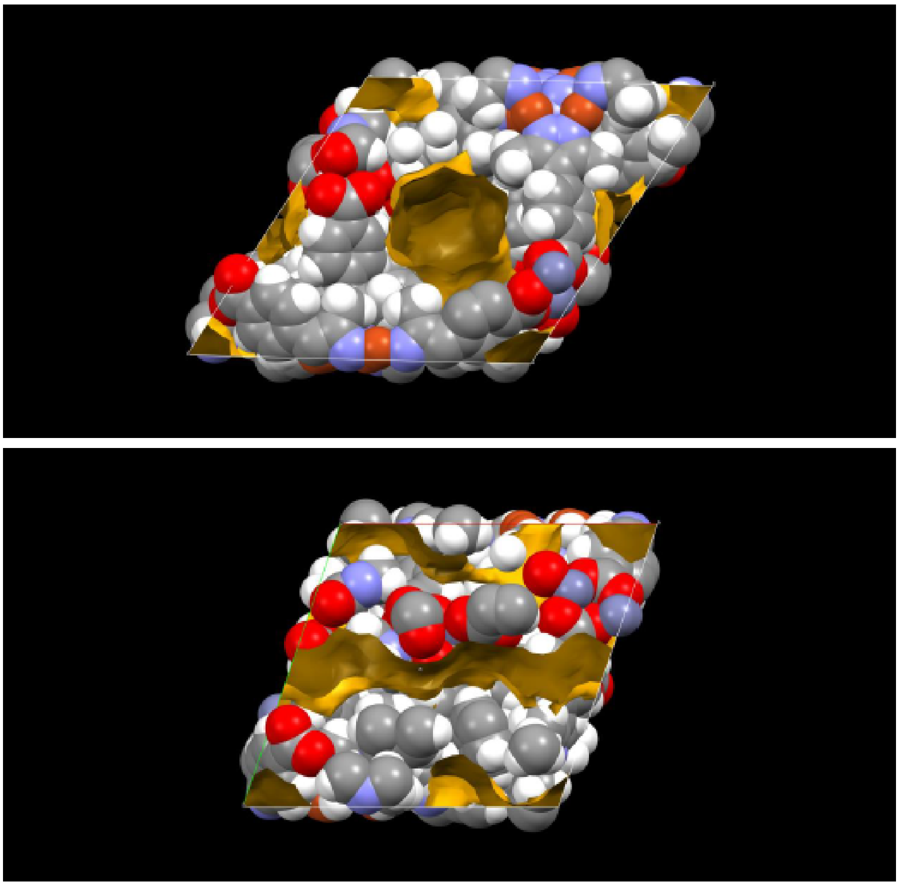

Fig. S38 Images from Mercury void calculations for compound **1** (no disorder), top: view along *a* (*b* to right, *c* to bottom); bottom: view along *c* (*a* to right, *b* to bottom).

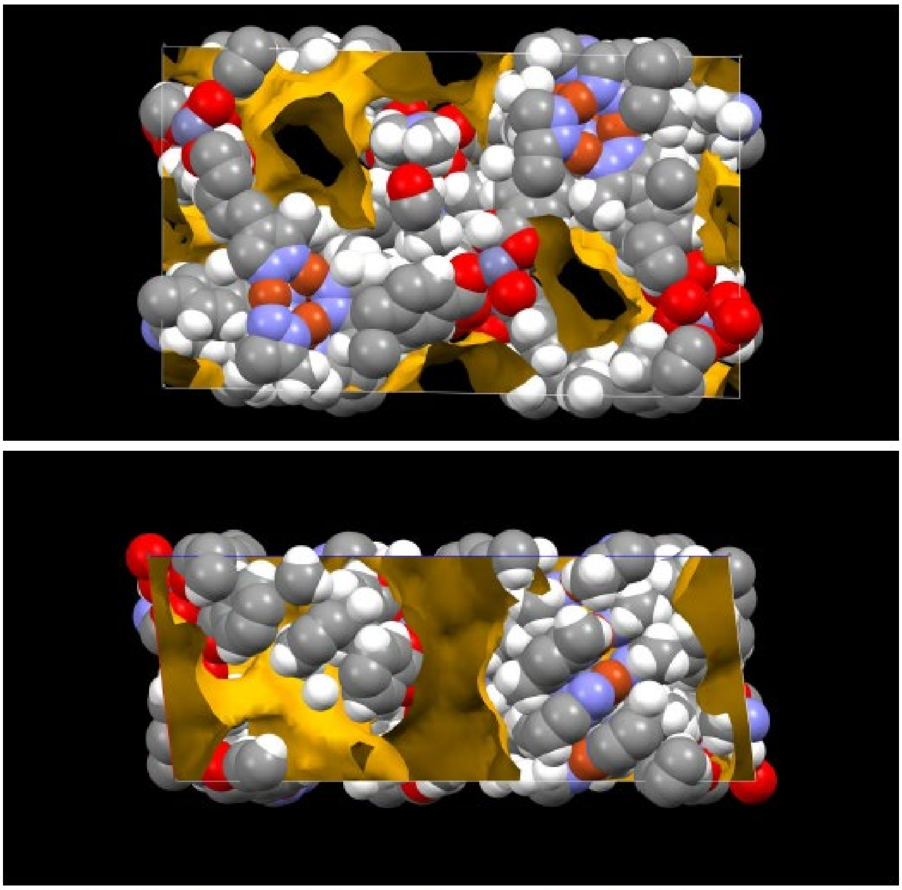

Fig. S39 Images from Mercury void calculations for compound 2 (no disorder), top: view along *a* (*c* to right, *b* to bottom); bottom: view along *b* (*c* to right, *a* to bottom).

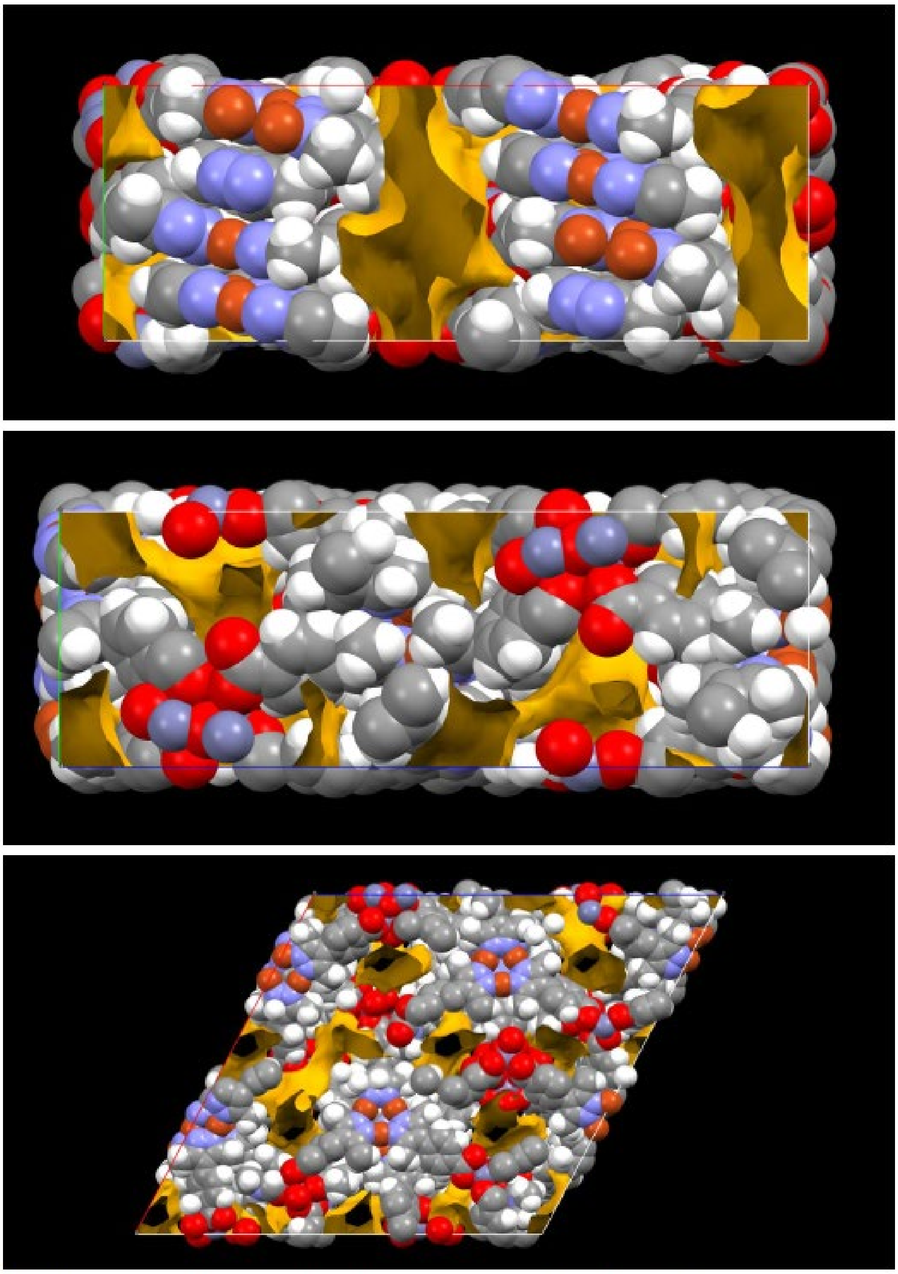

Fig. S40 Images from Mercury void calculations for compound 3 (no disorder), top: view along *c* (*a* to right, *b* to bottom); middle: view along *a* (*c* to right, *b* to top); bottom: view along *b* (*c* to right, *a* to bottom).

Mercury-calculated void with *contact surface*:

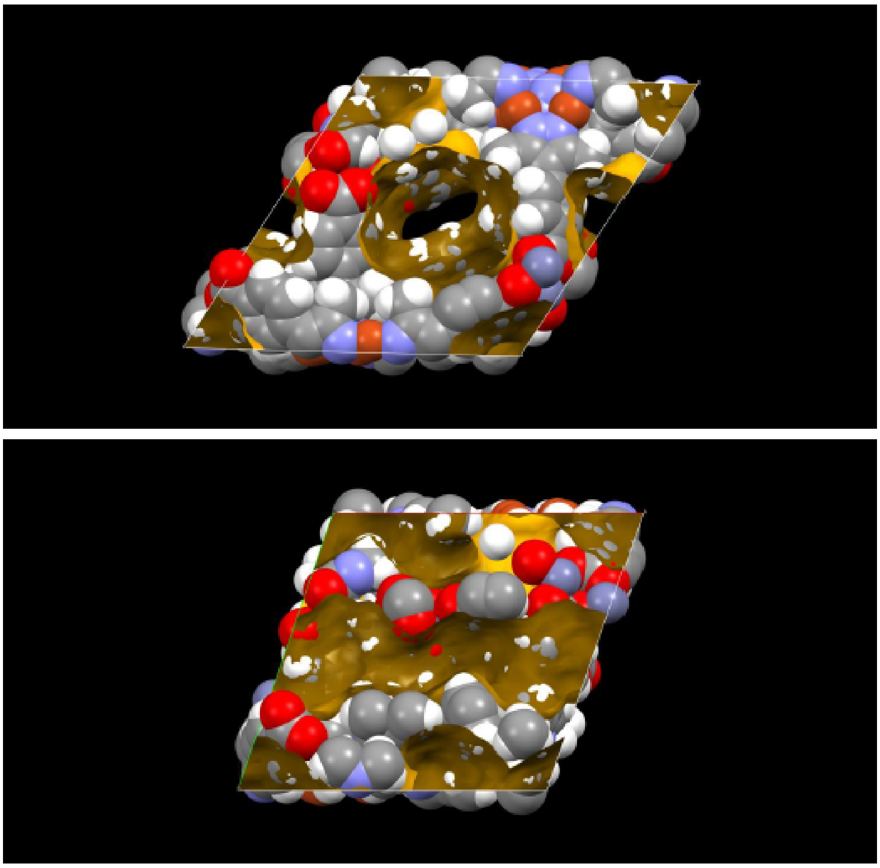

Fig. S41 Images from Mercury void calculations for compound **1** (no disord), top: view along *a* (*b* to right, *c* to bottom); bottom: view along *c* (*a* to right, *b* to bottom).

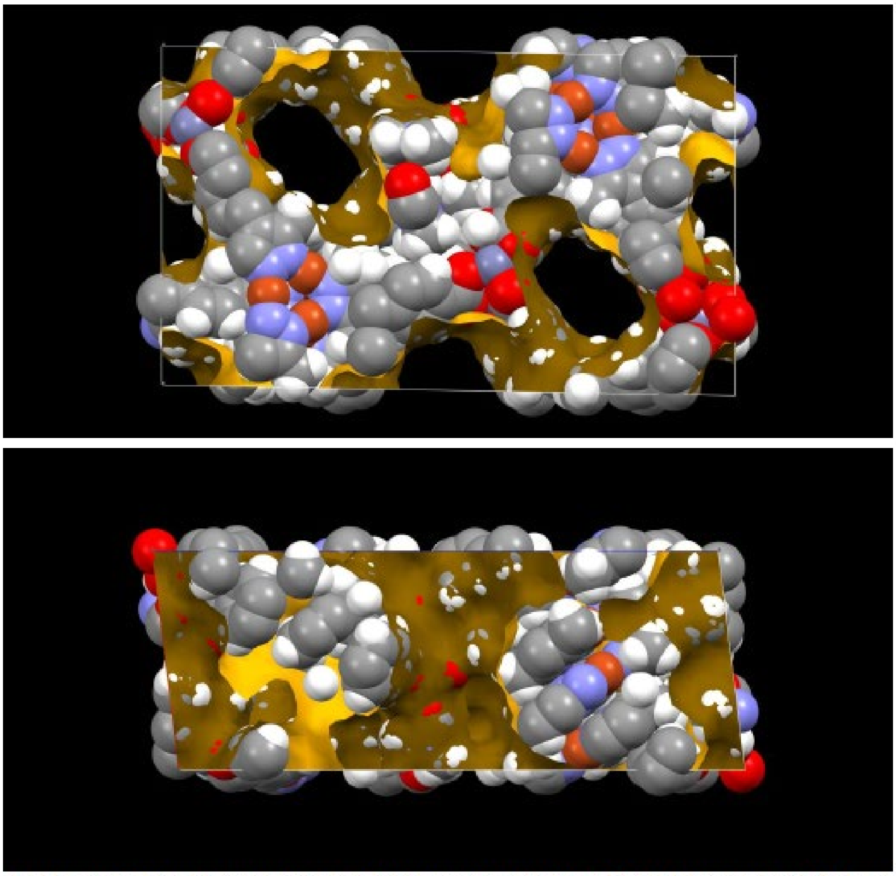

Fig. S42 Images from Mercury void calculations for compound 2 (no disorder), top: view along *a* (*c* to right, *b* to bottom); bottom: view along *b* (*c* to right, *a* to bottom).

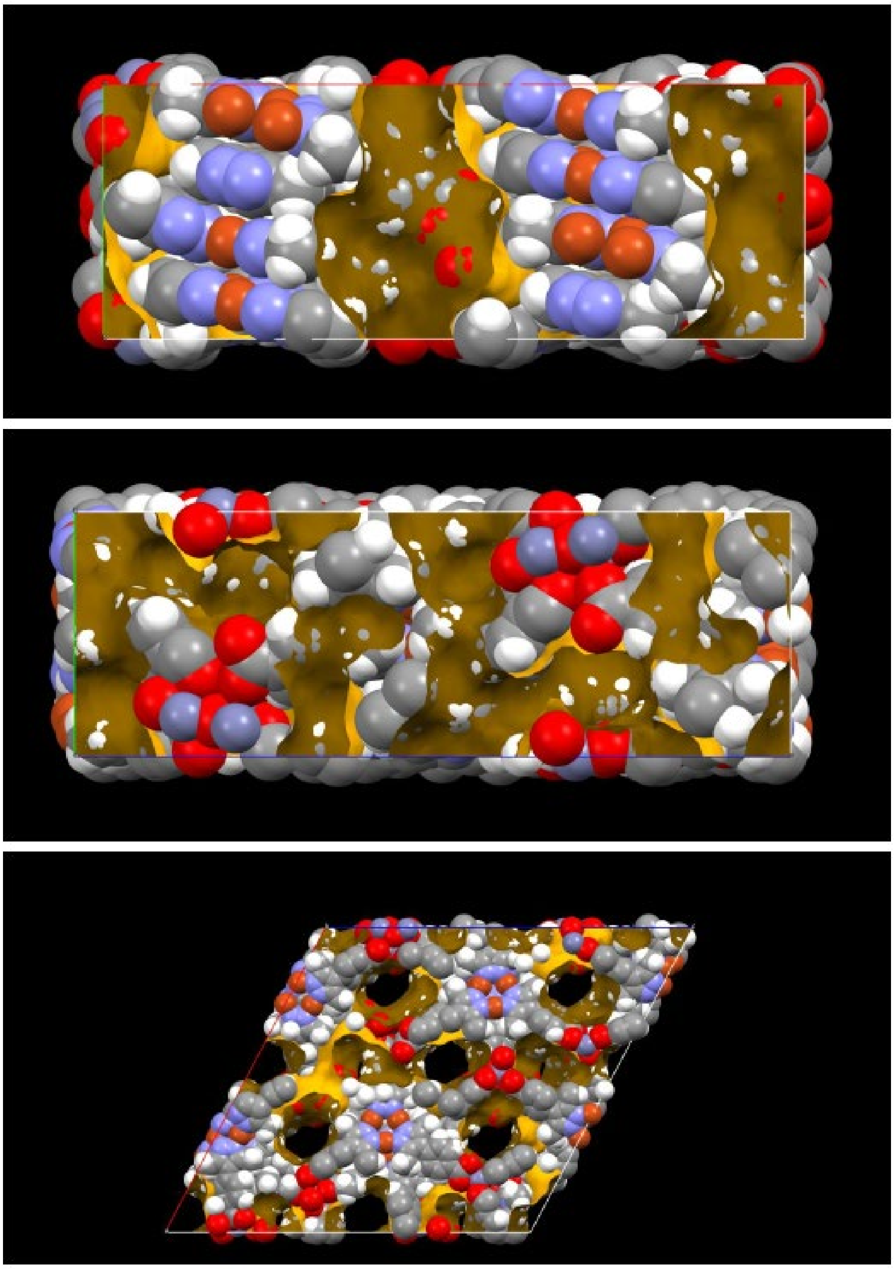

Fig. S43 Images from Mercury void calculations for compound **3** (no disorder), top: view along *c* (*a* to right, *b* to bottom); middle: view along *a* (*c* to right, *b* to top); bottom: view along *b* (*c* to right, *a* to bottom).

12. Linker flexibility

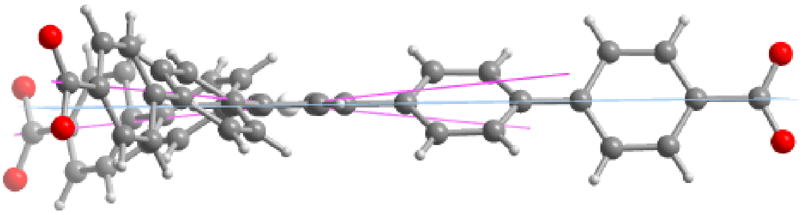

(a) bbc-linker in DUT-40(Zn) (CCDC 850713);[10] the symmetry-equivalent biphenyl-carboxylate groups at left bend up and down of the central ring plane by 3.1(5)°.

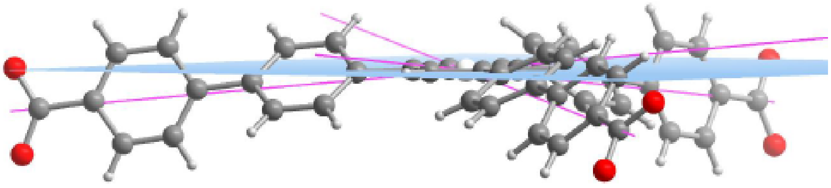

(b) bbc-linker in DUT-44(Co) (CCDC 850717);[10] the biphenyl-carboxylate group at left bends down of the central ring plane by 5.0(1)°, the one at front by 6.3(1)°, the one at rear-right by 5.2(1)°.

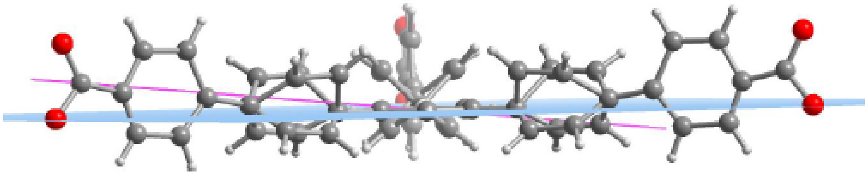

(c) bbc-linker in MOF-1005(Zr) (from deposited file MOF-1005_290K1_DMF.cif);[11] the three symmetry-equivalent biphenyl-carboxylate groups bend out of the central ring plane by 5.1(5)°.

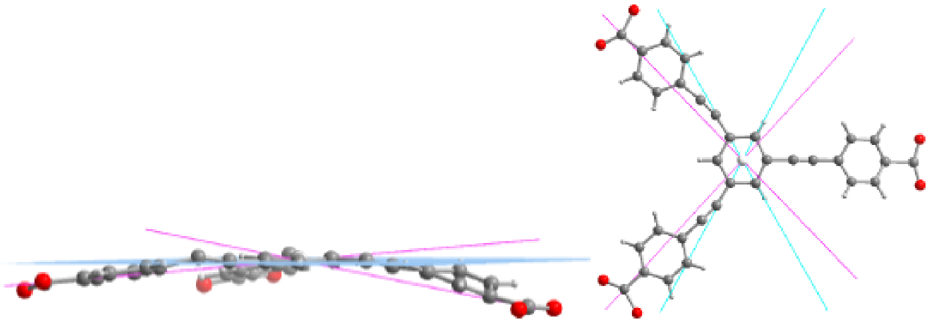

(d) bte-linker in MOF-1004(Zr) (from deposited file MOF-1004_100K_DMF.cif);[11] the two symmetry-equivalent ethinyl-benzoate groups at left and to the rear bend out of the central ring plane by 4(1)°, the one at right by 10(1)°. At the same time the two symmetry-equivalent ethinyl-benzoate groups (pink lines) deviate from a near 120° orientation (blue lines) by 14.5(1.5)° so that the angle between the pink lines is 94°.

Fig. S44 Examples of distortions in the trigonal linkers (a)-(c) 4,4′,4′′-(benzene-1,3,5-triyl-tris(benzene-4,1-diyl))tribenzoate (bbc^{3-}) = 1,3,5-tris(4'-carboxy[1,1'-biphenyl]-4-yl-)benzene (tcbpb^{3-}) and (d) 4,4′,4′′-(benzene-1,3,5-triyl-tris(ethyne-2,1-diyl))tribenzoate (bte^{3-}). The plane through the central benzene ring is shown in blue. The lines from the carboxylate C-atoms to the central benzene centroid are given in pink.

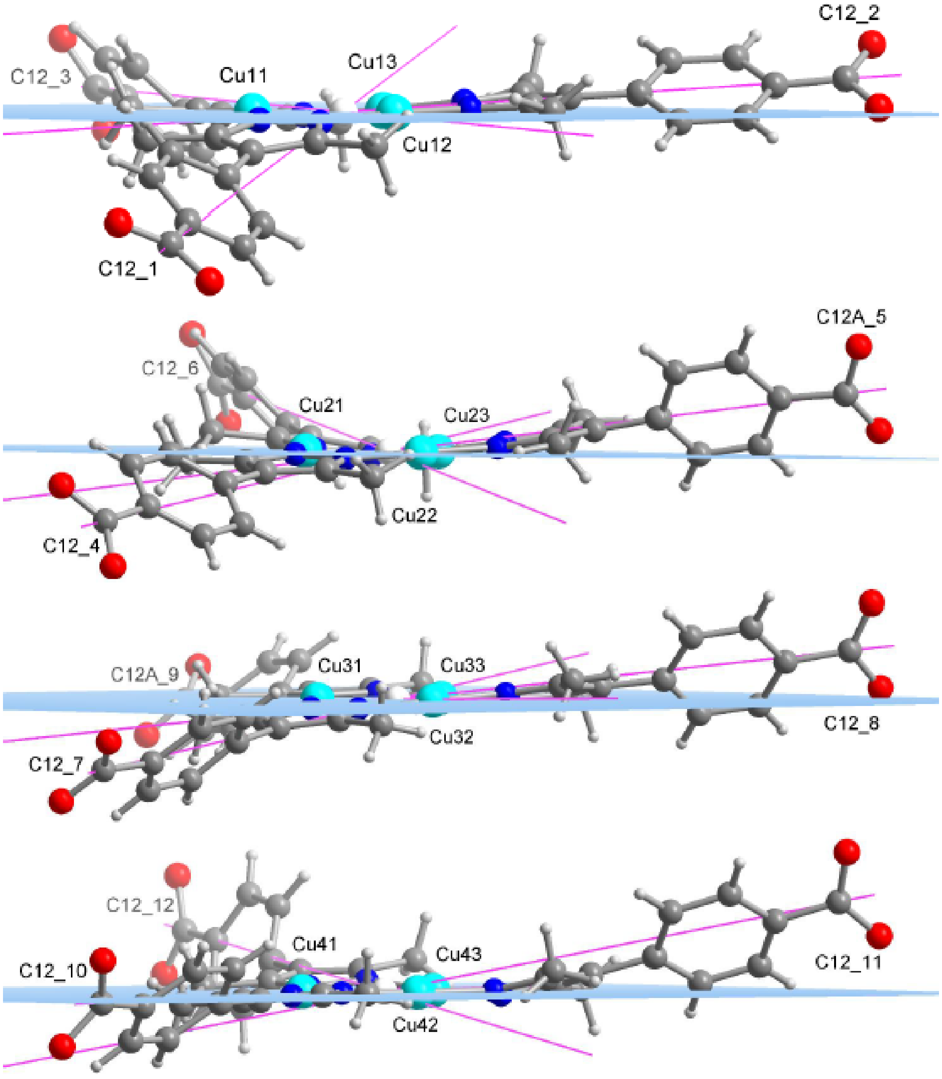

Linker plane through	Cu11-12-13		Cu21-22-23		Cu31-32-33		Cu41-42-43
line to Cu_3 centroid from	angle line-plane (°)	line to Cu_3 centroid from	angle line-plane (°)	line to Cu_3 centroid from	angle line-plane (°)	line to Cu_3 centroid from	angle line-plane (°)
C12_1	**14.5(1)**	**C12-4**	**8.6(1)**	**C12_7**	**7.9(1)**	**C12_10**	**0.7(1)**
C12_2	**3.8(1)**	**C12_5**	**7.8(1)**	**C12_8**	**6.0(1)**	**C12_11**	**11.0(1)**
C12_3	**1.9(1)**	**C12_6**	**7.6(1)**	**C12A_9**	**1.1(1)**	**C12_12**	**6.8(1)**

Fig. S45 Distortions in the $Cu^{I}_{3}(mpba)_{3}\}^{3-}$ metallo-linkers in the example of the structure of 2, $[Zn_6\{Cu^{I}_{3}(mpba)_3\}_4(DMF)_5]$, with its four crystallographically different $Cu^{I}_{3}(mpba)_{3}\}^{3-}$ metallo-linkers. The plane through the three Cu atoms is shown in blue. The lines from the carboxylate C-atoms to the Cu_3 centroid (white atom) are given in pink.

References

1 M. R. Bryant, A. D. Burrows, C. M. Fitchett, C. S. Hawes, S. O. Hunter, L. L. Keenan, D. J. Kelly, P. E. Kruger, M. F. Mahon and C. Richardson, *Dalton Trans.*, 2015, **44**, 9269–9280.

2 O. V Dolomanov, L. J. Bourhis, R. J. Gildea, J. A. K. Howard and H. Puschmann, *J. Appl. Crystallogr.*, 2009, **42**, 339–341.

3 A. L. Spek, Structure Validation in Chemical Crystallography, Acta Crystallogr., Sect. D: Biol. Crystallogr., 2009, **65**, 148–155; A. L. Spek, PLATON– *A Multipurpose Crystallographic Tool*, Utrecht University, Utrecht, TheNetherlands, 2008; Windows implementation; L. J. Farrugia, Version 280317, University of Glasgow, Scotland, 2020.

4 V. A. Blatov and D. M. Proserpio, *Acta Crystallogr., Sect. A*, 2009, **A65**, 202-212.

5 Database NIST Chemistry WebBook; 25.06.2019; link https://webbook.nist.gov/chemistry/ accessed 13.24 h.

6 CrystalExplorer21.5, Version 21.5; M. J. Turner, J. J. McKinnon, S. K. Wolff, D. J. Grimwood, P. R. Spackman, D. Jayatilaka and M. A. Spackman, © 2005-2021 University of Western Australia, 2021. https://crystalexplorer.net/

7 Turner, M. J.; McKinnon, J. J.; Jayatilaka, D.; Spackman, M. A. Visualisation and Characterisation of Voids in Crystalline Materials. *CrystEngComm*, 2011, **13**, 1804–1813.

8 Mercury 2021.2.0, Program for Crystal Structure Visualisation, Exploration and Analysis from the Cambridge Crystallographic Data Center, Copyright CCDC 2001-2021, http://www.ccdc.cam.ac.uk/mercury/

9 Mercury 4.0: from visualization to analysis, design and prediction C. F. Macrae, I. Sovago, S. J. Cottrell, P. T. A. Galek, P. McCabe, E. Pidcock, M. Platings, G. P. Shields, J. S. Stevens, M. Towler and P. A. Wood, *J. Appl. Cryst.*, 2020, **53**, 226-235. [DOI: 10.1107/S1600576719014092]

10 I. M. Hauptvogel, V. Bon, R. Grünker, I. A. Baburin, I. Senkovska, U. Mueller and S. Kaskel, *Dalton Trans.*, 2021, **41**, 4172-4179.

11 S. Lee, H.-B. Bürgi, S. A. Alshmiri and O. M. Yaghi, *J. Am. Chem. Soc.*, 2018, **140**, 8958-8964.

4 Zusammenfassung

Im Rahmen dieser Arbeit wurden neue Metall-organische Gerüstverbindungen auf Basis des N,O-heteroditopen, bifunktionellen Liganden 4-(3,5-Dimethyl-1*H*-pyrazol-4-yl)benzoesäure (H_2mpba) synthetisiert. Dies geschah unter der Annahme, dass der Ligand aufgrund seiner Bifunktionalität und des hart/weichen Charakters in der Lage ist verschiedene Metallkonnektivitäten einzugehen. Als Basis Metall wurde Kupfer verwendet, da aus vorangegangenen Arbeiten bekannt war, dass der Ligand mit diesem Metall koordiniert. Konsequenterweise wurden dann zuerst Versuche unternommen, um reine kupferhaltige Verbindungen mit diesem Liganden zu erhalten. Aus der Reaktion zwischen dem Liganden und $Cu(NO_3)_2 \cdot 2.5H_2O$ in einem DMF/H_2O- und einem ACN/H_2O-Gemisch sind die beiden neuen **sql** 2D MOFs [Cu(H_2mpba)$_2$]·L (L = DMF oder ACN) erhalten worden. Diese beiden Verbindungen sind supramolekulare Isomere des bereits Literatur bekannten 3D **lvt**-Netzwerkes [Cu(H_2mpba)$_2$]·4MeOH·1H_2O von Richardson *et al*. Die beiden neuen Verbindungen sowie die bereits bekannte Verbindung konnten anhand von Gassorptionsmessungen (CO_2 und CH_4) als mikroporöse Materialien klassifiziert werden. Alle drei Materialien zeigten nach der Aktivierung gute CO_2-Adsorptionskapazitäten mit Sättigungsaufnahmen von 113 cm^3/g (**lvt**-MeOH-act.), 111 cm^3/g (**sql**-DMF-act.) und 90 cm^3/g (**sql**-ACN-act.). Die Flexibilität des **lvt**-MeOH-act.-Netzwerkes kam dabei durch einen Gate-Opening-Effekt bei der 195 K CO_2-Messung und bei der gravimetrischen Hochdruck-CO_2-Messung zum Ausdruck. Die beiden anderen Verbindungen zeigten bei dieser Temperatur hingegen eine Typ-I-Isotherme mit einer bemerkenswerten Hysterese.

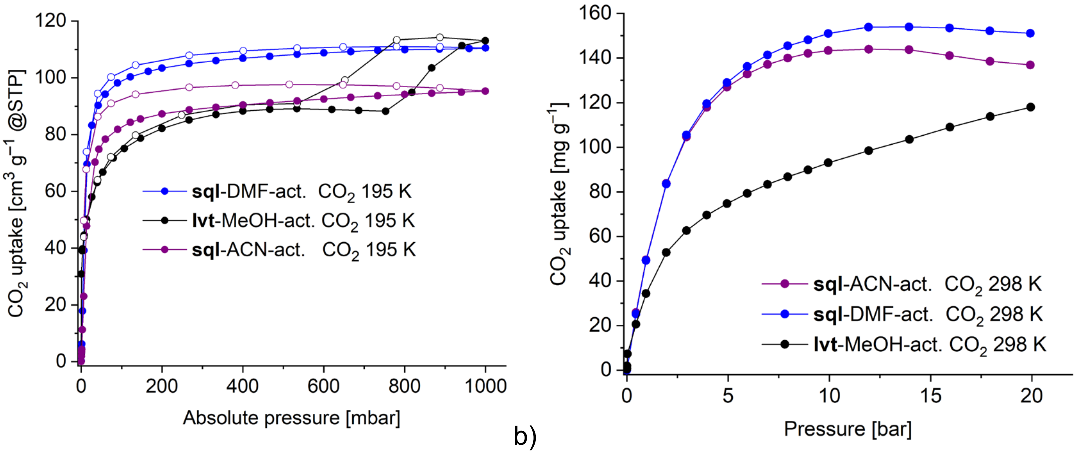

a)

b)

Abbildung 13: a) CO$_2$-Sorptionsisothermen von **lvt**-MeOH-act., **sql**-DMF-act. und **sql**-ACN-act. bei 195 K. (b) Hochdruck-CO$_2$-Adsorptionsisothermen von **lvt**-MeOH-act., **sql**-DMF-act. und **sql**-ACN-act. bei 298 K.

Die geringere CO$_2$-Aufnahme für **sql**-ACN-act. im Vergleich zu **sql**-DMF-act. spiegelte die engeren Poren und das geringere Porenvolumen wider, welche aufgrund des etwas unterschiedlichen Schichtpackungsmusters (AA‘ für **sql**-DMF und AB für **sql**-ACN.) zu Stande kam.

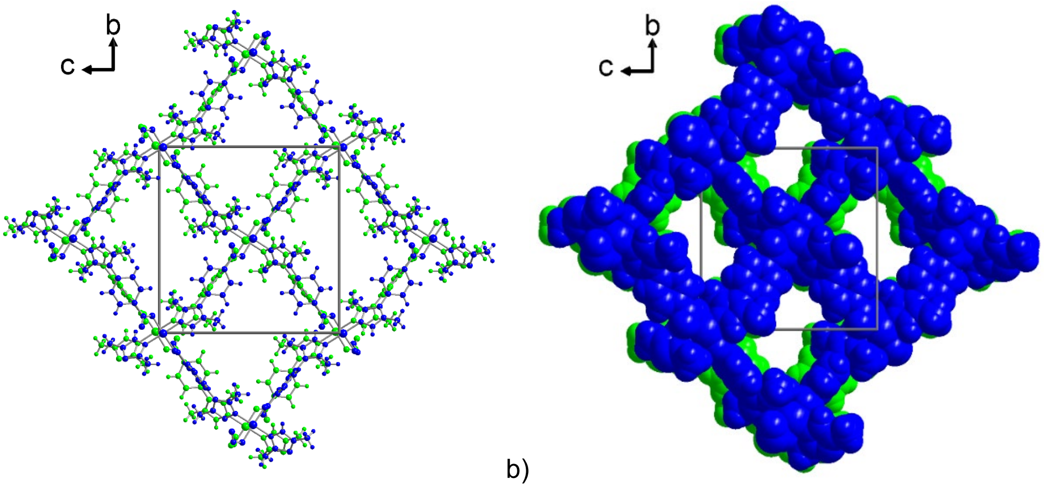

a)

b)

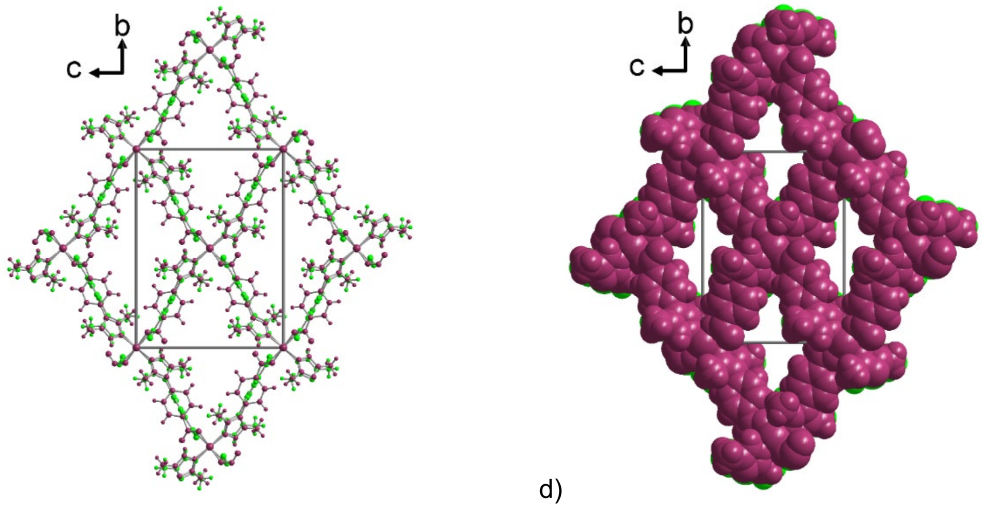

c) d)

Abbildung 14: Inversionssymmetrische AA'-Stapelung der Netze entlang der *a*-Richtung in **sql**-DMF in (a) ball-and-stick und (b) Space-Filling-Darstellung. AB-Stapelung von zwei symmetrieunabhängigen A- und B-Netzen entlang der *a*-Achse in **sql**-ACN in (c) Ball-and-Stick- und (d) Space-Filling-Darstellung.

Nach der Durchführung der Wasser- und Ethanol-Sorptionsmessungen konnten die neuen **sql**-Verbindungen im Gegensatz zur hydrophilen **lvt**-Verbindung als hydrophob eingestuft werden. Die Hydrophilie der **lvt**-Verbindung ist so weitreichend, dass das kristalline Lösungsmittel vollständig durch Wasser ausgetauscht werden konnte, wodurch ein reines Wassernetzwerk (**lvt**-H_2O), welches 3D-Anordnungen von S_4-symmetrischen $(H_2O)_{20}$-Clustern enthält, synthetisiert werden konnte. Dieser grundlegend verschiedener chemischer Charakter der Materialien ist bedingt durch den entscheidenden strukturellen Unterschied zwischen den supramolekularen **sql**- und **lvt**-[Cu(Hmpba)$_2$]-Isomeren. Die NH-Gruppe des Pyrazolrestes ist bei beiden **sql**-Verbindungen an der H-Brückenbindung zwischen den Netzwerken beteiligt, wohingegen diese bei den beiden **lvt**-Verbindungen an der H-Bindung im Kristallwasser beteiligt ist.

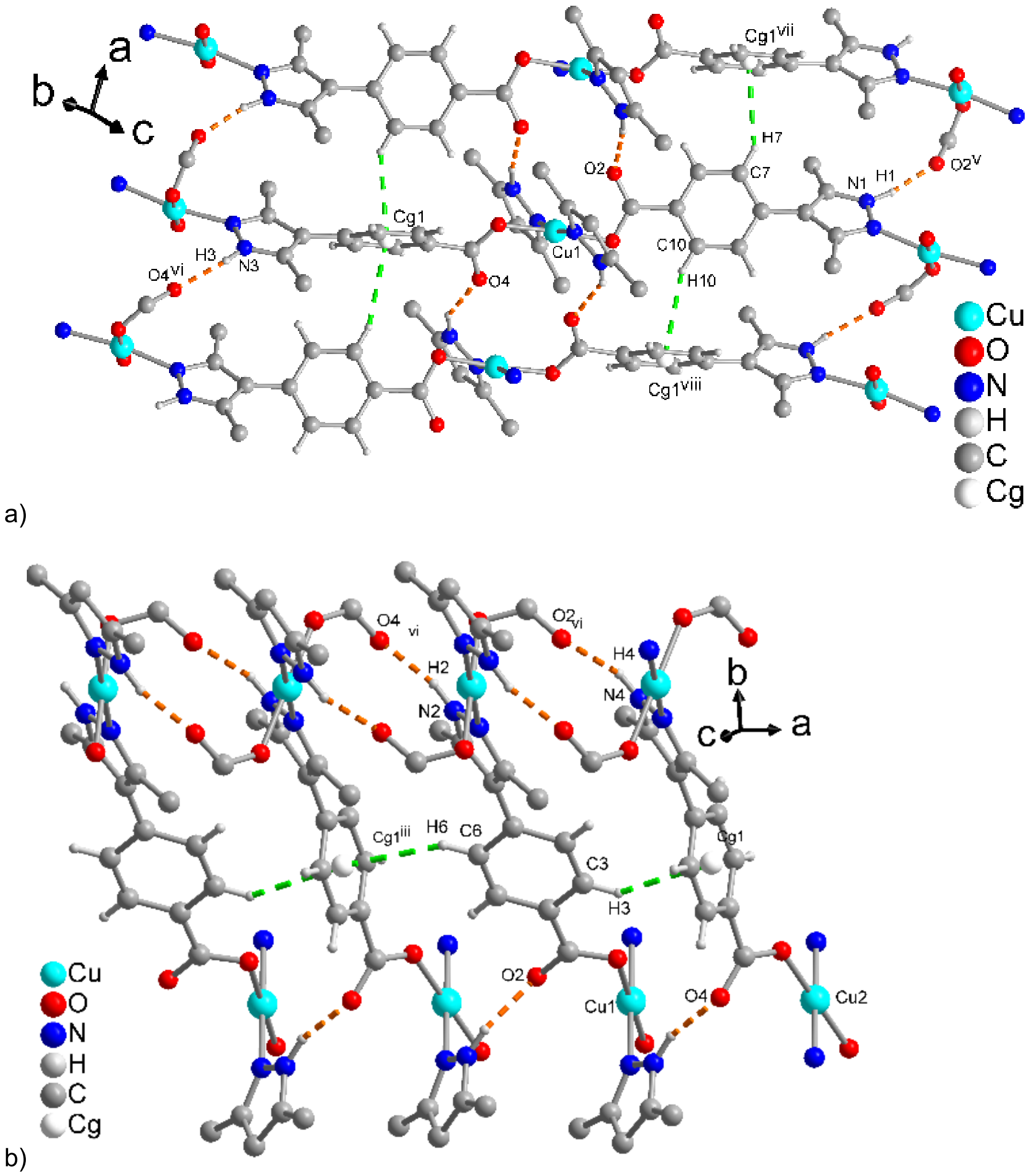
a)
a
b
c
Cg1vii
H7
C7
O2
N1
H1
O2v
Cg1
H3
N3
O4vi
Cu1
C10
H10
O4
Cg1viii
Cu
O
N
H
C
Cg
b)
O4 vi
O2 vi
H2
H4
N2
N4
b
c
a
Cg1iii
H6
C6
C3
H3
Cg1
O2
Cu1
O4
Cu2
Cu
O
N
H
C
Cg

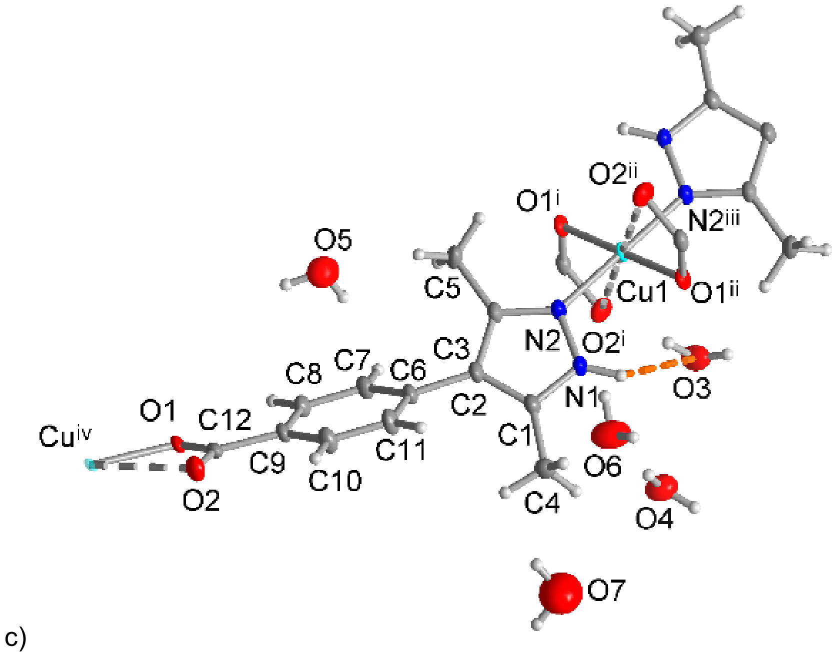

Abbildung 15: Darstellung der CH-π-Wechselwirkungen zwischen den einzelnen Schichten (grün-gestrichelte Linien) und der N-H···O-Wasserstoffbrücken (orange-gestrichelte Linien) in (a) **sql**-DMF und in (b) **sql**-ACN und (c) Metall-Ligand-Koordination in **lvt**-H_2O (H-Bindung in oranger gestrichelter Linie. 50% thermische Ellipsoide). Symmetrieumwandlungen: i = y-3/4, -x+3/4, -z+3/4; ii = -y+3/4, x+1/4, z-3/4; iii = -x, -y+1, -z; iv = y-1/4, -x+3/4, z+3/4).

Die erhaltenen $[M(Hmpba)_2]\cdot$Lösungsmittel Materialien sind relativ seltene Beispiele für supramolekulare Gerüstisomere, bei denen die Isomerie in den Gerüsten durch subtile Veränderungen der H-Bindung um die Metallzentren herum bedingt wird und somit zu erheblichen strukturellen Veränderungen der Strukturen und der Sorptionseigenschaften führte. Dieser Unterschied wurde durch die Verwendung des heteroditopen Liganden in Verbindungen mit den unterschiedlichen Synthesebedingungen (Lösungsmittel-Templating-Effekt) ausgelöst.

Ein gemischt-valentes, eindimensionales $Cu^{I/II}$-Koordinationspolymer mit der Formel $[Cu^{II}\{Cu^{I}_3(Hmpba)(mpba)_2\}DMF]\cdot{\sim}3DMF$ mit dem bifunktionellen Liganden 4-(3,5-Dimethyl-1*H*-pyrazol-4-yl)benzoesäure wurde unter Beibehaltung des Metalls (Kupfer), DMF als Lösungsmittel und unter Einsatz eines Modulators (HBF_4) durch solvothermale Reaktion erhalten. Die Konnektivität der Stickstoff- und Sauerstoffdonoratome des Liganden folgte des HSAB-Prinzips, so dass sich das in situ gebildete eher weiche Cu^{I} mit den weicheren Pyrazolat-Stickstoff-Donoratomen zu einem $\{Cu^{I}_3(Hmpba)(mpba)_2\}^{2-}$ Metallo-Linker verbindet. Dieser Metallo-Linker hat dann die härteren Cu^{II}-Ionen über seine freien eher härteren Carboxylatgruppen zu einer Kettenstruktur verbunden. Zwei Cu^{II}-Ionen bilden eine Schaufelradeinheit ähnlich derer in HKUST-1, sodass die Cu^{II}-Ionen fünffach koordiniert mit einem terminalen DMF-Ligand-Molekül sind. Die gebildeten parallelen Ketten sind durch das gemeinsame $R_2^2(8)$-Wasserstoffbrückenmotiv der einfach deprotonierten Carboxylatgruppen des heteroditopen Liganden zu supramolekularen 2D Schichten verbunden. Diese Schichten werden durch kurze Cu^I-Cu^I- (d^{10}-d^{10}) Kontakte zu einem supramolekularen 3D-Gerüst organisiert. Die Wasserstoffbrückenbindung der 1D-Stränge führt zu einem Netzt von bex, d.h es lag eine 3,4L13-Topologie vor. Das Vorhandensein von Cu^I und Cu^{II} konnte durch eine XPS-Messung nachgewiesen werden. Beim Vergleich mit der Literatur stellte sich die erhaltene Verbindung als Vorstufe zum PCN-91 von *Wei et al.* heraus.

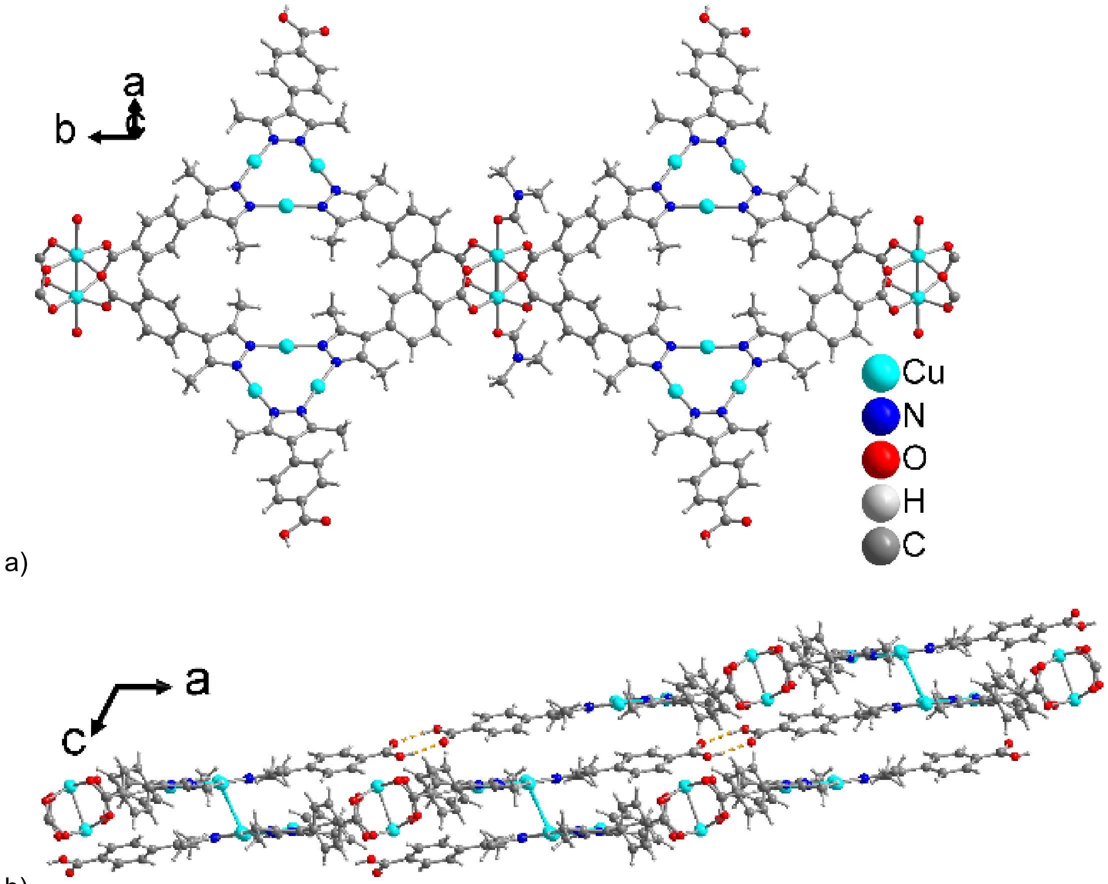

a)

b)

Abbildung 16: a) Schnitt durch den 1D-Netzwerkstrang aus zweikernigen Schaufelradeinheiten und den verbrückenden Metallo-Linkern. b) Stapelung von drei der supermolekularen 2D-Schichten mit den interschicht $Cu^I \cdots Cu^I$-Kontakten (cyane Linien) sowie den H-Brücken-Kontakten (orange, gestrichelte Linie).

Durch den Einsatz von Zink als zweites Metallion, unter Beibehaltung des Basismetalls Kupfer, DMF als Lösungsmittel, den solvothermalen Bedingungen und ggf. durch Einsatz eines Additivs (HBF_4) konnten anschließend drei weitere Verbindungen hergestellt werden. Die drei erhaltenen bimetallischen MOFs

$[Me_2NH_2][Zn_4\{Cu^I_3(mpba)_3\}_3Me_2NH(DMF)_2]$ (**1**), $[Zn_6\{Cu^I_3(mpba)_3\}_4(DMF)_5$ (**2**) und $[\{Zn_3\{Cu^I_3(mpba)_3\}_2(DMF)_3(H_2O)][Zn_4(\mu_4\text{-}O)\{Cu^I_3(mpba)_3\}_2(H_2O)_4]$ (**3**) enthalten alle den dreieckigen und dreikernigen 3-c $\{Cu^I_3(mpba)_3\}^{3-}$ Metallzyklus, welcher als Tricarboxylat-Linker zwischen den verschiedenen 4-6-c $\{Zn_x(O)_y(COO)_z\}$ (x=2-4, y=0-1, z=4-6) Sekundärbausteinen fungiert. Dies ist möglich, da aufgrund der HSAB-Hart-/Weichmetall-Liganden Selektivität die in situ gebildeten weicheren Cu^I-Atome mit den weicheren Pyrazolat-Stickstoffdonoratomen des Pyrazolat-Carboxylat-Liganden koordinieren und sich die eher härteren Carboxylatgruppen mit den Zn-Atomen verknüpfen. Da der dreieckige und dreikernige $\{Cu^I_3(mpba)_3\}^{3-}$ Metallzyklus als Tricarboxylat-Linker zwischen den Zn_X-Knoten fungiert, konnte er als eine erweiterte Version des Benzol-1,3,5-tricarboxylat-Linkers betrachtet werden.

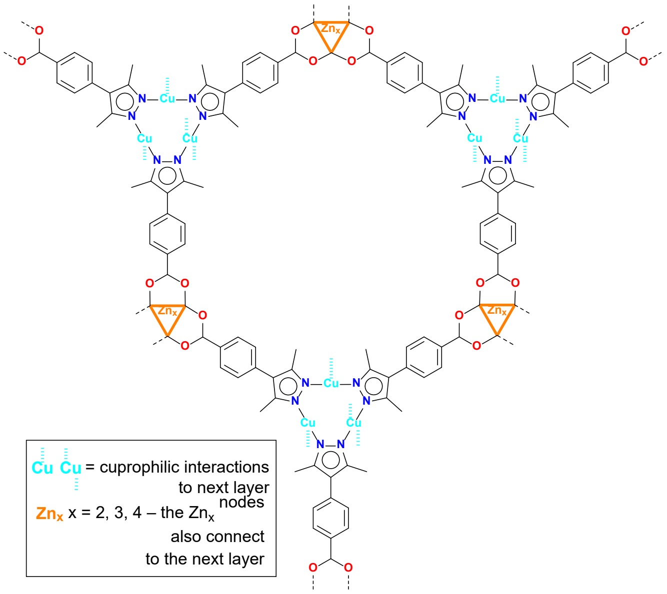

Schema 1: Gemeinsame Strukturmerkmale der Verbindungen **1-3** mit Zn_x-Knoten unterschiedlicher Nuklearität (x = 2-4) und den trigonalen $\{Cu^I_3(mpba)_3\}$-Knoten, die eine hexagonal-ringförmige Schicht ergeben. Sowohl die Zn_x-Knoten als auch die kuprophilen Wechselwirkungen von $\{Cu^I_3(mpba)_3\}$ verbinden sich mit der nächsten Schicht.

In allen drei Strukturen ist der $\{Cu^I_3(pz)_3\}$ -Anteil durch kuprophile Wechselwirkungen in unendliche Säulen gestapelt, was auf die anfängliche Bildung des $\{Cu^I_3(mpba)_3\}^{3-}$ Metallo-Liganden hindeutete. Die geometrisch variablen Zn-Cluster (schaufelrad, pyramidisch und trigonal-prismatisch) passten sich der gestapelten Orientierung der Carboxylatgruppen der $\{Cu^I_3(mpba)_3\}^{3-}$ Metallzyklen an. Daraus resultierte, dass die gebildeten Strukturen als Ableitung von gestapelten, hexagonalen, wabenförmigen **hcb**-Netzen betrachtet werden konnten, die durch ‚Fusion' von alternierenden gestapelten Knoten entstanden sind. Hinsichtlich ihrer Topologie enthalten alle Strukturen nur einen Netzwerktyp und stellen offene Strukturen da. Die kristallographisch unterschiedlichen Cu-basierten Knoten sind strukturell und in den meisten Fällen topologisch äquivalent mit Ausnahme von Verbindung **1**, wo es zwei topologisch unterschiedliche Cu-Knoten unter drei kristallographisch unterschiedlichen gibt. Die Zn-basierten Knoten sind in allen drei Strukturen unterschiedlich, mit Ausnahme der topologischen Äquivalenz der beiden unterschiedlichen Knoten in der Struktur von **3**. Sie wirken als tetraedrischer 4-c und tetragonal-pyramidaler 5-c Knoten in **1** und trigonal-prismatisch 6-c Knoten in **2** und **3**.

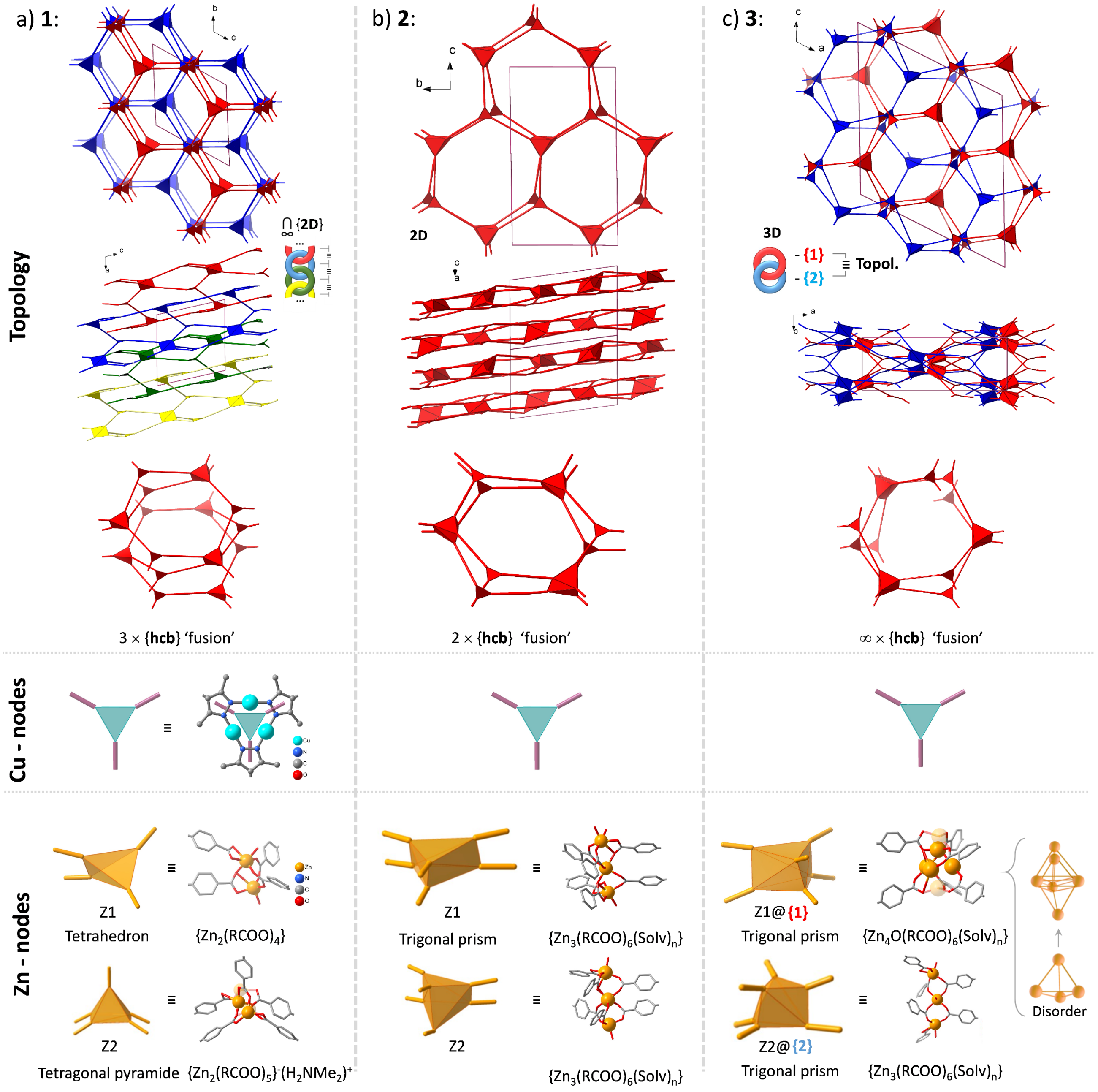

Abbildung 17: Topologischer Überblick über die Strukturen **1-3**.

Verbindung **2** weist 2D-Schichten mit einem doppelsträngigen **hcb**-Netzt auf, wohingegen Verbindung **1** aus paarweise, parallelen, interpenetrierenden 2D+2D-Netzen besteht. Diese Netze sind durch Kettenverlängerung zu einer topologischen 3D-Struktur verbunden. Verbindung **3** stellt ein Paar interpenetrierter 3D+3D-Netze da und konnte trotz der auftretenden Interpenetration unter Erhalt einer signifikanten Porosität aktiviert werden. Um eine permanente Porosität zu demonstrieren, wurde das MOF sowohl einer Ar- als auch einer CO_2- und CH_4-Sorptionsmessung unterzogen. Anhand der Ar-basierten 87 K Messung konnte eine BET-Oberfläche von 762 m^2/g determiniert werden. Das Material besaß ein Gesamtporenvolumen von 0.30 cm^3/g bei einem relativen Druck von $P/P_0 = 0.95$ und ein Mikroporenvolumen von 0.25 cm^3/g bei einem relativen Druck von $P/P_0 = 0.1$. Die Adsorptionsisotherme folgte einer Typ-I-Isotherme. Die Desorption zeigte eine kleine Hystereseschleife (Typ H4) was typisch für mikro-mesoporöse Materialien ist. Darüber hinaus konnte eine CO_2-Adsorptionskapazität bei 1 bar von 78 cm^3/g (273 K) und 46 cm^3/g (293 K) gemessen werden. Wie erwartet lagen die CH_4-Adsorptionskapazitäten mit 15 cm^3/g (273 K) und 14 cm^3 /g (293 K) bei 1 bar unterhalb derer von CO_2. Konsequenterweise ergab sich somit eine höhere CO_2 Selektivität gegenüber CH_4 (4.8:1 bei 273 K und 3.5:1 bei 293 K).

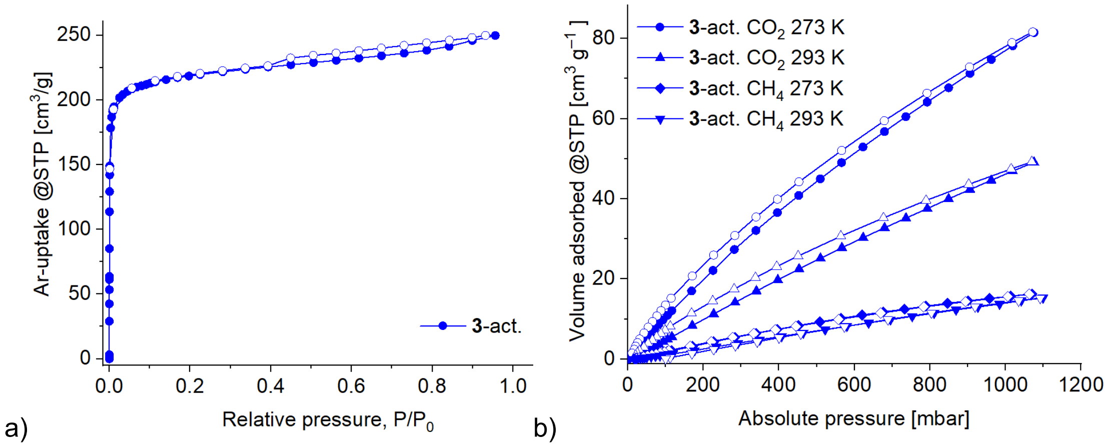

Abbildung 18: a) Ar-Sorptionsmessung bei 87 K; b) CO_2 und CH_4-Isothermen bei 293 K und 273 K.

Zusammenfassend kann herausgestellt werden, dass im Rahmen dieser Doktorarbeit eine Reihe an neuen kupferhaltigen Netzwerkstrukturen mit dem bifunktionellen H_2mpba Liganden synthetisiert wurden. Zur Vorhersage der grundsätzlichen Verknüpfungswahrscheinlichkeit zwischen dem Metall bzw. den Metallen und den funktionellen Gruppen des Liganden in den gemischt-valenten und bimetallischen Verbindungen konnte das HSAB-Konzept wertvolle Erkenntnisse liefern. Gerade die

Synthese von Mischmetall-MOFs basierend auf heteroditopen Liganden gewinnt zunehmend an Interesse aufgrund der Vielzahl an Variationsmöglichkeiten und daraus resultieren Eigenschaften und Anwendungsbereichen.

5 NMR-Kooperationsarbeiten mit Prof. Dr. Gerhard Hägele

Als kleines Randprojekt wurde innerhalb der Promotionszeit in einer Kooperation mit *Prof. Dr. Gerhard Hägele* die Ligandklasse der Phosphonate hinsichtlich der NMR-spektroskopischen Eigenschaften untersucht. Dazu wurde zunächst das $[AX]_3$-Spinsystem der deprotonierten 1,3,5-Benzoltriphosphonsäure untersucht. Anschließend sollte die 2-Phosphonobenzoesäure und die 4-Phosphonobenzoesäure synthetisiert werden und anschließend auch NMR-spektroskopisch untersucht werden. Die Bibliografie und die Nummerierung von Abbildungen und Tabellen ist eine Fortsetzung aus dem einleitenden Kapitel Nummer 1.

5.1 Einführung in die NMR-Spektroskopie

Die Kernspinresonanz-Spektroskopie (Nuclear Magnetic Resonance (NMR-Spectroscopy) ist eine gängige Analysemethode zur Strukturaufklärung von unter anderem organischen Molekülen. Die grundlegende Verfahrensweise wurde 1946 von den beiden Arbeitsgruppen Bloch und Purcell unabhängig voneinander publiziert und 1952 mit dem Nobelpreis in Physik ausgezeichnet. 1991 und 2002 ging der Nobelpreis in Chemie und Biochemie an R.R. Ernst und K. Wüthrich, die beide wichtige Beiträge zur Entwicklung der NMR-Strukturbestimmungsmethoden leisteten. 2003 erhielt P. Lauterbur zusammen mit P. Mansfield den Nobelpreis in Medizin, welche den Grundstein für die heutige MRT-Diagnostik (Magnetresonanztomographie) gelegt hatten. Anhand dieser rasanten zeitlichen Entwicklung und den erhaltenen Auszeichnungen wird die Wichtigkeit dieser Methode deutlich unterstrichen.

Die NMR-Spektroskopie basiert auf den magnetischen Eigenschaften der Atomkerne. Atomkerne bestehen unter anderem aus Protonen und Neutronen, die einen eigenen Drehimpuls (Spin) besitzen. Der Kernspin des Atoms setzt sich dabei additiv aus den Einzelspins der Nukleonen zusammen und muss für eine NMR-Detektion größer null sein. Leicht verständlich sind Spektren von Systemen mit Spins ½. Somit sind für eine NMR-spektroskopische Untersuchung besonders die Kerne ^{1}H, ^{13}C, ^{19}F und ^{31}P geeignet.

Ohne Anlegen eines äußeren Magnetfeldes besitzen alle magnetischen Kerne die gleiche Energie E_0, jedoch unterscheiden sie sich in der Richtung ihrer Drehimpulse.

Die Kerne sind somit entartet. Durch das Anlegen eines äußeren Magnetfeldes richten sich die Kernspins in eine Richtung aus; die Entartung wird aufgehoben. Dabei können sich die Kerne entweder mit (parallel) oder gegen (antiparallel) das Magnetfeld ausrichten, so dass sich das Energieniveau der Kerne von E_0 auf E_α (parallele Kernausrichtung) oder E_β (antiparallele Kernausrichtung) ändert. Dabei ist die Energiedifferenz der beiden resultierenden Energieniveaus E_α und E_β proportional zur Stärke des Magnetfeldes. Wird jetzt durch ein hochfrequentes elektromagnetisches Wechselfeld genau die Energie zugeführt, die dem Abstand der beiden Niveaus entspricht, tritt Resonanz zwischen dem eingestrahlten Wechselfeld und den Kernen ein. Das bedeutet, dass die Kerne von E_α nach E_β angeregt werden können (Adsorption) oder von E_β nach E_α zurückfallen können (induzierte Emission). Dabei ist ein Strom messbar, welcher sich in einem eindimensionalen Spektrum (Auftragung Frequenz (Hz oder ppm) gegen Intensität) als Peak bemerkbar macht. Allerdings werden durch die Elektronenhülle der Atome die Kerne vom äußeren Magnetfeld unterschiedlich stark abgeschirmt. Dadurch kommt es zu einer geringeren bzw. höheren effektiven Feldstärke (H_{eff}) am Kern. Deshalb beeinflussen benachbarte Atome oder Atomgruppen durch ihre induktiven oder mesomeren Effekte die Aufspaltung der Kernenergieniveaus und erwirken somit eine Verschiebung der Signale im Spektrum.

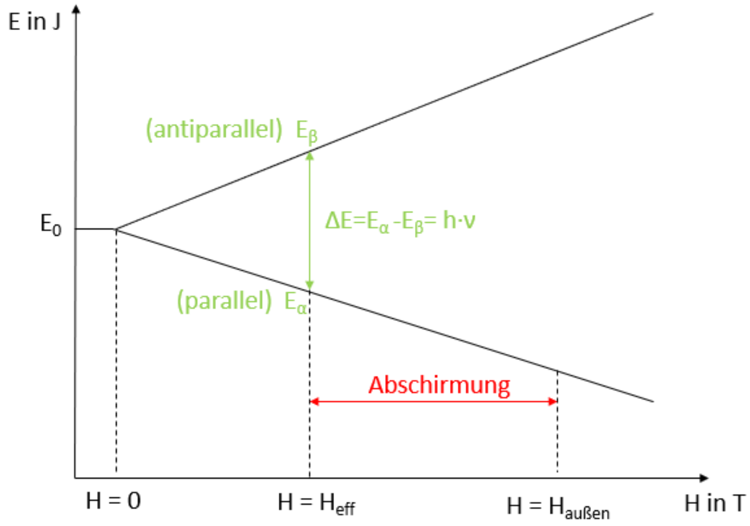

Schema 2: Energie der Kernorientierungen in Abhängigkeit von der magnetischen Feldstärke.

Mit der Veränderung der chemischen Umgebung geht somit eine Verschiebung der Resonanzfrequenz des betrachteten Kerns einher. Elektronenziehende Umgebungen wie z.B Sauerstoffatome verschieben das Signal von Protonen zu höherem ppm-Bereich, da die Abschirmung geringer wird. Alkyl-Gruppen hingegen erscheinen eher rechts im Spektrum. Aus dieser chemischen Verschiebung und dem Phänomen der Kopplung resultieren die NMR-Struktur-Informationen, welche zur Molekülstrukturaufklärung verwendet werden können. Die empfangenen Signale erlauben dabei Aussagen darüber zu treffen wie viel NMR-aktive Kerne vorhanden sind und wie ihre Bindungssituation ist. Es lassen sich so Einfach- und Mehrfachbindungen sowie Anzahl und Art der Bindungspartner eindeutig nachweisen und funktionelle Gruppen identifizieren. Die Aufspaltung der Signale in die Feinstruktur entsteht durch mögliche Kopplung der magnetischen Momente der benachbarten Kerne. Man unterscheidet dabei z.B zwischen einem Singulett (s), Doublett (d), Triplett (t), Quartett (q) oder Multiplett (m). Dadurch können Informationen über den nächsten Nachbarn der jeweiligen Atome/Atomgruppen erhalten werden.

Miteinander koppelnde Kerne bzw. Kerngruppen werden Spinsysteme genannt. Bei Spinsystemen mit magnetisch äquivalenten Kernen kann eine Einteilung gemäß A_2, A_3, A_4… erfolgen. Handelt es sich um ein Spinsystem mit chemisch aber nicht magnetisch äquivalenten Kernen, wird eine Kennzeichnung mit AA‘ oder XX‘ vorgenommen. Ist eine Verbindung aus mehreren Spinsystemen aufgebaut, so besteht das gemessene Spektrum aus ebenso vielen Teilspektren und es erfolgt eine Mischnotation der Spinsysteme. Anhand des Spinsystems kann festgestellt werden, ob es sich um ein Spektrum nullter, erster oder höherer Ordnung handelt. Gerade die Analyse von symmetrischen Spinsystemen und entsprechenden NMR-Spektren ist schon seit den NMR-Anfängen von Interesse.

Um entsprechenden Molekülstrukturinformationen aus einem NMR-Spektrum zu gewinnen, sollte das Spektrum möglichst hochaufgelöst sein. Hochaufgelöst bedeutet, dass die Linien möglichst schmal (scharf) sind und eine gute Differenzierbarkeit von eng benachbarten Linien vorliegt. Um das zu erreichen, ist unter anderem die Probenpräparation entscheidend. Bei Flüssig-NMR-Spektroskopie, die für diese Arbeit hauptsächlich verwendet wurde, werden die Probe vollständig in einem deuteriertem Lösungsmittel gelöst. Dabei sollte die Probe klar und die Konzentration nicht zu niedrig sein. Je nach Löslichkeitsverhalten können verschiedene deuterierte Lösungsmittel verwendet werden (z.B DMSO-d_6, Aceton-d_6, D_2O, $CDCl_3$). Wichtig ist, dass der Probe immer ein Standard zugesetzt wird, damit das Spektrum leichter referenziert werden kann. Als Standard eignet sich z.B Tetramethylsilan (TMS) oder 3-(Trimethylsilyl)propionsulfonsäure Natriumsalz (TMSP). Neben der Probenvorbereitung spielt auch die Qualität der NMR-Röhrchen eine Rolle. Es gibt verschiedene Genauigkeitsklassen (economic bis scientific) bei der die Geradheit und die Fehlerabweichung der Wandstärke voneinander variieren. Die Empfindlichkeit der Messung wird mit dem Verhältnis von Signal zum Hintergrund-Rauschen (Signal-to-Noise, S/N) angegeben. Sie ist abhängig vom Magnetfeld, der Probenmenge und der Anzahl der Scans. Bei hochaufgelösten Spektren sollte die Anzahl der Scans möglichst hoch sein.

In dieser Arbeit wurde der Fokus auf die NMR-kontrollierte Titration gelegt, auch bekannt als NMR-Titration. Diese vereint NMR mit analytischen Aspekten. Die Probe 1,3,5-Benzoltriphosphonsäure wurde für die Publikation jeweils bei $\tau = 0$ (autoprolytische Säure) und $\tau = 4$ (total deprotonierte Säure) gemessen. τ gibt dabei den Titrationsgrad (degree of titration) der Säure an. Dieser ist definiert als

$$\tau = \frac{\text{Anzahl Äquivalente (1−säurige Base)}}{\text{Anzahl Mol (n−basige Säure)}} \ (1).$$

Als starke 1-säurige Base kann z.B NaOD verwendet werden.

5.2 Publizierte Arbeit

5.2.1 The fully deprotonated anion of 1,3,5-benzene-triphosphonic acid: ^1H, ^{31}P and $^{13}C\{^1H\}$ NMR and some comments on corresponding $[AX]_3$ and AXX'_2 spin systems and spectra

Die in diesem Kapitel vorgestellte Arbeit wurde publiziert in:
Saskia Menzel, Konstantinos D. Demadis, Christoph Janiak, and Gerhard Hägele
Phosphorus, Sulfur, and Silicon and the Related Elements **2020**, *195*, 830-835.
DOI: 10.1080/10426507.2020.1757675

The article is reprinted with permission of Taylor & Francis Journal.

Die nachfolgend aufgeführte Publikation beschreibt die Synthese der 1,3,5-Benzoltriphosphonsäure und dessen iterierte ^1H-, ^{31}P- and $^{13}C\{^1H\}$-NMR-Spektren. In den ^1H- und ^{31}P-NMR Spektren konnte die 1,3,5-Benzoltriphosphonsäure dabei auf ein $[AX]_3$-Spinsystem zurückgeführt werden. Die $^{13}C\{^1H\}$ -NMR-Spektren zeigten zwei ^{13}C-Iostopomere, die über AXX'_2-Systeme identifiziert werden konnten.

Anteile an der Publikation:

- Aufbereitung und Probenpräparation der von Herr Demadis hergestellten Verbindung 1,3,5-Benzoltriphosphonsäure.
- Messung der Probe in Absprache mit dem zuständigen Messoperator und Anpassung der Messparameter.
- Erste Auswertung der erhaltenen NMR-Spektren und Vergleich mit der Literatur.
- Verfassen des experimentellen Teils und Korrekturlesung des Manuskripts. Die Iteration erfolgte durch Prof. Dr. Gerhard Hägele.
- Überarbeitung, finale Abstimmung und Revision des Manuskripts wurde in Zusammenarbeit mit Herrn Prof. Dr. Christoph Janiak und Prof. Dr. Gerhard Hägele durchgeführt.

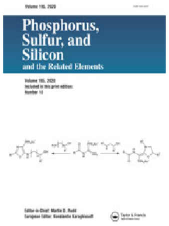

Phosphorus, Sulfur, and Silicon and the Related Elements

ISSN: 1042-6507 (Print) 1563-5325 (Online) Journal homepage: https://www.tandfonline.com/loi/gpss20

The fully deprotonated anion of 1,3,5-benzene-triphosphonic acid: ^{1}H, ^{31}P, and ^{13}C{^{1}H} NMR and some comments on corresponding [AX]$_3$ and AXX'$_2$ spin systems and spectra

Saskia Menzel, Konstantinos D. Demadis, Christoph Janiak & Gerhard Hägele

To cite this article: Saskia Menzel, Konstantinos D. Demadis, Christoph Janiak & Gerhard Hägele (2020) The fully deprotonated anion of 1,3,5-benzene-triphosphonic acid: ^{1}H, ^{31}P, and ^{13}C{^{1}H} NMR and some comments on corresponding [AX]$_3$ and AXX′$_2$ spin systems and spectra, Phosphorus, Sulfur, and Silicon and the Related Elements, 195:10, 830-835, DOI: 10.1080/10426507.2020.1757675

To link to this article: https://doi.org/10.1080/10426507.2020.1757675

PHOSPHORUS, SULFUR, AND SILICON AND THE RELATED ELEMENTS
2020, VOL. 195, NO. 10, 830–835
https://doi.org/10.1080/10426507.2020.1757675

The fully deprotonated anion of 1,3,5-benzene-triphosphonic acid: ^{1}H, ^{31}P, and ^{13}C{^{1}H} NMR and some comments on corresponding $[AX]_3$ and AXX'_2 spin systems and spectra

Saskia Menzel[a], Konstantinos D. Demadis[b], Christoph Janiak[a], and Gerhard Hägele[a]

[a]Institut für Anorganische und Strukturchemie, Heinrich-Heine-Universität Düsseldorf, Universitätsstraße 1, Düsseldorf, Germany;
[b]Department of Chemistry, University of Crete, Voutes Campus, Crystal Engineering, Growth and Design Laboratory, Heraklion, Greece

ABSTRACT

The fully deprotonated anion of 1,3,5-benzene-triphosphonic acid 1,3,5-$C_6H_3[PO_3{}^{2-}]_3$ gives rise to deceptively simple ^{1}H and ^{31}P NMR spectra due to a corresponding $[AX]_3$ spin system. The ^{13}C{^{1}H} NMR spectrum reveals two ^{13}C isotopomers which are identified *via* AXX'_2 systems. Results from analysis and iteration are described.

ARTICLE HISTORY
Received 28 February 2020
Accepted 7 April 2020

KEYWORDS
1,3,5-Benzene-triphosphonic acid; $[AX]_3$; AXX'_2; ^{1}H; ^{31}P; ^{13}C{^{1}H}

GRAPHICAL ABSTRACT

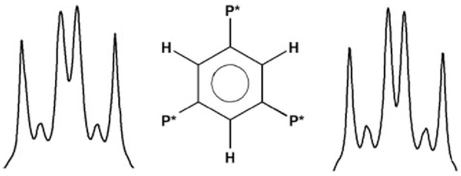

Introduction

The analysis of symmetric spin systems and corresponding NMR spectra has attracted interest since the early days of NMR spectroscopy.[1,2] Computer programs were developed for the simulation and iteration of NMR spectra involving chemical and magnetic equivalence of spins $I \geq 1/2$ and groups of spins $I \geq 1/2$ in isotropic or anisotropic solutions.[3,4] Interesting investigations focused upon fluorinated benzenes $C_6H_{6-i}F_i$ ($i = 0$–6). ^{1}H, ^{13}C, and ^{19}F NMR spectra characterized symmetric and asymmetric species.[5–10] Particular attention was drawn toward the D_{3h} symmetric 1,3,5-trifluorobenzene because of the characteristic $[AX]_3$ spin system studied by ^{1}H and ^{19}F NMR.[6] Fifty transitions are calculated for each of the ^{1}H and ^{19}F NMR spectra. Since the receptivities of both nuclear types are high and the half widths are low, excellent NMR spectra of high signal to noise (S/N) result, which justify spectral analysis based upon frequency iterations. Four coupling constants characterize this $[AX]_3$ system: $J_{AX} = {}^3J_{FH} = 9.12$ Hz, $J_{AX'} = {}^5J_{FH} = -1.68$ Hz, $J_{AA'} = {}^4J_{HH} = 2.31$ Hz, and $J_{XX'} = {}^4J_{FF} = 5.83$ Hz.[6] Those $[AX]_3$ spectra are field-invariant. ^{1}H and ^{19}F NMR spectra of 1,3,5-$C_6H_3F_3$ were simulated with WINDAISY[11] and are shown in Figure 1, where spectral centers are arbitrarily placed at 0 and −1000 Hz respectively. In this case, it is not necessary to apply the full D_{3h} symmetry for faster calculations, D_3 is sufficient for fast simulations.

Combining ^{15}N and ^{31}P nuclei in a hexachlorophosphazatriene $[^{15}NPCl_2]_3$ led to an $[AX]_3$ case, where a graphical method was applied to obtain coupling constants $J_{AX} = {}^1J_{PN}$ and $J_{XX'} = {}^2J_{PP}$ from ^{15}N and ^{31}P NMR spectra.[12] This method is restricted for cases where $J_{AX} = {}^1J_{PN}$ and $J_{AA'} = {}^2J_{NN}$ are zero. Corresponding results were obtained for $[^{15}NPR_2]_3$ where R = Br and S-Et.[12]

Figure 2 shows simulated ^{15}N and ^{31}P NMR spectra of $[^{15}NPCl_2]_3$. Twenty-three lines for the ^{15}N and 14 lines for the ^{31}P NMR spectra are calculated in Figure 2, using WINDAISY[11] and the coupling parameters $J_{AX} = {}^1J_{PN} = 31.7$ Hz, $J_{AX'} = {}^3J_{PN} = 0$ Hz, $J_{AA'} = {}^2J_{NN} = 0$ Hz, and $J_{XX'} = {}^2J_{PP} = 42.8$ Hz.[12]

Interest in spectral analysis continued and recently some remarks on $[AX]_3$ and related systems were published in a report on weak coupling between magnetically inequivalent spins.[13]

1,3,5-Benzene-triphosphonic acid and related structures

We expected that ^{1}H and ^{31}P NMR studies of 1,3,5-$C_6H_3[P(O)(OH)_2]_3$ and the corresponding deprotonated

---

CONTACT Gerhard Hägele haegele@uni-duesseldorf.de Institut für Anorganische und Strukturchemie, Heinrich-Heine-Universität Düsseldorf, Universitätsstraße 1, D-40225 Düsseldorf, Germany.

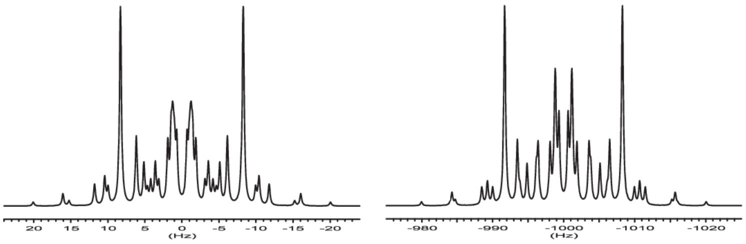

Figure 1. Simulated NMR spectra of 1,3,5-$C_6H_3F_3$. Left: ^1H NMR, A-part of $[AX]_3$. Right: ^{19}F NMR, X-part of $[AX]_3$.

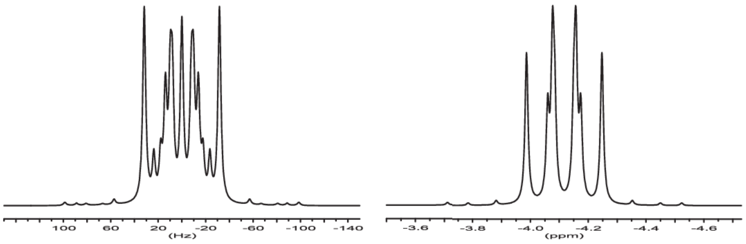

Figure 2. Simulated NMR spectra of $[^{15}NPCl_2]_3$. Left: ^{15}N NMR, A-part of $[AX]_3$. Right: ^{31}P NMR, X-part of $[AX]_3$.

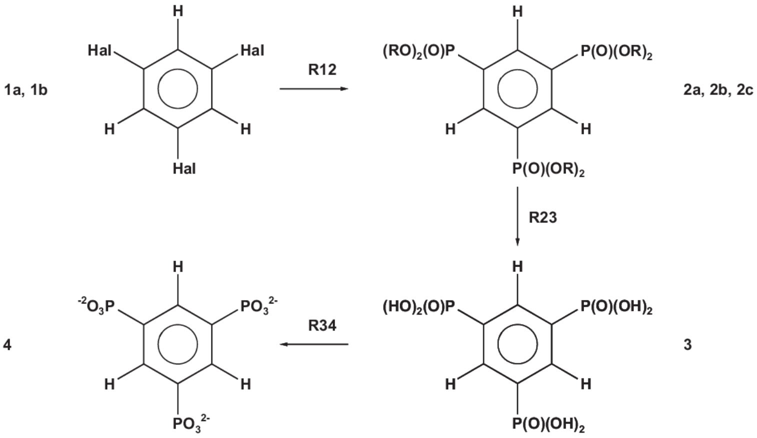

Scheme 1. 1,3,5-Benzene-triphosphonic acid **3** and related structures **2a**, **2b**, **2c**, and **4**. **1a:** Hal = Cl, **1b:** Hal = Br. **2a:** R = Me, **2b:** R = Et, **2c:** R = iPr.

anion 1,3,5-$C_6H_3[PO_3^{2-}]_3$ give rise to $[AX]_3$ spectra, characterizing molecular structures in aqueous solutions with D_{3h} symmetry. Those model compounds are accessible in reaction steps abbreviated as R12, R23, and R34 in Scheme 1.

R12 – Arbuzov reactions: An UV-activated but slow Photo-Arbuzov reaction between 1,3,5-$C_6H_3Cl_3$ **1a** and $P(OMe)_3$ leads to 1,3,5-$C_6H_3[P(O)(OMe)_2]_3$ **2a.**[14] Anhydrous $NiBr_2$ activated the faster Arbuzov reaction involving 1,3,5-$C_6H_3Br_3$ **1b** and $P(OEt)_3$ or $P(OiPr)_3$ yielding the corresponding esters 1,3,5-$C_6H_3[P(O)(OEt)_2]_3$ **2b**[15–19] and 1,3,5-$C_6H_3[P(O)(OiPr)_2]_3$ **2c.**[20,21]

R23 – Ester cleavage: 1,3,5-$C_6H_3[P(O)(OH)_2]_3$ **3** is accessible by aqueous acidolysis using conc. HCl/H_2O from methyl,[14] ethyl,[15–19] or isopropyl[15] esters (**2a**–**2c**). But it is more advantageous to apply McKenna's method[22] and cleave the isopropyl ester **2c** with $(CH_3)_3SiBr/CH_3OH$.[21]

R34 – Deprotonation: 1,3,5-Benzene-triphosphonic acid **3** is a six-basic acid of the general type H_6L. Potentiometric titrations vs. KOH were evaluated to yield pK data, titration, and molar fraction diagrams.[23] Those findings allow to conclude, that H_6L is fully deprotonated at $pH > 12$ where

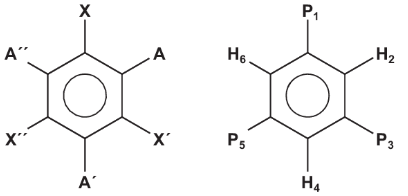

4

Scheme 2. The $[AX]_3$ spin system of the 1,3,5-benzene-triphosphonate(6⁻) anion **4**. P_1, P_3, $P_5 = PO_3^{2-}$.

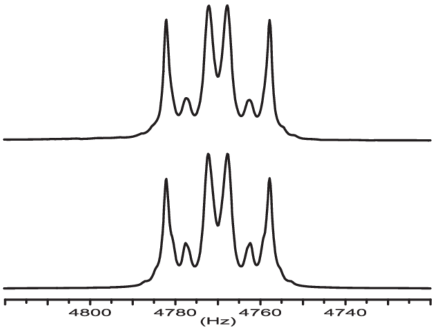

Figure 3. Iteration of the 600.13 MHz ^1H NMR spectrum of **4** using D_3 symmetry. A-part of $[AX]_3$. Upper: experimental. Lower: iterated.

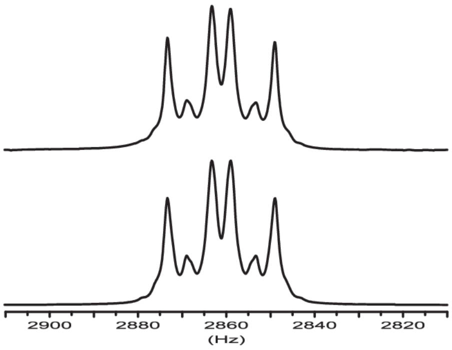

Figure 4. Iteration of the 242.94 MHz ^{31}P NMR spectrum of **4** using D_3 symmetry. X-part of $[AX]_3$. Upper: experimental. Lower: iterated.

Table 1. Results from direct analysis.

	^1H	^{31}P	
δ_H	7.948	–	ppm
δ_P	–	11.778	ppm
N_{PH}	24.280	24.296	Hz
HW (N_{PH})	1.82	2.15	Hz
Dig. res.	0.19	0.15	Hz
Frequency	600.13	242.94	MHz

the dominating species L^{6-} corresponds to the 1,3,5-benzene-triphosphonate(6⁻) anion (1,3,5-$C_6H_3[PO_3^{2-}]_3$) **4**. The degree of titration at pH 12 is calculated as $\tau = 7$.

Table 2. Results from iterations of ^1H and ^{31}P NMR spectra of **4**.

Parameter type			Data from		
			^1H iteration	^{31}P iteration	
ν_1	ν_X	ν_P	–	2861.08	Hz
ν_2	ν_A	ν_H	4769.89	–	Hz
J_{12}	J_{AX}	$^3J_{PH}$	11.40	11.49	Hz
J_{13}	$J_{XX'}$	$^4J_{PP}$	4.05	4.34	Hz
J_{14}	$J_{AX'}$	$^5J_{PH}$	1.63	1.51	Hz
J_{24}	$J_{AA'}$	$^4J_{HH}$	1.46	1.67	Hz
HWB_2	HWB_A	HWB_H	1.54	–	Hz
HWB_1	HWB_X	HWB_P	–	1.86	Hz
	N_{AX}	N_{PH}	24.42	24.49	Hz
R-factor			0.3202	0.2463	%

5

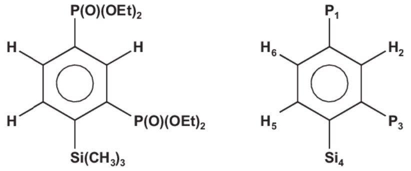

Scheme 3. $^4J_{PP}$ (P_1P_3) = 7 Hz.[24] $^3J_{PH}$ (P_1H_2 and P_3H_2) = 12 Hz[24] from 4-trimethylsilyl-1,3-benzene-bisphosphonic acid tetraethyl ester[24] **5**.

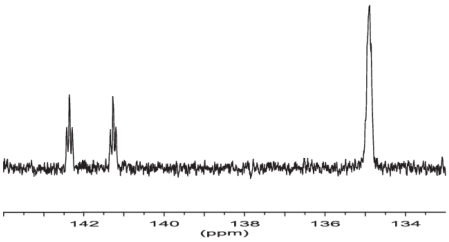

Figure 5. Proton decoupled 150.90 MHz $^{13}C\{^1H\}$ NMR spectrum of **4**. Left: A-part of AXX'_2 from C1. Right: A-part of AXX'_2 of C2 (not resolved).

Hence, it seemed justified to dissolve **3** in NaOD/D_2O to $\tau = 7$ and characterize the fully deprotonated anion L^{6-} **4** by ^1H and ^{31}P NMR spectra as shown below. Solutions from anions in D_2O give rise to narrower half widths than solutions of parent acids.

Results and discussion

The $[AX]_3$ system of 1,3,5-benzene-triphosphonate(6⁻) anion 4: ^1H and ^{31}P NMR spectra

The following section will deal with the 600.13 MHz ^1H and the 242.94 MHz ^{31}P NMR spectra using spin assignments given in Scheme 2.

Corresponding experimental spectra are shown in top traces of Figures 3 and 4, respectively. Both spectra appear as deceptively simple forms of an $[AX]_3$ system.

A total of six lines consisting of four relatively strong and two weak lines does not suffice for frequency-based iterations. Only three parameters are accessible. Both spectra are centered symmetrically at appropriate resonance frequencies (or chemical shifts). And in both spectra the significant pair of sharper outer lines is separated by a linear combination $N_{AX} = 2\,J_{AX} + J_{AX'}$ which is equivalent to $N_{PH} = 2\ {}^{3}J_{PH} + {}^{5}J_{PH}$. Results from direct analysis are listed in Table 1.

This is a classical situation where intensity based iterations are needed, which were successfully performed with WINDAISY[11] as shown in lower traces of Figures 3 and 4. Numerical results from iterations are given in Table 2.

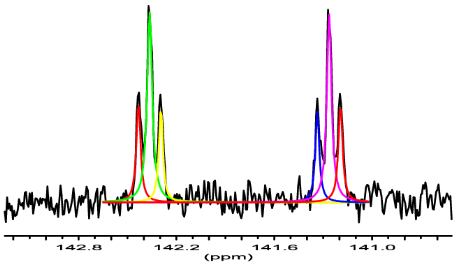

Figure 6. Proton decoupled 150.09 MHz $^{13}C\{^{1}H\}$ NMR spectrum of C1 from **4** shown with deconvolution.

The assignment of coupling constants is supported by comparison with data from 1,3,5-trifluorobenzene ($^{4}J_{HH} = 2.31$ Hz[6]) and 4-trimethylsilyl-benzene-1,3-bisphosphonic acid tetraethyl ester[24] **5** shown in Scheme 3.

Coupling constants of **4** are consistent with data from related structures. $^{4}J_{HH} = 1.46$ Hz and 1.67 Hz found from ^{1}H and ^{31}P iterations for the 1,3,5-benzene-triphosphonate(6^{-}) anion **4** is very similar to $^{4}J_{HH} = 2.31$ Hz[6] in 1,3,5-$C_6H_3F_3$. $^{4}J_{PP} = 4.05$ and 4.34 Hz of **4** is slightly smaller than $^{4}J_{PP}$ (P_1P_3) = 7 Hz[24] of 4-trimethylsilyl-benzene-1,3-bisphosphonic acid tetraethyl ester[24] **5**. Finally, $^{3}J_{PH} = 11.40$ and 11.49 Hz from **4** is very close to $^{3}J_{PH}$ (P_1H_2 and P_3H_2) = 12 Hz[24] from **5**.

Additional studies with $^{13}C\{^{1}H\}$ NMR

A proton decoupled 150.09 MHz $^{13}C\{^{1}H\}$ NMR spectrum of the 1,3,5-benzene-triphosphonate(6^{-}) anion **4** is shown in

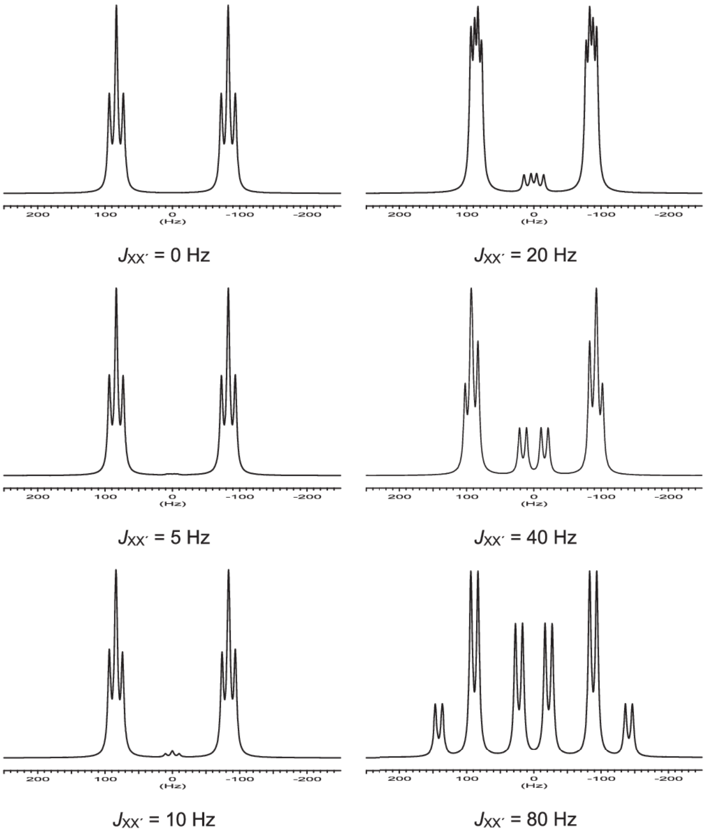

$J_{XX'}$ = 0 Hz
$J_{XX'}$ = 20 Hz
$J_{XX'}$ = 5 Hz
$J_{XX'}$ = 40 Hz
$J_{XX'}$ = 10 Hz
$J_{XX'}$ = 80 Hz

Figure 7. A-Part of a simulated AXX'_2 spectrum where ν_A is arbitrarily centered at 0 Hz. $J_{AX} = 166.2$ Hz ($^{1}J_{PC}$). $J_{AX'} = 10.6$ Hz ($^{3}J_{PC}$). $J_{XX'} = 0$–80 Hz ($^{4}J_{PP}$) in six steps. Half width $HW_A = 5$ Hz.

Figure 5 revealing deceptive simplicity. The isotopomer with ^{13}C in C1 yielded the A-part of an AXX$'_2$ spectrum, characterized by a doublet of triplets centered at $\delta_C = 141.8125$ ppm. The triplet is due to $^3J_{PC} = 10.5$ Hz while the doublet is affiliated with $^1J_{PC} = 166.2$ Hz. The averaged half width HW (C1) is calculated to 4.9 Hz. Data were obtained by deconvolution as shown in Figure 6. No second-order character for a corresponding AX$_2$Y spin system was detected, thus preventing the determination of $^3J_{PP}$ from C1 resonances. The isotopomer with ^{13}C in C2 gives rise to a broad band with HW (C2) = 16.5 Hz situated at $\delta_C = 134.9088$ ppm. Coupling constants $^2J_{PC}$ and $^4J_{PC}$ were not resolved.

It seemed interesting to compare ^{13}C{^{1}H} NMR studies of the parent compound 1,3,5-benzene-triphosphonic acid hexamethyl ester[12] **2a**. For C1 a triplet with $^3J_{PC} = 13.2$ Hz and a doublet due to $^1J_{PC} = 192.0$ Hz centered at $\delta_C = 129.01$ ppm were found while C2 was detected at 138.5 ppm and described as a multiplet.

A graphical approach to the estimation of $^4J_{PP}$ from ^{13}C{^{1}H} NMR spectra

Inspection of the experimental ^{13}C{^{1}H} NMR spectrum of the anion **4** reveals that the absolute value of $^4J_{PP}$ of **4** is very small (<5 Hz). In this case, $^4J_{PP}$ is not accessible in reliable accuracy *via* ^{13}C{^{1}H} NMR but fortunately *via* [AX]$_3$ analysis of ^{1}H and ^{31}P NMR spectra as shown in the preceding sections. For didactic purposes, a series of AXX$'_2$ simulations were performed using the following data: ν_A is arbitrarily centered at 0 Hz. Coupling constants were set to: $J_{AX} = 166.2$ Hz ($^1J_{PC}$). $J_{AX'} = 10.5$ Hz ($^3J_{PC}$) while $J_{XX'}$ varied from 0 to 80 Hz ($^4J_{PP}$) in six steps. Results are shown in Figure 7. By comparison of Figures 6 and 7 it is evident that $^4J_{PP}$ in **4** is expected to be below 5 Hz which is consistent with experimental findings from ^{1}H and ^{31}P NMR iterations.

Conclusions

The totally deprotonated anion **4** of the six-basic 1,3,5-benzene-triphosphonic acid **3** gives rise to deceptively simple ^{1}H and ^{31}P NMR spectra, each exhibiting only six broadened lines of an [AX]$_3$ system. By frequency-based iterations it is not possible to determine the four characteristic coupling constants $^3J_{PH}$, $^5J_{PH}$, $^4J_{HH}$, and $^4J_{PP}$. But intensity based total line shape analysis permits access to those parameters including chemical shifts, resonance frequencies and half widths. ^{13}C{^{1}H} NMR spectra of **5** reveal AXX$'_2$ character indicating the low values of $^4J_{PP} = J_{XX'}$.

Experimental

Synthesis: 1,3,5-benzene-triphosphonic acid **3** was studied within the context of crystal engineering studies[25,26] performed at the University of Crete, Heraklion, Crete, Greece. 1,3,5-Benzene-triphosphonic acid **3** was synthesized following methods described in references.[16,19]

Sample preparation: (a) NaOD/D$_2$O solvent: 1.0 g of a 40 wt-% solution of NaOD in D$_2$O (Acros Organics) was diluted with 9.0 g D$_2$O (Deutero). (b) NMR sample: 0.31 g (0.975 mmol) of **3** were dissolved in 0.7 mL of NaOD/D$_2$O solvent and transferred to a 5 mm high-throughput NMR tube (Wilmad-LabGlass). (c) 3-(Trimethylsilyl)propanesulfonicacid sodium salt ((CH$_3$)$_3$Si–CH$_2$–CH$_2$–CH$_2$–SO$_3$Na) (Sigma-Aldrich) was used as internal reference for δ_H, ν_H, δ_C, ν_C while δ_P and ν_P were referenced virtually to external 85% H$_3$PO$_4$. (Sigma-Aldrich). NMR spectra were obtained using a *Bruker Avance III* spectrometer at Heinrich Heine University at Düsseldorf, Germany. Sample temperature: 297.9 K. Experimental parameters: 600.13 MHz ^{1}H NMR: NS = 16. TD = 64 K. SW = 12335.526 Hz/20.5546 ppm. 242.94 MHz ^{31}P NMR: NS = 128. TD = 64 K. SW = 4854.369 Hz/19.9818 ppm. 242.94 MHz ^{31}P{^{1}H} NMR: NS = 16. TD = 64 K. SW = 5341.888 Hz/21.9885 ppm. 150.92 MHz ^{13}C{^{1}H} NMR: NS = 1024. TD = 64 K. SW = 360557.692 Hz/238.9226 ppm. For NMR calculations, the Bruker Topspin program with DAISY and the previous version of WINDAISY under WINNMR were used.

ORCID

Konstantinos D. Demadis http://orcid.org/0000-0002-0937-8769
Christoph Janiak http://orcid.org/0000-0002-6288-9605
Gerhard Hägele http://orcid.org/0000-0001-9815-2181

References

[1] Corio, P. L. *Structure of High-Resolution NMR Spectra*; Academic Press: New York, USA, **1966**; pp 330–405. DOI: 10.1002/bbpc.19670710722.

[2] Jones, R. G. The Use of Symmetry in Nuclear Magnetic Resonance. In *NMR Basic Principles and Progress. Grundlagen und Fortschritte*; Diehl, P., Fluck, E., Kosfeld, R., Eds.; Springer Verlag: Berlin, **1969**; Vol. 1, pp 97–174.

[3] Hägele, G.; Engelhard, M.; Boenigk, W. *Simulation und automatisierte Analyse Von Kernresonanzspektren*. VCH Verlagsgesellschaft mbH: Weinheim, Germany, **1987**.

[4] Weber, U.; Thiele, H. *NMR Spectroscopy: Modern Spectral Analysis;* Wiley-VCH: Weinheim, Germany, **1998**.

[5] Jones, R. G.; Hirst, R. C.; Bernstein, H. J. A Simplified Procedure for the Analysis of Complex Nuclear Magnetic Resonance Spectra. II. The Analysis of Symmetrical Trifluorobenzene, the AA′A″XX′X″ System. *Can. J. Chem.* **1965**, *43*, 683–699. DOI: 10.1139/v65-087.

[6] Wray, V.; Lincoln, D. N. The Complete ^{13}C, ^{19}F and ^{1}H NMR Spectral Analysis of the Fluorobenzenes C$_6$H$_n$F$_{6-n}$. I. 1,3,5-Trifluorobenzene. *J. Magn. Res.* **1975**, *18*, 374–382. DOI: 10.1016/0022-2364(75)90136-5.

[7] Ernst, L.; Lincoln, D. N.; Wray, V. The Complete C-13, F-19, and H-1 Spectral Analysis of the Fluorobenzenes C$_6$H$_n$F$_{6-n}$. II. 1,2-Difluorobenzene. INDO MO Calculations of J$_{HH}$ in the Fluorobenzenes and Related Molecules. *Magn. Res.* **1976**, *21*, 115–128. DOI: 10.1016/0022-2364(76)90260-2.

[8] Lustig, E.; Lincoln, D. N.; Wray, V. The Signs of the Coupling Constants between Protons and Fluorine Nuclei in Substituted Benzenes. *J. Magn. Res.* **1976**, *21*, 509–510. DOI: 10.1016/0022-2364(76)90059-7.

[9] Spearman, S. A.; Goldstein, J. H. NMR Studies of Fluorobenzenes Partially Oriented in a Lyotropic Liquid Crystal System. *J. Magn. Res.* **1977**, *26*, 237–251. DOI: 10.1016/0022-2364(77)90170-6.

[10] Wray, V.; Ernst, L.; Lustig, E. The Complete ^{13}C, ^{19}F and ^{1}H NMR Spectral Analysis of the Fluorobenzenes C$_6$H$_n$F$_{6-n}$. III. The Remaining Members of the Series; INDO MO Calculations

of J_{FH}, J_{FF}, J_{CH} and J_{CF}. *J. Magn. Res.* **1977**, *27*, 1–21. DOI: 10.1016/0022-2364(77)90188-3.

[11] Weber, W.; Spiske, R.; Höffken, H.-W.; Hägele, G.; Thiele, T.; *Win-DAISY. A Novel Program System for Simulation and Iteration of High Resolution NMR Spectra.* Manual and Program System. Bruker Manual; **1983**.

[12] Thomas, B.; Grossmann, G. ^{15}N-Labeled Cyclotriphosphazatrienes ($(^{15}NPR_2)_3$) as Examples for a Simplified AA′A″XX′X″ Spin System. *J. Magn. Res.* **1979**, *36*, 333–341. DOI: 10.1016/0022-2364(79)90110-0.

[13] Le Paige, U. B.; Smits, B.; Hart, P.; Lefeber, F.; Martin, N. L.; van Ingen, H. Weak Coupling between Magnetically Inequivalent Spins: The Deceptively Simple, Complicated Spectrum of a ^{13}C-Labeled Trimethylated Amine. *J. Magn. Res.* **2017**, *278*, 96–103. DOI: 10.1016/j.jmr.2017.03.016.

[14] Reiter, S. A.; Assmann, B.; Nogai, S. D.; Mitzel, N. W.; Schmidbaur, H. (Benzene-1,3,5-Triyl)Tris[Phosphine] ($C_6H_3(PH_2)_3$) and (Benzene-1,3,5-Triyl)Tris[Phosphonic Acid] ($C_6H_3[P(O)(OH)_2]_3$). Absence of Hydrogen Bonding in Solid Primary Phosphines. *HCA.* **2002**, *85*, 1140–1150. DOI: 10.1002/1522-2675(200204)85:4 < 1140::AID-HLCA1140 > 3.0.CO;2-X.

[15] Kong, D.; Clearfield, A.; Zoń, J. Crystal-Engineered Three-Dimensional Hydrogen-Bonding Networks Built with 1,3,5-Benzenetri(Phosphonic Acid) and Bipyridine Synthons. *Cryst. Growth Des.* **2005**, *5*, 1767–1773. DOI: 10.1021/cg050033w.

[16] Kong, D.; Zon, J.; McBee, J.; Clearfield, A. Rational Design and Synthesis of Porous Organic-Inorganic Hybrid Frameworks Constructed by 1,3,5-Benzenetriphosphonic Acid and Pyridine Synthones. *Inorg. Chem.* **2006**, *45*, 977–986. DOI: 10.1021/ic0509377.

[17] Pramanik, M.; Bhaumik, A. Self-Assembled Hybrid Tinphosphonate Nanoparticles with Bimodal Porosity: An Insight towards the Efficient and Selective Catalytic Process for the Synthesis of Bioactive 1,4-Dihydropyridines under Solvent-Free Conditions. *J. Mater. Chem. A* **2013**, *1*, 11210–11200. DOI: 10.1039/c3ta12476b.

[18] Pramanik, M.; Bhaumik, A. Organic-Inorganic Hybrid Supermicroporous Iron(III) Phosphonate Nanoparticles as an Efficient Catalyst for the Synthesis of Biofuels. *Chem. Eur. J.* **2013**, *19*, 8507–8514. DOI: 10.1002/chem.201300128.

[19] Luca, V.; Tejada, J. J.; Vega, D.; Arrachart, G.; Rey, C. Zirkonium(IV)-Benzene Phosphonate Coordination Polymers: Lanthanide and Actinide Extraction and Thermal Properties. *Inorg. Chem.* **2016**, *55*, 7928–7943. DOI: 10.1021/acs.inorgchem.6b00954.

[20] Henn, M.; Jurkschat, K.; Mansfeld, D.; Mehring, M.; Schürmann, M. Synthesis, Structure and DFT-Studies of 1,3,5-$[P(O)(i\text{-}PrO)_2]_3C_6H_3$ and Its $CHCl_3$ Adduct – Analysis of the $Cl_3C–H\cdots OP$ Hydrogen Bond. *J. Mol. Struct.* **2004**, *697*, 213–220. DOI: 10.1016/j.molstruc.2004.04.013.

[21] Mehring, M. Two- and Three-Dimensional Hydrogen-Bonded Networks Built from1,3,5-$[(HO)_2(O)P]_3C_6H_3$ and 4-(Dimethylamino)Pyridine. *Eur. J. Inorg. Chem.* **2004**, *2004*, 3240–3246. DOI: 10.1002/ejic.200300843.

[22] Marma, M. S.; Khawli, L. A.; Harutunian, V.; Kashemirov, B. A.; McKenna, C. E. Synthesis of α-Fluorinated Phosphonoacetate Derivatives Using Electrophilic Fluorine Reagents: Perchloryl Fluoride versus 1-Chloromethyl-4-Fluoro-1,4-Diazoniabicyclo[2.2.2]Octane Bis(Tetrafluoroborate) (Selectfluor®). *J. Fluorine Chem.* **2005**, *126*, 1467–1475. DOI: 10.1016/j.jfluchem.2005.04.002.

[23] Kong, D.; Yao, J.; Clearfield, A.; Zon, J. Hydrogen-Bonded Structures Formed from the Reaction of 1,3,5-Benzene-Triphosphonic Acid and Adamantane. *Cryst. Growth Des* **2008**, *8*, 2892–2898. (Remark: this paper deals with 1-aminoadamantane, not with adamantane) DOI: 10.1021/cg701253u.

[24] Mehring, M.; Schürmann, M.; Jurkschat, J. The First Rigid O,C,O-Pincer Ligand and Its Application for the Synthesis of Penta- and Hexacoordinate Organotin(IV) Compounds. *Organometalics* **1998**, *17*, 1227–1236. DOI: 10.1021/om970847c.

[25] Athanasopoulos, E. D.; Armakola, E.; Koutsoukos, P. G.; Demadis, K. D. Nucleation and Crystal Growth of Barium Sulfate: Inhibition in the Presence of Rigid and Flexible Triphosphonate Additives. *CrystEngComm* **2018**, *20*, 6589–6601. DOI: 10.1039/cc8ce01116h.

[26] Fidelli, A. M.; Armakola, E.; Demadis, K. D.; Kessler, V. G.; Escuer, A.; Papaefstathiou, G. S. Cu^{II} Framework from Di-2-Pyridyl-Ketone and Benzene-1,3,5-Triphosphonic Acid. *Eur. J. Inorg. Chem.* **2018**, *2018*, 91–98. DOI: 10.1002/ejic.201701165.

5.3 Unveröffentliche Ergebnisse

Im folgenden Kapitel werden weitere bisher unveröffentliche Ergebnisse aus der Zusammenarbeit mit Prof. Dr. Gerhard Hägele präsentiert.

In der publizierten Arbeit aus 5.2.1 wurde gezeigt, dass Carboxylat-Phosphonat-Verbindungen für die NMR-Spektroskopie sehr interessante Verbindungen darstellen. Deshalb wurde entschieden noch zwei weitere Verbindungen 4-Phosphonobenzoesäure (4-PBA) und 2-Phosphonobenzoesäure (2-PBA) spektroskopisch zu untersuchen (^{1}H-, ^{31}P-, $^{31}P\{^{1}H\}$- und $^{13}C\{^{1}H\}$-NMR-Spektren). Die erhaltenen Säuren sollten anschließend bei $\tau = 4$ (vollständig deprotoniert) und bei $\tau = 0$ (im autoprotolytischen Zustand) vermessen. (Der Titrationsgrad τ wurde durch Zugabe von NaOD eingestellt). Ein vollständiger Bericht über die vollständig spektroskopischen Untersuchungen soll in einer kommenden Publikation noch folgen. Im nachfolgenden Teil, ist nur die Synthese der Verbindung 2-PBA beschrieben.

5.3.1 Synthese und Charakterisierung von 2-Phosphonobenzoesäure (2-PBA)

Die Reaktionsfolge zur 2-Phosphonobenzoesäure ist in **Schema 3** angegeben. Im ersten Schritt wurde die 2-Iodobenzoesäure zum Ethylester mit Hilfe von konzentrierter Schwefelsäure verestert (**1**). Anschließend wurde **1** durch eine Nickel katalysierte Abruzov-Reaktion zur Ethyl 2-(diethoxyphosphoryl)benzoesäure umgesetzt und anschließend sauer mit konzentrierter Salzsäure hydrolysiert zur 2-Phosphonobenzoesäure (**3**).

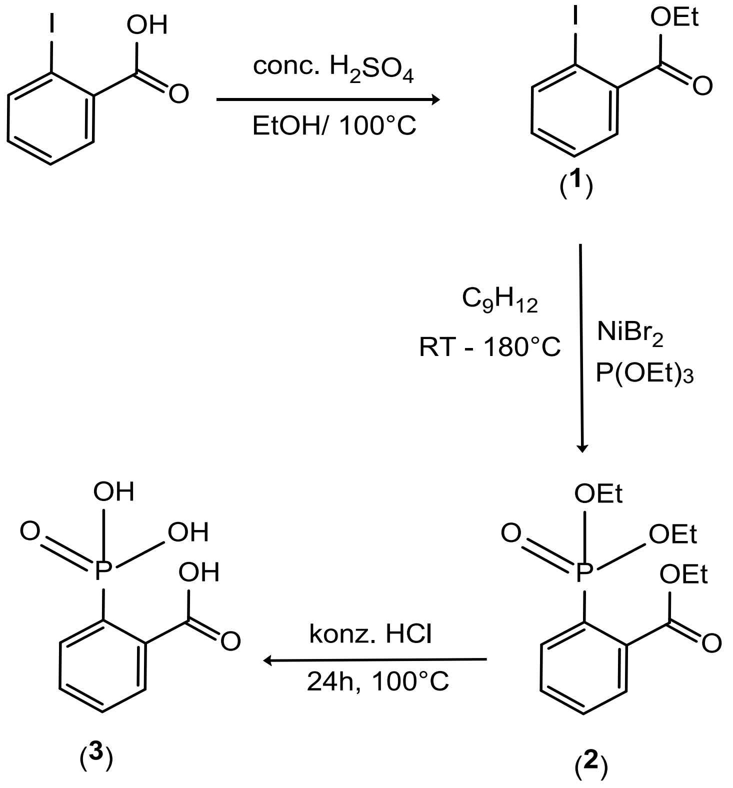

Schema 3: Reaktionsschema für die Synthese von 2-Phosphonobenzoesäure (**3**).

Im Folgenden werden die einzelnen Reaktionsschritte genauer beschrieben, die Ausbeuten sowie die NMR-Signale angegeben.

Alle verwendeten Reagenzien und Ausgangstoffe waren im Handel erhältlich und wurden ohne weitere Aufreinigung verwendet. Die NMR-Spektren wurden mit einem Bruker Avance DRX (500 MHz) oder einem Bruker Avance III-300 (300 MHz) an der Heinrich-Heine-Universität in Düsseldorf, Deutschland aufgenommen. Die Probentemperatur betrug um die 297 K.

5.3.1.1 Synthese von Ethyl 2-Iodobenzoesäure (1)

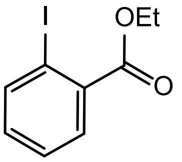

$C_9H_9IO_2$
[276,07]

15,1 g 2-Iodobenzoesäure (6,08 mmol) wurden in einem 500 ml Rundkolben in 243 ml Ethanol gelöst und mit 1,56 ml (29,1 mmol; 5 Äq.) konzentrierter Schwefelsäure versetzt. Anschließend wurde über Nacht zum Rückfluss erhitzt. Nach dem Abkühlen auf Raumtemperatur wurden ca. 200 ml entionisiertes Wasser und 325 ml Ethylacetat zugegeben. Nach Abtrennung der wässrigen Phase wurde die organische Phase einmal mit 100 ml gesättigter Natriumchloridlösung und einmal mit 100 ml di-H_2O gewaschen, bevor diese über Na_2SO_4 getrocknet wurde. Nach Entfernen des Ethanols unter Vakuum wurde ein weißliches Öl zu erhalten.

Ausbeute: 15,8 g (5,72 mmol, 94 %)

^{1}H-NMR (300 MHz, $CDCl_3$) δ [ppm]: 7,92-7,89 (dd, 1H), 7,74-7,70 (dd, 1H), 7,35-7,29 (m, 1H), 7,09-7,03 (m, 1H), 4,35 (q, 2H), 1,35 (t, $^4J_{H,H}$ =1,35 Hz, 3H).

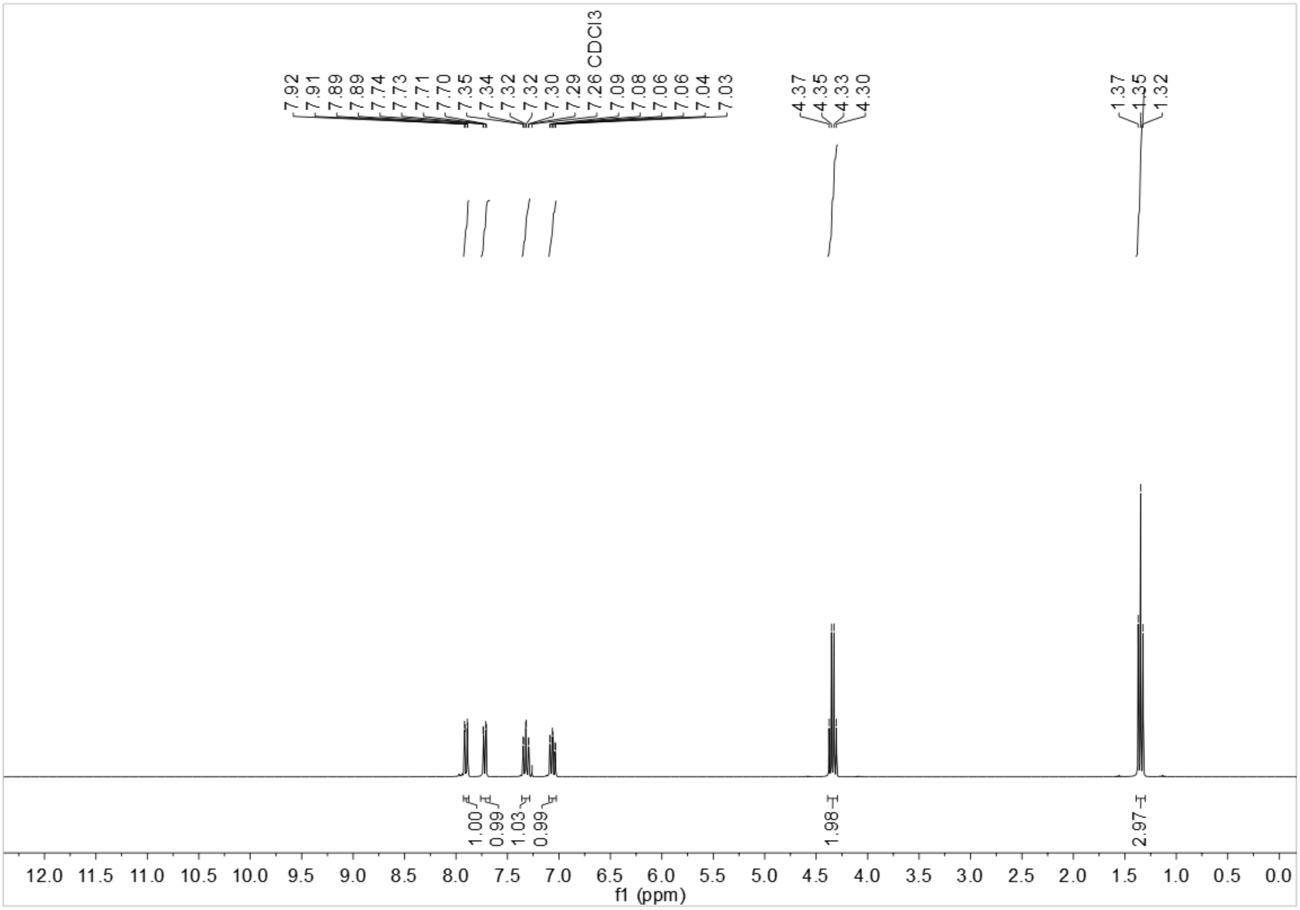

Abbildung 19: ^{1}H-NMR-Spektrum von Ethyl 2-Iodobenzoesäure in $CDCl_3$.

5.3.1.2 Synthese von Ethyl 2-(diethoxyphosphoryl)benzoesäure (2)

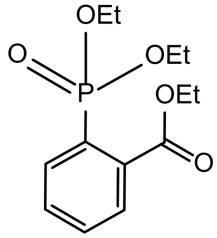

$C_{13}H_{19}O_5P$
[286,26]

0,24 g Nickelbromid (1,07 mmol) werden in einem sekurierten Kolben in der Glovebox eingewogen. Mesitylen (4,00 mL) wird unter Stickstoffatmosphäre zugegeben. 3,65 ml Triethylphosphit (21,0 mmol, 1,5 Äq.) wird tropfenweise über 30 Minuten bei Raumtemperatur zugegeben. Vor dem Erhitzen auf 185°C wird 10 Minuten lang bei RT nachgerührt. 2,35 ml Ethyl-2-iodobenzoat (14,0 mmol) werden langsam bei Siedetemperatur zu der entstandenen violetten Lösung gegeben. Nach dem Erhitzen über Nacht ist ein Farbumschlag von violett nach orange zu beobachten. Nach dem Abkühlen auf 40°C wird das Mesitylen unter Vakuum entfernt. 40 ml Di-H_2O wurde zugegeben und das Produkt mit zwei Mal 40 ml Diethylether extrahiert. Die organische Phase wurde mit 30 ml gesättigter Natriumchloridlösung gewaschen und über $MgSO_4$ getrocknet. Das Reaktionsgemisch wurde im Vakuum konzentriert, um ein orangefarbenes viskoses Öl zu erhalten, das durch Kieselgelsäulenchromatographie aufgereinigt wurde. Zunächst wurde mit Hexan/Ethylacetat 4:1 vorgesäubert und dann zu Hexan/Aceton: 2:1 als Eluent gewechselt. Das erhaltene Produkt ist ein orangefarbenes viskoses Öl.

Ausbeute: 0,20 g (0,70 mmol, 65 %)

^{1}H-NMR (300 MHz, DMSO-d_6) δ [ppm]: 8,01-7,97 (m, 1H), 7,72-7,69 (m, 1H), 7,59-7.52 (m, 1H), 4,21-4.08 (m, H) 4,42-4,08 (q, 2H), 1,42 (t, $^4J_{H,H}$ =7,2 Hz, 3H).1,35 (t, $^4J_{H,H}$ =7,1 Hz, 6H).

^{31}P{^{1}H}-NMR (500 MHz, DMSO-d_6) δ [ppm]: 17.18 (s, 1P).

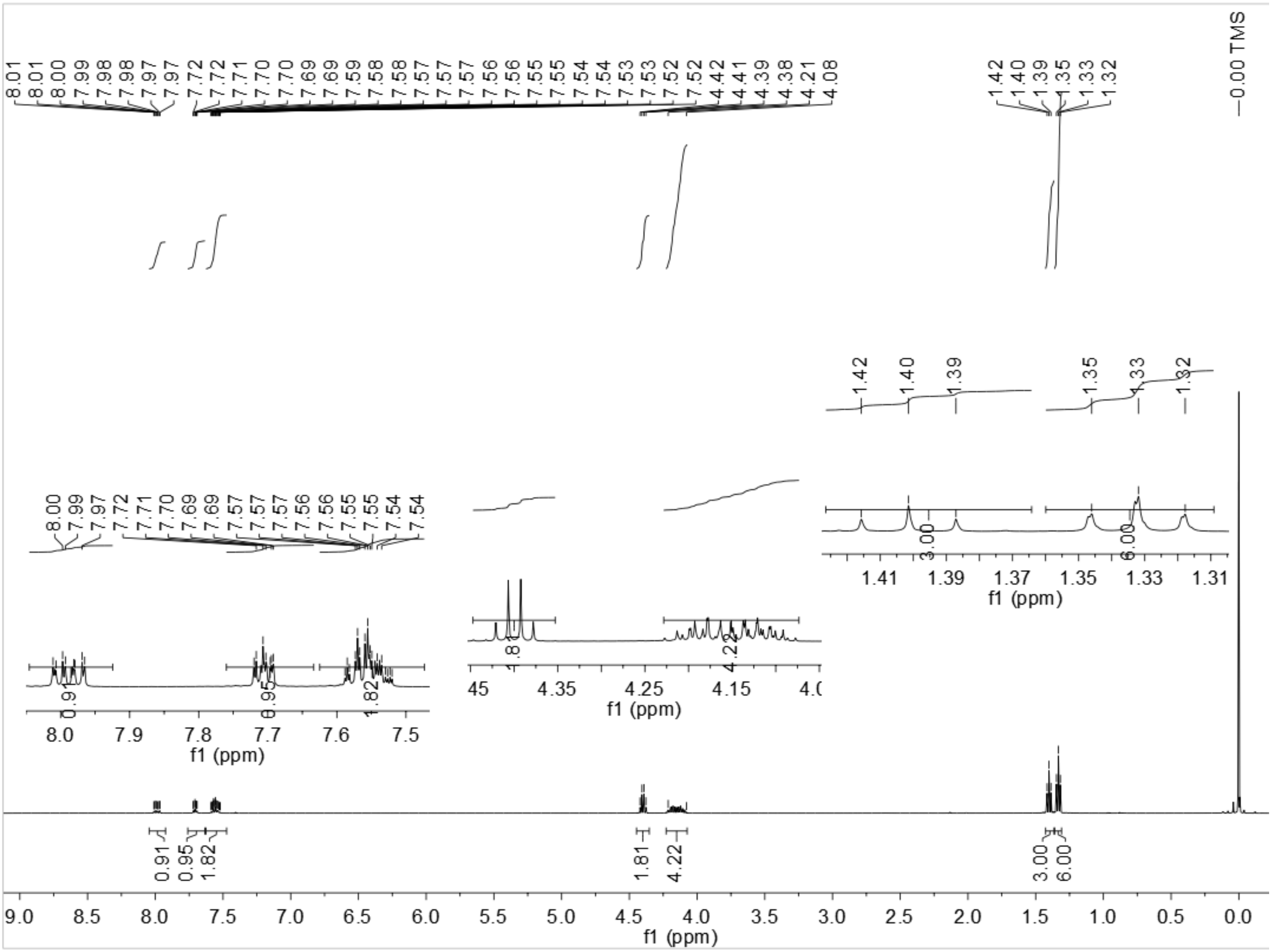

Abbildung 20: ^{1}H-NMR-Spektrum von Ethyl 2-(diethoxyphosphoryl)benzoesäure in $CDCl_3$.

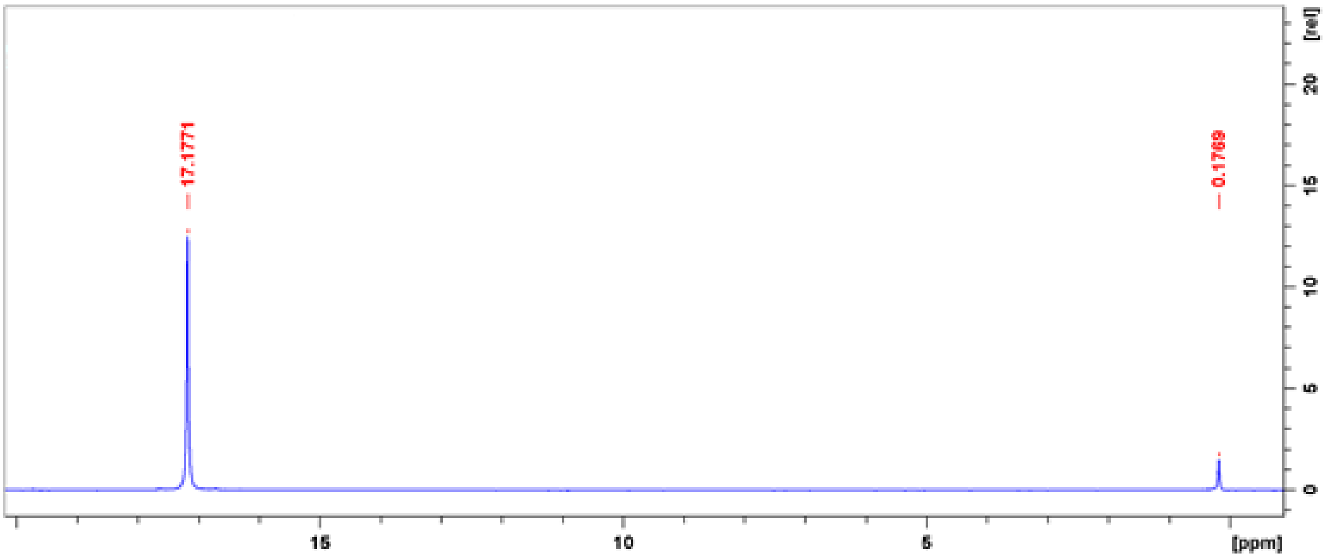

Abbildung 21: ^{31}P{^{1}H}-NMR-Spektrum von Ethyl 2-(diethoxyphosphoryl)benzoesäure in $CDCl_3$.

5.3.1.3 Synthese von 2-Phosphonobenzoesäure (3)

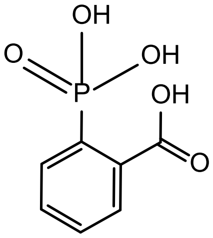

$C_7H_7O_5P$
[202,10]

0,20 g Ethyl 2-(Diethoxyphosphoryl)benzoat (0,70 mmol) wurde in 5 ml konz. HCl suspendiert und über Nacht zum Rückfluss erhitzt. Nach dem Abkühlen auf Raumtemperatur wurde das Produkt filtriert und zwei Mal mit 10 ml Di-H_2O gewaschen. Das Produkt wurde über Nacht im Vakuumtrockenschrank (40°C, 10^{-2} bar) getrocknet, um ein weißes Pulver zu erhalten.

Ausbeute: 60,0 mg (0,30 mmol; 43 %)

^{1}H-NMR (300 MHz, DMSO-d_6) δ [ppm]: 7,89-7.80 (m, 1H), 7,71-7,67 (m, 1H), 7,61-7,56 (m, 2H).

^{31}P{^{1}H}-NMR (500 MHz, DMSO-d_6) δ [ppm]: 11.95 (s, τ =0).

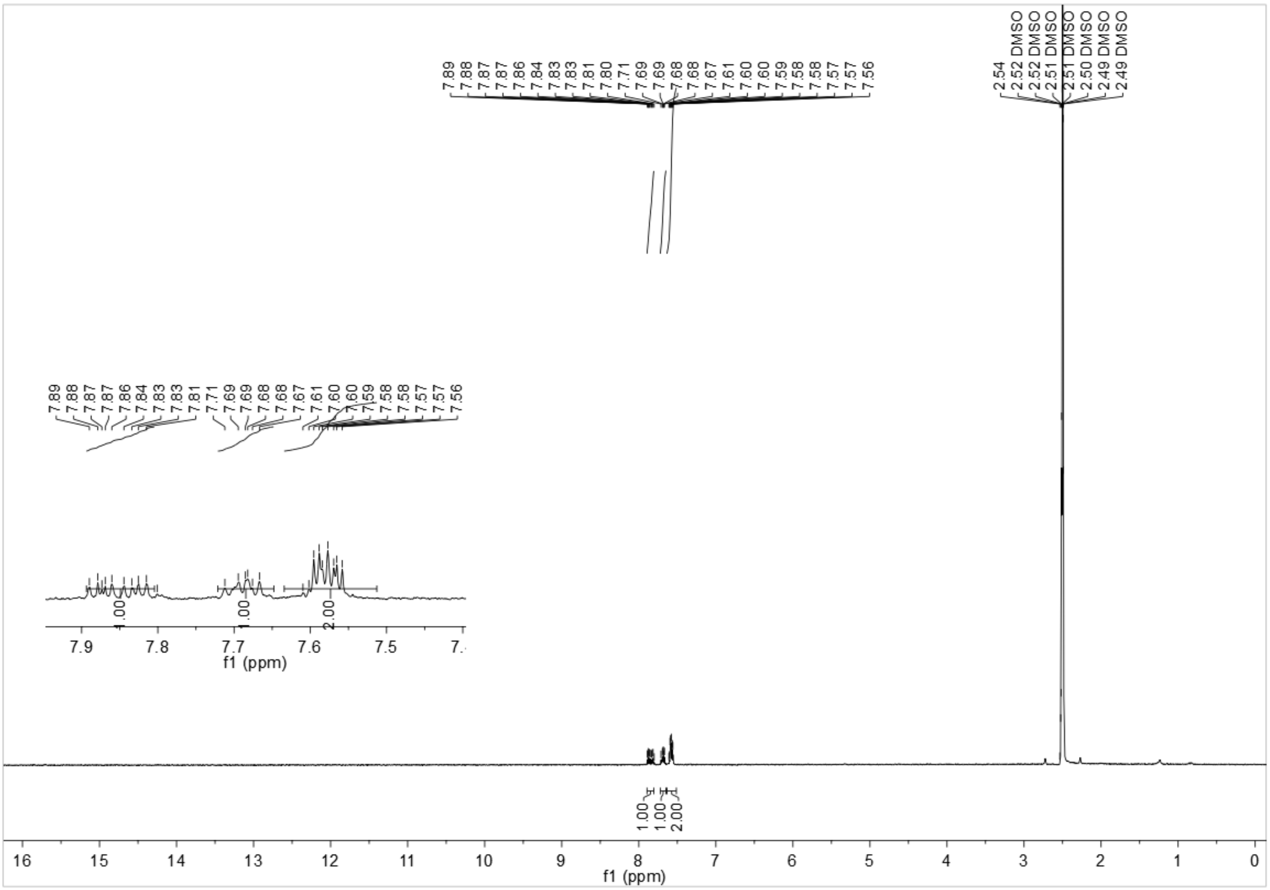

Abbildung 22: ^{1}H-NMR-Spektrum von 2-Phosphonobenzoesäure in DMSO-d$_6$.

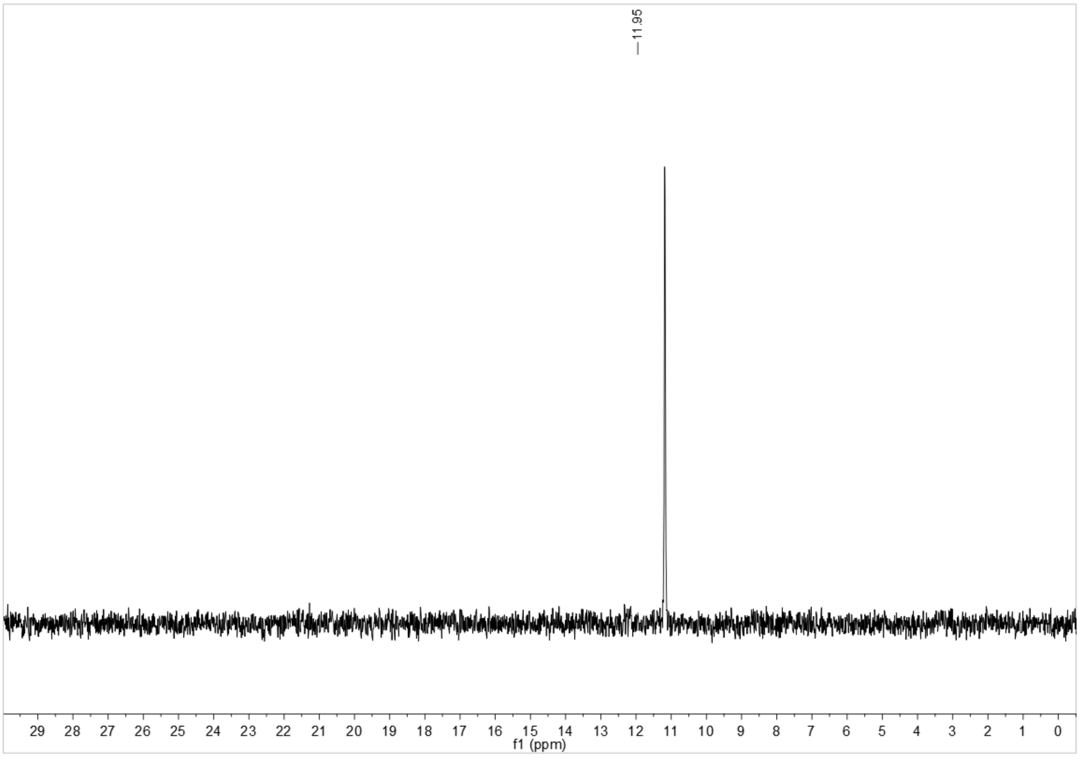

Abbildung 23: ^{31}P{^{1}H}-NMR-Spektrum von 2-Phosphonobenzoesäure in DMSO-d$_6$.

6 Literaturverzeichnis

[1] R. Fischer, I. Schwedler, *Angew. Chem*. **2014**, *126*, 7209-7214.
[2] S. R. Batten, N. R. Champness, X.-M. Chen, J. Garcia-Martinez, S. Kitagawa, L. Öhrström, M. O'Keeffe, M. P. Suh, J. Reedijk *Pure Appl. Chem* **2013**, *85*, 1715-1724.
[3] S. R. Battern, S. M. Neville, D. R Turner *Coordination Polymers: Design, analysis and application*, Royal Society of Chemistry, Cambrige, **2009**.
[4] K. A. Hofmann, F. Höchtlen *Berichte der deutschen chemischen Gesellschaft* **1903,** *36* (1), 1149-1151.
[5] K. A. Hofmann, H. Arnoldi *Berichte der deutschen chemischen Gesellschaft* **1906,** *39* (1), 339-344.
[6] A. S. Allison, R. M. Barrer *J. Chem. Soc. A* **1969,** *0* (0), 1717-1723.
[7] O. M. Yaghi, H. Li *J. Am. Chem. Soc.***1995**, *117*, 10401–10402.
[8] O. M. Yaghi, G. Li, H. Li *Nature* **1995**, *378*, 703–706.
[9] S. Kitagawa, K. Uemura *Chem. Soc. Rev.* **2005**, *34*, 109-119.
[10] M. Li, D. Li, M. O'Keeffe, O. M. Yaghi *Chem. Rev.* **2014**, *114*, 1343–1370.
[11] C. Janiak, J. K. Vieth *New J. Chem.* **2010**, *34*, 2366–2388.
[12] X. Liu, W. Fu, E. Bouwman *Chem. Commun.*, **2016**, 52, 6926-6929.
[13] D.-A. Yang, H.-Y. Cho, J. Kim, S.-Tae, W.-S. Ahn *Energy Environ. Sci.* **2012**, *5*, 6465-6473.
[14] A. de Oliveira, G. F. de Lima, H. A. De Abreu *Chem. Phys. Lett*. **2018**, *691*, 283-290.
[15] M. Mazaj, N. Z. Logar *Cryst. Growth Des.* **2015**, *15*, 617-624.
[16] J. Sun, T. Huang, Q. Yin, L. Li, T.-F. Liu, X.-S. Huang, R. Cao *Cryst. Growth. Des.* **2020**, *20*, 8021-8027.
[17] V. Zima, J. Svoboda, L. Beneš, K. Melánová, M. Trchová, J. Dybal *J. Solid State Chem.* **2007**, *180*, 929-939.
[18] P. Leo, D. Briones, J. A. Gracia, J. Cepeda, G. Orcajo, G. Callaeja, A. Rodriguez-Diéguez, F. Martinez *Inorg. Chem.* **2020**, *59*, 18432-18443.
[19] D. Alezi, Y. Belmabkhout, M. Suyetin, P. M. Bhatt, Ł. J. Weseliński, V. Solovyeva, K. Adil, I. Spanopoulos, P. N. Trikalitis, A. H. Emwas, M. Eddaoudi *Acc. Chem. Res.* **2015**, *137*, 13308-13318.
[20] T. J. Matemb Ma Ntep, H. Reinsch, P. P. C. Hügenell, S.-J. Ernst, E. Hastürk, C. Janiak *J. Mater. Chem. A* **2019**, *7*, 24973–24981.
[21] O. I. Lebedev, F. Millange, C. Serre, A. G. Van Tendeloo, G., Férey*, Chem. Mater.* **2005**, *17*, 6525–6527.
[22] D.-Y Hong Y.K. Hwang, C. Serre, G. Férey, J.-S. Chang, *Adv. Funct. Mater.* **2009**, *19*, 1537–1552.
[23] M. Riou-Cavellec, C. Lesaint, M. Noguès, J.-M. Grenèche, G. Férey, *Inorg. Chem.* **2003**, *42*, 5669–5674.
[24] Q. Shi, Z. Chen, Z. Song, J. Li, J. Dong, *Angew. Chem.* **2011**, *50*, 672–675.
[25] F. Eubank, L. Wojtas, M. R. Hight, T. Bousquet, V. Ch. Kravtsov, M. Eddaoudi *J. Am. Chem. Soc.* **2011**, *133*, 17532-17535.
[26] S. S.-Y. Chui, S. M.-F. Lo, J P. H. Charmant, A. G. Orpen, I. D. Williams *Science* **1999**, *283*, 1148-1150.
[27] D. J. Tranchemontagne, J. R. Hunt, O. M. Yaghi *Tetrahedron* **2008**, *64*, 8553-8557.
[28] K. S. Park, Z. Ni, A. P. Cote, J. Y. Choi, R. Huang, F. J. Uribe-Romo, H. K. Chae, M. O'Keeffe, O. M. Yaghi *PNAS* **2006**, *103*, 10186–10191.
[29] Y. Zhao, Q. Zhang, Y. Li, R. Zhang, G. Lu *ACS Appl. Mater. Interfaces* **2017**, *9*, 15079-15085.
[30] T. Matemb Ma Ntep, H. Breitzke, L. Schmolke, C. Schlüsener, B. Moll, S. Millan, N. Tannert, I. El Aita, G. Buntkowsky, C. Janiak *Chem. Mater.* **2019**, *31*, 8629–8638.
[31] H. Furukawa, K. E. Cordova, M. O'Keeffe, O. M. Yaghi *Science* **2013**, *341*, 1230444.
[32] J. J. Perry, J. A. Perman, M. J. Zaworotko *Chem. Soc. Rev.* **2009**, *38*, 1400–1417.
[33] O. M. Yaghi, M. O'Keeffe, N. W. Ockwig, H. K. Chae, M. Eddaoudi, M., J. Kim *Nature*, **2003**,*423*, 705–714.
[34] C. Pettinari, A. Tăbăcaru, S. Galli *Coord. Chem. Rev.* **2016**, *307*, 1-31.
[35] M. A. Halcrow, *Dalton Trans.* **2009**, *12*, 2059-2073.

[36] J.-P. Zhang, Y.-B.Zhang, J.B. Lin, X.M. Chen *Chem Rev.* **2012**, *112*,1001-1033.
[37] P. Lu, Y. Wu, H. Kang, H. Wie, H. Liu, M. Fang *J. Mater. Chem. A* **2014**, *2*, 16250-16267.
[38] A. E. Martell, R. D. Hancock, in: *Metal Complexes in Aqueous Solutions*, (Ed.: J. P. Fackler) SpringerLink, 1996.
[39] R. B. Martin, in: Encyclopedia of Inorganic Chemistry, (Ed.: R. B. King), Wiley, **1994**, p. 2185ff.
[40] (a) J. He, Y-G. Yin, T. Wu, D. Li, X.-C. Huang *Chem. Commun.* **2006**, 2845-2847. (b) J.-P Zhang, S. Horike, S. Kitagawa *Angew. Chem., Int.Ed.* **2007**, *46*, 889-892. (c) S.-Z. Zhan, M. Li, X.-P. Zhou, J.-H. Wang, J.-R. Yang, D. Li *Chem. Commun.* **2011**, *47*, 12441-12443. (d) M. A. Omary, M. A. Rawashdeh-Omary, M. W. A. Gonser, O. Elbjeirami, T. Grimes, T. R. Cundari *Inorg. Chem.* **2005**, *44*, 8200-8210. (e) A. Hayashi, M. M. Olmstead, S. Attar, A. L. Balch *J. Am. Chem. Soc.* **2002**, *124*, 5791-5795.
[41] L. Hou, Y.-Y. Lin, X.-M. Chen *Inorg Chem* **2008,** *47* (4), 1346-1351.
[42] F. ZareKarizi, M. Joharian, A. Morsali *J. Mater. Chem. A* **2018**, *6*, 19288–19329.
[43] L. Hou, Y.-Y. Lin, X.-M. Chen *Inorg. Chem.* **2008**, *47*, 1346–1351.
[44] L.-N. Jia, Y. Zhao, L. Hou, L. Cui, H.-H. Wang, Y.-Y. Wang *J. Solid State Chem.* **2014**, *210*, 251–255.
[45] P. Pachfule, B. Garai, R. Banerjee *Inorg. Chem.* **2016**, *55*, 7200–7205.
[46] G. Mehlana, V. Chitsa, T. Mugadza *RSC Adv.* **2015**, *5*, 88218–88233.
[47] C. Heering, B. Francis, B. Nateghi, G. Makhloufi, S. Lüdeke, C. Janiak *CrystEngComm* **2016**, *18*, 5209-5223.
[48] M. Deng, Y. Liang, B. Xing, Z. Chen, Y. Zhou, X. Liu, B. Yue, H. He *Chem. Eur. J.* **2011**, *17*, 10323-10328.
[49] A. Goldmann, B. Gil-Hernández, S. Millan, S. Gökpinar, C. Heering, I. Boldog, C. Janiak *CrystEngComm* **2020**, *22*, 2933-2944.
[50] B. Nateghi, C. Janiak *Z. Naturforsch. B.* **2019**, *74*, 891-899.
[51] C. Montoro, F. Linares, E. Quartapelle Procopio, I. Senkovska, S. Kaskel, S. Galli, N. Masciocchi, E. Barea, J. A. R. Navarro *J. Am. Chem. Soc.* **2011**, *133*, 11888-11891.
[52] C. Heering, I. Boldog, V. Vasylyeva, J. Sanchiz, C. Janiak *CrystEngComm* **2013**, *15*, 9757-9768.
[53] S. Menzel, S. Millan, S.-P. Höfert, A. Nuhnen, S. Gökpinar, A. Schmitz, C. Janiak *Dalton Trans* **2020**, *49*, 12854–12864.
[54] S. Menzel, S.-P. Höfert, S. Öztürk, A. Schmitz, C. Janiak *Z. Anorg. Allg. Chem. **2021**, 647, 803-808.*
[55] C. Heering, I. Boldog, V. Vasylyeva, J. Sanchiz, C. Janiak *CrystEngComm* **2013**, *15*, 9757-9768.
[56] E. Quartapelle Procopio, T. Fukushima, E. Barea, J. A. R. Navarro, S. Horike, S. Kitagawa *Chemistry – A European Journal* **2012,** *18* (41), 13117-13125.
[57] J. Wang, S. Yao, G. Li, Q. Huo, L. Zhang, Y. Liu *RSC Advances* **2015,** *5* (124), 102525-102529.
[58] Z. W. Wei, D. Q. Yuan, X. L. Zhao, D. F. Sun, H.-C. Zhou *Sci. China Chem.* **2013**, *56*, 418-422.
[59] K.Brandenburg, DIAMOND, version 4.0; Crystal and Molecular Structure Visualization; Crystal Impact—K, Brandenburg & H. Putz Gbr, Bonn, Germany, 2009–2018.
[60] B. Zu, Q. Pang, E. Ning, W. Yan, Y. Qi, D. Wu, Q. Li *J. Am. Chem. Soc.* **2015**, *137*, 13459-13459.
[61] B. Tu, Q. Pang, H. Xu, X. Li, Y. Wang, Z. Ma, L. Wenig, Q. Li *J. Am. Chem. Soc.* **2017**, *139*, 7998-8007.
[62] L. Chen, H.-F. Wang, C. Li, Q. Xu *Chem. Sci.* **2020**, *11*, 5369-5403.
[63] N. Stock, S. Biswas *Chem. Rev.* **2012**, *112*, 933–969.
[64] E. Bagherzdeh, S. M. Zebarjad, H. R. M. Hosseini *Eur. J. Inorg. Chem.* **2018**, *18*, 1909-1915.
[65] R. S. Forgan Chem. Sci. **2020**,*11*, 4546-4562.
[66] J. Zhang, K. Huang, L. Yuan, S. Feng *CrystEngComm*. **2018**, *20*, 470-476.
[67] T. Hu, H. Lv, S. Shan, Q. Jia, H. Su, N. Tian, S. He *RSC Adv.* **2016**, *6*, 73741-73747.
[68] T. Zhao, F. Jeremias, I. Boldog, B. Nguyen, S. K. Henninger, C. Janiak *Dalton Trans.* **2015**, *44*, 16791-16801.

[69] W. Zhang, A. Bu, Q. Ji, L. Min, S. Zhao, Y. Wang, J. Chen *ACS. Appl. Mater. Interfaces* **2019**, *11*, 33931-33940.

[70] J. Goura, V. Chandrasekhar *Chem. Rev.* **2015**, *115*, 6854-6965.

[71] A. Nowacka, P. Briantais, C. Prestipino, F. X. Llabrés i Xamena *Cryst. Growth Des.* **2019**,*19*, 4981-4989.

[72] Y. Wang, B. Bredenkötter, B. Rieger, D. Volkmer *DaltonTrans.* **2007**, 689–696.

[73] X. Yang, Q. Xu *Cryst. Growth Des.* **2017**, *17*, 1450−1455

[74] B. F. Hoskins, R. Robson *J. Am. Chem. Soc.* **1990**, *112*, 1546 -1554.

[75] Z. Wang and S. M. Cohen *J. Am. Chem. Soc.* **2007**, *129*, 12368 -12369.

[76] P. Deria, J. E. Mondloch, O. Karagiaridi, W. Bury, J. T. Hupp, O. K. Farha *Chem. Soc. Rev.* **2014**, *43*, 5896-5912.

[77] T. K. Prasad, D. H. Hong, M. P. Suh *Chem.–Eur. J.* **2010**,*16*, 14043-14050.

[78] X.-S. Wang, M. Chrzanowski, L. Wojtas, Y.-S. Chen, S. Ma *Chem.–Eur. J.* **2013**,*19*, 3297–3301.

[79] X. Song, T. K. Kim, H. Kim, D. Kim, S. Jeong, H. R. Moon, M. S. Lah *Chem. Mater.* **2012**, *24*, 3065–3073.

[80] T. K. Prasad, D. H. Hong, M. P. Suh *Chem.-Eur. J.* **2010**,*16*, 14043–14050.

[81] L. Mi, H. Hou, Z. Song, H. Han, H. Xu, Y. Fan, S.-W. Ng *Cryst. Growth Des.* **2007**, *7*, 2553-2561

[82] C. K. Brozek, A. F. Cozzolino, S. J. Teat, Y.-S. Chen, M. Dincă *Chem. Mater.* **2013**, *25*, 2998-3002.

[83] Q. Yao, J. Sun, K. Li, J. Su, M. V. Peskov, X. Zou, *Dalton Trans*. **2012**, *41*, 3953–3955

[84] T. K. Prasad, D. H. Hong, M. P. Suh *Chem. -Eur. J.* **2010**, *16*, 14043–14050.

[85] Z.-J. Zhang, W. Shi, Z. Niu, H.-H. Li, B. Zhao, P. Cheng, D.-Z. Liao, S.-P. Yan *Chem. Commun.* **2011**, *47*, 6425–6427.

[86] T.-T. Lian, S.-M. Chen, F. Wangb, J. Zhang *CrystEngComm*. **2013**, *15*, 1036–1038

[87] G. Mukherjee, K. Biradha *Chem. Commun.* **2012**, *48*, 4293–4295.

[88] Z. Mai, D. Liu *Cryst. Growth Des*. **2019**, *19*, 7439–7462.

[89] H. Furukawa, Y. B. Go, N. Ko, Y. K. Park, F. J. Uribe-Romo, J. Kim, M. O'Keeffe, O. M. Yaghi *Inorg. Chem*. **2011**, *50*, 9147–9152.

[90] B. Chen B, M. Eddaoudi S. T. Hyde ST, M. O'Keeffe, O. M. Yaghi *Science* **2001**, *291*(5506), 1021–1023.

[91] H. Furukawa, Y. B. Go, N. Ko, Y. K. Park, F. J. Uribe-Romo, J. Kim,M. O'Keeffe, O. M. Yaghi *Inorg. Chem.* **2011**, *50*, 9147-9152.

[92] K. Gedrich, I. Senkovska, N. Klein, U. Stoeck, A. Henschel, M. R. Lohe, I. A. Baburin, U. Mueller and S. Kaskel, *Angew. Chem. Int. Ed.* **2010**, *49*, 8489-8492.

[93] H. K. Chae, D. Y. Siberio-Pérez, J. Kim, Y. B. Go, M. Eddaoudi, A. J. Matzger, M. O'Keeffe, O. M. Yaghi *Nature* **2004**, *427*, 523-527.

[94] H. Furukawa, M. A. Miller, O. M. Yaghi, *J. Am. Chem.* **2007**, *17*, 3197-3204.

[95] H. Furukuwa, N. Ko, Y. B. Go, N. Aratani, S. B. Choi, E. Choi, A. O. Yazaydin, R. Q. Snurr, M. O'Keeffe, J. Kim, O. M. Yaghi, *Science* **2010**, *329*, 424-428.

[96] J. Rong, W. Zhang, J. Bai, *CrystEngComm*. **2016**, *18*, 7728-7736.

[97] D. Sun, S. Ma, Y. Ke, D. J. Collins and H.-C. Zhou, *J. Am. Chem. Soc.* **2006**, *128*, 3896-3897.

[98] S. Ma and H.-C. Zhou, *J. Am. Chem. Soc.* **2006**, *128*, 11734-11735.

[99] B. Rungtaweevoranit, C. S. Diercks, M. J. Kalmutzki, O. M. Yaghi *Faraday Discuss*. **2017**, *201*, 9-45.

[100] Y.-Z. Li, G.-D. Wang, X.-J. Shi, L. Hou, Y.-Y. Wang, Z. Zhu *ACS Appl. Mater. Interfaces* **2020**, *12*, 41785-41793.

[101] C. A. Trickett, A. Helal, B. A. Al-Maythalony, Z. H. Yamani, K. E Cordova, O. M. Yaghi *Nature Reviews Materials* **2017,** *2*, 17045.

[102] J. R. Li, J. Sculley, H. C Zhou *Chemical Reviews* **2012,** *112* (2), 869-932.

[103] R. Chen, Z. Yao, N. Han, X. Ma, L. Li, S. Liu, H. Sun, S. Wang *ACS Omega* **2020**, *5*, 15402-15408.

[104] M. Wenig, G. Li, H. Liu, J. Chen, T. An, H. Yamashita *Environ. Sci.: Nano* **2019**, *6*, 1006-1025.

[105] G. Ferey, C. Serre, T. Devic, G. Maurin, H. Jobic, P. L. Llewellyn, G. De Weireld, A. Vimont, M. Daturi, J.-S. Chang *Chem. Soc. Rev.* **2011**, *40*, 550-562.
[106] S. Keskin, T. M van Heest, D. S Sholl *ChemSusChem* **2010**, *3*, 879-891.
[107] L. Sun, M. Wang *J. Environ. Manage.* **1996**, *46(4)*, 327-343.
[108] K. Sumida, D. L. Rogow, J. A. Mason, T. M. McDonald, E. D. Bloch, Z. R. Herm, T.-H. Bae, J. R. Long *Chem. Rev.* **2012**, *112*, 724-781.
[109] D. M. D'Alessandro, B. Smit, J. R. Long *Angew. Chem. Int. Ed.* **2010**, *49*, 6058-6082.
[110] B. Wang, A. P. Cote, H. Furukawa, M. O'Keeffe, M. O. Yaghi *Nature* **2008**, *453*,207-212.
[111] D.-C. Zhong, W.-G. Lu, L. Jiang, X.-L. Feng, T.-B. Lu *Cryst. Growth Des.* **2010**, *10, 2*, 739-746.
[112] J. An, S. J. Geib, N. L. Rosi *J. Am. Chem. Soc.* **2010**, *132*, 38-39.
[113] X. Si, C. jiao, F. Li, J. Zhang, S. Wang, S. Liu, Z. Li, L. Sun, F. Xu, Z. Gabelica, C. Schick *Energy Environ. Sci*. **2011**, *4*, 4522-4527.
[114] R. Vaidhyanathan, S. S. Iremonger, G. K. H. Shimizu, P. G. Boyd, S. Alavi, T. K. Woo *Science* **2010**, *330*, 650-653.
[115] G. Ferey, C. Serre, T. Devic, G. Maurin, H. Jobic, P. L. Llewellyn, G. D. Weireld, A. Vimont, M. Daturi, J.-S. Chang *Chem. Soc. Rev.* **2011**, *40*, 550-562.
[116] S. Bourrelly, P. L. Llewellyn, C. Serre, F. Millange, T. Loiseau, G. Ferey *J. Am. Chem. Soc.* **2005**, *127*, 13519-13521.
[117] S. Millan, B. Gil-Hernandez, E. Miles, S. Gökpinar, G. Makhloufi, A. Schmitz, C. Schlüsener, C. Janiak *Dalton Trans.* **2019**, *48*, 8057-8067.
[118] H. Miura, V. Bon, I. Senkovska, S. Ehrling, S. Watanabe, M. Ohba, S. Kaskel *Dalton Trans.* **2017**, *46*, 14002-14011.
[119] T. K. Maji, G. Mostafa, R. Matsuda, S. Kitagawa *J. am. Chem. Soc.* **2005**, *127*, 17152-17153.
[120] R. Kitaura, K. Seki, G. Akiyama, S. Kitagawa *Angew. Chem.* **2003**, *115*, 444-447.
[121] M. Thommes, K. Kaneko, A. V. Neimark, J. P. Oliver, F. Rodriguez-Reinso, J. Rouquerol, K. S. W. Sing *Pure Appl. Chem.* **2015**, *87*, 1051-1069.
[122] Q.-Y. Yang, P. Lama, S. Sen, M. Lusi, K.-J. Chen, W.-Y. Gao, M. Shivanna, T. Pham, N. Hosono, S. Kusaka, J. J. Perry IV, S. Ma, B. Space, L. J. Barbour, S. Kitagawa, M. J. Zaworotko *Angew. Chem. Int. Ed.* **2018**, *57*, 5684-5689.
[123] M. R. Bryant, A. D. Burrows, C. M. Fitchett, C. S. Hawes, S. O. Hunter, L. L. Keenan, D. J. Kelly, P. E. Kruger, M. F. Mahon, C. Richardson *Dalton Trans.* **2015**, *44*, 9269–9280.